Machine Learning for Intelligent Monitoring of Perovskite Thin-Film Fabrication for Photovoltaics

Zur Erlangung des akademischen Grades eines

DOKTORS DER INGENIEURWISSENSCHAFTEN
(Dr.-Ing.)

von der KIT-Fakultät für
Elektrotechnik und Informationstechnik des
Karlsruher Instituts für Technologie (KIT)

angenommene

DISSERTATION

von

M.Sc. Felix Laufer
geb. in Heilbronn

Tag der mündlichen Prüfung:	07.04.2025
Hauptreferent:	Prof. Dr. Ulrich W. Paetzold
Korreferent:	TT-Prof. Dr. Sebastian Krumscheid

Kurzfassung

Die dringende Notwendigkeit, die Klimakrise zu bewältigen, erfordert einen raschen Übergang zu erneuerbaren Energien, wobei der Solarenergie eine Schlüsselrolle bei der Deckung des weltweit steigenden Energiebedarfs zukommt. Während die siliziumbasierte Photovoltaik den Markt dominiert, nähert sich ihr Wirkungsgrad den theoretischen Grenzen, sodass neue Ansätze erforderlich sind, um die Wirkungsgrade von Solarzellen weiter zu verbessern und den geplanten massiven Ausbau der Photovoltaik-Kapazität zu realisieren. Tandemsolarzellen, die Silizium mit Metallhalogenid-Perowskiten kombinieren, bieten einen vielversprechenden Weg zu höheren Wirkungsgraden und kostengünstiger Herstellung durch lösungsmittelbasierte Verfahren. Die ausgezeichneten optoelektronischen Eigenschaften von Perowskiten, wie einstellbare Bandlücken und hohe Absorptionskoeffizienten, machen sie zu idealen Kandidaten für die nächste Generation der Photovoltaik.

Trotz bemerkenswerter Fortschritte bei der Perowskit-Photovoltaik im Labormaßstab bleiben Langzeitstabilität und gleichbleibend hohe Wirkungsgrade bei der industriellen Skalierung auf große Flächen zentrale Herausforderungen für die Kommerzialisierung der Perowskit-Technologie. Die Überführung in die industrielle Produktion erfordert die Ablösung des derzeitigen Standardverfahrens Rotationsbeschichtung für die kleinflächige Fertigung durch skalierbare Techniken wie die Klingen- oder Schlitzdüsenbeschichtung. Neben der ohnehin schon komplexen Formationsdynamik bringt die Skalierung auf große Flächen zusätzliche Herausforderungen mit sich, da die Wahrscheinlichkeit von Defekten und Inhomogenitäten steigt, was die Herstellung gleichmäßiger, qualitativ hochwertiger Dünnschichten erschwert. Da *Ex-Situ*-Techniken diese dynamischen Prozesse nicht erfassen können, sind fortschrittliche *In-Situ*-Überwachungssysteme unerlässlich, um die Dünnschichtbildung zu überwachen und zu steuern, die Homogenität zu gewährleisten, Defekte zu minimieren und Fertigungsparameter zu optimieren.

Diese Arbeit greift dieses Problem auf, indem sie ein System entwickelt, das fortschrittliche *In-Situ*-Bildgebung mit maschinellem Lernen kombiniert, um die Bildung von Perowskit-Dünnschichten zu überwachen, zu analysieren und zu optimieren und so eine Brücke zwischen Laborprozessen und industrieller Produktion zu schlagen. Ein auf Photolumineszenz und diffuser Reflexion basierendes bildgebendes System wird vorgestellt, das räumliche, zeitliche und spektrale Informationen während der Filmbildung erfasst und so die Erkennung von Defekten wie Löchern und Schichtdickenschwankungen ermöglicht. Mit hoher zeitlicher Auflösung liefert das System Einblicke in die kritischen Phasen der Perowskit-Dünnschichtbildung, bestehend aus Trocknung, Nukleation und Kristallwachstum. Mit diesem Monitoringsystem werden zwei umfangreiche experimentelle Datensätze erstellt, die Daten von mehr als 3300 klingenbeschichteten Perowskit-Solarzellen und 4448 Dünnschichten enthalten. Diese Datensätze bilden die Grundlage für eine datenbasierte Analyse der komplexen Zusammenhänge zwischen *In-Situ*-Überwachungsdaten und dem Wirkungsgrad von Solarzellen.

Da die Komplexität der Daten die analytischen Fähigkeiten des Menschen übersteigt, werden maschinelle Lernverfahren auf diesen Daten trainiert, um Materialzusammensetzungen, Dünnschichteigenschaften und Wirkungsgrade von Solarzellen präzise vorherzusagen, noch bevor deren Herstellung abgeschlossen ist. Maschinelles Lernen verbessert die *In-Situ*-Charakterisierung, indem es komplexe Daten in frühzeitige Qualitätsbeurteilungen umwandelt, Materialinkonsistenzen erkennt, Dünnschichtvariationen identifiziert und Wirkungsgradvorhersagen für eine verbesserte Dünnschichtqualität und Reproduzierbarkeit liefert. Die Modelle übertreffen dabei deutlich Referenzwerte, die menschliche Vorhersagefähigkeiten repräsentieren. Neuronale Netze zeigen insbesondere für industrielle Anwendungen vielversprechende Ergebnisse, da ihre Leistungsfähigkeit mit zunehmender Datensatzgröße stärker ansteigt. Der Übergang von prädiktiver zu präskriptiver Analyse ermöglicht durch maschinelles Lernen gesteuerte Handlungsempfehlungen zur Prozessoptimierung, indem Überwachungsdaten anhand variabler Prozessparameter

prognostiziert und der entsprechende Solarzellenwirkungsgrad vorhergesagt wird. Methoden der erklärbaren künstlichen Intelligenz identifizieren kritische Phasen der Dünnschichtbildung, beleuchten Zusammenhänge zwischen *In-Situ*-Daten und Solarzellenwirkungsgrad und übersetzen diese Erkenntnisse in anwendbare Empfehlungen.
Dieser Ansatz der fortschrittlichen *In-Situ*-Charakterisierung integriert mit maschinellem Lernen überwindet die Einschränkungen der manuellen Defekterkennung, erlaubt eine Zuordnung der Prozessdaten zum Wirkungsgrad und ermöglicht eine verbesserte Prozesskontrolle. Durch die Überwindung zentraler Hürden für die Kommerzialisierung wird eine skalierbare Hochdurchsatz-Produktion von Perowskit-Solarzellen mit verbesserter Reproduzierbarkeit und Qualität ermöglicht, welche die industrielle Verbreitung beschleunigt und zur globalen Energiewende beiträgt.

Abstract

The pressing need to address the climate crisis requires a rapid transition to renewable energy, with solar energy playing a key role in meeting the world's growing energy demands. While silicon-based photovoltaics dominate the market, their efficiency approaches theoretical limits, requiring new approaches to improve solar cell performance to realize the projected massive expansion of photovoltaic capacity. Tandem solar cells combining silicon with metal halide perovskites offer a promising path forward, enabling higher efficiencies and the potential for low-cost manufacturing through solution processing. The exceptional optoelectronic properties of perovskites, such as tunable bandgaps and high absorption coefficients, make them ideal candidates for next-generation photovoltaics.

Despite remarkable progress in laboratory-scale devices, long-term stability and maintaining high performance over large areas during industrial scale-up remain challenges for the commercialization of perovskite photovoltaics technology. The transition from small-scale fabrication to industrial production requires replacing the state-of-the-art spin coating process with scalable techniques like blade coating or slot-die coating. Beyond the inherently complex formation dynamics, scaling to large areas introduces additional challenges as the likelihood of defects and inhomogeneities increases, complicating the fabrication of uniform, high-quality thin films. Since *ex situ* techniques cannot capture these dynamic processes, advanced *in situ* monitoring systems are essential to observe and control the thin-film formation to ensure uniformity, minimize defects, and optimize fabrication parameters.

This work addresses this need by developing a system that combines advanced *in situ* imaging with machine learning to monitor, analyze, and optimize the perovskite thin-film formation, providing a framework for scaling laboratory processes to industrial production. A multi-channel photoluminescence and diffuse reflection imaging system is introduced that captures spatial, temporal, and spectral information during thin-film formation, enabling the detection of defects such as pinholes and thickness variations. With high temporal resolution, the system provides insight into the critical phases of the perovskite thin-film formation, including drying, nucleation, and crystal growth. Using this monitoring system, two extensive experimental datasets are generated, including data from over 3300 blade-coated perovskite solar cells and 4448 thin films, which provide the basis for data-driven analysis of the complex relationship between *in situ* monitoring data and solar cell device performance.

As the complexity of the data exceeds human analytical capabilities, machine learning models are trained on this data to accurately predict material composition, thin film properties, and device performance before fabrication is complete. Machine learning enhances *in situ* characterization by transforming complex data into early quality assessments, enabling the detection of material inconsistencies, identification of thin film variations, and performance predictions for improved quality and reproducibility. The models substantially outperform baselines representing human predictive capabilities. Neural networks are particularly promising for industrial applications, showing stronger performance improvements as the dataset size increases. Moving from predictive to prescriptive analysis, machine-learning-driven recommendations actively guide process optimization by forecasting monitoring data based on a variable process parameter and predicting the corresponding device performance. Explainable artificial intelligence techniques identify critical phases of the thin-film formation, elucidating relationships between *in situ* data and device performance, and translating insights into actionable recommendations.

This integrated approach of advanced *in situ* characterization and machine learning overcomes the limitations of manual defect detection, establishes the mapping of process data to photovoltaic performance, and enables improved process control. By addressing key barriers to commercialization, it enables scalable, high-throughput production of perovskite solar cells with improved reproducibility and quality, accelerating their industrial adoption and contributing to the global transition to renewable energy.

Contents

Kurzfassung . . . . . **i**

Abstract . . . . . **iii**

List of Abbreviations . . . . . **ix**

1 Introduction **1**
1.1 Motivation 1
1.2 Research Objectives 4
1.3 Outline 5

2 Fundamentals **7**
2.1 Hybrid Perovskite Semiconductors 8
2.1.1 Crystal Structure 8
2.1.2 Optoelectronic Properties 9
2.2 Perovskite Solar Cells 10
2.2.1 Working Principle 10
2.2.2 Electrical Characteristics and Photovoltaic Metrics 13
2.3 Machine Learning 14
2.3.1 Learning Approaches 15
2.3.1.1 Supervised Learning 15
2.3.1.2 Unsupervised Learning 16
2.3.2 Regression and Classification 17
2.3.3 Tree- and Neighbor-Based Machine Learning 17
2.3.4 Neural Networks 19
2.3.5 Training, Validation, and Testing 20
2.3.6 Model Evaluation 22
2.3.7 Explainable Artificial Intelligence 23
2.3.8 Dimensionality Reduction 25
2.3.9 Computational Resources 26
2.4 Machine Learning for Perovskite Photovoltaics 27

3 Methods **31**
3.1 Perovskite Solar Cell Fabrication 32
3.1.1 Solution Processing 32
3.1.1.1 Blade Coating 32
3.1.1.2 Vacuum Quenching 33
3.1.1.3 Perovskite Thin-Film Formation 34
3.1.2 Vapor Phase Deposition 35
3.1.2.1 Thermal Sublimation 36
3.1.2.2 Sputtering 36
3.1.3 Solar Cell Architecture and Materials 37
3.2 Characterization 39
3.2.1 Optoelectronic Characterization 39
3.2.2 Profilometry 40

3.2.3 Photoluminescence . . . 40
3.2.3.1 Luminescence Imaging . . . 42
3.2.3.2 Photoluminescence Versus Electroluminescence . . . 43

4 *In Situ* Multi-Channel Imaging of Perovskite Thin Films . . . 45
4.1 Motivation . . . 46
4.2 Spatially Resolved Characterization with Multi-Channel Imaging . . . 48
4.2.1 Setup: Photoluminescence and Diffuse Reflection Imaging . . . 48
4.2.2 Photoluminescence Peak Wavelength Imaging . . . 49
4.2.3 Detection of Thin Film Inhomogeneities and Defects . . . 51
4.2.4 Correlating Defects in Perovskite Thin Films with Device Performance . . . 51
4.2.5 Electroluminescence Imaging . . . 52
4.3 *In Situ* Imaging for Thin-Film Formation Monitoring with Temporal Resolution . . . 55
4.3.1 Thin-film Formation during Vacuum Quenching . . . 56
4.3.2 Thin-film Formation during Laminar Gas Flow Quenching . . . 59
4.3.2.1 Differentiating Process Parameters using *In Situ* Monitoring . . . 60
4.4 Summary . . . 61

5 Machine Learning for a Data-Driven Analysis of the Perovskite Thin-Film Formation . . . 63
5.1 Motivation . . . 64
5.2 Experimental *In Situ* Photoluminescence Imaging Dataset for Blade-Coated Perovskite Photovoltaics 66
5.3 Advantages of *In Situ* Monitoring over *Ex Situ* Measurements . . . 68
5.4 Data Exploration with Unsupervised Machine Learning . . . 71
5.4.1 Clustering Human-Selected Data Features . . . 72
5.4.2 Clustering *In Situ* Photoluminescence Transients without Human Data Selection . . . 74
5.4.3 Spatial Distribution of Clusters Reveals Heterogeneous Thin-Film Quality . . . 78
5.5 Predicting Solar Cell Performance Prior to Device Completion using Supervised Machine Learning . 82
5.6 Prediction Accuracy of Various Machine Learning Algorithms using Different Input Data . . . 86
5.7 Summary . . . 91

6 Deep Learning for Enhanced Monitoring of the Perovskite Thin-Film Formation . . . 93
6.1 Motivation . . . 94
6.2 *In Situ* Photoluminescence Dataset for Exploring Material and Processing Variabilities in Blade-Coated Perovskite Photovoltaics . . . 96
6.3 Detecting Material Composition Inconsistencies . . . 99
6.4 Predicting Holistic Device Performance with Varying Process Parameters . . . 106
6.5 From Passive Analysis to Active *In Situ* AI Recommendation . . . 112
6.5.1 *In Situ* Data Forecasting and Device Performance Prediction . . . 113
6.5.1.1 Perovskite Thin Film Morphology Forecasting . . . 119
6.5.2 *In situ* AI recommendation system . . . 120
6.6 Summary . . . 122

7 Enhanced Understanding of the Perovskite Thin-Film Formation through Explainable AI . . . 125
7.1 Motivation . . . 126
7.2 Importance of Capturing Temporal *In Situ* Data . . . 127
7.3 Insights into the Thin-Film Formation From Explainable AI . . . 129
7.3.1 Feature Attribution . . . 129
7.3.2 Counterfactual Explanations . . . 131
7.4 From XAI Findings to Data-Driven Recommendations for Experimental Research . . . 133
7.5 Summary . . . 134

8 Conclusion . . . **137**
8.1 Summary . . . 137
8.2 Outlook . . . 140

Appendix . . . **143**
A.1 Resources, Funding, and Tools . . . 143
A.2 Author Contributions According to CRediT System . . . 144
A.2.1 Correlative In Situ Multichannel Imaging for Large-Area Monitoring of Morphology Formation in Solution-Processed Perovskite Layers . . . 145
A.2.2 Process Insights into Perovskite Thin-Film Photovoltaics from Machine Learning with In Situ Luminescence Data . . . 146
A.2.3 Deep learning for augmented process monitoring of scalable perovskite thin-film fabrication . . . 147
A.2.4 Discovering Process Dynamics for Scalable Perovskite Solar Cell Manufacturing with Explainable AI . . . 148
A.3 Photoluminescence Versus Electroluminescence . . . 149
A.4 *In Situ* Imaging Setup – Applications . . . 150
A.5 Exploration of *In Situ* Imaging Data . . . 152
A.5.1 Clustering Human-Selected Features . . . 152
A.5.2 Clustering Transients of Diffuse Reflection and Photoluminescence Peak Wavelength . . . 154
A.5.3 Spatial Distribution of Clusters and Subclusters . . . 156
A.5.4 Solar Cell Performance Dependent on Substrate Location . . . 157
A.5.5 Solar Cell Performance Dependent on Date for Both Datasets . . . 158
A.6 Material Classification and PCE Regression . . . 159
A.7 Generating *In Situ* AI Recommendations . . . 162
A.7.1 Function Approximation by Interpolation with Gaussian Processes . . . 162
A.7.2 Quenching-Time-Dependent Thin Film Morphology . . . 163
A.7.3 Quenching-Time-Dependent Power Conversion Efficiency . . . 164
A.7.4 Spatially-Resolved Forecasting and Predictions . . . 165
A.8 Enhanced Understanding of Thin-Film Formation through Machine Learning . . . 167

List of Figures . . . **169**

List of Tables . . . **173**

Bibliography . . . **175**

List of Publications, Conference Contributions, Awards, and Published Datasets . . . **201**
Journal Articles . . . 201
Peer-Reviewed Publications (First Author) . . . 201
Peer-Reviewed Publications (Co-Author) . . . 201
Conference Contributions . . . 203
Conference Proceedings . . . 203
Oral and Poster Contributions (First Author Only) . . . 203
Invited Contributions . . . 204
Awards . . . 204
Published Datasets . . . 204
Supervised Student Projects . . . 205

Acknowledgments . . . **207**

List of Abbreviations

AI	Artificial Intelligence
CE	Counterfactual Explanation
DCP	Double Cation Perovskite (here: $Cs_{0.17}FA_{0.83}Pb(I_{0.91}Br_{0.09})_3$)
DL	Deep Learning
EL	Electroluminescence
FF	Fill Factor
IPDRI	*In Situ* Photoluminescence and Diffuse Reflection Imaging
$\mathbf{J_{SC}}$	Short-Circuit Current Density
LP	Longpass Filter
ML	Machine Learning
MAE	Mean Absolute Error
MSE	Mean Squared Error
MAPI	Methylammonium Lead Iodide
NN	Neural Network
PCE	Power Conversion Efficiency
PL	Photoluminescence
PLQY	Photoluminescence Quantum Yield
PSC	Perovskite Solar Cell
PV	Photovoltaics
$\mathbf{R^2}$	Coefficient of Determination
$\mathbf{R_{diff}}$	Diffuse Reflection
RMSE	Root Mean Square Error
Si	Silicon
SP	Shortpass Filter
TCAV	Testing of Concept Activation Vectors
$\mathbf{V_{OC}}$	Open-Circuit Voltage
XAI	Explainable Artificial Intelligence

1 Introduction

1.1 Motivation

The climate crisis is one of the most critical challenges of our time, demanding immediate global action.[1] Driven by massive increases in greenhouse gas emissions for energy generation from fossil energy resources such as coal and natural gas, global warming continues to drive up temperatures.[2] To address anthropogenic climate change and meet the Paris Agreement goal of limiting global warming to a maximum of 2 °C above pre-industrial levels, it is essential to develop and implement alternative energy technologies with minimal greenhouse gas emissions to replace current fossil fuel-based systems.[3] Without transformative mitigation efforts, global warming will exceed 2 °C within decades, leading to more frequent extreme weather events, rising sea levels, and loss of biodiversity.[1] To avoid irreversible ecological and societal damage, energy generation must shift from fossil fuels to sustainable energy sources to "sustain life on planet Earth, our only home"[4].

At the same time, global energy demand is growing rapidly, driven by population growth, improvements in living standards, and the electrification of traditionally fossil-fuel-dependent sectors. For example, the electrification of heating, transportation, and industrial processes represents a transformative shift in energy consumption (see Figure 1.1a). Decarbonization of electricity, combined with widespread electrification of nearly all sectors of the energy system, represents the most effective path to a low-carbon, sustainable energy future.[5, 6]

Achieving this goal requires a rapid and comprehensive transition to renewable energy sources, with solar power, in addition to wind power, playing a central role in decarbonizing the global energy system and meeting the world's

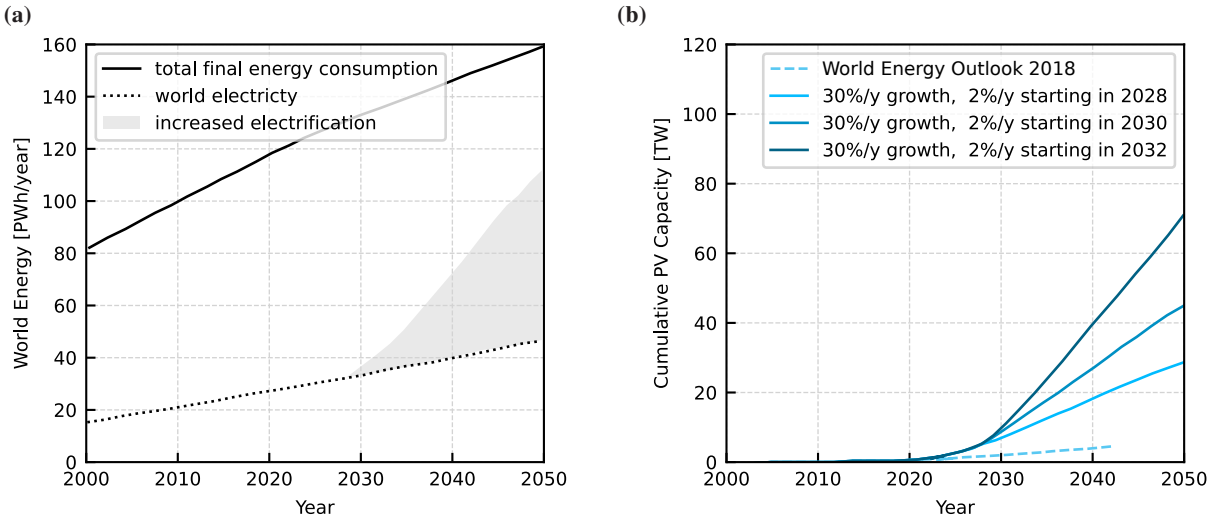

Figure 1.1: Global energy trends and projected photovoltaic (PV) capacity growth. (a) The increasing global energy demand driven by electrification of sectors like heating, transportation, and industrial sectors. The total final energy consumption and electricity demand are projected to rise sharply, especially under scenarios of accelerated electrification. (b) Projections of cumulative PV capacity under various growth scenarios. The World Energy Outlook 2018 baseline is compared with scenarios of 30% annual growth transitioning to 2% annual growth starting in different years. These projections highlight the critical role of PV in achieving global decarbonization goals. Reproduced from [5, 6].

growing energy needs. As an abundant, renewable, and cost-effective resource, it has the potential to replace fossil fuels on a large scale. Photovoltaic (PV) technology, which converts sunlight into electricity, is at the heart of this transition. The PV market is experiencing remarkable growth, with a compound annual growth rate of approximately 26% in cumulative installations between 2013 and 2023. By the end of 2023, cumulative PV installations worldwide reached 1581 GW, with Germany accounting for 82.7 GW.[7] Silicon (Si) wafer-based PV technology dominates the market, accounting for about 97% of total production in 2023. This growth in PV installations is largely due to significant cost reductions achieved through upscaling and technological advances in solar cell manufacturing, resulting in levelized costs of electricity (LCOE) falling below 0.05 €/kWh.[7] Underscoring their economics, PV systems in Germany now generate electricity at a much lower cost than conventional power plants such as coal, gas, or nuclear, even when combined with battery storage systems.[8]

However, meeting the growing energy demand requires an even more massive expansion of PV capacity, as solar energy is projected to provide 56% of global electricity by 2050, while the share of fossil fuels declines from 62% in 2020 to just 21%.[9] Achieving global climate goals and meeting future energy needs will require tens of terawatts of installed PV, with estimates reaching as much as 75 TW of installed PV worldwide by 2050[10] and potentially scaling up to 170 TW by 2100[11], representing a dramatic increase from current deployment levels (see Figure 1.1b). Although realizing the potential of solar energy at the terawatt scale presents challenges, historical trends indicate that renewable energy deployment has consistently exceeded predictions, with past projections proving to be overly pessimistic.[12] To further accelerate PV deployment and meet energy demand targets, continued efforts to reduce costs remain essential.

While the dramatic decline in PV module costs has been critical to market growth, further cost reductions in module manufacturing alone will have diminishing returns on overall system economics. Module costs now account for only about 30% of total system costs, with the balance of system (BOS) components such as inverters, mounting structures, land, and installation labor accounting for the rest (see Figure 1.2a).[7] This limits the impact of further module price reductions on overall costs. Instead, increasing solar cell efficiency can substantially improve the economics of the PV system.[13]

While Si PV technology dominates the market, major improvements in solar cell performance require new technological approaches. Si-based laboratory solar cells are nearing their theoretical efficiency limit of about 29.4%, with certified records exceeding 27%.[14] To surpass the theoretical single-junction limit of about 33.7%, multi-junction solar cells have emerged as a promising solution.[15, 16] Among these, tandem solar cells, which stack two cells with different band gaps, provide a practical route to higher efficiency. The combination of well-established Si solar cells with emerging metal halide perovskite semiconductor technology offers a particularly effective strategy for achieving high-performance tandem solar cells.

Due to their tunable bandgap, metal halide perovskites enable optimized utilization of the solar spectrum when paired with silicon cells. Their exceptional optoelectronic properties, including high absorption coefficients and long carrier diffusion lengths, make them ideal candidates for next-generation photovoltaics. Over the past decade, perovskite solar cells (PSCs) have demonstrated an unprecedented increase in power conversion efficiency (PCE) (see Figure 1.2b).[17] Single-junction perovskite cells have achieved certified PCE exceeding 26%[17–19], while perovskite-silicon tandem cells have achieved around 34%[14, 17, 20, 21]. While there is ongoing research into thermal evaporation techniques, such as co-evaporation of precursor materials or sequential layer deposition, academic efforts are predominantly focused on solution processing methods.[22] A key advantage of perovskite solar cells is their potential for low-cost fabrication in future industrial production, which is made possible by solution processing at low temperatures.[23]

However, laboratory-scale efficiency records are achieved using spin-coating, a method that is not scalable to large-area solar cell fabrication. Therefore, in addition to improving long-term stability[24, 25], the ability to upscale perovskite solar cell fabrication to large areas remains a critical challenge on the path to commercialization of perovskite photovoltaics.[26, 27] Scalable methods such as blade coating, slot-die coating, and inkjet printing enable large-area PSCs.[28] However, the PCEs of large-area PSCs fabricated by scalable methods remain lower than their smaller counterparts, with the PCE decreasing as the area increases (see Figure 1.2c).[29] In contrast, upscaling

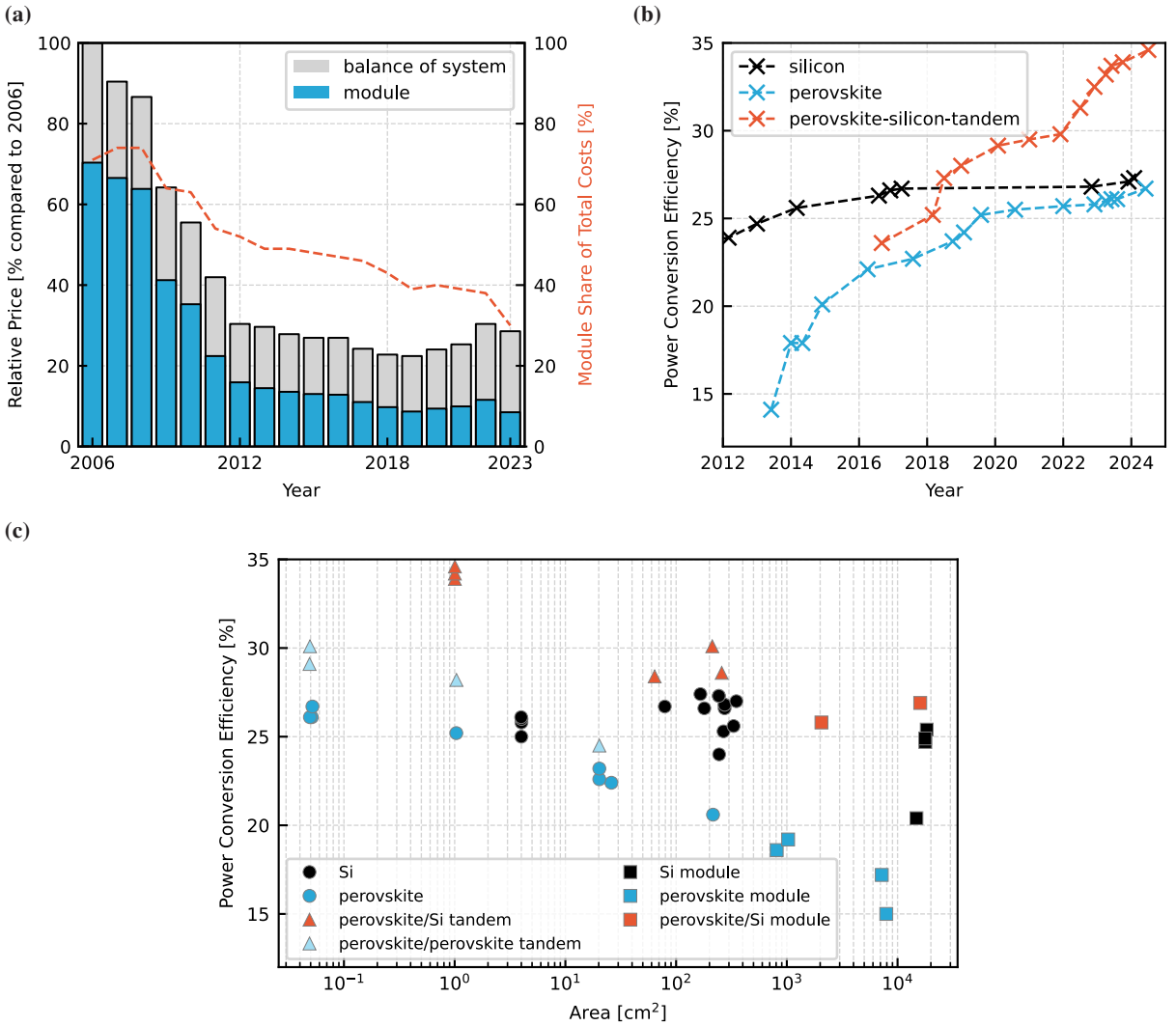

Figure 1.2: Trends in photovoltaic (PV) system costs and efficiencies. (a) Balance of system (BOS) and module cost trends, illustrating the significant decline in relative prices and the decreasing share of module costs in total system costs. Reproduced from [7]. (b) Increase of power conversion efficiencies (PCEs) of silicon, perovskite, and perovskite-silicon tandem solar cells, highlighting the rapid advances and the potential of perovskite PV to complement traditional silicon-based solar cells.[17] (c) PCE versus solar cell area comparison for different PV technologies, demonstrating the scalability challenges for perovskite-based systems, with efficiency decreasing as the device area increases, unlike silicon solar cells, which maintain stable performance across different sizes.[14]

of Si solar cells does not result in a significant decrease in PCE, with efficiencies of 27.4% at 166 cm^2 and 25.4% at 18342 cm^2 for crystalline Si cells (both LONGi).[14] Perovskite single-junction cells achieve over 26% PCE on small areas[18, 19], but drop to 19.2% at 1027 cm^2 (SolaEon), 17.2% at 7200 cm^2 (Renshine), and 15.0% at 7906 cm^2 (Microquanta).[14] Similarly, perovskite-silicon tandem cells decrease from 34.6% to 25.8% at 2054 cm^2 (both LONGi).[14] However, promising recent advances in perovskite-silicon tandem modules include Oxford PV's 60-cell residential module with a record 26.9% efficiency, surpassing the best silicon modules at around 25%, for a similar area of 1.6 m^2.[14, 30] In addition, their first commercial panels, with a module efficiency of 24.5%, further demonstrate the potential of high-efficiency perovskite-silicon tandems, offering performance above commercial silicon technology.[31]

Reducing the cost of perovskite PV modules is critical to their competitiveness with silicon-based solar cells, which

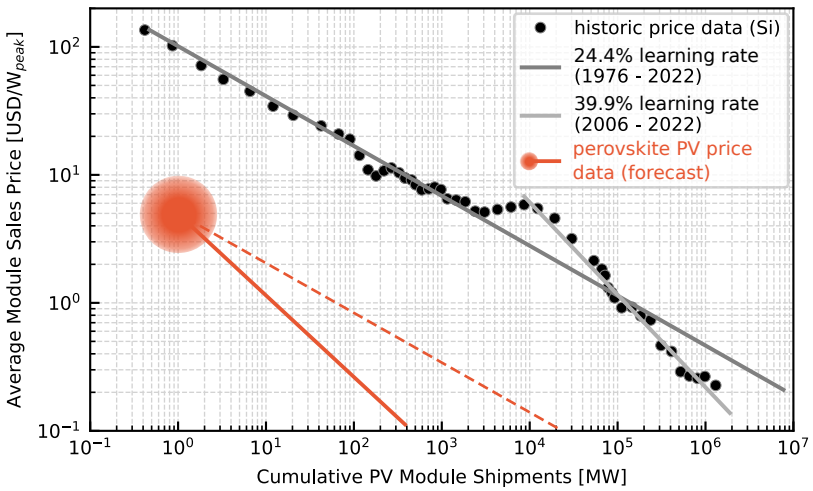

Figure 1.3: Learning rates and projected price reductions for photovoltaic (PV) modules. Cumulative PV module shipments versus average module sales price for silicon-based PV modules, demonstrating historical price reductions with high learning rates.[32] The perovskite PV price data highlights the potential for dramatic cost reductions, as projected by techno-economic analyses.[33–38] These trends underline the cost-competitiveness of perovskite PV as production scales up, positioning it as a promising complement to silicon technology in the solar market. Reproduced from [32, 38].

have benefited from decades of price reductions and technological improvements (see Figure 1.3).[32, 38] Techno-economic analyses suggest that scaling up production capacity could reduce costs from \$3.30/W for a small-scale annual production[39] to minimum sustainable prices of \$0.30– \$0.70/W for larger factory sizes.[33–37] Pilot production lines, such as 100 MW plants from Oxford PV, Mellow Energy, and Auner, as well as GCL Group's planned 2 GW production line, demonstrate progress in scaling perovskite PV manufacturing.[40] Utmolight claims module costs as low as \$0.11/W with its upcoming 1 GW commercial line.[41] While perovskite PV is still in the early stages of industrial production, its potential for rapid cost reductions positions it as a promising complement to silicon technology in the global solar market.

Building on the extensive global research on perovskite PV, the integration of machine learning (ML) offers powerful new approaches to address key challenges and accelerate commercialization. Traditional experimental approaches in perovskite research are often limited by time-consuming and labor-intensive processes, particularly when exploring the vast parameter space of material compositions and processing conditions. ML has emerged as a transformative tool that can extract meaningful insights from complex datasets, enabling rapid material discovery, process optimization, stability prediction, and laboratory automation (see section 2.4). This thesis focuses on using ML-driven methods to improve the reproducibility, uniformity, and scalability of the large-area perovskite thin-film fabrication. As the performance gap between small-scale laboratory devices and large-area modules remains a critical challenge, this work demonstrates how ML can advance characterization techniques to detect and quantify spatial inhomogeneities and temporal inconsistencies, supporting the development of high-performance large-area perovskite solar cells required for commercialization.

1.2 Research Objectives

One of the key challenges remaining for the commercialization of perovskite PV technology is the reproducible large-area fabrication of the perovskite absorber layer. Upscaling to larger areas required for modules limits the achievable PCE, given that the probability of material defects scales with the area. In addition to deposition techniques for large-area fabrication, suitable characterization methods are required to detect spatial inhomogeneities or temporal variations. Due to the complex experimental process, detecting and quantifying differences in the

acquired data is challenging without the support of data-driven methods. Machine learning is used to enhance the evaluation of imaging data acquired from perovskite thin films.
This work leverages the strengths of machine learning to evaluate imaging data of perovskite thin films by investigating the following research objectives:

I: **Novel imaging technique for large-area characterization**
Establishment of a novel imaging technique for large-area characterization of perovskite thin films and its application to *in situ* monitoring of perovskite thin-film formation from solution.

II: **Laboratory-scale experimental datasets**
Generation of multiple laboratory-scale experimental datasets of *in situ* photoluminescence and reflection data to investigate the perovskite thin-film formation using machine learning.

III: **Material and device property prediction**
Prediction of precursor material composition, perovskite thin film thickness, and device characteristics such as solar cell performance from experimental photoluminescence and reflection data before completing the remaining processing steps.

IV: **Enhanced experimental data analysis**
Demonstration of the essential role of machine learning in enhancing experimental data analysis and its ability to provide *in situ* recommendations to improve control of experimental processes.

V: **Insights into thin-film formation**
Leverage explainable artificial intelligence to render the complex correlations between monitoring data and metrics of interest humanly understandable.

The research objectives are addressed in the motivation and in the summary of the respective chapters and their implementation is discussed. The summary in Chapter 8 compares all the results generated in this work with the research objectives and discusses how successfully they were implemented and which future research objectives could be defined.

1.3 Outline

A brief introduction is provided in Chapter 1, which places perovskite photovoltaics in the broader context of future renewable energy generation, outlines the motivation for this work, and states the research objectives. Chapter 2 introduces the key concepts necessary to understand this work, covering the properties of hybrid perovskite semiconductors and their application in perovskite solar cells, the working principle of solar cells, and the fundamentals of machine learning.
Section 2.4 summarizes state-of-the-art machine learning applications that address challenges in perovskite photovoltaics research.
Chapter 3 introduces the experimental fabrication methods for solar cells and the measurement techniques used for their characterization in this work.
Chapter 4 introduces photoluminescence and diffuse reflection imaging, demonstrating its effectiveness as *in situ* characterization method during perovskite thin-film formation (research objective **I**).
Chapter 5 analyzes the first dataset with constant processing parameters, revealing correlations between *in situ* data, perovskite thin film thickness, and solar cell performance metrics through unsupervised and supervised machine learning (research objectives **II & III**).
Chapter 6 extends these findings to a second dataset with varying processing parameters, showing that deep learning models can predict precursor molarity, molar ratio, and PCE based on monitoring data. Furthermore, *in situ*

forecasting enables the generation of actionable recommendations to improve process control during the perovskite thin-film formation (research objectives **II, III, & IV**).
Chapter 7 demonstrates how explainable AI enhances model interpretability by identifying the key factors influencing predictions and providing insights into why they are important (research objective **V**).
The key findings of this work are summarized in Chapter 8, where they are contextualized in relation to the defined research objectives (see section 1.2). In addition, the outlook discusses future directions for machine learning in perovskite photovoltaics, focusing on advanced monitoring, defect detection, process optimization, and its role in scaling up fabrication for industrial applications.

2 Fundamentals

This chapter provides the theoretical background required for understanding and evaluating the results presented in this thesis. The material class of hybrid metal halide perovskites is introduced, focusing on the crystal structure of the material and its optoelectronic properties. The fundamental working principle of a perovskite solar cell is explained and the photovoltaic performance metrics are introduced. A concise overview of the fundamentals of machine learning is given, covering different learning approaches, problem types, model architectures, and the methods used for their training and evaluation. Due to the interdisciplinary topic presented in this thesis, the intersection of machine learning and perovskite photovoltaics is explored. The section highlights how data-driven approaches enable materials discovery, property prediction, process optimization, and improved scientific understanding.

2.1 Hybrid Perovskite Semiconductors

Given the extensive and rapidly evolving field of perovskite photovoltaics, this section provides a concise overview of the key concepts and the background relevant to this thesis.

The term *perovskite* originates from the mineral calcium titanate ($CaTiO_3$), named after the Russian mineralogist Lev Aleksevich Perovski. Originally derived from the crystal structure of the mineral, the term nowadays typically refers to the general class of compounds characterized by the same ABX_3 structure.

2.1.1 Crystal Structure

The perovskite crystal structure is represented by the chemical formula ABX_3, where A is a monovalent cation, B is a divalent cation, and X is an anion. Due to the integration of both organic and inorganic components in their structure, many perovskites are classified as *hybrid*, with either an organic or inorganic (Cs^+) cation occupying the A site, a metal cation occupying the B site, and a halide anion occupying the X site. The positions of the ions in the crystal structure can be described by a cubic unit cell (see Figure 2.1a). In the perovskite unit cell, the A cations are located at the corners of the cube, the B cations at the body center, and the X anions at the face centers. The formation of a cubic perovskite structure is determined by the ionic radii in the crystal lattice. The Goldschmidt tolerance factor (t) is a measure for estimating the formation of a perovskite crystal structure[42]:

$$t = \frac{r_A + r_X}{\sqrt{2}(r_B + r_X)} \tag{2.1}$$

where r_A, r_B and r_X are the ionic radii of the corresponding ions. The perovskite phase is formed when $0.8 < t < 1.0$. A tolerance factor of 0.9 - 1.0 results in an ideal cubic structure, while smaller tolerance factors lead to tetragonal, orthorhombic, or rhombohedral perovskite structures with tilted BX_6^{4-} octahedra, because the A cation is too small or the B cation is too large. Even smaller tolerance factors ($t < 0.8$) or values of $t > 1$ lead to non-perovskite structures.[43–45] Perovskite materials with a given chemical composition often exhibit multiple structural phases, depending on the temperature and methods used during their preparation.[45] The photoactive perovskite phases are commonly referred to as the α, β, and γ phases (in order of highest to lowest symmetry), while the non-perovskite phases (e.g., trigonal or hexagonal crystal structures) are referred to as the δ phase.[46] While the choice of A

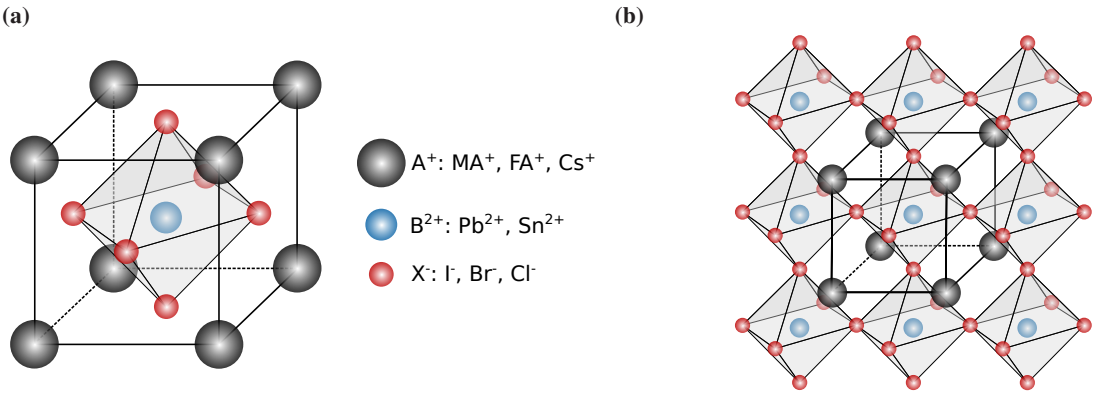

Figure 2.1: Schematic representation of the perovskite crystal structure. (a) The cubic perovskite unit cell with the general chemical formula ABX_3, where A is a monovalent cation, B is a divalent metal cation, and X is a halide anion. The A cation occupies the cube corners, B the body center, and X the face centers. (b) The arrangement of the ions and the lattice structure determine the optoelectronic properties of the material, which are critical for photovoltaic applications. In hybrid organic-inorganic perovskites, the large A cations are organic molecules, while B is typically lead or tin.

cations is important for the formation of 3D perovskite material (as very large A cations lead to the formation of 2D perovskite structures[47]), the BX_6^{4-} octahedra mostly determine the bandgap of the semiconductor.[48]
By engineering the crystal structure of the compound, perovskites with outstanding optoelectronic properties are realized, making them attractive candidates for next-generation photovoltaics. For PV applications, hybrid organic-inorganic metal halide perovskites have attracted substantial research and industrial interest. In their crystal structure, the relatively large A cation site is occupied by organic cation molecules such as Methylammonium (MA^+,$CH_3NH_3^+$), Formamidinium (FA^+ $CH(NH_2)_2^+$), or by cesium (Cs^+) cations. The smaller B cation site is occupied by metallic cations such as lead (Pb^{2+}) or tin (Sn^{2+}), and halogenic anions like iodine (I^-), bromine (Br^-), or chlorine (Cl^-) occupy the X sites.
Different cations can be incorporated into the perovskite structure, allowing materials engineering. By mixing various relatively large cations, metal cations, and halide anions in different molar ratios, the properties of perovskites can be effectively tailored. Due to improved stability and reproducibility, state-of-the-art perovskite compositions typically contain mixtures of A cations forming double (Cs_xFA_{1-x}) or triple cation perovskites ($Cs_xFA_yMA_{1-x-y}$) while taking into account the tolerance factor.[44, 49] In this work, results are presented mainly based on double cation perovskites, specifically with the composition $Cs_{0.17}FA_{0.83}Pb(I_{0.91}Br_{0.09})_3$.
While this section has explicitly addressed the different meanings of the term *perovskite*, in other sections of this work the term is used synonymously with lead halide perovskites.

2.1.2 Optoelectronic Properties

Hybrid metal halide perovskites have been in the focus of PV research since 2006[50, 51], as they possess exceptional optoelectronic properties while promising a wide range of applications and economical production routes. The attractive properties of hybrid perovskite thin films are discussed below:

- **Tunable bandgap:** Through compositional engineering, i.e., by varying the ions in the ABX_3 structure, the direct bandgap of perovskites can be tuned over a wide range of 1.2 - 3 eV. Adjusting the ratio of I^-, Br^-, and Cl^- at the X site increases the bandgap from iodide to bromide to chloride, while partial substitution of Pb^{2+} with Sn^{2+} at the B site reduces the bandgap.[52, 53] This tunability allows precise alignment with the desired absorption spectrum, making perovskites ideal for single-junction and tandem solar cells in combination with established photovoltaic technologies, such as silicon and copper indium gallium selenide (CIGS).

- **High absorption coefficient:** Perovskites exhibit exceptionally high absorption coefficients ($> 10^4\,cm^{-1}$), exceeding those of conventional thin-film PV materials such as GaAs by almost an order of magnitude. This enables efficient light harvesting even with thin absorber layers of a few hundred nanometers. The absorption spectrum of lead halide perovskites covers a broad range of visible light, with a sharply defined onset characteristic of direct semiconductors.[54, 55]

- **Low exciton binding energy:** Metal halide perovskites have low exciton binding energies, which are below the thermal energy at room temperature. This allows photo-generated excitons (bound electron-hole pairs) to spontaneously dissociate into free charge carriers upon light absorption, enabling efficient charge separation and extraction.[56, 57]

- **Long charge carrier lifetimes and diffusion lengths:** Perovskites show remarkable tolerance to intrinsic defects[58, 59], enabling long charge carrier lifetimes exceeding $1\,\mu s$ even in polycrystalline thin films. Combined with high charge carrier mobilities($> 10\,cm^2\ V^{-1}\ s^{-1}$), this results in diffusion lengths of several micrometers.[60–62] These properties, combined with the need for only thin absorber layers due to their high absorption coefficients, significantly increase the probability of charge carrier extraction, making perovskites highly efficient for PV applications.

- **Solution-based fabrication:** Perovskites are well-suited for solution-based processing due to their high defect tolerance and low crystallization temperatures (100 - 150 °C).[28] These temperatures are significantly lower than those required for conventional PV materials like silicon, resulting in energy and cost savings. Solution-based methods reduce the capital investment needed for manufacturing equipment and offer the potential for higher production throughput. In addition, the precursor materials are energy-efficient to synthesize, abundant, and required in minimal quantities due to the thin absorber layers enabled by the high absorption coefficients of perovskites, making fabrication potentially very cost-effective.[33, 63]

Because of their numerous advantages, lead halide perovskites are exceptional absorber materials for next-generation photovoltaics. The functionality of the perovskite solar cells is discussed in detail in the following section.

2.2 Perovskite Solar Cells

2.2.1 Working Principle

Solar cells convert the energy of incident photons into electrical energy using the photovoltaic effect. Upon illumination, the passive devices generate electrical power by simultaneously generating electrical current and electrical voltage. The basic working principle of perovskite solar cells can be summarized in four steps (see Figure 2.2a): (1) absorption of incident photons in the absorber, (2) generation of electron-hole pairs, (3) spatial separation of the electrons and holes, and (4) extraction of the two types of charge carriers at the different contacts and potentials of the solar cell. In a closed electrical circuit, the flow of these charges through the external load constitutes the photocurrent, while the photovoltage arises from a potential difference between the two contacts.[64–66]
After transmission through the transparent electrode, photons with energy above the bandgap (E_G) of the perovskite absorber material are absorbed. Photons with lower energy pass through the material while the additional energy of photons with higher energy results in thermalization losses. The absorption of a photon leads to the generation of a electron-hole pair. The electron-hole pair quickly dissociates into free positive (hole) and negative (electron) charge carriers, which can move freely in the valence band (E_V) and conduction band (E_C), respectively. To generate electrical energy, the two different types of charge carriers need to be separated and extracted from the solar cell device at different locations.

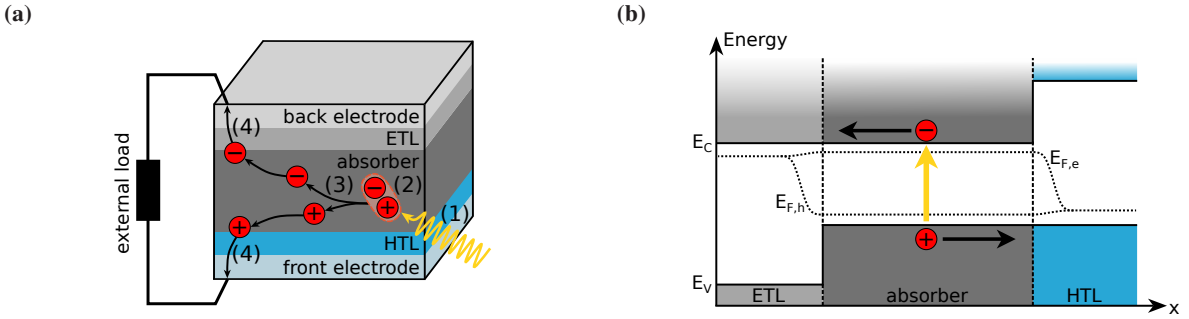

Figure 2.2: Working principle of a perovskite solar cell illustrating charge carrier generation and extraction. (a) Schematic representation of the fundamental processes in a p-i-n perovskite solar cell: (1) photon absorption in the absorber layer, (2) generation of a electron-hole pair, (3) spatial separation of the charge carriers, and (4) extraction at the respective electrodes. (b) Energy band diagram under illumination, showing electron accumulation in the conduction band (E_C) and hole accumulation in the valence band (E_V). The splitting of the Fermi level into quasi-Fermi levels for electrons ($E_{F,e}$) and holes ($E_{F,h}$) creates a potential difference between the electrodes. The selective electron and hole transport layers (ETL and HTL) enable efficient charge carrier separation and extraction.

The charge carrier separation is explained in the following according to Würfel *et al.*[64, 67] who explain the working principle based on gradients of the quasi-Fermi levels and different conductivities for the two charge carrier types in different areas of the solar cell. Electrons and holes are mostly exposed to two different forces in the device. If there is only the electrical force due to an electric field E, the charge current of electrons e or holes h is given by

$$j_{elect,e,h} = en_{e,h}\mu_{e,h}\mathrm{E} = \sigma_{e,h}\mathrm{E} = -\frac{\sigma_{e,h}}{z_{e,h}e}\mathrm{grad}(z_{e,h}e\varphi) \tag{2.2}$$

where e is the elementary charge (with $z_e = -1$ and $z_h = 1$), $n_{e,h}$ the concentration of the charge carriers, $\mu_{e,h}$ is their mobility, and $\sigma_{e,h}$ is their electrical conductivity. φ is the electric potential that causes the charge carriers to be subjected to the electric force $-\mathrm{grad}(z_{e,h}e\varphi)$.
If there is only the second force acting on the charge carriers which is caused by a gradient in the charge carrier concentration, the resulting charge current is given by Fick's law

$$j_{diff,e,h} = z_{e,h}e\left(-D_{e,h}\mathrm{grad}\, n_{e,h}\right) = -\frac{\sigma_{e,h}}{z_{e,h}e}\mathrm{grad}\,\Phi_{\mathrm{chem},e,h} \tag{2.3}$$

where $D_{e,h} = \mu_{e,h}k_\mathrm{B}T/e$ is the diffusion coefficient with the Boltzmann constant k_B and temperature T. $\Phi_{\mathrm{chem},e,h}$ is the chemical potential that causes the charge carriers to be exposed to the chemical force $-\mathrm{grad}\,\Phi_{\mathrm{chem},e,h}$.
Since charge carriers are exposed to both forces simultaneously, the forces $-\mathrm{grad}(z_{e,h}e\varphi)$ and $-\mathrm{grad}\,\Phi_{\mathrm{chem},e,h}$ have to be added

$$j_{total,e,h} = -\frac{\sigma_{e,h}}{z_{e,h}e}\mathrm{grad}\left(z_{e,h}e\varphi + \Phi_{\mathrm{chem},e,h}\right) = -\frac{\sigma_{e,h}}{z_{e,h}e}\mathrm{grad}\left(\eta_{e,h}\right) \tag{2.4}$$

where $\eta_{e,h}$ is the electrochemical potential of the charge carriers.[67]
In the next step, the identity between the electrochemical potential and the Fermi level (E_F) is used. E_F represents the energy level at which the probability of electron states being occupied is 50% at equilibrium, according to the Fermi-Dirac distribution. For $T > 0$, electron states below E_F are more likely to be occupied, while states above E_F are less likely to be occupied. Under illumination, an increase in charge carrier density should move E_F closer to the conduction band minimum due to the increased electron density, while simultaneously shifting E_F closer to the valence band maximum due to the increased hole density. In steady state, this contradiction is resolved by introducing two separate Fermi distributions, one for electrons and one for holes, splitting the Fermi level into two distinct quasi-Fermi levels. In the dark, the Fermi level (E_F) is in equilibrium in all three layers. Under illumination, the Fermi level splits into quasi-Fermi levels of electrons ($E_{F,e}$) and holes ($E_{F,h}$), as the photo-generated carriers lead to increased charge carrier densities in the conduction and valence bands. The splitting of E_F into $E_{F,e}$ and $E_{F,h}$ is called quasi-Fermi level splitting (QFLS).[68, 69] The energy levels of a p-i-n perovskite solar cell under illumination near open-circuit conditions are shown in Figure 2.2b.
The identity between the electrochemical potential of electrons in the conduction band and their quasi-Fermi level ($\eta_e = E_{F,e}$) reflects the occupation of electronic states in the conduction band. Similarly, the electrochemical potential of holes corresponds to their quasi-Fermi level ($\eta_h = -E_{F,h}$), which describes the occupation of states in the valence band. With $z_e = -1$ and $z_h = 1$, the charge current of electrons and holes is given by

$$j_{\mathrm{total},e} = \frac{\sigma_e}{e}\mathrm{grad}(E_{F,e}); \quad j_{\mathrm{total},h} = \frac{\sigma_h}{e}\mathrm{grad}(E_{F,h}). \tag{2.5}$$

Thus, the charge carrier currents are governed by the gradients of the quasi-Fermi levels and the electrical conductivities.
To generate electrical current in a solar cell, electrons and holes must move toward opposite contacts. However, the gradients of the quasi-Fermi levels cannot inherently be engineered to guide electrons toward one contact and holes toward the other. Accordingly, in addition to the gradients, the selective carrier transport in solar cells also requires different conductivities for electrons and holes as they move toward their respective contacts. In perovskite solar cells, the charge carriers are separated using a p-i-n heterostructure with a hole-selective and electron-selective layer sandwiching the intrinsic absorber. Layers that interface with the absorber and facilitate the extraction of electrons

are called electron transport layers (ETLs). Similarly, layers that interface with the absorbing semiconductor to extract holes are called hole transport layers (HTLs).
In a heterostructure of ETL, absorber, and HTL, the desired charge carrier current is in the opposite direction to the maximum gradient of the quasi-Fermi levels (see Figure 2.2b). Therefore, the ETL must have a large difference in the E_V to the absorber, high electron conductivity, and low hole conductivity. Similarly, the HTL must have a large difference in E_C compared to the absorber, high hole conductivity, and low electron conductivity. This selective conductivity ensures that electrons are efficiently transported through the ETL while being blocked by the HTL, and holes are efficiently transported through the HTL while being blocked by the ETL. The selective charge transport layers act like membranes, allowing only the desired charge carrier species to pass while blocking the other species. Given the long charge carrier lifetimes and diffusion lengths of perovskites, nearly all electrons and holes are extracted from the absorber through the ETL and HTL, respectively. The extraction of charge carriers at the respective electrodes allows an electric current to flow through the external load.[64]
The energy difference $E_{F,e}$ - $E_{F,h}$ can be expressed in terms of energy eV, where V represents the voltage drop between the contacts on the ETL and HTL sides. Under short-circuit conditions, i.e., when the n-type and p-type regions are connected, there is no potential barrier, but a net current flows due to the charge carrier gradients and the selective contacts (short-circuit current I_{SC}). Under open-circuit conditions, i.e., when the n-type and p-type regions are not connected, no net current flows in the junction, but the open-circuit voltage (V_{OC}) is measured, which is the difference between the two quasi-Fermi levels converted into electrical potential. In operation, under illumination and with an external load connected, the solar cell operates between these two extreme points and, therefore, generates both photovoltage and photocurrent, resulting in the generation of electrical power. At intermediate operating points, the external load creates a finite resistance that simultaneously permits partial current flow and maintains a voltage.
To determine the steady-state current generated by a solar cell under continuous illumination, all the generated and extracted charge carriers within the absorber must be summed up. The current density is given by

$$j = \int_0^d e(G(x) - R(x))\, dx. \tag{2.6}$$

with the absorber thickness d. The generation rate G can be divided into the generation rate caused by thermal radiation at room temperature and the non-equilibrium generation rate caused by illumination ($G(x) = G_{dark} + G_{illu}(x)$). In non-equilibrium, the recombination rate R is increased compared to equilibrium at room temperature due to the additional charge carriers generated by illumination

$$R(x) = R_{dark} \cdot \frac{n_e n_h}{n_i^2} = R_{dark} \exp\left(\frac{E_{F,e}(x) - E_{F,h}(x)}{k_\mathrm{B} T}\right) \tag{2.7}$$

where n_i is the intrinsic charge carrier density and n_e, n_h are the charge carrier concentrations during illumination. Since the generation rate and the recombination rate are equal in equilibrium ($G_{dark} = R_{dark}$), the current density is given by

$$j = -e \int_0^d \left[G_{dark}\left(1 - \exp\left(\frac{E_{F,e}(x) - E_{F,h}(x)}{k_\mathrm{B} T}\right)\right) + G_{illu}(x)\right] dx. \tag{2.8}$$

Charge carrier extraction is only possible if electrons and holes are generated within their respective diffusion lengths (L_e for electrons and L_e for holes) before reaching the selective contact. Consequently, the integral is solved only within the absorber, constrained by the boundaries $[-L_e, L_h]$. Since the electrochemical potentials of the charge carriers inside the absorber as well as the thermal generation rate do not depend on the location (see Figure 2.2b), the equation changes to

$$j = eG_{dark}(L_e + L_h)\left(\exp\left(\frac{E_{F,e} - E_{F,h}}{k_\mathrm{B} T}\right) - 1\right) - e \int_{-L_e}^{L_h} G_{illu}(x)\, dx. \tag{2.9}$$

The two remaining terms of the generation rates can be identified by analyzing two extreme cases. Under illumination and with an external short circuit (V=0), the resulting short-circuit current density j_{SC} is given by $-e\int_{-L_e}^{L_h} G_{illu}(x)\,dx$. In the dark ($G_{illu}(x)$ = 0) and for large negative voltages ($\exp(eV/k_{\mathrm{B}}T) \ll 1$), the dark saturation current density j_0 is given by $-eG_{dark}(L_e + L_h)$. As discussed, the energy difference $E_{F,e}$ - $E_{F,h}$ can be expressed in terms of energy eV and the final current density is described by

$$j = j_0 \left(\exp\left(\frac{eV}{k_{\mathrm{B}}T} \right) - 1 \right) + j_{SC}. \tag{2.10}$$

This equation defines the characteristic current-voltage behavior of a solar cell, where varying the resistance of the external load shifts the operating point along a curve, maintaining both a photovoltage (reduced from V_{OC}) and a photocurrent (less than I_{SC}), thereby enabling power output.

2.2.2 Electrical Characteristics and Photovoltaic Metrics

Equivalent circuits are used to describe the electrical behavior of solar cells. A comparison of Equation 2.10 with the Shockley equation, which describes the electrical behavior of a diode, shows that an ideal solar cell can be modeled with an equivalent circuit consisting of a diode and a current source. The photocurrent I_{ph} increases with illumination intensity and the current I_{d} represents radiative recombination losses. To describe a real solar cell, a series (R_{s}) and shunt (R_{sh}) resistance are added to the equivalent circuit resulting in the single-diode model of a solar cell (see Figure 2.3a). The shunt resistance represents unwanted leakage current paths due to imperfections in the absorber, while losses due to limited charge carrier transport through the solar cell are described with the series resistance.[64] Accordingly, the photocurrent minus the diode and shunt resistance currents equals the output current I of the solar cell:

$$I = I_{\mathrm{ph}} - I_{\mathrm{d}} - I_{\mathrm{sh}} \tag{2.11}$$

Using the diode equation the output current can be described as

$$I(V) = I_{\mathrm{ph}} - I_0 \left(\exp\left(\frac{e(V - IR_{\mathrm{s}})}{nk_{\mathrm{B}}T} \right) - 1 \right) - \frac{V + IR_{\mathrm{s}}}{R_{\mathrm{sh}}} \tag{2.12}$$

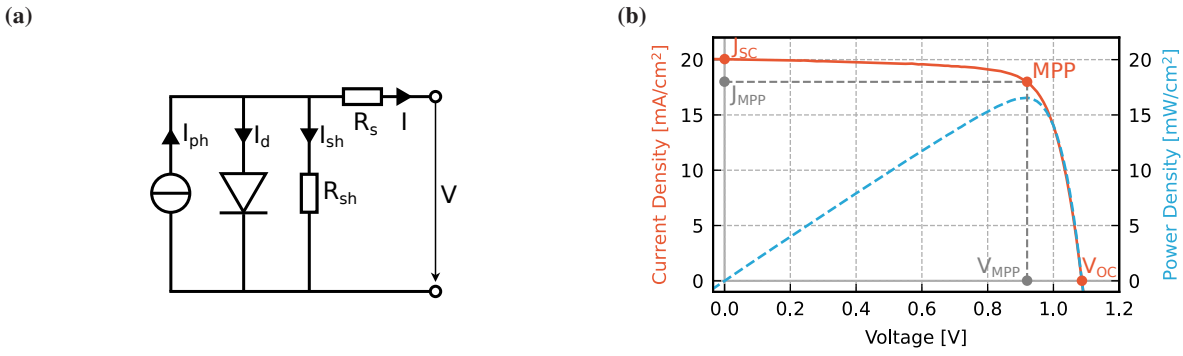

Figure 2.3: Electrical and photovoltaic characteristics of a solar cell. (a) The single-diode equivalent circuit model describes the electrical behavior, consisting of a photocurrent source (I_{ph}), a diode representing radiative recombination (I_{d}), and resistive elements for series (R_{s}) and shunt (R_{sh}) losses. (b) The current density-voltage (J-V) curve under illumination shows the photovoltaic performance metrics short-circuit current density (J_{SC}) and open-circuit voltage (V_{OC}). The power density curve illustrates the maximum power point (MPP), where J_{MPP} and V_{MPP} determine the maximum power output. Fill factor (FF) and power conversion efficiency (PCE) are derived from these parameters.

where I_0 is the dark saturation current, n is the ideality factor, e is the elementary charge, k_B is the Boltzmann constant, T is the absolute temperature and V is the voltage at the terminals of the solar cell. The single diode model can be extended with an additional diode in parallel to also include non-radiative recombination losses. For a ideal solar cell the equation can be simplified, as $R_\mathrm{s} \to 0$ and $R_\mathrm{sh} \to \infty$:

$$I(V) = I_\mathrm{ph} - I_0 \left(\exp\left(\frac{eV}{nk_\mathrm{B}T} \right) - 1 \right) \tag{2.13}$$

Fundamental parameters of the solar cell can either be extracted from the current voltage curve or can be calculated. The short-circuit current is measured when the applied voltage is 0.

$$I_{SC} = I(V = 0V) \approx I_\mathrm{ph} \tag{2.14}$$

The short-circuit current is the maximum current the solar cell can output. When the output current $I(V)$ of the solar cell is 0, the open-circuit voltage is measured. Using Equation 2.13, V_{OC} is expressed as:

$$V_{OC} = \frac{nk_\mathrm{B}T}{e} \ln\left(\frac{I_\mathrm{ph}}{I_0} + 1 \right) \tag{2.15}$$

For better comparability of different active area sizes A, the current is converted to short-circuit current density ($J_{SC} = I_{SC}A^{-1}$). A characteristic current density-voltage curve of a solar cell and the corresponding generated power output density is shown in Figure 2.3b. The maximum power output is generated when the solar cell is operated at the maximum power point (MPP):

$$P_{MPP} = I_{MPP}\, V_{MPP} \tag{2.16}$$

The fill factor (FF) is defined as a measure of the difference between the maximum possible power output $V_{OC}I_{SC}$ and the actual value of $V_{MPP}I_{MPP}$:

$$\mathrm{FF} = \frac{I_{MPP}\, V_{MPP}}{I_{SC}\, V_{OC}} \tag{2.17}$$

The power conversion efficiency is the most important metric of a solar cell and is defined as the power density at the MPP as a fraction of the power density of the incident light:

$$\mathrm{PCE} = \frac{P_{MPP}}{P_{incident}} = \frac{\mathrm{FF}\, J_{SC}\, V_{OC}}{E_{AM1.5G}} = \frac{\mathrm{FF}\, J_{SC}\, V_{OC}}{1000\,\mathrm{W\,m^{-2}}} \tag{2.18}$$

Under testing conditions, the standard AM1.5G spectrum is used for illumination of the solar cell with an integrated power density $P_{incident}$ of $1000\,\mathrm{W\,m^{-2}}$.

2.3 Machine Learning

Given the extensive and rapidly evolving field of machine learning, this section provides a concise overview of the key concepts and the background relevant to this thesis.

Machine learning can be defined as the development and use of algorithms that identify patterns in data to perform tasks or make predictions without being explicitly programmed to do so.[70] Instead of relying on an explicit predefined set of rules, ML models learn patterns from the data on which it is trained, iteratively tuning the internal parameters to capture complex relationships and structures. The main goal of ML models is to generalize, which represents the ability of a model to perform well on new, unseen data after having learned general patterns on the training data.[71–73]

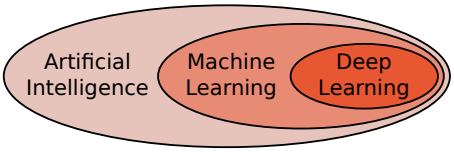

Figure 2.4: Relationship between artificial intelligence (AI), machine learning (ML), and deep learning (DL). AI encompasses tasks that require human-like intelligence. ML, a subset of AI, consists of algorithms that learn patterns from data without explicit programming. DL, a subset of ML, uses artificial neural networks to learn hierarchical representations of data.

ML is a core component within the broader field of artificial intelligence (AI), which encompasses methods that enable machines to perform tasks typically associated with human intelligence (see Figure 2.4). Within ML, deep learning (DL) is a specialized subset that uses artificial neural networks inspired by biological neurons to learn complex representations of data. While AI provides the overarching conceptual framework for intelligent systems, ML focuses on data-driven model building, and DL, powered by neural networks, refines this approach by enabling the learning of complex data patterns.
A typical ML workflow starts with data acquisition and preprocessing to ensure that the input data is cleaned and uniformly structured, followed by the selection of the appropriate learning approach (supervised or unsupervised, see section 2.3.1). Next, the problem type is defined, such as regression or classification (see section 2.3.2), and based on the task, a suitable model is chosen, ranging from tree-based and neighbor-based algorithms (see section 2.3.3) to neural networks (see section 2.3.4). Methods of feature engineering and dimensionality reduction (see section 2.3.8) can be used to simplify high-dimensional data. Model performance is evaluated using a structured training, validation, and testing procedure (see section 2.3.5), with appropriate prediction error metrics guiding model selection, training, and hyperparameter optimization. Explainable AI (XAI) techniques (see section 2.3.7) can be used to interpret model decisions.

2.3.1 Learning Approaches

Depending on the learning approach, ML applications can be categorized into three different types: supervised, unsupervised, and reinforcement learning. In all of these learning approaches, the model is iteratively trained to optimize model parameters.[71, 73]
In reinforcement learning, an agent learns to make sequential decisions by interacting with the environment. The agent receives feedback in the form of rewards or penalties and through trial and error, the agent improves its strategy to maximize rewards over time.[74] Supervised and unsupervised learning are discussed in more detail below, as these approaches are used in this work.

2.3.1.1 Supervised Learning

Supervised ML models require labeled datasets, where a training set with known input feature and label pairs is used to learn a mapping between the features and the label, also called the target variable. By iteratively adjusting its internal parameters to minimize prediction errors when compared to the ground truth labels on the training data, the model learns a mapping from input features to target outputs. Once this mapping is established after training, the model can generalize and apply the learned patterns to accurately predict the corresponding target values for new, previously unseen input samples.
This approach is commonly used for tasks such as classification and regression (see section 2.3.2), with real-world applications including predicting house prices based on property features or classifying emails as spam. Evaluation metrics such as accuracy, mean absolute error, or mean squared error are used to quantify model performance and

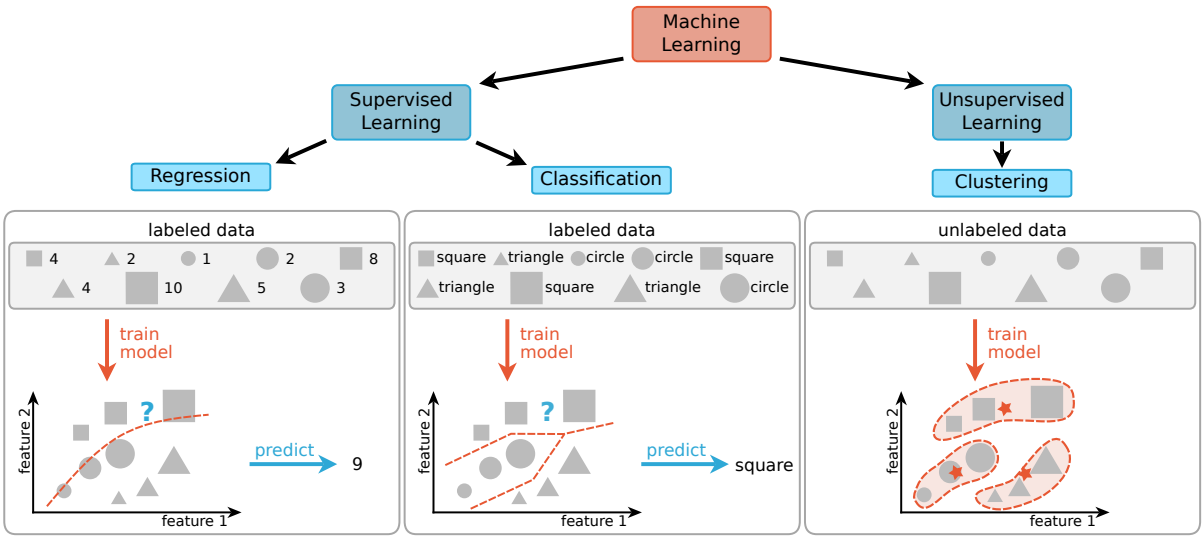

Figure 2.5: Overview of supervised and unsupervised learning approaches in machine learning. Supervised learning uses labeled datasets to train models for regression (left) and classification (middle) tasks, where the goal is to predict continuous values or assign samples to predefined categories, respectively. Unsupervised learning (right) discovers inherent patterns and clusters in data, enabling exploratory analysis without relying on predefined labels.

guide model selection and optimization (see section 2.3.6). However, supervised learning models require large, high-quality labeled datasets and are susceptible to challenges such as overfitting, where a model performs well on training data but poorly on unseen data (see section 2.3.5).
Common models used for supervised learning which are also used in this work are for example k-nearest neighbors, random forest (see section 2.3.3), and neural networks (see section 2.3.4).

2.3.1.2 Unsupervised Learning

In contrast to supervised learning, unsupervised learning does not rely on labeled data. Instead, these methods identify inherent structures, patterns, or groupings in the input data without predefined target values. By analyzing similarities and differences between data samples, this approach is particularly useful for exploratory analysis, allowing the discovery of underlying patterns and clusters without the need for costly manual annotation. This exploratory approach often provides valuable insights into data distributions and underlying relationships that may not be immediately apparent.
A common technique in unsupervised learning is clustering, which organizes samples into subsets based on their similarities (see Figure 2.5). The resulting clusters can then be further explored to extract insights and guide further data analysis. Among clustering methods, the k-means algorithm[75] is one of the most widely used techniques. It divides the unlabeled dataset into `k` clusters, each defined by a centroid, and assigns each sample to the cluster with the nearest centroid (see Figure 2.6a). The algorithm iteratively updates the cluster centroids to minimize the squared sum of distances between each sample and its assigned centroid. The k-means algorithm implemented in scikit-learn[76] is used in this work.
To determine a suitable number of clusters `k`, the elbow method[77] can be used to find the value of `k` where adding more clusters does not substantially improve the model. The heuristic plots the sum of squared error as a function of different values of `k` and suggests selecting the point where the decrease in error begins to level off, forming an *elbow* in the plot.
In this work, the unsupervised k-means clustering algorithm is used to explore and analyze the training dataset, helping to identify fundamental patterns and relationships and guiding subsequent supervised analyses.

2.3.2 Regression and Classification

Supervised ML applications can be categorized by problem type into regression and classification. While both approaches involve learning a mapping between input features and target variables, they differ in the type of target variable that is predicted.[71, 73]
Regression is used when the target variables are continuous and the goal is to predict a numerical value based on input features.[78] For example, predicting house prices based on characteristics such as location and size. Models used for regression aim to minimize the difference between predicted and actual target values by approximating the underlying function (see Figure 2.5). After learning the function, the regression model predicts a target value for a new sample of input data. The model performance is typically quantified by metrics such as mean squared error (MSE) or mean absolute error (MAE) (see section 2.3.6). Key challenges in regression include handling outliers and ensuring that the model generalizes well to unseen data. Linear regression, random forest regression, and neural network regressors are commonly applied algorithms.
Classification is used when the target variable is categorical and the goal is to assign each input sample to one of a set of discrete categories. Common applications include email spam detection, where emails are classified as "spam" or "not spam," and image recognition tasks, such as identifying hand-written characters.[79] In classification, the model learns a decision boundary that divides the input space into distinct regions, each corresponding to one of the target classes (see Figure 2.5). Model performance is evaluated using confusion matrices and error metrics such as accuracy, precision, recall, and F1-score (see section 2.3.6). Challenges in classification include handling imbalanced datasets where some classes are underrepresented and ensuring robustness to mislabeled data. Popular classification algorithms include k-nearest neighbors, support vector machines, random forest classifiers, and neural networks.
In summary, while a regression model learns to predict a continuous value by approximating a mathematical relationship between input features and the target variable, a classification model aims to assign discrete categorical labels by learning decision boundaries that separate classes in the feature space. Both approaches involve iterative training, validation, and refinement to optimize model performance based on appropriate evaluation metrics. In this work, both regression and classification approaches are used to address different tasks, demonstrating the versatility of supervised learning methods in exploring and analyzing experimental data.

2.3.3 Tree- and Neighbor-Based Machine Learning

Tree- and neighbor-based machine learning methods are traditional supervised ML models that are widely used for their versatility and robustness. These approaches form the basis of many supervised learning tasks. Due to their superior performance on the datasets generated in this work, the focus in this work is mainly on the classical ML methods k-nearest neighbors (kNN), random forest (RF), and histogram-based gradient boosting trees (HGB).
kNN[80] is a simple but powerful supervised method that, like the unsupervised k-means clustering, is based on distance. kNN assumes that similar samples are close to each other in the feature space. Therefore, it predicts a target value based on the `k` closest training samples that kNN assumes are most similar to the new input sample (see Figure 2.6b). In this work, the kNN algorithm implemented in scikit-learn[76] is used and the distance is computed with the default Euclidean distance metric. For classification tasks, the algorithm assigns a class label based on a majority vote among the `k` neighbors, while for regression, it predicts a value by averaging the outputs of the `k` closest neighbors. The optimal `k` can be determined using cross-validation on the training set (see section 2.3.5). Because of its interpretability, kNN is an effective tool for exploring datasets. However, it is computationally expensive for large datasets, because predictions require comparisons with each training sample and it is sensitive to irrelevant features and the choice of `k`. In this work, kNN is used for exploratory analyses and as a baseline model for evaluating the performance of more complex approaches.
Random forest[81] is a tree-based ensemble method that builds an ensemble of decision trees. A decision tree is a model that recursively splits data into subsets based on the values of the most informative features to make

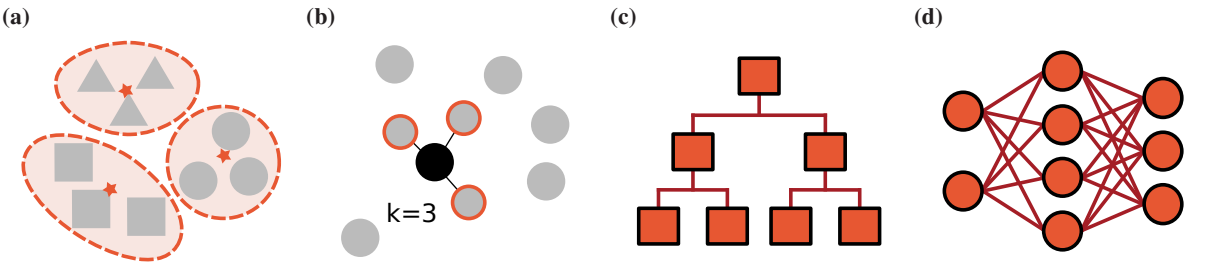

Figure 2.6: Illustration of the machine learning models used in this work. (a) k-means clustering is an unsupervised learning approach that groups data based on proximity in the feature space to minimize intra-cluster variance. (b) k-nearest neighbors (kNN) is a supervised learning algorithm that makes predictions based on the closest k neighbors in the feature space. (c) Tree-based models, including decision trees, random forests, and gradient boosting, split data hierarchically based on feature thresholds to make predictions. (d) Neural networks consist of interconnected layers of neurons with weights and activation functions that allow the modeling of complex patterns through iterative optimization of parameters.

predictions.[82] Starting from a root node, the algorithm selects the feature and threshold that best separate the target variable. The data is recursively split at each node, creating branches until a stopping condition is met (see Figure 2.6c). At the leaf nodes, predictions are made based on the majority class for classification and the average target value is predicted for regression tasks. To make predictions, new data samples pass through the tree from root to leaf, following the appropriate branches and eventually reaching a leaf node that determines the output. Single decision trees are prone to overfitting. To reduce overfitting, random forest models introduce randomness into the tree-building process by training individual trees on a random subset of the data and features. Random forests combine the outputs of multiple decision trees to improve predictive performance, robustness, and generalization. Randomness for individual decision trees is realized through bootstrap sampling, i.e., randomly selecting samples from the training dataset with replacement creating multiple subsets, and random feature selection, i.e., choosing a random subset of features when splitting nodes, resulting in diverse trees. To produce a final output, the predictions of individual trees are aggregated by majority voting for classification or by averaging for regression. This ensemble approach improves robustness and reduces overfitting compared to single decision trees, while also providing useful insights into feature importance. In this work, the random forest algorithm implemented in scikit-learn[76] is used as a baseline for PCE regression and material property classification as well as forecasting of monitoring data.

While random forests build ensembles of decision trees by training them independently, boosting methods[83] build trees sequentially, with each tree trying to correct the errors of its predecessors. This iterative process allows boosting methods to focus more on the difficult-to-predict samples, resulting in models with higher predictive accuracy. For gradient-boosted trees[84, 85], the output is optimized by minimizing a loss function using gradient descent. Gradient boosting ensembles are a widely used technique for prediction tasks on structured, tabular data[86, 87], but suffer from slow model training, especially for large datasets. Histogram-based gradient boosting extends gradient boosting methods by using histogram-based binning for feature values, making it computationally efficient for large datasets.[88] HGB accelerates the training of the trees added to the ensemble by discretizing (binning) the continuous input variables into discrete intervals (histograms). In this work, the histogram-based gradient boosting algorithm implemented in scikit-learn[76] is used as a baseline for PCE regression and material property classification.

In addition, several other machine learning methods are used in this work to provide a comparative evaluation of the primary models. Support vector machines, adaBoost, elastic net, logistic regression, and naive Bayes are used to benchmark the performance of the primary tree- and neighbor-based algorithms as well as neural networks, and to underscore the suitability of the chosen models by highlighting their strengths and limitations compared to alternative approaches.

2.3.4 Neural Networks

Deep learning is based on feedforward neural networks, also called multilayer perceptrons, inspired by biological neural networks.[89–91] They consist of interconnected layers of artificial neurons, i.e., basic computational units, arranged sequentially in an input layer, one or more hidden layers, and an output layer. They process information in the forward direction from one layer to the next (see Figure 2.6d). Due to the presence of multiple hidden layers between the input and output layers, these neural networks are considered *deep*. All neurons of two neighboring layers are linked forming fully connected layers. Since this architecture allows the network to model intricate data patterns and approximate complex functions, neural networks are universal function approximators.[92–94]
The input layer of a neural network receives the data features. In this layer, each neuron represents one input feature. To perform computations, the hidden layers consist of neurons that apply weights, biases, and non-linear activation functions to their inputs. Activation functions are critical because they introduce non-linearity, enabling the network to approximate complex, non-linear functions. Without non-linear activation functions, a sequence of linear transformations collapses into a single linear transformation, limiting the network's ability to model complex patterns. In hidden layers, the rectified linear unit (ReLU) is a commonly used activation function. The output layer generates predictions. The activation function of the output layer depends on the task of the model. While a linear activation is used to produce continuous regression outputs, classification often uses a softmax function to produce probabilities for each class. In short, the architecture consists of multiple layers, where the output of one layer serves as input to the next and the network performs alternating linear and non-linear transformations.
Each connection between two neurons has a corresponding weight and bias. During training, these parameters are iteratively adjusted to minimize a loss function. The training process of a neural network consists of a forward pass and a backward pass. During the forward pass, data flows from the input layer through the hidden layers to the output layer. Each neuron computes a weighted sum of its inputs, adds a bias, and applies an activation function:

$$y = \sigma\left(\sum_{i=1}^{n}(w_i \cdot x_i) + b\right) \tag{2.19}$$

where y is the output of the neuron, n the number of inputs to the neuron, x_i the *i*-th input to the neuron, w_i the weight associated with the *i*-th input, b the bias, and σ the activation function applied to the weighted sum. The final output of the network is compared to the true label using a loss function, which defines the optimization objective and quantifies the error. Common loss functions are MSE for regression tasks and cross-entropy loss for classification.
After the forward pass computes the loss, backpropagation computes the gradients of the loss function with respect to the weights and biases. Backpropagation propagates this error backward through the network using the chain rule of calculus.[95, 96] The gradients of the loss indicate the direction and magnitude of parameter updates needed to minimize the loss. Based on the computed gradients, an optimizer uses gradient descent to update the weights and biases. By following the negative gradient scaled by a learning rate, the optimizer minimizes the loss to improve the model's performance.
Finding the best-performing parameters of the neural network is an optimization problem, where the algorithm searches for an optimum given the training data. This iterative process continues until the network converges, i.e., loss is minimized, and the model generalizes well to previously unseen data. By combining the power of activation functions, backpropagation, gradient descent, and efficient optimization, feedforward neural networks serve as a versatile tool for solving a wide range of machine learning problems. In this work, neural networks implemented in PyTorch[97] are used for PCE regression and material property classification.

2.3.5 Training, Validation, and Testing

The goal of machine learning models is to learn patterns in given data and generalize well to new, unseen data. To ensure an unbiased evaluation of the model performance, the dataset has to be split into three subsets, namely training, validation, and test set. The training data comprises the largest portion of the total data to teach the machine learning model the patterns in the data and the mapping between the input feature and the target variable. The model is trained by adjusting its parameters, such as weights and biases, to minimize the loss function. During the training phase, the validation set provides an unbiased evaluation of the prediction performance on data that is not included in the training set. It is used to compare different models, to optimize model parameters, and to evaluate model performance during training to ensure that the model is neither overfitting to particular samples nor underfitting by failing to learn meaningful patterns. Finally, the test set is used to evaluate the generalization performance of the model after model selection and parameter optimization have been completed (see Figure 2.7a). The test set is reserved for the final stage of the ML process and is never seen by the model during training or validation to ensure an unbiased evaluation of the model's predictive capability. While training and validation sets are used iteratively, the test set is used only once at the end for final evaluation. It represents new real-world data that the model has never encountered before.

In addition, the concept of cross-validation is used to make full use of the available data and to obtain a more robust and unbiased evaluation of model performance. Specifically, k-fold cross-validation is used, where the training set is split into `k` subsets (folds), and the model is trained `k` times (see Figure 2.7b).[98] In each iteration, one fold serves as the validation set while the remaining `k-1` folds are used for training. The results of all folds are averaged to produce a final evaluation score. While cross-validation is computationally expensive, this approach reduces the variance in model performance evaluation and is particularly useful for smaller datasets. In this work, five-fold cross-validation is used, where the training data is split into five distinct subsets, with solar cells from the same substrate consistently grouped within the same subset.

During training, a loss function is minimized to optimize the model parameters. The loss function measures the difference between the model's predictions and the true target values, thus defining the optimization objective (see section 2.3.4). For regression tasks, common loss functions are MSE and MAE

$$\mathrm{MSE} = \frac{1}{n}\sum_{i=1}^{n}(y_i - \hat{y}_i)^2 \tag{2.20}$$

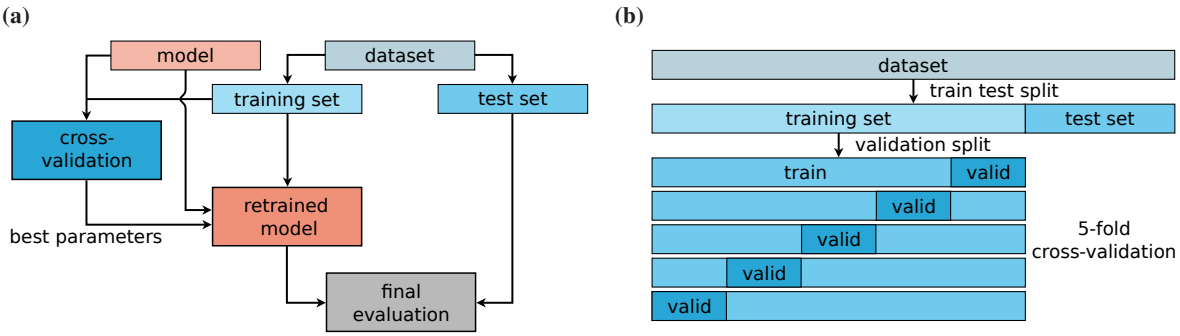

Figure 2.7: Machine learning workflow of training, validation, and testing. (a) The dataset is divided into training and test sets. A model is selected and trained on the training set using cross-validation to identify optimal parameters. The model with optimized parameters is then retrained on the entire training set and evaluated on the test set to assess its generalization performance. (b) Illustration of 5-fold cross-validation, where the training set is split into five subsets (folds). Each fold is used once for validation, while the remaining folds are used for training. To optimize hyperparameters and compare models, results are averaged across all folds for robust performance evaluation. The held-out test set is reserved for final, unbiased evaluation.

$$\text{MAE} = \frac{1}{n}\sum_{i=1}^{n}|y_i - \hat{y}_i| \tag{2.21}$$

where n is the total number of samples, y_i the true value (ground truth) for sample *i*, and $\hat{y}_i$ the model output (predicted value) for sample *i*. MSE is more sensitive to outliers as it squares the errors, penalizing large errors more severely. For classification tasks, cross-entropy loss (CE) is commonly used to assign high probabilities to the correct classes:

$$\text{CE} = -\sum_{i=1}^{C} y_i \log(\hat{y}_i) \tag{2.22}$$

where C is the number of classes, y_i the true label (1 for the correct class, 0 otherwise), and $\hat{y}_i$ the predicted probability for class *i*. During training, the cross-entropy loss, like the MSE and MAE, is summed and averaged over all samples.

During the training process of neural networks, an optimizer iteratively updates the model parameters to minimize the loss function. The optimizer performs gradient descent, which computes the gradients of the loss function with respect to the model parameters and updates the weights in the direction that reduces the loss (see section 2.3.4). The learning rate determines the step size for each update and has to be carefully tuned. If the learning rate is too large, the model may overshoot the minimum, while a value too small may lead to slow convergence. In this work, the *Adam* optimizer is used because it improves gradient descent by dynamically adjusting individual learning rates for each parameter based on past gradient information, while also incorporating a moving average of past gradients to smooth updates and accelerate convergence in relevant directions.[99] In addition, a learning rate schedule can be used to adjust the learning rate stepwise or gradually during training.

To balance computational efficiency and training stability, the training dataset is not processed all at once but instead is split into smaller batches of samples. Each batch is used to compute the gradients, and the model parameters are updated accordingly. Batch size affects model accuracy and generalization, as smaller batches introduce useful noise that helps explore the parameter space by escaping local minima and often leads to better performance on the test set. Larger batches offer faster training and more stable gradients but introduce the risk of overfitting and poorer generalization to unseen data.[100]

Because neural networks have many tunable parameters, they are highly flexible and capable of fitting complex data. However, they are also prone to overfitting, which results in poor generalization to unseen data. Overfitting occurs when the model becomes too complex and learns the training data, including the noise, too well, resulting in memorization of the training data. The model then performs exceptionally well on the training data but poorly on new, unseen data. In contrast, underfitting occurs when the model fails to learn the dominant trends in the data, resulting in poor performance on both the training and test sets. Avoiding underfitting and overfitting by balancing model complexity and generalization is referred to as the bias-variance tradeoff.[98] A high bias indicates that the model is too simple to capture the underlying patterns in the data, resulting in systematic errors, while a high variance indicates that the model is overly complex and sensitive to fluctuations in the training data.

To prevent overfitting and improve generalization, regularization techniques are applied during training. *Dropout* is a common method that randomly deactivates some neurons during each training iteration, preventing the model from relying too heavily on certain neurons and forcing the network to learn more robust features.[101] *Weight decay* penalizes large weights by adding a penalty term to the loss function that is proportional to the square of the weights. This penalty encourages the model to use smaller and simpler weights, effectively reducing model complexity and improving generalization.[102] In addition, *early stopping* helps mitigate overfitting by monitoring the validation loss during training and stopping the process when the validation performance no longer improves.[103] This prevents the model from overfitting to the training data by stopping the training before the model starts learning noise.

Finally, for deep neural networks, problems such as exploding and vanishing gradients can arise during training.[104, 105] *Exploding gradients* occur when gradients become too large, resulting in large weight updates that cause the model to diverge and lead to unstable training. This issue can be mitigated using gradient clipping, which limits

gradients to a predefined threshold. In contrast, *vanishing gradients* occur when gradients become very small, especially with activation functions such as sigmoid or tanh, causing the optimization to get stuck. This problem can be addressed by using activation functions such as ReLU, which maintain stronger gradients for positive inputs. In addition, *shattered gradients* refers to gradients in standard feedforward networks that exhibit increasingly chaotic and unstructured behavior during backpropagation, resembling white noise.[106] To mitigate shattered gradients, skip connections are introduced, as seen in model architectures such as residual networks (ResNets). Skip connections provide alternative pathways for gradients to flow, reducing gradient degradation and helping to maintain stable gradient magnitudes during backpropagation.[94]
In summary, the training, validation, and testing process involves splitting the dataset, using suitable loss functions, and optimizing model parameters using gradient descent with appropriate learning rate and batch size. While cross-validation is used to ensure robust performance evaluation, regularization techniques such as dropout, weight decay, and early stopping are used to improve generalization and prevent overfitting. By combining these strategies, the model can effectively learn patterns from the training data and generalize to unseen validation and test sets.

2.3.6 Model Evaluation

Model evaluation is a critical step in the machine learning process, ensuring that the trained model generalizes well to unseen data. Model evaluation quantifies model performance, enables comparisons between different models, and guides model parameter tuning and model selection. Without rigorous evaluation, models may overfit to training data or underperform when applied to new data. By selecting appropriate metrics and using robust evaluation strategies, the reliability and effectiveness of machine learning models can be evaluated.
To evaluate model performance, appropriate performance metrics are selected based on the type of machine learning task. For regression tasks, where the goal is to predict continuous target values, evaluation metrics quantify how well the predicted values approximate the true target values. MAE and MSE are commonly used metrics:

$$\text{MAE} = \frac{1}{n}\sum_{i=1}^{n}\left|y_i - \hat{y}_i\right|, \quad \text{MSE} = \frac{1}{n}\sum_{i=1}^{n}\left(y_i - \hat{y}_i\right)^2 \tag{2.23}$$

where y_i is the true value (ground truth), $\hat{y}_i$ the predicted value, and n the total number of samples. While MAE measures the average magnitude of the prediction errors and provides an interpretable average error, MSE is more sensitive to large errors due to the squared term. The root mean squared error (RMSE) is derived as:

$$\text{RMSE} = \sqrt{\text{MSE}} \tag{2.24}$$

offering the error in the same units as the target variable. Additionally, the R^2 score, or coefficient of determination, describes the proportion of variance in the target variable explained by the model:

$$R^2 = 1 - \frac{\text{residual sum of squares}}{\text{total sum of squares}} = 1 - \frac{\sum_{i=1}^{n}\left(y_i - \hat{y}_i\right)^2}{\sum_{i=1}^{n}\left(y_i - \bar{y}\right)^2} \tag{2.25}$$

where $\bar{y}$ is the mean of the true values. R^2 evaluates how well the model explains the variance in the target variable. For MAE, MSE, and RMSE, lower values indicate better performance, while R^2 typically ranges from 0 to 1, with higher values indicating a better fit. An R^2 value close to 1 indicates that the model explains most of the variability in the data. Negative R^2 values suggest that the model performs worse than using the test set mean ($\bar{y}$) as a constant predictor. To visualize regression performance, parity plots are commonly used to provide intuitive insight into model performance. In a parity plot, the true target values are plotted against the predicted values, with a perfect model aligning the predictions along the diagonal line, indicating that $y_i = \hat{y}_i$.
While regression metrics focus on predicting continuous values, classification metrics evaluate a model's ability to assign samples into discrete categories. A fundamental tool for classification evaluation is the confusion matrix,

which summarizes model performance by comparing predicted and true class labels. The matrix provides counts of true positives (TP), false positives (FP), true negatives (TN), and false negatives (FN), allowing a detailed analysis of model performance. From the confusion matrix, key metrics such as accuracy, which measures the proportion of correctly classified samples, can be computed as

$$\text{Accuracy} = \frac{\text{number of correct classifications}}{\text{total number of classifications}} = \frac{\text{TP + TN}}{\text{TP + TN + FP + FN}} \tag{2.26}$$

While accuracy is intuitive, it may not be sufficient for imbalanced datasets where certain classes dominate. In such cases, additional metrics such as precision, recall (also called sensitivity), and F1-score can be used:

$$\text{Precision} = \frac{\text{TP}}{\text{TP} + \text{FP}}, \quad \text{Recall} = \frac{\text{TP}}{\text{TP} + \text{FN}}, \quad \text{F1-Score} = 2 \cdot \frac{\text{Precision} \cdot \text{Recall}}{\text{Precision} + \text{Recall}} \tag{2.27}$$

Precision focuses on minimizing false positives, recall emphasizes minimizing false negatives, and the F1-score balances both. In addition, for multi-class classification tasks, the top-`k` score is useful, where a prediction is considered correct if the true class label is among the top `k` predicted probabilities. These metrics, combined with visual tools such as confusion matrices, provide a comprehensive understanding of classification model performance. In this work, the visual evaluation of model predictions is performed using parity plots and confusion matrices. To quantify prediction errors, the metrics MAE, RMSE, and R^2 are used for the regression task, and given the balanced classification dataset, accuracy and top-2 score are used to evaluate the performance for the classification task.

2.3.7 Explainable Artificial Intelligence

ML models, particularly deep neural networks, have demonstrated remarkable predictive capabilities in various domains. However, these complex models often operate as black boxes, making predictions without providing insight into their decision-making process.[107, 108] To address this fundamental challenge, explainable artificial intelligence aims to make ML model predictions transparent, interpretable, trustworthy, and understandable to humans.[109, 110]

While often used interchangeably, interpretability and explainability have nuanced differences.[111] Interpretability refers to the intrinsic transparency of simpler models, which allow humans to understand their internal workings and decision-making processes directly. In inherently interpretable models, such as linear regression or decision trees, the relationships between inputs and outputs are directly understandable. In contrast, explainability uses *post hoc* methods to understand the predictions of complex, opaque models such as deep neural networks. These methods are applied after the model has been trained to explain its behavior. While interpretable models are advantageous for their transparency, they often lack the flexibility and predictive power of black-box models, making explainability techniques essential for understanding the more complex models.

Explanations can be categorized into two categories, namely local and global explanations.[109] Global explanations provide a broad understanding of the overall behavior of the model across multiple predictions and elucidate general decision patterns. They are helpful in revealing which input features are important to the model overall. Aggregated feature importance across multiple predictions is often used for global explanations. In contrast, local explanations investigate individual predictions to understand why the model made a particular prediction for a specific input. Local explanations are useful for deep insights through individual feature attribution, counterfactual explanations for specific inputs, and saliency maps that highlight parts of an image that most influenced the prediction.

XAI techniques can be further divided into model-agnostic and model-specific approaches. Model-agnostic methods, such as Shapley additive explanations (SHAP)[112], are universally applicable to different types of machine learning models, regardless of their internal architecture. They focus on the relationship between input-output pairs of trained models without requiring access to the internal mechanisms of the model. In contrast, model-specific methods, such as saliency maps[113], are tailored to particular model architectures by exploiting the unique characteristics of specific machine learning algorithms. By accessing the model's internal representations, these

techniques can provide more precise and intrinsic explanations.
To gain a robust understanding of machine learning models, a combination of multiple appropriate XAI techniques should be employed. By using complementary methods, it is possible to uncover a broader range of insights, reduce the risk of confirmation bias, and ensure more faithful explanations. Before applying XAI methods, it is important to ensure that the underlying machine learning models are well-trained and demonstrate reliable predictive performance, as XAI methods analyze the learned patterns encoded in the models. The value of XAI lies in interpreting and validating the learned patterns of reliable models, as poorly trained models explain incorrect behavior.
The application of XAI in materials science and perovskite solar cell research has only recently started. Publications frequently rely on SHAP for feature attribution, which quantifies the contributions of individual features to a model's predictions.[114–117] While SHAP offers valuable insights, its effectiveness can be limited by its assumption of feature independence[112] as this assumption may not hold in many cases where features are highly interdependent. Relying solely on SHAP when features are correlated risks providing incomplete or misleading explanations of model behavior.[118]
While a variety of XAI methods exist, this work uses feature attribution using expected gradients, counterfactual explanations, and testing with concept activation vectors (TCAV) because of their complementary strengths. Expected gradients provide detailed, gradient-based insights into the importance of individual features, counterfactual explanations explore how small changes in input features affect predictions through what-if scenarios, and TCAV examines the influence of high-level abstract concepts on the model output. Combined, these methods address different parts of model explainability, ensuring that both feature-level and conceptual insights are considered.
Feature attribution methods assign importance scores to input features based on their influence on a model's predictions.[109, 119] Expected gradients is a gradient-based feature attribution method that evaluates the relationship between input features and model outputs by analyzing how changes in the input affect the prediction.[120] The method begins by selecting a baseline, which represents a reference point in the input space for comparison. For each feature in the input, the gradient of the model's output with respect to that feature is calculated. This gradient indicates how much a change in the feature would affect the model's prediction. Instead of computing the gradient for just one input, expected gradients computes the gradient for different inputs, sampled between the baseline and the actual input. After averaging these gradients, a more robust measure of how much each feature contributes to the output is obtained. The result is an attribution score for each input feature. Features with high scores have a significant impact on the prediction, while those with low scores are less important.
Counterfactual explanations explore what-if scenarios by perturbing input data to observe how changes affect the model's predictions.[121–123] To find a version of the input that produces a desired change in the model's prediction, this technique slightly alters the input features to see how small changes affect the output. A counterfactual explanation shows how certain changes in the input features would result in a different predicted class or a higher or lower numerical prediction. Counterfactual methods aim to find the smallest or most realistic changes to the input that will produce the counterfactual result. By demonstrating the changes necessary to alter the prediction, counterfactual explanations provide insight into the model's decision-making process and the relationship between input features and outputs.
TCAV examines how abstract, high-level concepts influence a model's predictions.[124] The method involves defining a concept, such as a particular pattern, and identifying its representation in the model's internal activation space. A linear classifier is trained on the model's activations to distinguish between samples that exhibit the investigated concept and those that do not. The method then generates a concept activation vector (CAV), which represents the direction in the activation space associated with the concept. To assess the importance of the concept, TCAV modifies the input along this concept vector to make it slightly more or less representative of the concept and observes the corresponding changes in the model's predictions. If the prediction is significantly affected by this change, the concept is considered important to the model's decision-making. By linking the behavior of the network to the high-level concepts, TCAV provides insight into which abstract features are important to the model's predictions.

By combining multiple XAI techniques, this work aims to achieve a holistic understanding of the model's decision-making process, bridging the gap between predictive performance and explainability to increase confidence in the model's outputs.

2.3.8 Dimensionality Reduction

Dimensionality reduction simplifies data by reducing the number of features in a dataset while preserving as much essential information as possible.[125, 126] It transforms high-dimensional data into a lower-dimensional form, making it easier to process, visualize, and analyze. Dimensionality reduction addresses the curse of dimensionality, which refers to the challenges of analyzing data in high-dimensional space. As dimensions increase, the volume of the space grows exponentially and data points become sparser and more scattered, making it difficult to find meaningful patterns. Transforming data into a lower-dimensional space reduces sparsity and makes it easier to find patterns in the data while eliminating irrelevant, redundant, or noisy features to help ML models focus on the most relevant information. By simplifying the data, it prevents overfitting, where models fit too closely to noise in the training data and improves generalization to new, unseen data. While it helps with both exploratory analysis and predictive modeling, it also leads to computational benefits such as more efficient model training and fewer computational resources required.
There are several approaches to dimensionality reduction, categorized into feature selection, feature transformation,

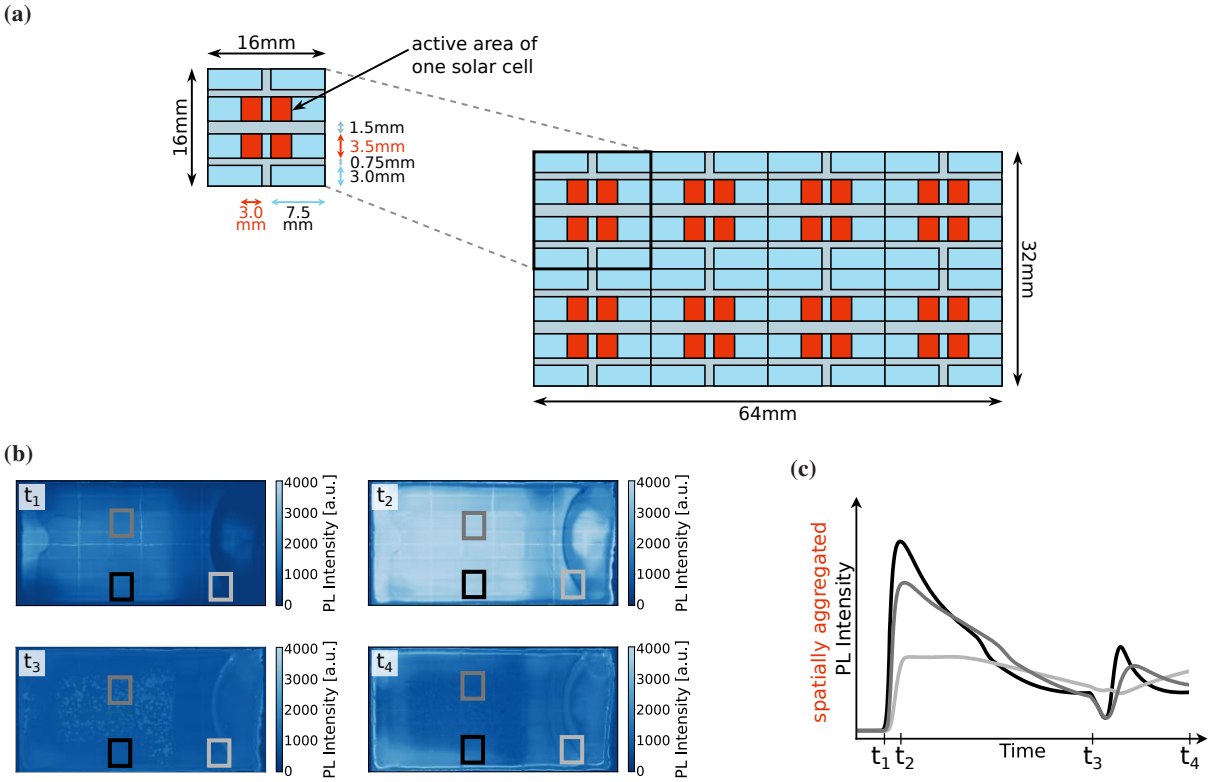

Figure 2.8: Dimensionality reduction for high-dimensional video data of the perovskite thin-film formation. (a) Layout showing the location of the active area of each solar cell on the large-area substrate. (b) Video frames capturing multiple channels of spatially resolved photoluminescence (PL) and diffuse reflection signals over time. (c) Knowledge-based feature aggregation is performed by transforming the video data into timeseries data. To preserve meaningful patterns while reducing complexity, the spatial mean intensity of the active areas is computed at each time step for all channels. The resulting transients represent the temporal evolution of the thin-film formation process, enabling simplified visualization and machine learning applications.

and feature aggregation. Feature selection reduces the dimensionality by selecting a subset of the most relevant features from the original dataset. This approach emphasizes preserving the most meaningful information while discarding irrelevant or redundant features.[127] Approaches such as filter methods are used, which compute a score for each individual feature and select a specified number of top features. Wrapper methods search through possible sets of features. For each possible combination of features, a model is trained and the validation scores are used to select the best sets. Embedded methods integrate feature selection directly into the model training process by evaluating the importance of features as part of the optimization. Feature selection techniques are particularly useful when the interpretability and relevance of individual features are critical.
In contrast, feature transformation reduces the dimensionality of the data by computing new features based on the original features. Principal component analysis (PCA) identifies orthogonal directions (principal components) that capture the maximum variance in the data. By projecting the original data onto a subset of these principal components, PCA reduces dimensionality while preserving most of the variance of the dataset.[128] An autoencoder is a more flexible and non-linear alternative to PCA that uses neural networks to learn compact, low-dimensional data representations. It consists of an encoder, which compresses the input data into a reduced latent representation, and a decoder, which reconstructs the original data from this compressed form. The latent representation serves as a lower-dimensional feature that preserves meaningful original patterns of the data. By passing data through a bottleneck structure, autoencoders are able to uncover non-linear relationships and complex patterns that traditional linear methods such as PCA might miss.[129]
Feature aggregation reduces dimensionality by grouping original features and summarizing each group into an aggregated feature to create lower-dimensional representations.[130] Data-driven feature aggregation uses ML algorithms to automatically cluster and combine features directly from raw data without relying on predefined human knowledge. Knowledge-based feature aggregation uses domain expertise and predefined rules to combine features based on expert understanding and structured hierarchies. Feature aggregation is particularly effective for high-dimensional data such as images or time series, because it captures meaningful patterns while reducing complexity.
While dimensionality reduction offers significant benefits, it also involves trade-offs. Reducing the number of dimensions can result in the loss of some information, and the interpretability of transformed features, such as PCA components or autoencoder latent variables, may be less intuitive than that of the original data. However, dimensionality reduction techniques can improve the performance of machine learning models substantially, making them a powerful tool in data analysis.
In this work, knowledge-based feature aggregation is used to reduce the complexity of high-dimensional video data while preserving essential temporal information about the thin-film formation process. Leveraging domain expertise on the critical role of the temporal component in the formation dynamics, emphasis is placed on the temporal sequence of the experiment by distilling the video data into time curves. The image frames capturing the active areas of the solar cells (0.105 cm^2, see Figure 2.8a) are aggregated by computing their spatial mean intensity at each time step. This approach transforms the high-dimensional multi-channel video data of each solar cell (see Figure 2.8b) into transients representing the temporal evolution of the spatial mean intensity over multiple channels, namely $PL_{LP\,725nm}$, $PL_{LP\,780nm}$, $PL_{SP\,775nm}$, and R_{diff} (see Figure 2.8c). By applying this dimensionality reduction, the raw video data is distilled into a compact representation that highlights the critical temporal progression of the thin-film formation process. It facilitates data visualization and downstream applications of ML models that exploit the temporal patterns in the aggregated time series.

2.3.9 Computational Resources

Performing machine learning analyses in this work was only made possible by several free and open source software libraries as well as access to high performance computing (HPC) resources.
For all classical ML models, such as tree- and neighbor-based models, the *scikit-learn* (1.3.0)[76] implementations were used and *PyTorch* (2.0.1)[97] was used to build and train neural networks. All code was written in *Python*

(3.9.7)[131]. To facilitate interactive computing, *Jupyter notebooks*[132] were used, enabling seamless integration of code, results, and visualizations. For preprocessing the raw image data, the *Python* packages *tifffile* (2021.4.8)[133], *OpenCV* (4.5.4.60)[134], and *Pillow* (9.0.1)[135] were used. Data handling, visualization, and analyses were enabled by the packages *h5py* (3.9.0)[136], *pandas* (2.1.0)[137], *NumPy* (1.24.3)[138], *matplotlib* (3.7.3)[139], *SciPy* (1.11.2)[140], and *statsmodels* (0.14.2)[141].

The computational experiments were performed on the HPC clusters *bwUniCluster 2.0* and *Helmholtz AI computing resources (HAICORE)@KIT*, hosted at the Scientific Computing Center of the Karlsruhe Institute of Technology. These clusters are equipped with *NVIDIA A100-40* GPUs and *Intel Xeon Platinum 8368* or *AMD "Rome" EPYC 7742* CPUs, providing substantial computational power for efficient parallelization and acceleration of large-scale experiments. The author acknowledges support by the state of Baden-Württemberg through bwHPC. This work was supported by the Helmholtz Association Initiative and Networking Fund on the HAICORE@KIT partition.

2.4 Machine Learning for Perovskite Photovoltaics

This section is dedicated to familiarize the reader with the *state of the art* of applying machine learning to solve challenges in perovskite photovoltaics research.

Traditional approaches in perovskite materials science and device engineering rely heavily on countless trial-and-error experiments that drive progress in material discovery, process development, characterization, full device evaluation, and stability testing. However, due to the large experimental parameter space, these challenges are inherently complex and performing manual experiments is expensive, labor-intensive, and time-consuming.[142] As these approaches are limited in their ability to address the remaining challenges of scalability, stability, and efficiency, more systematic methods are needed, motivating the adoption of data-driven techniques and autonomous experimentation. ML has emerged as a transformative tool in many scientific disciplines, revealing previously unidentified relationships and providing insights into fundamental mechanisms. In addition to pattern recognition, ML enables classifications, predictions, and the extraction of novel insights from complex datasets.[143] As a result, ML techniques have been successfully applied to an increasing number of challenges in materials science.[144–152] In recent years, ML has found its way into perovskite photovoltaics research, where several reviews[153–162] and perspectives[163–167] underscore the growing interest in ML as a powerful tool to address the challenges in perovskite PV research (see Figure 2.9a). The interest in integrating ML into PSC research not

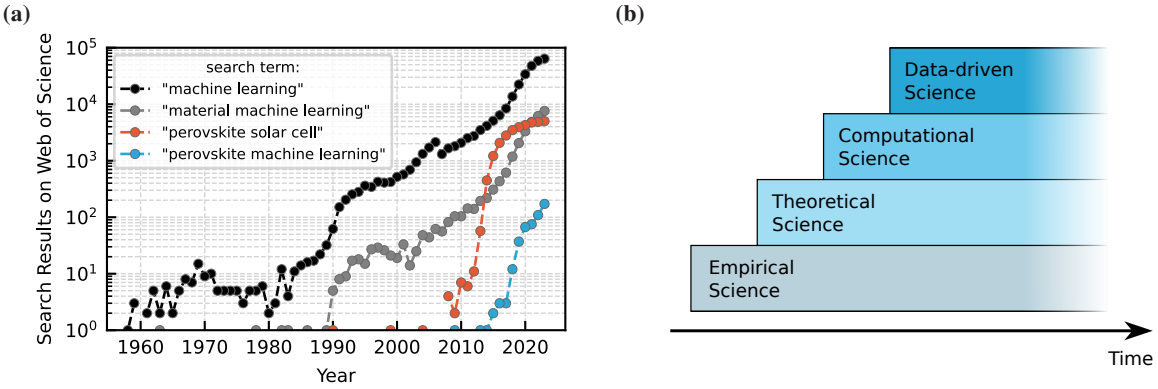

Figure 2.9: Machine learning (ML) in materials science and perovskite photovoltaics. (a) The exponential growth of academic publications reflects the increasing adoption of ML in materials science and its recent extension to perovskite solar cell research. (b) Schematic of the evolution of scientific methods from empirical to theoretical and computational paradigms, now advancing into the data-driven paradigm. This fourth paradigm uses big data and ML to make predictions, uncover insights, and accelerate scientific discovery.

only reflects its transformative potential but also demonstrates the extension of scientific methodology towards data-driven approaches. The evolution of materials research can be characterized into four paradigms, namely experimental and empirical, model-based theoretical, computational simulation, and data-driven science driven by AI (see Figure 2.9b). The emerging fourth paradigm uses big data analytics and machine learning to analyze large datasets and build predictive models, revolutionizing research in many scientific fields.[168–170]

The discovery of novel materials is a major goal of applying ML in energy materials research. By accelerating the discovery process with high-throughput experimental and computational methods, materials with enhanced properties can be identified more efficiently, reducing both time and cost.[171–173] In perovskite PV research, ML is used to predict important material properties such as bandgap, stability, and carrier mobility, enabling the identification of stable compositions, optimization of optoelectronic properties, and improvement of material stability. By rapidly screening large compositional spaces, ML models have successfully identified stable lead-free perovskite alternatives[174–176] and optimized perovskite compositions to improve efficiency and stability.[177–181] Exploration of chemical spaces through high-throughput screening facilitates the discovery of materials tailored for specific applications, such as additives, passivation, or charge transport layers.[182–185] Building on these advances, generative AI, through techniques such as generative adversarial networks (GANs) and variational autoencoders (VAEs), provides a powerful tool for designing novel perovskite materials by creating new compositions with targeted properties, extending the exploration of chemical spaces beyond traditional methods.[156] Emerging techniques like inverse design allow researchers to generate material compositions that meet precise property requirements, revolutionizing the approach to materials development and accelerating innovation in the field.[186]

Since the prediction of material properties is essential for discovery, ML is used to predict intrinsic optoelectronic properties. For example, the bandgap of different perovskite compositions is predicted based on theoretical physical material features like ionization energy, atomic/molecular sizes, or lattice constant.[177, 187–192] In addition to optoelectronic properties such as bandgap and charge carrier mobility[193, 194], ML models are used to predict various structural characteristics of materials, including crystal structures[195–197], formability[198, 199], and thermodynamic stability[200–202].

While it is easier to predict intrinsic material properties, predicting holistic device properties is more complex. Building on these capabilities, ML is also used to predict holistic device-level metrics such as PCE.[116, 178, 203–206] By integrating material properties, stack designs, and processing conditions, ML models provide assessments of the expected performance of the solar cell. ML approaches for predicting PCE can be divided into models that predict general PCE based on material properties, stack design, and process conditions, and models that predict PCE of individual solar cells using real experimental measurements of thin film properties. Most commonly the models are based on datasets generated by extracting data from previously published research articles with hundreds to thousands of data points.[116, 178, 203, 204, 207] While these models provide a theoretical estimate of performance across a range of configurations, they cannot be used for dynamic feedback during fabrication to facilitate immediate optimization for specific devices.

In addition to materials discovery, a key application of ML is the optimization of fabrication processes by predicting how changes in fabrication parameters will affect device performance. By enabling iterative optimization, ML significantly improves material formation processes, leading to improved solar cell performance in both organic photovoltaics[208–210] and perovskite photovoltaics[211–214]. Furthermore, ML is expected to play a key role in establishing robust baseline fabrication processes, monitoring and maintaining them against external variations, and continuously improving these baselines by integrating advances from ongoing research.[156]

In addition to optimizing materials and device performance, addressing stability remains a critical challenge for the commercial viability of PSCs. ML methods can be used as powerful tools to predict and improve stability by analyzing degradation patterns and identifying stability-enhancing material and process configurations. ML tasks related to perovskite stability can be broadly divided into two areas. During materials discovery, ML optimizes material stability by identifying compositions with enhanced thermodynamic and structural robustness.[200–202, 215–220] Second, ML models predict long-term device stability by forecasting degradation to study solar cell performance over time.[155, 221] The challenges of long-term stability are addressed with ML by optimizing configurations for

improved durability while identifying key factors that influence stability, such as material composition, structural properties, and environmental conditions.[192, 222–225] These predictive approaches enhance traditional accelerated aging tests by using ML models to forecast degradation curves and to predict stability metrics like T_{80} lifetimes (time to decay to 80% of initial PCE value), as well as providing deeper insights into the mechanisms governing device degradation.[226–228]

While ML often relies on tabular data from simulated datasets or literature databases, it can also predict PCE or stability using experimental data from perovskite thin film characterization as input, providing a direct link between material properties and individual device performance. Characterization data provides insight into the physical and chemical properties of perovskite materials, but its complexity often limits manual interpretation.[229] ML techniques, such as supervised learning and computer vision, enable automated analysis of imaging and spectroscopic data to extract meaningful information on material morphology, defects, and optoelectronic properties.[230, 231] For example, machine vision is used to classify substrate coverage and quantify pinholes or cracks.[232, 233] To explore the correlation between microstructural features such as grain boundaries and conductivity in perovskite thin films, ML is used to drive automated scanning probe microscopes.[234] To perform accelerated stability testing, experimental data such as environment-dependent transmittance[217] and photoluminescence (PL)[235, 236] are forecasted by ML. Furthermore, ML methods are used to increase the information yield from measurements such as time-resolved photoluminescence[237], to automatically determine the crystal structure of materials based on X-ray diffraction data[195, 197], and recently to predict device performance based on the optical properties of the corresponding thin films.[238] Bridging this gap between material-level properties and device-level performance with ML-enhanced characterization methods is required to address the challenges of reliability, batch-to-batch reproducibility, and high fabrication yield at industrial scale.[156, 239] In addition, as high-throughput automation accelerates material synthesis and experimentation, scalable automated characterization tools and ML-driven integration are required to match the pace of high-throughput experiments by efficiently analyzing material properties to guide experimental decisions and close the loop for autonomous discovery.[230, 240]

By accelerating labor-intensive and slow manual fabrication, high-throughput experimentation enabled by automation and robotics transforms traditional trial-and-error methods into systematic, data-rich processes.[210, 241–245] By synthesizing and testing samples in parallel, automated platforms can substantially reduce the time required to explore compositional and processing parameter spaces. Integrated with machine learning, these platforms have been used to synthesize perovskite materials[246–250], discover stable compositions[251, 252], explore compositional stability[216], optimize thin-film fabrication parameters[211, 213, 253], screen antisolvents[254], and identify passivation materials for enhanced performance[183]. Although high-throughput experimentation accelerates data generation through automation, experimental designs are typically created by human experts or predefined at the beginning of a campaign. In contrast, self-driving labs leverage advances in AI, robotics, and automation to perform fully autonomous experimentation.[255–261] Using AI to analyze data, these systems make intelligent decisions about subsequent experiments without human intervention. By using the iterative, closed-loop workflow of design, execution, and learning, self-driving labs have the potential to accelerate research significantly while reducing its carbon footprint.

In addition to research applications, AI-driven tools are increasingly used in commercial (silicon) PV systems, where they play a critical role in optimizing system operation, monitoring, and maintenance to ensure reliable and sustainable energy production.[262, 263] For PV system monitoring, ML- and DL-based strategies are applied in fault detection and diagnosis, power forecasting, and smart energy management.[264, 265] Unmanned aerial vehicles enable the identification of common problems such as hot spots, cracks, bypass diode failures, soiling, and shading.[266, 267] Imaging techniques such as infrared thermography are used to detect hot spots, visual inspection identifies issues like burn marks, delamination, discoloration, snail trails, glass breakage, shading, and bird droppings, while electroluminescence and photoluminescence imaging reveal cracks and series resistance. Instead of pinpointing exact defect locations within individual cells, efforts are often focused on identifying the overall probability of defects across modules to quickly address defective areas.[268] Beyond visual inspection, monitoring and control of various electrical system components, such as inverters, is essential to meet contracted

power production targets, predict the remaining useful life of PV system components, enable predictive maintenance, and ensure the long-term durability of PV systems.

AI systems can significantly enhance scientific understanding[269] by improving the transparency of ML models through explainable AI, allowing researchers to uncover relationships between material properties and device performance.[161, 270] Because most scientific knowledge is encoded in text and figures of academic literature rather than in structured databases, natural language processing (NLP) enables automated extraction of insights and identification of research priorities.[269, 271–274] Large language models (LLMs) further advance these capabilities by enabling rapid literature review, molecular design, property prediction, and synthesis planning.[275–281]

While AI and ML techniques are powerful tools for advancing photovoltaic research, their effectiveness depends on the availability of high-quality datasets as a basis for training reliable models and extracting meaningful insights. Although experimental collections such as the perovskite database[282], the emerging-PV database[283], and the 2D perovskite database[284] exist, datasets are often small and cover only narrow ranges of process conditions, material compositions, and device architectures. This limitation hinders the generalization of models to different experimental environments and production settings. Addressing this issue requires the creation of large, diverse datasets that are accurate, reproducible, and unbiased, avoiding skew toward high-performing devices.[161] Efforts to standardize data reporting using ontologies[285] and initiatives like Materials Project[286] and NOMAD[287, 288], which promote the FAIR principles (findable, accessible, interoperable, reusable), are important for improving data quality and sharing. High-throughput experimentation and self-driving labs further enable the generation of large, consistent datasets[261], while automated data extraction through NLP enriches datasets with information from scientific literature[274]. Generative AI complements this by simulating rare conditions or exploring underrepresented parameter spaces.[289, 290] Integrating experimental and computational data into hybrid datasets and leveraging multimodal sources expands the possibilities for ML-driven insights. Foundation models pre-trained on massive datasets acquire broad knowledge and generalize to new tasks without requiring task-specific training.[291] By leveraging advanced datasets and AI methods, future research can enhance materials discovery, device optimization, and process improvement, accelerating innovation and commercialization of PSC technology.

3 Methods

This chapter presents the experimental methods used to fabricate, characterize, and evaluate perovskite thin films and solar cells. The fabrication section describes the scalable solution-based deposition of perovskite thin films, focusing on blade coating and vacuum quenching. In addition, vapor phase deposition techniques, solar cell architectures, and materials used in this work are discussed. The characterization section covers the techniques used to evaluate thin film properties and device performance. After establishing profilometry for thin film thickness measurements and current-voltage analysis for quantifying photovoltaic performance metrics, photoluminescence imaging for monitoring perovskite thin-film formation is introduced. The data acquired by these methods is used to generate experimental datasets that provide both the input features and the target labels for machine learning models, allowing data-driven insights into the relationships between the fabrication process and perovskite thin film quality and solar cell performance.

3.1 Perovskite Solar Cell Fabrication

The deposition of the perovskite thin film, a critical step in solar cell fabrication, can be accomplished using two primary approaches: solution processing and vapor phase deposition. Solution-based methods involve depositing inks containing precursor materials dissolved in suitable solvents onto substrates using techniques such as spin coating, blade coating, slot-die coating, spray coating, and inkjet printing, followed by controlled drying and crystallization to form high-quality thin films.[28] In contrast, vapor phase deposition uses solvent-free processes in which the precursor materials are converted to their vapor phase through sublimation under vacuum conditions. The vapor then deposits onto the substrate, forming a uniform perovskite thin film.[22]
Vapor phase deposition is a mature and widely used technology in the coating and semiconductor industries, dominating the production of other thin-film PV technologies and optoelectronic devices.[22, 292] Its success can be attributed to the precise control of deposition parameters, which enables reproducible processes, scalable fabrication for large-area applications, and the ability to produce multi-layer architectures with tailored functional layers while avoiding the use of toxic solvents typical in solution processing.[293–295] However, the simplicity and accessibility of solution-based fabrication have led to the broader adoption of solution processing techniques for lab-scale deposition of perovskite thin films, as these methods enable rapid prototyping and experimentation, making them a cornerstone of academic perovskite research.[22, 293]
The following section focuses on solution processing, highlighting the scalable blade coating method. Combined with vacuum quenching, blade coating enables the production of high-quality perovskite thin films, making it suitable for large-area applications.

3.1.1 Solution Processing

Solution processing is widely used in academic research for perovskite PV because it is simple, cost-effective, and requires minimal process equipment. Solution-based deposition involves dissolving precursor salts in a solvent system, depositing the solution onto a substrate, and removing the solvent to crystallize the thin film.[28] The formulation of the perovskite precursor solution with the composition $Cs_{0.17}FA_{0.83}Pb(I_{0.91}Br_{0.09})_3$ used in this work is detailed in section 3.1.3, along the materials for other device layers.
After preparing the precursor solution, several techniques can be used to deposit it onto the substrate, each suitable for different scales and purposes. While spin coating is commonly employed for small-scale laboratory optimization, transitioning to industrial production requires scalable methods for large-area deposition. Techniques such as blade coating, slot-die coating, spray coating, and inkjet printing have emerged as promising alternatives to spin coating for high-throughput fabrication.[23, 26, 296]

3.1.1.1 Blade Coating

Blade coating, also known as doctor blading, is a scalable solution processing technique used to fabricate thin films. The liquid precursor solution is deposited onto the substrate and a blade is moved across the surface to distribute the solution into a uniform wet film (see Figure 3.1a). The formation of the thin film is driven by the meniscus that develops between the blade and the substrate. The thickness of the deposited wet film depends on the material concentration in the ink and the meniscus between the blade and the substrate. Key parameters that affect the meniscus include the gap height between the blade and substrate, the relative speed of the blade, the viscosity of the ink, and the wettability of the substrate.[28, 296] Once the wet film with the dissolved precursor salts is deposited, the perovskite thin film forms through drying, nucleation, and crystal growth as discussed in section 3.1.1.3.
Blade coating is a popular choice for lab-scale perovskite solar cell research because it is cost-effective, produces minimal ink waste, and is compatible with both rigid and flexible substrates. These advantages make it particularly suitable for optimizing perovskite formulations and device architectures. In small-scale devices, PCEs exceeding

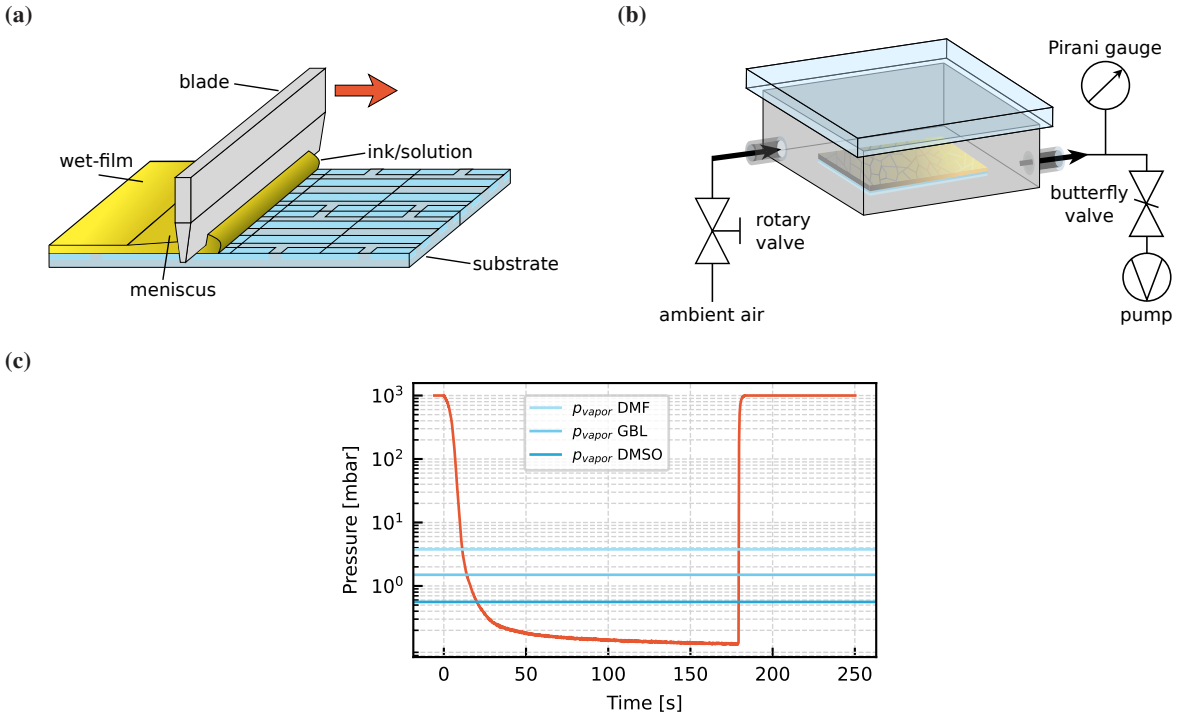

Figure 3.1: Blade coating and vacuum quenching process. (a) Schematic of blade coating, where a blade moves across the substrate to evenly distribute the precursor solution, forming a uniform wet film. (b) Vacuum quenching setup: the coated substrate is placed in a vacuum chamber where pressure reduction, combined with gas flow during evacuation, accelerates solvent evaporation, enabling rapid nucleation and crystallization. (c) Pressure-time curve for vacuum quenching, showing the decrease in chamber pressure during the process for perovskite wet films prepared with the solvents DMF, GBL, and DMSO.

25% for single-junction devices[297] and 31% for perovskite-silicon tandems[298] have been achieved in solar cells with blade-coated perovskite thin films, highlighting the method's potential for high-performance thin films. Blade coating also serves as a prototype for slot-die coating, a related technique designed for industrial-scale production. Both methods share the same fundamental principles, but slot-die coating features a continuous ink supply through a slit in the slot-die head, enabling stabilized and uniform film deposition for large-area manufacturing, such as roll-to-roll processing.[28, 296, 299, 300] While slot-die coating offers additional control over wet film thickness through adjustable ink feeding rates, its higher material requirements and more complex setup make blade coating the preferred choice for lab-scale experiments and prototyping.
In this work, blade coating is performed at room temperature in an ambient atmosphere using a Zehntner ZAA 2300.H automatic film applicator with a ZUA 2000 universal applicator. A blade gap of 100 μm is used for the deposition, with a blade speed of 25 $mm\,s^{-1}$ for perovskite deposition. The HTL layer is coated twice in the forward direction at a speed of 16 $mm\,s^{-1}$.

3.1.1.2 Vacuum Quenching

The drying of the deposited perovskite precursor wet film and the subsequent nucleation process are critical steps in solution-based deposition techniques. To initiate nucleation and crystallization, solvent removal must be carefully controlled, as the drying dynamics directly affect the quality of the thin film. Quenching methods are widely used to optimize this process by inducing a rapid increase in supersaturation of the perovskite precursor solution at the onset of crystallization. This accelerated supersaturation promotes a high nucleation rate, resulting in a densely packed and homogeneous thin film, which is essential for high-quality perovskite solar cells.[301]

Commonly used quenching methods include antisolvent quenching, gas quenching, and vacuum quenching.[302–304] Antisolvent quenching involves applying a secondary solvent to extract the primary solvent and induce crystallization. While effective for spin-coated devices with small areas, it is challenging to scale up and relies on toxic solvents.[305–307] Gas quenching, which uses controlled convection of a drying gas over the wet film, is better suited for roll-to-roll processing, but can deform the wet film at high gas flow rates, particularly when high-boiling-point solvents are used.[299, 308–310] Vacuum quenching, in contrast, offers scalability and avoids the use of harmful solvents. By placing the substrate in a vacuum chamber and evacuating the atmosphere to create low pressure, vacuum quenching accelerates solvent evaporation and promotes rapid nucleation.[303, 311–313] Similar to gas quenching, vacuum quenching is widely used as an in-line drying method in conjunction with scalable coating and printing techniques, such as blade coating, spray coating, slot-die coating, and inkjet printing, making it suitable for both small-area and large-area applications.[303, 304] It achieves high supersaturation rates over large areas and is primarily applied in batch-to-batch processing.[301] Unlike antisolvent quenching, vacuum quenching eliminates the need for toxic solvents and avoids deformation of the wet film caused by high gas flow rates, making it more environmentally friendly and suitable for large-scale applications.[304]
While often assumed to rely solely on solvent evaporation due to reduced pressure, vacuum quenching also benefits significantly from the gas flow generated during air evacuation, which enhances nucleation and crystallization.[303] This gas flow creates a favorable drying environment that accelerates supersaturation and promotes high nucleation density, ensuring the formation of dense perovskite films with minimal defects.[301] The venting process at the end of quenching and parameters such as chamber pressure, size, pump rate, and duration further influence thin-film formation.[303] To further enhance solvent extraction, a moderate nitrogen flow can be introduced during evacuation to increase the rate of solvent removal from the sample surface.[314]
In this work, a vacuum quenching setup is used to obtain high-quality thin films. The system consists of a vacuum chamber equipped with a rotary valve to control air entry, a butterfly valve to regulate evacuation, and a pump (first dataset: Agilent TriScroll 600, second dataset: Leybold Trivac D4B) to achieve the desired pressure reduction (see Figure 3.1b). A Pirani gauge monitors the chamber pressure throughout the process. The substrate is placed inside the chamber and the pressure is reduced to around 10^{-1} mbar (see Figure 3.1c). The rotary valve introduces a controlled gas flow during venting, which facilitates final solvent evaporation and accelerates the crystallization process. To allow photoluminescence measurements during quenching, the vacuum chamber lid is made of acrylic glass, allowing transmission in the visible and near-infrared range.
Although a significant part of the quenching process is driven by gas flow over the substrate, this technique is referred to as "vacuum quenching" throughout this thesis, while alternative terms such as "gas-assisted vacuum quenching" or "vacuum-assisted gas quenching" may also be appropriate. Overall, vacuum quenching combines rapid solvent removal with controlled nucleation dynamics, providing a scalable approach to producing high-quality perovskite thin films suitable for both laboratory-scale research and industrial manufacturing.

3.1.1.3 Perovskite Thin-Film Formation

The formation of high-quality perovskite thin films is a critical step in the fabrication of efficient perovskite solar cells. Multicrystalline thin films with large individual crystals and minimal crystal boundaries are highly desirable for optimal charge carrier transport and reduced recombination losses. However, while the crystallization of the perovskite thin film is critical, understanding and precisely controlling the underlying processes remains a complex challenge. The transformation from a liquid precursor solution to a crystalline thin film involves the entangled process phases of drying, nucleation, and crystal growth (see Figure 3.2).[28] After the precursor solution is deposited onto a substrate, the drying phase begins, characterized by solvent extraction from the wet film. Nucleation starts, during which crystalline seeds form through supersaturation of the solution. This is succeeded by crystal growth, where the nuclei grow and coalesce into larger crystalline grains.
The nucleation and crystallization processes in perovskite thin films are commonly described based on the solution concentration over time using the LaMer model.[296, 315, 316] Solvent extraction drives precursor concentration

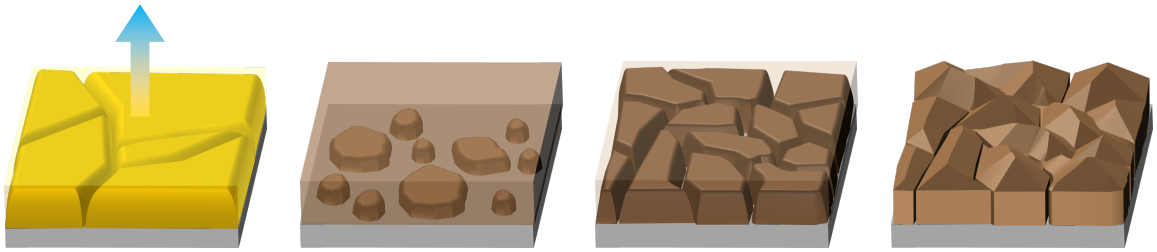

Figure 3.2: Entangled phases of perovskite thin-film formation. Illustration of the four key phases during thin-film formation, extended from [28]: (i) drying phase, during which solvent is extracted, and no photoluminescence (PL) signal is observed; (ii) nucleation phase, characterized by the formation of crystalline seeds and the onset of a PL signal; (iii) crystal growth phase, during which nuclei coalesce into larger grains with a decrease in PL signal due to non-radiative recombination at grain boundaries; and (iv) final surface morphology phase, during which the thin film develops its final surface roughness (see Figure 7.4 for correlation between formation phases and acquired PL signals).

above saturation (C_s), but nucleation requires exceeding the critical concentration (C_c). Above C_c, both nucleation and crystal growth occur simultaneously, with higher supersaturation accelerating nucleation. This step can occur by homogeneous nucleation, where nuclei form spontaneously in the bulk solution, or heterogeneous nucleation, where pre-existing surfaces or impurities serve as nucleation sites. While continued solvent removal increases the concentration, the consumption of precursor materials by nucleation and growth causes the concentration to decrease. Once the concentration falls below C_c, nucleation stops, but crystal growth continues until the solution returns to C_s.[46, 296] The interplay between nucleation and growth determines the morphology of the thin film. Slow solvent removal, which keeps the concentration between C_s and C_c, leads to limited nucleation and uncontrolled crystal growth, resulting in incomplete coverage and defect-rich films. In contrast, rapid solvent removal maintains concentration above the critical threshold C_c, promoting dense nucleation and ensuring complete substrate coverage. These densely packed films initially consist of small crystals that grow and coalesce into larger grains over time.[46, 303]

Growth rate and direction strongly affect grain size and film uniformity, which are critical for minimizing defects and improving charge carrier transport. Optimizing thin-film formation requires balancing nucleation and growth, as excessive nucleation creates many small grains, while insufficient nucleation results in poor coverage and irregular morphology. This process can be influenced by the choice of solvent, environmental conditions, and quenching methods, which are critical to controlling the crystallization process as they accelerate solvent removal and induce supersaturation. However, achieving rapid, uniform solvent removal becomes increasingly challenging as substrate size increases.[296]

In this work, the commonly used phases to describe thin-film formation (drying, nucleation, and crystal growth)[28] are extended by an additional phase of final surface morphology formation (see Figure 3.2). These four phases correspond to the *in situ* photoluminescence transients recorded during vacuum quenching. In phase (i), no PL signal is observed during drying as the precursor material remains dissolved. Phase (ii) begins with the onset of nucleation, producing a strong PL signal as perovskite nuclei and small grains form. In phase (iii), the PL signal decreases due to non-radiative recombination at grain boundaries and reduced photon outcoupling, coinciding with crystal growth and coalescence. Finally, in phase (iv), the evolution of the PL signal during venting reflects the formation of the final surface morphology of the thin film, including surface roughness (see Figure 7.4 for correlation between formation phases and acquired signals).

3.1.2 Vapor Phase Deposition

Next to solution processing, various vapor phase deposition techniques can be used to fabricate homogeneous thin films. Physical vapor deposition (PVD) refers to vacuum-based processes in which a material transitions from the

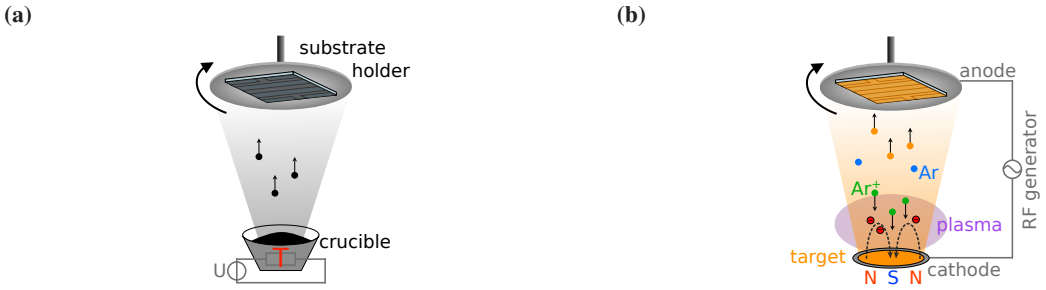

Figure 3.3: Vapor phase deposition techniques used in this work. (a) Thermal sublimation: A material is heated in a crucible or boat by resistive heating in a high-vacuum environment, causing it to vaporize and deposit as a thin film on the substrate. The substrate is rotated during deposition to ensure uniformity. (b) Sputtering: Plasma-assisted argon (Ar) ion bombardment ejects atoms from a solid target, which deposit on the substrate to form a uniform thin film. A magnetic field enhances plasma density, while alternating voltage enables sputtering of insulating materials. Both methods are used for deposition of functional layers needed for solar cell fabrication.

condensed phase to the vapor phase and then deposits as a thin film on a substrate. The two PVD processes used in this work, thermal sublimation and sputtering, are briefly described below.

3.1.2.1 Thermal Sublimation

Like other PVD processes, thermal sublimation, also known as thermal or resistive evaporation, is performed in a high-vacuum environment to minimize particle collisions and ensure a high mean free path for sublimed atoms or molecules. A standard thermal sublimation system consists of three key components: a vacuum chamber, a thermal source, and a substrate holder. The material to be deposited, typically in a solid state such as powder or lumps, is placed in a heat-resistant boat or crucible (see Figure 3.3a). The sublimation boat, made of a heat-resistant metal, conducts high electrical currents to generate the heat required for vaporization. Alternatively, a ceramic crucible surrounded by a metal wire coil heats up when an electric current is applied. Through resistive heating, the material is heated to its sublimation temperature, transitioning to the gas phase.[317]
The vaporized atoms follow the sublimation cone in the vacuum chamber and deposit on the cooler substrate positioned above, forming a thin film. To ensure uniform thickness across the surface, the substrate is rotated during deposition. The sublimation rate, which is critical to achieving reproducible and precise layer thickness, is controlled by adjusting the applied current and monitored using oscillating quartz crystal measurements. This precision makes thermal sublimation particularly well-suited for depositing metals and charge-selective contact materials. In addition, shadow masks can be used to pattern specific designs directly during sublimation.
In this study, a Coat 320 system from Vactec GmbH is used to achieve reliable and precise coatings under high-vacuum conditions (around 10^{-6} mbar), ensuring uniform thin-film quality essential for high-performance solar cell devices.

3.1.2.2 Sputtering

Sputtering uses plasma-assisted ion bombardment to eject individual atoms or molecules from a solid target, which then deposit onto a substrate to form a thin film. The process is performed in a high-vacuum chamber, which minimizes particle collisions and ensures precise material transfer. A process gas, typically argon, is ionized by an electric field applied between an anode and a cathode, producing positively charged ions. These ions are accelerated toward the target material mounted on the cathode and strike its surface with sufficient force to eject individual atoms from the target. The ejected atoms move through the vacuum chamber and deposit on the substrate positioned above, forming a uniform thin film (see Figure 3.3b). Rotation of the substrate during the process ensures

a homogeneous film across the surface.[317]
A magnetic field can be applied above the target surface to trap electrons near the target, increasing plasma density and improving ionization and sputtering rates. Radio frequency (RF) sputtering alternates the voltage polarity at high frequency, enabling the sputtering of insulating materials by preventing charge buildup on the target. The faster response of lighter electrons to the alternating electric field compared to the slower movement of heavier ions creates an average negative voltage on the target, similar to DC sputtering. In addition, reactive gases such as oxygen can be introduced to fabricate materials like transparent conductive oxides (e.g., indium tin oxide). This flexibility makes sputtering ideal for materials that are challenging to deposit by thermal sublimation, particularly those that are difficult to vaporize by heating.
In this study, a Pro Line PVD 75 sputtering system from Kurt J. Lesker Company is used to deposit NiO_x hole transport layers.

3.1.3 Solar Cell Architecture and Materials

The following describes the perovskite solar cell architectures used in this work, the materials used to make them, and how they are manufactured. In planar solar cells, the active layer is sandwiched between two planar charge carrier selective layers. Depending on the polarity of the charge carrier selective layer on the substrate side, a distinction is made between "conventional" n-i-p and "inverted" p-i-n architectures. When designing and fabricating the layer stack of perovskite solar cells, several design criteria have to be considered. For example, it must be ensured that the layers are deposited on the underlying layer without causing damage. This can be achieved by using orthogonal solvent systems or buffer layers and ensuring that they can be thermally processed. In addition, the electron and hole-selective layers must be selected so that their valence and conduction bands are aligned with those of the absorber or have a high blocking barrier. Furthermore, the thickness of the thin film must be optimized to reduce electrical transport and reflection losses.
Most of the results presented in this work are based on the inverted p-i-n architecture, which is used in all experiments based on vacuum quenching (partly chapter 4 and all chapters 5, 6, and 7). Only the results based on laminar gas flow quenching in the drying channel are obtained with solar cells having the n-i-p structure. Both stacks will now be discussed:
The p-i-n layer stack consists of the glass substrate, the transparent electrode, the hole transport layer, the perovskite absorber, the electron transport layer, and the metal electrode. Glass substrates with pre-patterned indium tin oxide (ITO) are used as front electrodes (Luminescence Technology). For blade coating, $32\times64\,mm^2$ substrates are used, which are mechanically cut on the backside and broken into eight standard-size $16\times16\,mm^2$ substrates after absorber deposition for further processing (see Figure 2.8a for the layout of the large-area substrates). The large-area glass substrates with pre-patterned ITO are cleaned in acetone and isopropanol in an ultrasonic bath for 15 and 5 min, respectively, and an oxygen plasma is applied for 3 min.
The nickel oxide (NiO_x) hole transport layer is sputtered to a thickness of 10 nm (NiO_x target from Kurt J. Lesker Company, 99.995% metallic purity) using a Pro Line PVD 75 sputtering system from Kurt J. Lesker Company at 1 mTorr process pressure with the process gas argon under RF conditions at 100 W (see Figure 3.4a). After 1 min low power oxygen plasma treatment, 16 μL 2PACz solution ((2-(9H-carbazol-9-yl)ethyl)phosphonic acid, >98%, TCI Chemicals, 1.5 mg mL^{-1} in ethanol) is deposited onto the $32\times64\,mm^2$ substrate by blade coating in ambient air ($\approx$ 21 °C, 45% relative humidity) using a Zehntner ZAA 2300.H automatic film applicator in combination with a ZUA 2000 universal applicator with a blade gap of 100 μm. The substrate is coated twice in the forward direction with 2PACz at a blade speed of 16 mm s^{-1} and then annealed for 10 min at 100 °C.
The double cation perovskite (DCP) composition $Cs_{0.17}FA_{0.83}Pb(I_{0.91}Br_{0.09})_3$ is used for the perovskite absorber layer. The standard solution (0.67 M, 1.0 molar ratio) is prepared by dissolving PbI_2 (0.875 M, TCI Chemicals), and $PbBr_2$ (0.125 M, TCI Chemicals) in a 4:1 (vol%) mixture of N,N-dimethylformamide (DMF, anhydrous, Sigma-Aldrich) and dimethyl sulfoxide (DMSO, anhydrous, Sigma-Aldrich). The PbX_2 solution is then added

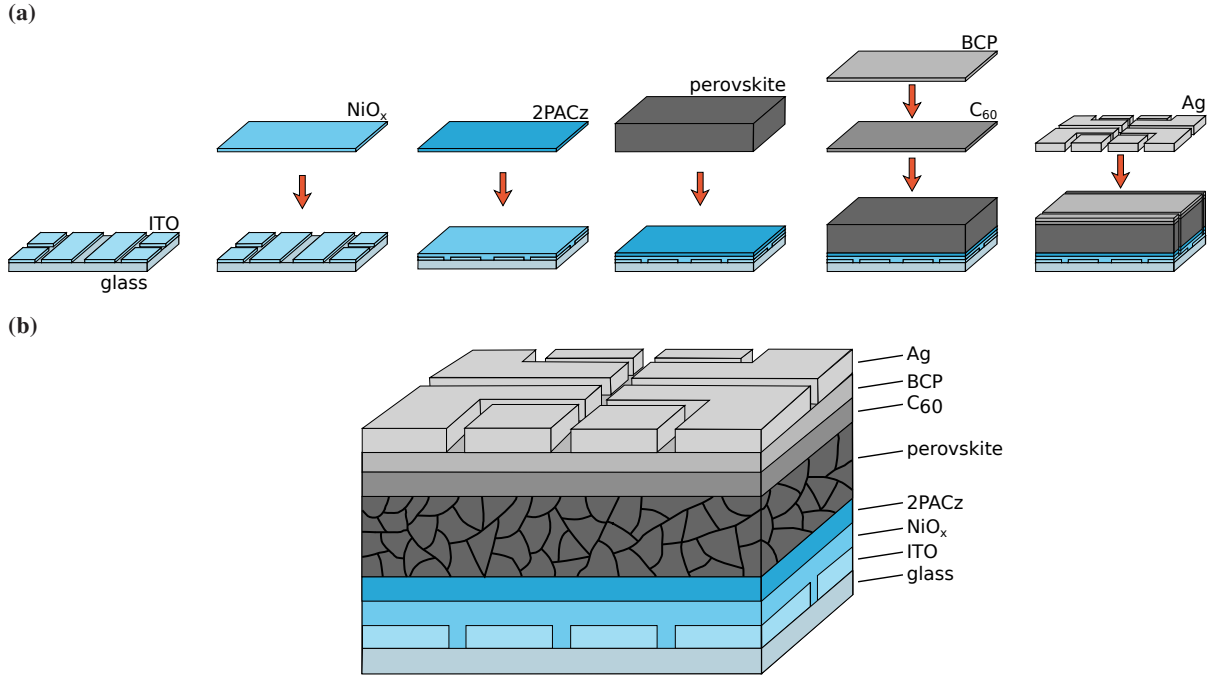

Figure 3.4: Fabrication process of an inverted p-i-n perovskite solar cell. (a) Schematic representation of the sequential layer-by-layer fabrication of the inverted p-i-n solar cell architecture, starting with a glass substrate with pre-patterned ITO electrodes, followed by sputtering of NiO_x, blade coating of 2PACz and the perovskite absorber, and thermal sublimation of C_{60}, BCP, and the silver (Ag) electrode. (b) Illustration of the final solar cell stack and its layout, detailing the layer stack of glass, ITO, NiO_x, 2PACz, perovskite absorber, C_{60}, BCP, and Ag. This architecture is used in all experiments involving vacuum quenching, which is used to generate both datasets.

to $CH(NH_2)_2I$ (FAI, 0.825 M, GreatCell Solar) and CsI (0.175 M, abcr) and then diluted 2:1 (vol%) with γ-butyrolactone (GBL, Sigma-Aldrich). To vary the molar ratio as done in chapter 6, i.e., the Pb/A-cation ratio, the $(CsI : FAI)$:$(PbBr_2 : PbI_2)$-ratio in the precursor solution is varied from 0.9 (lead deficiency) to 1.1 (lead excess). For this purpose, the base solutions for the molar ratios 0.9, 1.0, and 1.1 are weighed and then mixed in a ratio of 1:1 (vol%) to obtain the intermediate molar ratios. To vary the precursor molarity between 0.56 M and 0.84 M, the amount of solvent added is varied. Starting from the standard molarity of 0.67 M, the other molarities are obtained by decreasing the amount of total solvent ((DMF : DMSO 4:1 (vol%)):GBL 2:1 (vol%)) by 10% and 20%, respectively, and increasing the amount of total solvent by the same percentages.

Using 25 μL of the precursor solution, the perovskite thin film is then blade-coated onto the $32\times64\,mm^2$ substrate in ambient air using a Zehntner ZAA 2300.H automatic film applicator in combination with a ZUA 2000 universal applicator with a blade gap of 100 μm and a blade speed of $25\,mm\,s^{-1}$. After blade coating of the perovskite thin film, the samples are placed in a custom-built chamber for vacuum quenching with a standard duration of 3 min, unless otherwise specified. After quenching, the chamber is vented with ambient air and the samples are annealed at 150 °C for 30 min.

The large $32\times64\,mm^2$ substrates are cut into eight $16\times16\,mm^2$ samples and finalized into functional solar cells by thermal sublimation of a 25 nm C_{60} fullerene electron transport layer (Sigma Aldrich, 98%), a 5 nm bathocuproine (BCP) buffer layer (Luminescence Technology), and a 100 nm silver (Ag) back contact. By using a shadow mask during the deposition of the silver back contact, each $16\times16\,mm^2$ sample yields four cells with an active area of $10.5\,mm^2$ per solar cell. The resulting p-i-n stack consists of glass, ITO, NiO_x, 2PACz, DCP, C_{60}, BCP, and Ag (see Figure 3.4b).

In parts of chapter 4, the n-i-p architecture is used, which consists of the glass substrate, the transparent electrode, the electron transport layer, the perovskite absorber, the hole transport layer, and the metal electrode. The glass

substrates with pre-patterned ITO (Luminescence Technology) are used as front electrodes. The $64\times64\,\mathrm{mm}^2$ substrates are cleaned with acetone and isopropanol in an ultrasonic bath and an oxygen plasma is applied for 3 min. After cleaning, the electron transport layer is deposited by spin coating a 2% colloidal dispersion of SnO_2 nanoparticles (Alfa Aesar, diluted from 15%) at 4000 rpm for 30 s with an initial volume of 400μL per substrate. The coated substrates are annealed at 250 °C for 60 min, after which they are cut into $32\times48\,\mathrm{mm}^2$ substrates. A second, low power oxygen plasma treatment is applied to these smaller substrates for 1 min.
The perovskite absorber layer, methylammonium lead iodide (MAPI, $CH_3NH_3PbI_3$, $MAPbI_3$) is deposited by blade coating. A 0.75 M solution is prepared by dissolving methylammonium iodide (MAI) and lead chloride ($PbCl_2$) in DMF, as well as methylammonium iodide (MAI) and lead acetate trihydrate ($Pb(CH_3COO)_2 \cdot 3H_2O$) in DMF, maintaining a molar ratio of MAI:Pb of 3:1. After mixing the two individual solutions, the final solution is blade-coated using a ZUA 2000 universal applicator with a blade gap of 100 μm attached to a stepper motor that moves the blade across the substrate at $15\,\mathrm{mm\,s}^{-1}$. After deposition, the film is dried for 3 min, followed by a total of 6 min of annealing using a Peltier module (TRU COMPONENTS TEC1-12715), which includes a 4 min temperature ramp to stabilization at 100 °C. The edges of the substrates are cleaned with a GBL-soaked Q-tip to create a 3 mm thick reference frame for subsequent characterization.
The substrates are then cut into $16\times16\,\mathrm{mm}^2$ samples. The Spiro-OMeTAD hole transport layer is deposited by spin coating. A solution of 80 mg Spiro-OMeTAD (Luminescence Technology) in 1 mL chlorobenzene is doped with 28.5 $\mu\mathrm{L\,mL}^{-1}$ 4-tert-butylpyridine and 17.5 μL of lithium bis(trifluoromethanesulfonyl)imide ($520\mu\mathrm{g\,mL}^{-1}$ in acetonitrile). Each $16\times16\,\mathrm{mm}^2$ substrate is spin-coated at 4000 rpm for 30 s, and the resulting layer is doped by 12-15 hours of oxygen exposure in air ($\approx$ 30% humidity). Finally, a 75 nm gold (Au) electrode is thermally sublimed on the substrates using a shadow mask yielding four individual solar cells per sample with an active area of $10.5\,\mathrm{mm}^2$ per cell. The resulting n-i-p stack is glass, ITO, SnO_2, MAPI, Spiro-OMeTAD, Au.

3.2 Characterization

Experimental measurement techniques are essential to probe and characterize the properties of perovskite thin films and fully fabricated solar cells. This work aims to establish a link between thin-film quality and the resulting solar cell efficiency by leveraging measurement data. In this section, the characterization methods used to acquire *in situ* data and to quantitatively assess the properties and performance of perovskite solar cells are presented. These experimental techniques provide both the input data for subsequent data-driven analyses as well as the target labels for ML models, specifically PV performance metrics and thin film thickness.

3.2.1 Optoelectronic Characterization

Measuring the current density-voltage (J-V) characteristics of a solar cell under standard test conditions is the fundamental measurement for determining key PV performance metrics such as PCE, J_{SC}, V_{OC}, and FF (see section 2.2.2).
For J-V measurements, the solar cells are illuminated with a class AAA 21-channel LED solar simulator (Wavelabs Solar Metrology Systems Sinus-70) under AM1.5G conditions, which describe the solar spectrum for transmission through 1.5 times the global air mass, corresponding to an angle of incidence of 48.2° with a light intensity of $100\,\mathrm{mW\,cm}^{-2}$. For a small subset of solar cells fabricated using laminar gas flow quenching (see chapter 4), a class AAA xenon lamp-based solar simulator (Newport Oriel Sol3A) is used.
The intensity of the solar simulator is calibrated to the certified J_{SC} of a silicon reference solar cell filtered with a KG5 bandpass filter (Newport). The temperature of the solar cells is kept constant at 25 °C throughout the measurements using a Peltier element controlled by a microcontroller for regulation. A shadow mask with an aperture size of $7.84\,\mathrm{mm}^2$ is used to ensure precise area control during illumination. All measurements are

performed in a nitrogen atmosphere.
A Keithley 2400 source measurement unit is used to measure the current-voltage characteristics electrically. The J-V curves are recorded in both forward and backward scan directions at a scanning rate of 0.6 V s^{-1} (see Figure 2.3b for a current density-voltage J-V curve). From these measurements, PCE, J_{SC}, V_{OC}, and FF are obtained directly, while R_{s} and R_{sh} are calculated from linear fits near V_{OC} and J_{SC}, respectively.
Boxplots are used to compare the distributions of PV performance metrics across different data subsets. The box represents the interquartile range (IQR) from the first to the third quartile, with the median indicated as a black line and the mean as a white diamond. Whiskers extend to the most extreme data points within 1.5 times the IQR, while data points beyond the whiskers are marked as outliers.
Due to the light-soaking effect commonly observed in perovskite solar cells, where efficiency improves with prolonged illumination, three consecutive measurements are made and the best result is included in the dataset. While the true PCE under constant voltage operation may be systematically lower due to hysteresis and stability issues, the J-V measurements serve as a reliable method to determine an upper limit of the achievable PCE. This approach is sufficient to evaluate the potential of ML for predicting PCEs based on *in situ* data and allows relative comparisons between samples.

3.2.2 Profilometry

Profilometry is a technique for characterizing the surface profile, roughness, and thickness of thin films. During the measurement, a diamond stylus is moved laterally across the sample surface while maintaining direct contact. Changes in the vertical position of the stylus during the lateral scan are recorded and the measured deflection of the stylus is used to generate the surface profile.
Thin film thickness measurements are performed by profiling either the edge of a thin film or a dedicated notch extending to the substrate. The absolute thickness of the thin film is then determined as the height difference between the thin film surface and the reference substrate surface.
In this work, a Dektak XT profilometer by Bruker is used as an efficient and reliable approach to measure the thickness of perovskite thin films. For each solar cell active area, three spatially offset profilometer scan lines are acquired. The spatial average of these scans is used as the thin film thickness label for the solar cells included in the first generated dataset (see chapter 5).

3.2.3 Photoluminescence

Photoluminescence is a powerful technique for examining the optoelectronic properties of perovskite thin films. Luminescence occurs when an electron transitions from an excited state to a lower energy ground state, emitting a photon in the process. Depending on how the electron is excited from the valence band (ground state) to the conduction band (excited state), the process is classified into different types of luminescence such as photoluminescence and electroluminescence (EL). Photoluminescence involves the absorption of an incident photon with energy higher than the bandgap, which provides the energy to excite an electron to the excited state. After thermal relaxation, the electron radiatively recombines with a hole, emitting a photon of lower energy (see Figure 3.5). PL intensity is influenced by the balance between radiative and non-radiative recombination processes and is strongly affected by material quality, crystal structure, and composition.[318]
Recombination, where electrons and holes neutralize each other, is central to the optoelectronic performance of materials. Radiative recombination, also known as band-to-band recombination, occurs when an electron and a hole recombine while emitting a photon. In contrast, non-radiative recombination mechanisms include Shockley-Read-Hall (SRH), surface/interface, and Auger recombination, which do not emit photons but represent loss paths that degrade device performance.[319, 320] For high-quality optoelectronic devices, the unwanted loss mechanism of non-radiative recombination must be minimized. Reducing non-radiative recombination increases radiative

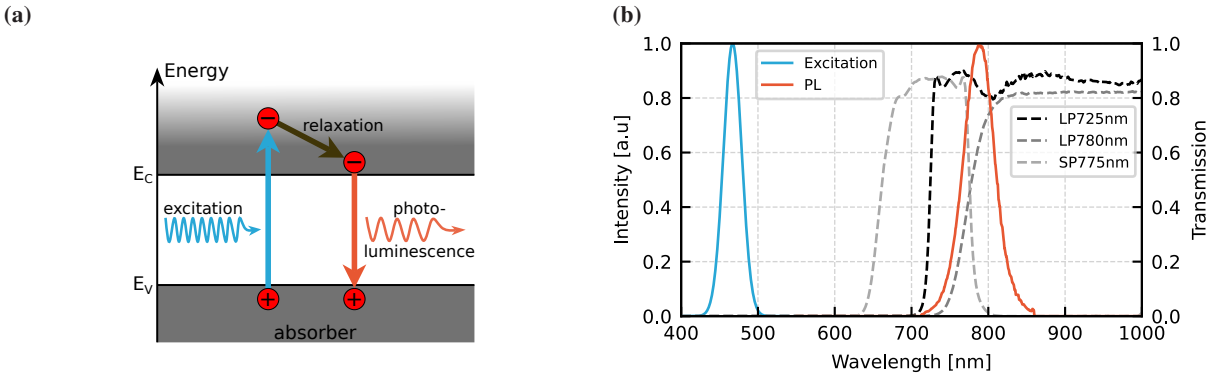

Figure 3.5: Band diagram and photoluminescence (PL) spectrum of a perovskite thin film. (a) Schematic representation of photoluminescence, showing excitation of an electron from the valence band (E_V) to the conduction band (E_C), followed by thermal relaxation and radiative recombination, emitting a photon with lower energy. (b) Excitation spectrum (467 nm center wavelength) and PL emission spectrum of a perovskite thin film, combined with the transmission characteristics of various spectral filter combinations used in this work.

recombination, indicating good material quality and efficient light-harvesting capability.[321] The charge carrier density in a perovskite thin film is described by the rate equation

$$\frac{dn}{dt} = -an - bn^2 - cn^3, \tag{3.1}$$

where n is the charge carrier density and a, b, and c are the rate constants for the respective fundamental recombination processes, with the exponents indicating the number of charge carriers involved in each mechanism. SRH recombination is a trap-assisted process, caused by defects within the bandgap, where charge carriers are trapped by defect states and recombine non-radiatively. SRH recombination is characterized by the rate constant a because it involves a single charge carrier interacting with the defect states. Second-order recombination, expressed by rate constant b, arises from radiative bulk recombination, which reflects good absorber quality, and non-radiative interface recombination, which depends on factors like interfacial trap density and band misalignment.[322] Since high PL intensity indicates low non-radiative recombination losses, radiative recombination is often used as a benchmark for material quality. Non-radiative bimolecular recombination at interfaces complicates interpretation and can significantly impact recombination rates, particularly in systems with unoptimized interfaces. Auger recombination is a higher-order process involving three carriers, expressed by the rate constant c, where the recombination energy is transferred to a third carrier that thermalizes without photon emission. In perovskite solar cells, non-radiative SRH recombination and interfacial recombination are the primary mechanisms responsible for losses in perovskite solar cells, while Auger recombination is negligible under standard solar irradiation but becomes relevant at much higher irradiation intensities due to very high carrier densities.[323]

Radiative recombination, as the inverse process of photon absorption, is intrinsically linked to the light-harvesting ability of the material.[321] However, radiative recombination directly competes with non-radiative processes, which act as loss mechanisms in perovskite semiconductors.[324] To enhance solar cell performance, it is essential to minimize non-radiative recombination pathways, such as SRH and interfacial recombination while maximizing radiative recombination.[323] A high radiative recombination rate indicates a strong ability to absorb light, which is critical as absorption drives charge carrier generation, combined with reduced non-radiative recombination, which limits the charge carrier loss and allows for improved charge carrier extraction during operation.

PL serves as an indicator of perovskite material quality because its intensity is influenced by the balance between radiative and non-radiative recombination.[325] A high PL signal reflects low non-radiative recombination losses and, consequently, fewer defects in the material. This makes PL a powerful tool for evaluating the optoelectronic

properties of perovskite thin films. However, the interpretation of absolute PL measurements is challenging because the captured PL intensity is affected by photon outcoupling, surface roughness, scattering, interfaces, and temperature effects, which complicate data interpretation.[326–329]

3.2.3.1 Luminescence Imaging

Conventional PL spot measurements average the PL response over a single excitation area, limiting their ability to resolve spatial variations. In contrast, PL imaging provides spatially resolved data over the entire sample, allowing direct visualization of uniformity, defect distribution, and optoelectronic quality in perovskite thin films and solar cells.[229] Rather than assuming that a single spot represents the entire sample, PL imaging captures spatial heterogeneities that manifest at multiple scales from microscopic features like crystallites, grain boundaries, and compositional variations to macroscopic effects such as series resistance gradients or interfacial non-uniformities.[330, 331] These inhomogeneities, often caused by processing or residual particles, highlight the need for spatially resolved characterization to optimize fabrication processes and device performance.
While PL spot measurements provide insight into charge carrier recombination and material quality, PL imaging extends this concept by spatially resolving the luminescence across a perovskite film or device, providing a visual and qualitative assessment of optoelectronic properties. In practice, PL imaging involves uniformly exciting the perovskite sample with a laser or LED and detecting the emitted PL signal with a camera equipped with spectral filters to filter out the excitation wavelength and isolate the PL signal. The resulting intensity images reveal local defects, depending on the resolution of the setup, crystallites and grain boundaries, or large-area thin film inhomogeneities, pinholes, and cracks. For perovskite solar cells, this technique identifies regions of non-radiative recombination, correlates morphological features with optoelectronic losses, and assesses thin film uniformity. Unlike point-based PL measurements, large-area PL imaging provides a spatially resolved macroscopic view of the entire sample, enabling rapid, non-destructive screening of large thin films by quantifying spatial heterogeneity, which is critical for optimizing scalable fabrication processes needed for commercialization.
Unlike mapping or scanning methods, which acquire data point-by-point and are time-consuming over large areas, PL imaging captures spatially resolved data over the entire sample in a single acquisition. This provides a fast, global view of spatial heterogeneities, enabling the identification of defects, non-uniformities, and optoelectronic properties with significantly reduced measurement time. While scanning is impractical for large-area imaging and applications in high-throughput production lines, the rapid characterization and large-area coverage of PL imaging makes it particularly advantageous for *in situ* process monitoring and quality control in scalable fabrication processes.
While PL imaging is a powerful tool for characterizing perovskite thin films and solar cells, it comes with some challenges and limitations. The ability to image large substrates inherently limits resolution, preventing the capture of microscopic details such as grain boundaries or sub-micron defects. In addition, PL imaging primarily probes near-surface regions due to the limited penetration depth of higher-energy photons, which can range from tens to a few hundred nanometers, while lower-energy photons may not be absorbed if their energy is insufficient for the material's bandgap.[332] Artifacts such as reflections, scattering from rough surfaces, or inhomogeneous excitation alter PL images and complicate data interpretation. Furthermore, the time-dependent variations of PL signals introduce an additional layer of complexity. Luminescence can vary over time due to factors like light soaking, trap filling, and ionic defect transport.[333] This makes the timing of image acquisition critical, as these dynamic processes can affect the observed PL intensity and complicate the correlation of PL signals with material and device properties.
Accordingly, quantitative interpretation of PL image data is complex because PL intensity is affected not only by material quality, but also by factors such as surface roughness, optical effects, and measurement conditions. However, the acquisition of transient *in situ* data during material formation, combined with data-driven evaluation, provides an approach to correlate PL data with material quality and device performance. In this work, a monochrome sCMOS camera with a lens mounted on an aluminum frame is used next to two angled blue LED bars for sample

excitation, while spectral filters prevent reflected excitation light from reaching the camera. A detailed description of the setup is given in section 4.2.

3.2.3.2 Photoluminescence Versus Electroluminescence

In contrast to PL, where an absorbed incident photon provides the energy to excite the electron to an excited state, electroluminescence involves exciting electrons by applying an external electrical voltage at the contacts, which provides the energy to excited the electron to an excited state. Instead of relying on optical excitation, EL imaging involves applying an external voltage to inject charge carriers, causing radiative recombination and photon emission from the device.

PL and EL imaging are often used in complementary roles in the characterization of perovskite solar cells, providing insight into different aspects of material quality and device performance.[334] PL imaging is primarily used to investigate the optical and electronic properties of perovskite thin films. It allows the detection of defects, variations in material quality, and the assessment of uniformity across the absorber layer. Because PL imaging does not require electrical contacts, it is particularly advantageous for characterizing films in the early stages of fabrication, making it a non-invasive tool for monitoring process variations and optimizing deposition techniques. This flexibility allows PL imaging to be applied at any stage of device fabrication, from initial thin-film formation to fully processed solar cells.[334] In contrast, EL imaging is used to examine fully processed solar cells under electrical excitation. This makes EL particularly useful for detecting electrical defects such as shunt paths and series resistance variations that affect charge transport. In addition, EL imaging provides information about the entire device stack, including transport layers and interfaces, since the luminescence response depends on charge injection at the contacts.

The experimental setup for EL imaging is simpler than that for PL imaging because it does not require uniform optical excitation or spectral filtering, but it does require electrical contacts, which limits its application to finished devices. In contrast, PL does not need contacts, allowing early, non-destructive material evaluation at any stage of fabrication. Because of their different strengths, PL and EL imaging are often used in combination to obtain a comprehensive understanding of perovskite solar cells. PL imaging provides crucial insights into the intrinsic optoelectronic properties of the absorber, while EL imaging reveals electrical losses and transport-related issues in functional devices.[320]

While both PL and EL signals are affected by the balance between radiative and non-radiative recombination, the signal intensities are also influenced by distinct factors. In PL imaging, the crystal quality and uniformity of the perovskite layer primarily determine the local charge carrier concentration and, consequently, the observed luminescence. Radiative recombination competes with several non-radiative pathways, meaning that spatial variations in PL intensity may reflect differences in defect density, trap states, or surface roughness, which affects photon outcoupling.[320] A brighter PL signal typically indicates lower defect density and higher local carrier populations, whereas PL quenching results from non-radiative centers, high surface recombination, or poor perovskite film quality.

EL imaging, in contrast, relies on the electrical injection of charge carriers and is influenced not only by the intrinsic quality of the perovskite absorber but also by the properties of the transport layers, the interface resistances, and the overall device stack design.[335] High series resistance, for example due to poor interfaces, hinders carrier injection and therefore reduces EL intensity without necessarily affecting PL. As a result, EL images reveal resistive losses due to series and shunt resistances rather than purely optical or morphological non-uniformities. However, severe shunting can quench both PL and EL due to excessive non-radiative recombination pathways. In addition, high non-radiative bulk and surface recombination reduces both PL and EL signals, underscoring the importance of high-quality perovskite films and optimized interfaces to ensure reliable device performance.

Luminescence imaging has long been established as a powerful characterization method for silicon photovoltaics and is increasingly adopted in perovskite solar cell research.[336] The technique allows the extraction of parameters including correlations between luminescence intensity and QFLS[337], spatial mapping of non-radiative recombination centers[338], determination of local series resistance[339], and detection of bandgap variations across the

absorber.[340] Because of its non-destructive nature and ability to provide rapid, spatially resolved measurements, in particular, PL imaging is well suited for in-line quality control during industrial-scale production, which is necessary for the successful commercialization of perovskite PV technology.

4 *In Situ* Multi-Channel Imaging of Perovskite Thin Films

*In this chapter, a novel imaging technique for large-area characterization of perovskite thin films is established and applied to in situ monitoring of perovskite thin-film formation from solution (research objective **I**). Achieving uniform, defect-free thin films over large areas is critical to maintaining high PCEs as PSC fabrication is scaled from laboratory scale to industrial production. In situ photoluminescence and diffuse reflection imaging (IPDRI) addresses this challenge by enabling in situ monitoring of thin-film formation with spatial, temporal, and spectral resolution. Designed for large-area imaging characterization of perovskite thin films, IPDRI allows detection and analysis of morphological inhomogeneities and defects, such as pinholes and absorber quality variations, which can significantly affect device performance. In addition to ex situ studies of deposited perovskite thin films, the system's ability to monitor the dynamic processes in situ during the complex thin-film formation phases of drying, nucleation, and crystal growth under different quenching conditions, i.e., vacuum and laminar airflow quenching, is investigated. It is shown that IPDRI can discriminate between different quenching parameters, allowing process optimization and control in industrial production lines.*

Parts of this chapter were published in the research article "Correlative In Situ Multichannel Imaging for Large-Area Monitoring of Morphology Formation in Solution-Processed Perovskite Layers", *Solar RRL* 6.3 (2021), by *Simon Ternes (S.T.)**, *Felix Laufer (F.L.)**, *Philip Scharfer*, *Wilhelm Schabel*, *Bryce S. Richards*, *Ian A. Howard*, and *Ulrich W. Paetzold*. *In situ* multichannel imaging was developed in close collaboration with Simon Ternes.[341] *S.T.* and *F.L.* contributed equally to this work. The initial proof of concept for luminescence imaging was outlined in [342]. Some figures in this chapter were adapted with permission from [341].
F.L. contributed to this project by co-developing the methodology, leading data curation, software implementation, formal analysis, and visualization, while also making significant contributions to experimental investigations, result validation, and manuscript review. The contributions of all authors according to the CRediT system are listed in Table A.2.

The characterization method showcased in this chapter has already been used in multiple publications to investigate various research questions in the field of perovskite-based photovoltaics at KIT.[304, 314, 326, 341, 343–352]

4.1 Motivation

On laboratory scales, highly efficient perovskite solar cells have reached PCEs exceeding 26%[17–19], but for successful commercialization, the perovskite PV technology has to be transferred to large areas. Fabrication methods that enable state-of-the-art devices on small areas, namely spin coating, cannot be used for deposition on industrial-relevant areas. Accordingly, scalable techniques have to be used for depositing the solar cell layer stack, including the perovskite absorber thin film.[28] However, PCEs of large-area PSC fabricated with scalable methods still lag behind the highly efficient smaller counterparts, as evident by a decrease in PCE when the area is scaled up (see Figure 1.2c). For example, the decrease in PCE over aperture area can be extracted from the *Solar cell efficiency tables* by Martin Green *et al.*[14], which are consolidated tables showing an extensive listing of the highest independently confirmed efficiencies for solar cells and modules. For perovskite single-junction solar cells, the PCE drops from over 26% on small areas [18, 19] to 19.2% on 1027 cm^2 (SolaEon[14]) and to 15.0% on 7906 cm^2 (Microquanta[14]). The record PCE of perovskite/Si tandems decreases from 34.6%[353] to 25.8% on 2054 cm^2 (LONGi[14]).

One of the most critical challenges when scaling up perovskite fabrication is the deposition of high-quality and reproducible perovskite thin films on large areas. To achieve highly efficient large-area PSCs, smooth and pinhole-free perovskite thin films with large grains, high crystallinity, and uniform stoichiometry have to be deposited across large areas while also incorporating low surface roughness and uniform coverage of the entire substrate.[23, 27] As with other thin-film photovoltaic technologies[354], morphological defects in the absorber layer, shunt paths, micro-cracks, and material inconsistencies must be avoided. As the cell area increases, the likelihood of defects, such as parasitic shunts, increases due to the greater opportunity for imperfections to occur during the manufacturing process, and a single defect can potentially shunt an entire cell or degrade its performance by facilitating non-radiative recombination.[341, 343, 355] Therefore, these morphological defects and material inconsistencies must be diligently circumvented or promptly identified, both in research laboratory environments and in industrial fabrication processes. While the focus of this work is placed on scalable perovskite processing from solution, monitoring of the thin-film formation is of paramount importance for both promising approaches for upscaling perovskite thin film deposition, namely thermal evaporation and solution-based deposition.

In order to assess the quality of perovskite thin films, *ex situ* and *in situ* techniques are necessary for characterization. *Ex situ* methods are used after the experimental process, i.e., after annealing during which the perovskite thin films have undergone crystallization. In contrast, *in situ* methods are used during the experimental process, i.e., during the drying and crystallization stages of the perovskite thin-film formation. For *ex situ* characterization of perovskite thin films, different imaging techniques like optical microscopy, scanning electron microscopy (SEM), atomic force microscopy (AFM), and whitelight interferometry (WLI) already allow spatially resolved investigations of the large-area perovskite thin film morphology. However, the formation of perovskite thin films from solution with its entangled phases of drying, nucleation, and crystal growth represents one of the most critical processing steps for solution-based deposition. Consequently, this process must be monitored, characterized, and controlled in order to obtain high-quality large-area optoelectronic perovskite thin films (see section 3.1.1.3 for more details on the thin-film formation).[28, 356] Since only *in situ* techniques allow monitoring the formation of perovskite thin films from precursors solution, spatially resolved *in situ* characterization methods are essential as a complement to *ex situ* techniques.

X-ray-based characterization techniques like X-ray diffraction (XRD) and grazing incidence wide-angle X-ray scattering (GIWAXS) are powerful techniques for *in situ* investigation of perovskite crystal structure evolution.[357–365] However, *in situ* imaging of large areas with these techniques is challenging. *In situ* transmission electron microscopy (TEM)[366, 367] allows monitoring the morphology formation of perovskite thin films, but is also impractical for use in industrial production lines. In contrast, optical characterization techniques using photons in the UV to near-infrared range have been successfully implemented in production environments. For instance, photoluminescence imaging can be conducted under ambient conditions and has already been applied to Si- and

$Cu(In,Ga)Se_2$ photovoltaics[336, 368]. In perovskite PV research, next to thermography[369, 370] in the long-infrared range, also characterization methods in the optical wavelengths range are applied *in situ*, namely (i) *in situ* Raman spectroscopy[371, 372], (ii) *in situ* absorption and reflection measurements[304, 373–382], and (iii) *in situ* photoluminescence techniques[364, 374, 377, 381–386]. In addition to being easily applicable for monitoring deposition processes such as spin coating[374, 383, 387] and blade coating[388, 389], these techniques can be adapted to provide large-area imaging information using high-power light-emitting diodes as excitation sources and cameras as detectors. Already established in Si[336], GaAs[390], CdTe[391], and CIGS[392] photovoltaics, luminescence and reflection imaging methods also provide valuable insight into the quality of perovskite thin films and allow correlating the imaging data with the PCE of the corresponding devices.[334, 335, 339, 393, 394]
Although integration of *in situ* large-area characterization tools into fabrication environments is essential for (industrial) production in-line quality control, this topic only has been "subject of a small number of scientific studies so far, indicating that much more research interest and investments have to be done on this topic" (see review article on *in situ* characterization of perovskite solar cells[395]). Since *in situ* PL has great potential to monitor, control and research the perovskite thin-film formation[341, 374, 377, 378, 382], *in situ* PL imaging is used to gain insight into the complex fabrication process. Accordingly, a novel imaging technique for large-area characterization of perovskite thin films is established and applied for *in situ* monitoring of perovskite thin-film formation from solution (research objective **I**).[341] While there was literature on *in situ* PL imaging microscopy for characterizing charge carrier dynamics in perovskite thin films on small scales[396–400], at the time of publication, there was no published technique combining large-area imaging capability with real-time *in situ* operation for monitoring the perovskite formation.
The *in situ* photoluminescence and diffuse reflection imaging (IPDRI) system is designed to fulfill essential requirements for large-area *in situ* characterization of the perovskite thin-film formation:

1. **Large-Area Imaging:** The system captures high-resolution images over large substrates, enabling direct transfer to industrial-scale production while resolving morphological thin-film features in detail.

2. **High Temporal Resolution:** With sub-second temporal resolution, the system tracks rapid changes during key phases of thin-film formation, including drying, nucleation, and crystal growth.

3. **Versatile Application:** The system is adaptable for both *in situ* and *ex situ* applications, supporting real-time process monitoring and detailed post-process analysis.

4. **Multi-Channel Monitoring:** The system uses multiple channels to monitor reflection, photoluminescence intensity, and approximate peak wavelength, providing comprehensive spatial, temporal, and spectral data.

5. **Non-Invasive Measurements:** The system ensures measurements do not alter or damage samples, maintaining the integrity of the perovskite films.

6. **Ambient Operation:** Designed to operate effectively in ambient environments, the system can be integrated directly into production lines without the need for specialized environmental controls such as vacuum.

The IPDRI system satisfies the critical requirements for scalable, non-invasive, large-area *in situ* characterization, making it a valuable tool for advancing perovskite solar cell development in both academic research and industrial settings.[341] The following sections introduce the capabilities of the IPDRI system, beginning with its use in *ex situ* investigations. First, the system's ability to examine large-area blade-coated perovskite thin films is demonstrated using reflection, photoluminescence, and PL peak wavelength imaging. It is discussed how IPDRI facilitates the localization and classification of inhomogeneities, and how detected defects can be correlated with device performance. Next, *ex situ* photoluminescence images are compared to electroluminescence imaging for the characterization of perovskite-perovskite tandem solar modules. Two use cases of *in situ* monitoring of large-area substrates are then presented investigating temporal changes during (i) vacuum quenching of blade-coated perovskite thin films and (ii) drying of blade-coated perovskite thin films in a laminar airflow channel. Finally, the potential of

IPDRI for identifying process parameter variations and its suitability as a tool for in-line monitoring of large-area PSC production lines is discussed.

4.2 Spatially Resolved Characterization with Multi-Channel Imaging

The established method generates data with spatial, temporal, and spectral resolution. This section focuses on the system's large-area imaging capabilities, examining the various aspects of (*ex situ*) multi-channel imaging. Initially, blade-coated perovskite thin films are investigated using reflection and photoluminescence images captured by the system, as well as calculated approximations of PL peak wavelength images. Subsequently, the investigation is extended to encompass entire PSC devices, with a discussion of the potential of electroluminescence. The information contained in temporal data obtained during *in situ* experiments is addressed in the following section (see section 4.3).

4.2.1 Setup: Photoluminescence and Diffuse Reflection Imaging

In order to meet the above requirements, a modular multi-channel imaging setup has been established that allows *in situ* monitoring of the perovskite thin-film formation from solution with spatial, temporal, and spectral resolution. To realize multi-channel imaging, the main components are a camera, an excitation source, and various filters with different spectral transmission (see Figure 4.1). Accordingly, a monochrome sCMOS camera (CS2100M-USB Quantalux, 1920×1080 pixels, Thorlabs) is equipped with a lens (MVL25M23, Thorlabs) and mounted on a scaffolding made of aluminum rails. Two blue LED bars (LDL2, 146X30BL2-WD, CCS Inc.) are mounted in parallel and tilted towards each other. The samples are illuminated (≈0.08 suns, 467 nm center wavelength) without visible reflections of the LED bars in the images captured by the camera. The spectral filters are placed between the camera and the excitation LEDs to filter out residual, reflected excitation light. To quickly change the filter used for

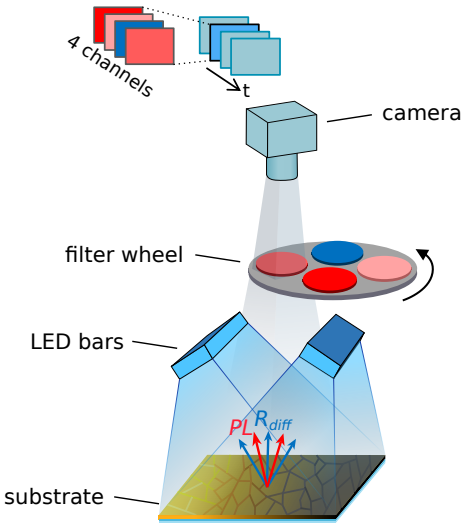

Figure 4.1: Schematic of the multi-channel imaging system. Two slightly tilted blue LED bars illuminate and excite the sample. The reflected excitation light and the emitted PL pass through optical filters and are captured by the camera. By synchronizing the camera trigger with the rotation of the wheel carrying different spectral filters, the IPDRI system acquires time series of images with four different channels, namely one reflection channel and three differently filtered PL channels (see Figure A.2a and Figure A.2b for photographs of the setup mounted on a vacuum quenching chamber and on a laminar gas flow channel).

image acquisition, the filters are placed in a rotating wheel. A microcontroller (Arduino Uno Rev3 combined with a camera trigger board (TSI-IOBOB2, Thorlabs) and a stepper motor driver board (Motor Shield Rev3, Arduino)) is used to synchronize the filter wheel's rotation (180 rpm) with the camera's trigger (10 ms exposure time).
To enable IPDRI, the four different spots in the filter wheel are equipped with: (1) a 725 nm longpass (Edmund Optics, stacked below a 620 nm longpass, RG620, Thorlabs), (2) a 780 nm longpass (RG780, Thorlabs, stacked above a 715 nm longpass, RG715, Thorlabs), (3) a 775 nm shortpass combined with a 665 nm longpass (Edmund Optics and RG665, Thorlabs), and (4) an adjustable transmission neutral density filter (two stacked linear polarizers LPVISE200-A, Thorlabs). This results in four channels capturing different parts of the reflected excitation spectrum and of the emitted PL spectrum (see Figure 3.5a for spectral transmission of the channels). Since the PL emission peak of the perovskite used in this work is at around 780 nm, channel (1) captures the entire PL spectrum and the reflected excitation light is filtered out. Channels (2) and (3) also detect the PL signal, but only the long and short wavelength portions of the emitted PL spectrum, respectively, whose data is needed to approximate the PL peak wavelength. In channel (4), the excitation light is not filtered out, resulting in the acquisition of images showing the intensity of the diffuse reflection (R_{diff}).
Accordingly, the IPDRI system allows to capture the thin-film formation with spatial, temporal, and spectral resolution by providing image sequences with a frame rate of three frames per second, i.e., videos, of the diffuse reflection (one channel) and the PL intensity (three channels). The additional PL peak wavelength approximation channel is calculated from the three spectrally filtered PL channels.

4.2.2 Photoluminescence Peak Wavelength Imaging

Given the monochrome camera, only images of intensity values can be captured by the camera. Through implementation of the rotating filter wheel, the setup allows capturing four channels acquired through filters with different spectral transmission. While one channel captures the reflection signal, a dedicated choice of the remaining three filters allows calculating images which spatially resolve the PL peak wavelength emitted from the investigated sample. The calculation of the PL peak wavelength images from three single PL images is performed by using the method introduced by Chen *et al.*[340]
The method takes advantage of the fact that the three PL images differ slightly from each other, since the differences in spectral transmission of the filters result in different spectral portions of the PL spectrum being captured in the three channels. The image acquired through the 725 nm longpass filter is divided once by the image acquired through the 780 nm longpass and once by the image acquired through the 775 nm shortpass, yielding "images" of two ratios $R_1 = I_{LP\,725nm}/I_{LP\,780nm}$ and $R_2 = I_{LP\,725nm}/I_{SP\,775nm}$. For each image pixel, these two ratios R_1 and R_2 are calculated and compared to two previously generated tables containing the R_1 and R_2 values of simulated PL peaks with varying values of peak wavelength (λ_0) and full width at half maximum ($FWHM$). The calculated PL peak wavelength of each image pixel corresponds to the value of λ_0 of the tuple (λ_0, $FWHM$) whose simulated R_1 and R_2 values are closest to the experimentally generated R_1 and R_2 values obtained by dividing the original PL images. Assuming the perovskite PL spectra can be reasonably fitted with a Gaussian distribution, the look-up tables are generated by simulating $R_1 = I_{LP\,725nm}/I_{LP\,780nm}$ and $R_2 = I_{LP\,725nm}/I_{SP\,775nm}$ for a range of (λ_0, $FWHM$) with

$$I_{filter} = A \times \int Gaussian_{\lambda_0,FWHM}(\lambda) \times R_{camera}(\lambda) \times T_{lens}(\lambda) \times T_{filter}(\lambda)\, d\lambda \tag{4.1}$$

where I_{filter} is the intensity captured by the camera through the filter, R_{camera} (λ) is the spectral response of the camera, T_{lens} (λ) the transmission of the camera lens, and T_{filter} (λ) the transmission of the corresponding spectral filter or the stack of spectral filters, respectively. The intensity scaling factor A would have to be calibrated to convert the luminescence intensity into the absolute photon number but cancels out when generating the ratio R_1 and R_2.[340]
The Gaussian distribution is chosen since perovskite PL spectra typically exhibit a symmetric, bell-shaped profile,

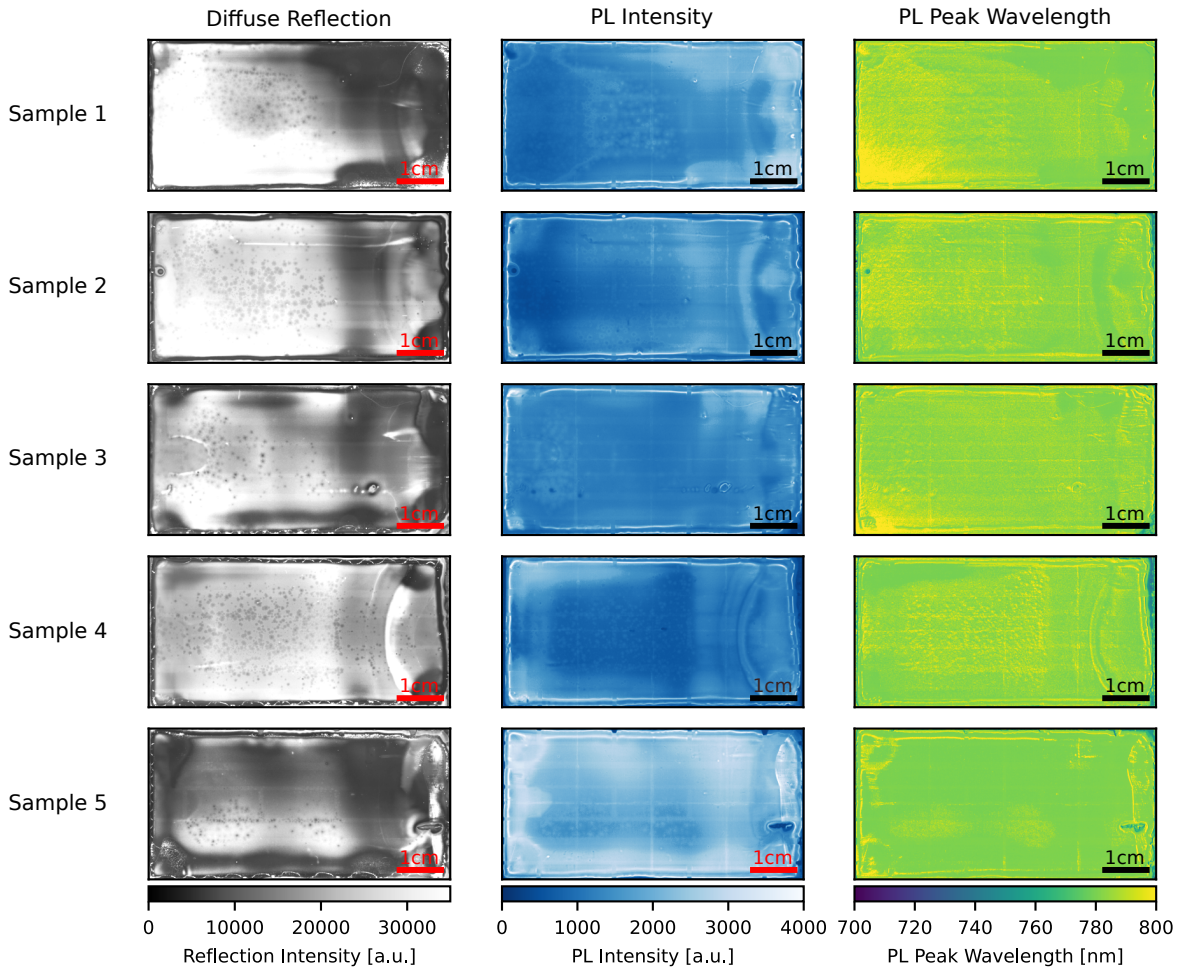

Figure 4.2: Exemplary images of blade-coated DCP thin films after vacuum quenching (coating direction left to right). The diffuse reflection and the PL images (shown here: 725 nm longpass channel) are obtained as raw data from the camera while the PL peak wavelength images are calculated from the three spectrally different PL images. Multi-channel imaging provides a comprehensive assessment of the homogeneity of the perovskite thin films, as the different channels resolve different defects and thin film properties.

making it a reasonable and widely used assumption for modeling emission spectra. Deviations from this assumption, for example, due to multiple PL peaks or inhomogeneous broadening caused by phase segregation, can introduce errors in the calculated PL peak wavelengths. In addition, if the selected filters are not optimized for the investigated bandgap, they can distort the calculated PL peak wavelength.[340]

In addition to the reflection and PL images, the calculated images of the spatial distribution of the PL peak wavelength provide additional insight into the investigated thin film. Since the PL peak corresponds to the absorption threshold and is therefore considered to be an approximation of the optical bandgap of the material, the additional channel extends the imaging capabilities of the IPDRI setup for characterization of large-area perovskite thin films. It should be noted that the PL spectrum and therefore its peak wavelength is a superposition of directly emitted PL and reabsorbed, red-shifted scattered PL, which affects the PL spectrum and leads to slight deviations of the PL peak wavelength from the actual bandgap of the material.[327, 401–405]. However, the extension of Chen *et al.*'s method[340] by rapid filter exchange using a rotating wheel allows the quick generation of spectral images and is therefore considered a low-cost alternative to hyperspectral luminescence imaging setups[406], which can also be applied *in situ* with its sub-second temporal resolution.

4.2.3 Detection of Thin Film Inhomogeneities and Defects

To showcase the large-area monitoring capabilities of the IPDRI system, *ex situ* measurements of various large blade-coated double cation perovskite (DCP, $Cs_{0.17}FA_{0.83}Pb(I_{0.91}Br_{0.09})_3$) thin films ($32 \times 64\,mm^2$) are investigated after vacuum quenching and the images of the different channels are compared (see Figure 4.2). Due to the large-area acquisition (spatial resolution $\approx 53\,\mu m$), the system allows localizing morphological inhomogeneities and defects. The observed coating inhomogeneities are categorized into three groups: (i) severe pinholes/particles, (ii) absorber quality defects/sub-surface defects, and (iii) minor thickness variations.[341] Pinholes, e.g., caused by particles, are visible in both reflection and PL images (see in Figure 4.2 on sample 2 middle-left, sample 3 bottom-right, and sample 5 bottom-right). Local inhomogeneities in absorber semiconductor quality and sub-surface defects are mainly visible in the PL channels as dark spots caused by quenched PL intensity (see in Figure 4.2 on sample 3 bottom-left and sample 4 middle-center). These local absorber quality inhomogeneities are not visible in reflection images or other *ex situ* measurement techniques like WLI. Minor thickness variations are also more pronounced in the PL images, indicated by slight variations in PL intensity and can be confirmed with *ex situ* WLI.[341] The stronger correlation between absorber thickness and absorber quality (represented through devices' PCEs) with PL intensity is further substantiated by the findings presented in section 5.6, which demonstrate the superior predictive capacity of the PL intensity signal in comparison to reflection intensity (see Figure 5.15). However, other optical effects are best visible in the reflection channel. Voids between the perovskite thin film and the underlying hole transport layer[407] are most strongly visible in reflection images as dark spots (see in Figure 4.2 all samples). Also, differences in surface roughness are differentiable in the reflection images. Since the IPDRI setup captures only diffuse and no specular reflection, increased surface roughness leads to higher reflection intensity due to more scattering of the excitation light at the sample surface (see Figure 6.24). In the PL peak wavelength channel, inhomogeneities in the form of pinholes are detectable. Also, areas of higher PL peak wavelength can be attributed to locally increased surface roughness leading to more outcoupling of red-shifted PL that was initially trapped before coupling out upon scattering.[327]
In summary, reflection images resolve many defects as morphological features, but the additional PL imaging reveals slightly more defects than reflection imaging alone, highlighting the importance of combining the benefits of PL and reflection imaging. However, while *ex situ* measurements allow the qualitative study of large-area thin film morphology, the IPDRI setup, and in particular the information provided by PL peak wavelength imaging, provides additional insight when applied *in situ* during material formation while the properties of the thin films are still changing. Accordingly, the *in situ* capabilities of the setup are discussed in section 4.3.

4.2.4 Correlating Defects in Perovskite Thin Films with Device Performance

Having showcased the ability to image and detect thin film inhomogeneities and defects, the morphological features detected by IPDRI are correlated with the performance of devices built incorporating these thin films. To correlate the thin film morphology with device performance, a dataset was generated containing 132 solar cells processed using constant fabrication parameters to investigate IPDRI capabilities of identifying defects occurring due to unintended process deviations.[341] The blade-coated thin films were quenched, i.e., dried, using laminar airflow and the entire process was monitored using the IPDRI system, yielding two sets of PL and reflection images obtained at two different points in time, namely *in situ* images (acquired at the time of maximum PL intensity) and *ex situ* images (acquired at the end of the annealing process).
Investigating the morphology, e.g., finding defects, in the image patches associated to the perovskite thin film locations of the active areas (see Figure 2.8a) enables correlating the morphology with the performance of the corresponding solar cell. Devices having PCEs exceeding 15% are mainly associated with active areas that are free from detectable defects. On average, the detection of a defect in the active area of a solar cell results in poorer device performance. The previously defined categories of inhomogeneities are investigated in more detail: (i) Pinholes negatively affect all PV performance parameters, preventing optimal device performance and often creating shunts

that result in not working, shorted solar cells. (ii) Absorber quality variations lead to a considerably lower V_{OC} and lower FF due to increased non-radiative recombination resulting in a PCE drop below 10% for most devices. (iii) Thickness variations mostly lead to devices with PCEs between 10% and 15% caused by a decrease in FF due to inhomogeneous excited charge carrier diffusion.
However, the correlation is not always confirmed and a more detailed analysis is performed using only solar cells with PCEs below 10%.[341] Only 9 out of 86 low-performing solar cells (PCE < 10%) were categorized as having no irregularities in the IPDRI images (false negatives). This suggests that IPDRI can be a valuable tool for identifying potentially defective thin film areas, as the number of false negatives can also be increased by PCE drops caused by subsequent processing problems and adjacent layers of the device, and therefore undetectable when only monitoring the absorber layer. However, IPDRI also detects many irregularities (24% of total devices) that do not cause the PCE to drop below 10% (false positives). While detected (i) pinholes always lead to a reduced PCE and identified (ii) absorber quality inhomogeneities decrease the PCE below 10% in about 80% of all cases, only half of the devices categorized as (iii) thickness variations show inferior PCEs of less than 10%. The high number of false positives for (iii) thickness variation indicates that this category of identified defects does not contain sufficient information to decide whether the corresponding device is expected to have a high PCE or not. But since the combined false positive rate of categories (i) and (ii) is quite low (2 out of 55 devices), it is concluded that IPDRI can be used to identify most of the severe defects that result in non-functional solar cells (see [341, 408] for more details).
The goal of the correlation task is to reduce the number of false negatives and false positives as much as possible. The reduction of false negatives, i.e., the cases where no defect is detected but the device performance is poor, is influenced by the fact that the PCE of the device is impacted by several processing steps after the perovskite layer. This leads to cases where a decrease in PCE is caused by subsequent processing of the device while IPDRI images still show high-quality perovskite thin films without processing defects. This limitation can only be tackled by introducing additional setups to monitor the deposition of the preceding and subsequent layers. The false positive rate, i.e., the cases where a defect is detected but the corresponding device still performs well, can be improved by implementing a more sophisticated defect classification, e.g., based on the temporal evolution of the signals acquired by IPDRI during the thin-film formation. In addition to defect classification, (*in situ*) data can be used to perform PCE prediction (see section 4.3 for temporal data and chapter 5 for more details analysis using machine learning).

4.2.5 Electroluminescence Imaging

The demonstration of IPDRI's ability for large-area photo- and electroluminescence imaging of two-terminal all-perovskite tandem solar modules was made possible only by Bahram Abdollahi Nejand and coworkers who fabricated the solar modules and provided them for characterization.[314]

Photoluminescence imaging allows large-area characterization of the optical properties of the perovskite thin film and identification of thin film inhomogeneities and defects in the early stages of solar cell fabrication. In contrast, electroluminescence imaging is primarily used to detect electrical defects such as shunts and increased series resistance in fully fabricated solar cells.[320] While PL imaging relies on optical excitation to induce light emission as charge carriers relax from excited states, EL imaging uses an external voltage to inject charge carriers, which then emit light upon recombination (see Figure 4.3a and Figure 4.3b). While PL imaging can be performed on individual perovskite thin films, allowing in-line characterization of thin film uniformity, EL imaging can only be performed on fully fabricated solar cells, as electrodes are required for charge carrier injection. However, while PL imaging mainly examines the optical properties of the perovskite thin film, EL imaging allows the examination of the electrical quality of the finished solar cell as it is affected by the entire device, including the functional layers and interfaces. The intensity of the detected PL is influenced by the optical properties of the perovskite material, such as crystal quality, non-radiative recombination centers, material composition, and surface passivation. EL intensity is affected by both optical and electrical properties, with prominent features in EL images predominantly

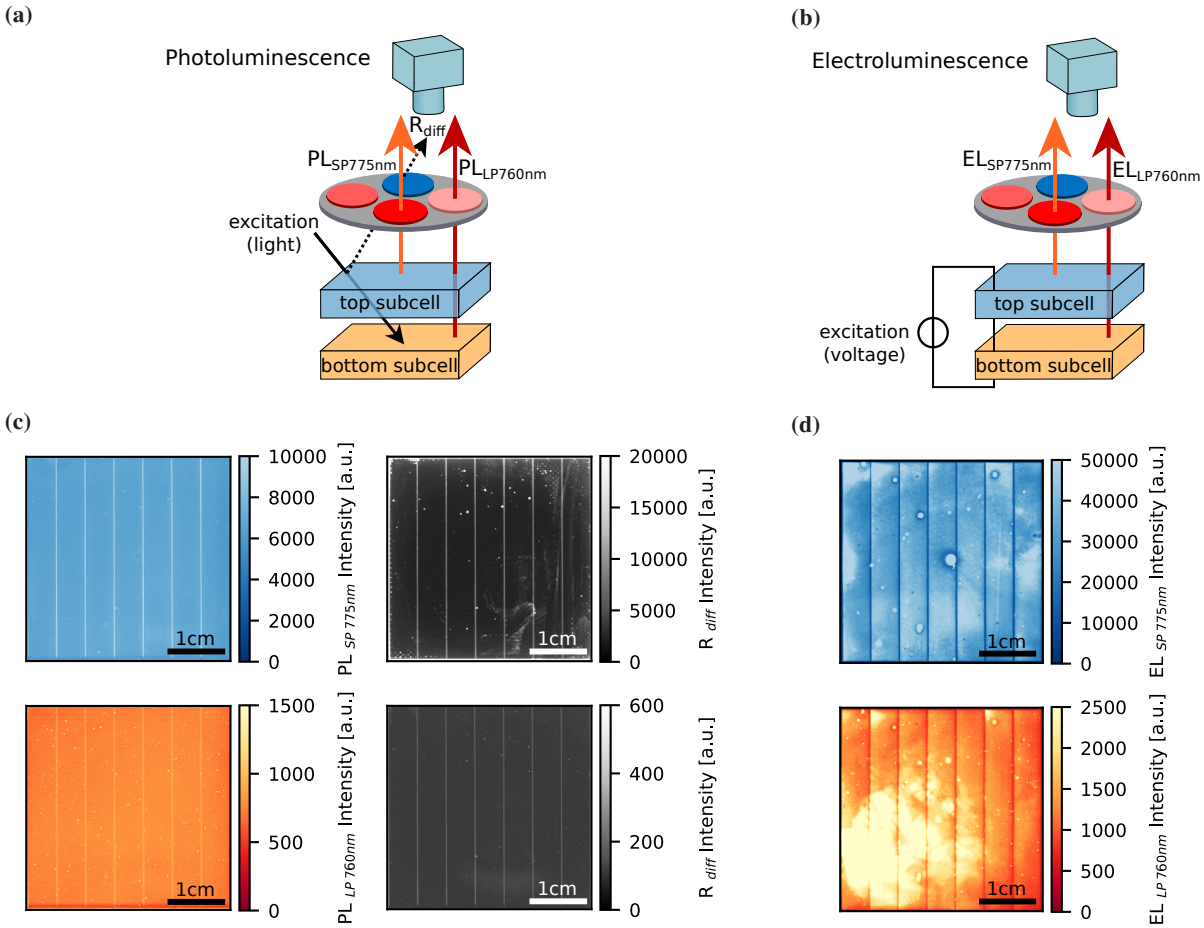

Figure 4.3: PL and EL imaging of individual subcells of an all-perovskite tandem solar module using multi-channel imaging. (a) Using optical excitation (blue LEDs), the PL response is captured using a 760 nm longpass filter to image the bottom subcell ($E_G \approx 1.26$ eV) and a 775 nm shortpass filter (combined with a 665 nm longpass) to image the top subcell ($E_G \approx 1.78$ eV). (b) For EL imaging, an external voltage is applied to excite the charge carriers and individual subcells are imaged through the different filters as in the PL case. (c) PL images of both individual subcells as well as reflection images with (top right) and without LED excitation (bottom right) show high uniformity of the layer stack with only a few small inhomogeneities. (d) EL images reveal numerous defects in both subcells, as the top subcell shows mostly localized defects, while the bottom subcell displays a large-area diffuse inhomogeneity. Partially adapted with permission from [314].

due to resistive effects caused by either series resistances or by shunts.[409] Accordingly, EL imaging may be less effective at detecting certain types of optical defects compared to PL imaging, but is highly effective at identifying electrical defects that may not be visible by PL imaging. It provides a direct correlation between the luminescence characteristics and the electrical performance of the device (see section 3.2.3.2 for more details on electroluminescence).

Here, IPDRI's electroluminescence image acquisition capabilities are demonstrated by characterizing two-terminal all-perovskite tandem solar modules reported by Abdollahi Nejand *et al.*[314]. The ability to obtain multi-channel images is used to acquire dedicated EL (and PL) images showing only the luminescence signals emitted from the individual top and bottom subcells. The all-perovskite tandem solar modules consist of a wide-bandgap perovskite ($E_G \approx 1.78$ eV) as top subcell and a narrow-bandgap perovskite ($E_G \approx 1.26$ eV) as bottom subcell in combination with numerous additional functional layers (see [314] for the complete solar module stack). The EL emission was measured spectrally with the wide-bandgap top subcell having its EL peak at 688 nm and the narrow-bandgap bottom subcell having its EL peak at 977 nm. To distinguish the luminescence signals of the two subcells in tandem

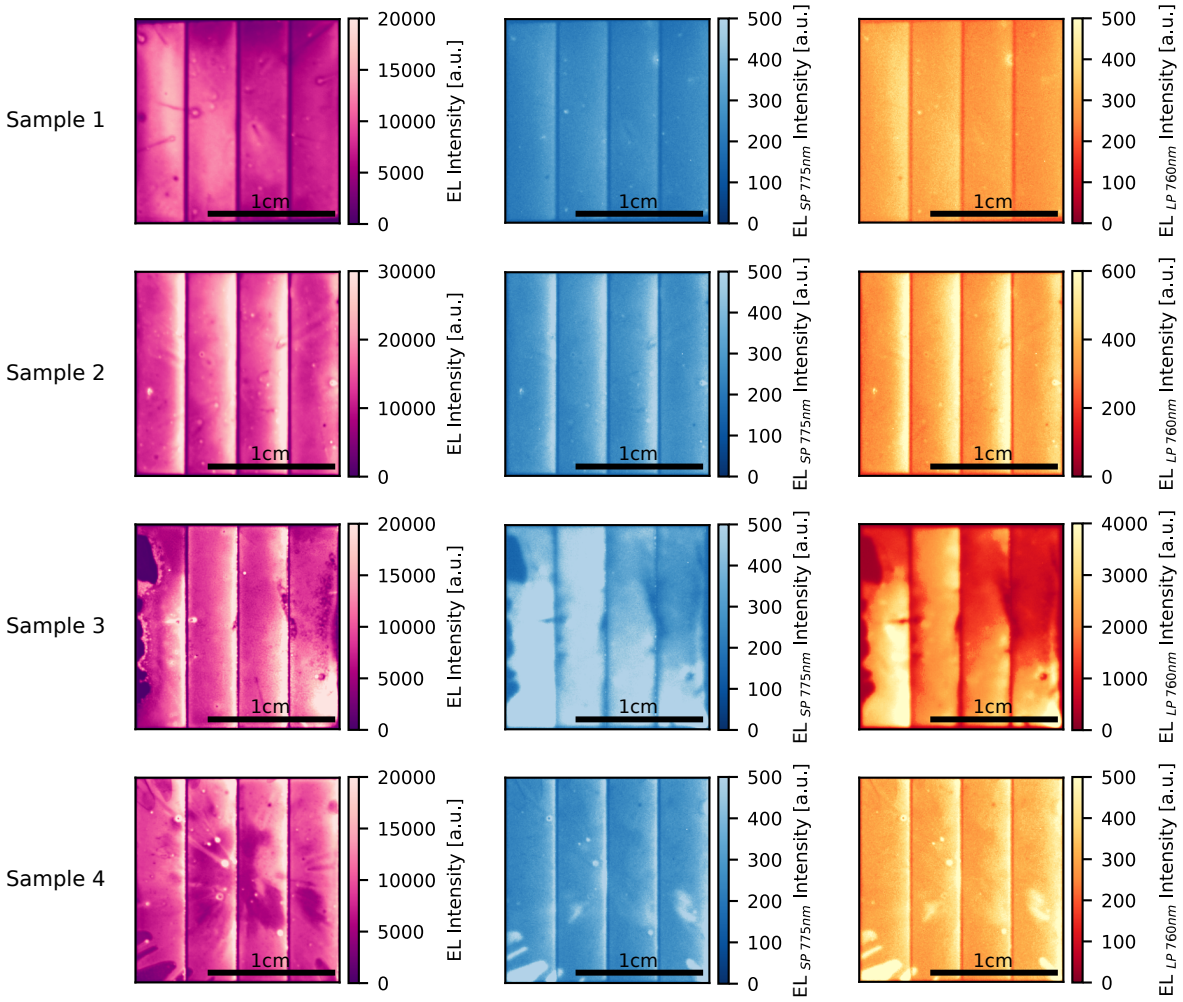

Figure 4.4: Exemplary images of combined EL signals from both subcells and individual subcell EL images. Without optical excitation, the neutral density filter is used to image the combined electroluminescence signal (left) from the wide-bandgap top subcell (middle) and the narrow-bandgap bottom subcell (right). EL images reveal local shunting as dark spots, areas of current crowding due to low shunt resistance as local bright spots, radial spin coating patterns spreading out from the center, and large areas without EL signal due to increased local series resistance. Partially adapted with permission from [314].

module, the luminescence signals are imaged using different spectral filters. For photo- and electroluminescence, a 760 nm longpass filter was used for imaging the bottom subcell and a 775 nm shortpass filter (combined with a 665 nm longpass) for imaging the top subcell. Additionally, the neutral density filter was used for imaging the reflection through the front side glass with and without LED excitation. In the electroluminescence case, the neutral density filter was used to image the combined electroluminescence signal from both subcells. Photoluminescence images of both individual subcells as well as reflection images with and without LED excitation show a high uniformity of the scalable mini-module (aperture area 12.25 cm^2) and only a few small, localized inhomogeneities are visible (see Figure 4.3c). However, electroluminescence reveals numerous defects in the top and bottom subcell of the mini-module (see Figure 4.3d), which are associated with losses in FF and V_{OC}.[314] Compared to photoluminescence, electroluminescence imaging visualizes more defects since it is affected by the entire device stack while being highly sensitive to spatial changes in resistivity, e.g., caused by shunts or series resistances due to thickness variations. The EL image of the top subcell shows mostly inhomogeneities in the form of localized defects. While there are also some localized defects, the EL image of the bottom subcell shows an additional prominent non-localized diffuse large-area inhomogeneity. The localized defects can be associated with local shunting, while the diffuse inhomogeneities might be caused by resistive losses due to thickness variations.

In the appendix, an additional example of PL and EL imaging of all-perovskite tandem solar mini-modules shows similar diffuse large-area inhomogeneities in the EL images of both the top and bottom subcell (see Figure A.1).
Next to mini-modules, Abdollahi Nejand *et al.* reported small-scale spin-coated two-terminal all-perovskite tandem solar modules (aperture area 2.25 cm^2). Electroluminescence images were leveraged to reveal overall good homogeneity of the deposited layer stack (see sample 1 in Figure 4.4). However, numerous localized defects are detected, which are attributed to either local variations in charge carrier injection caused by fluctuations in series resistance or to local differences in EL outcoupling, potentially due to variations in surface roughness and thickness.[314] Introducing EL images of additional small-scale two-terminal all-perovskite tandem solar modules (see samples 2 - 4 in Figure 4.4), more individual defects and inhomogeneities in top and bottom subcells are visible. For example, spin coating artifacts are revealed in samples 1, 2, and most prominently in sample 4 as radial patterns spreading out from the center towards the outside. In sample 3, a large-area inhomogeneity is potentially caused by interconnection problems between different layers leading to a strongly increased local series resistance indicated by no emittance of EL from this area. Furthermore, localized dark spots in EL images indicate local shunting, where current bypasses the absorber layer instead of injecting charge carriers for radiative recombination. In contrast, localized bright spots are associated to areas of current crowding caused by reduced shunt resistance, potentially near shorted pathways.[410]
In summary, electroluminescence imaging serves as a valuable complement to photoluminescence imaging by revealing individual fabrication defects and spatial inhomogeneities. Although its application is limited to fully fabricated devices, it provides additional insight into the electrical quality of the final device as it is affected by the entire layer stack, including functional layers and interfaces. Combined with PL imaging, EL imaging allows qualitative visualization of defects caused by the complexity of large-area processing, which introduces spatial variations and additional defects. Revealing these individual defects that occur in any of the numerous fabrication steps facilitates process optimization for high-efficiency perovskite solar cells and tandem solar modules.

4.3 *In Situ* Imaging for Thin-Film Formation Monitoring with Temporal Resolution

Photoluminescence and reflection imaging allows large-are characterization of perovskite thin films (see section 4.2). In addition to these large-area imaging capabilities, the IPDRI system is able to obtain series of images, i.e., videos, with a high temporal resolution. This enables tracking the complex dynamics during the thin-film formation, including the phases of drying, nucleation, and crystal growth, which is necessary to monitor, characterize, and control the process to obtain high-quality large-area perovskite thin films. To initialize and control the nucleation process, several strategies involving antisolvent quenching[305–307], (laminar) gas flow quenching[299, 308–310], and vacuum quenching[303, 311–313] are used. While antisolvent spray coating[411] and bathing[412] have been demonstrated, the application of antisolvent quenching is mainly limited to spin-coated small-area devices. For large-area deposition techniques, gas quenching is advantageous for in-line fabrication combined with blade or slot-die coating[299, 308, 309], while inkjet-printed thin films can be processed in batches using vacuum quenching[28, 302, 304].
In the following, *in situ* monitoring of the blade-coated perovskite thin-film formation using the IPDRI system is demonstrated for two large-area quenching strategies, namely (a) vacuum quenching and (b) laminar airflow quenching. Showcasing the system's versatility, IPDRI is integrated into two existing experimental setups (see Figure 4.5). Photographs of IPDRI integrated into the vacuum quenching setup (see Figure A.2a) and onto the laminar airflow channel (see Figure A.2b) can be found in the appendix. Additionally, a second copy of the IPDRI system was integrated into the slot-die coating setup to monitor the thin-film formation of slot-die-coated perovskite thin films after gas quenching using a slot jet.

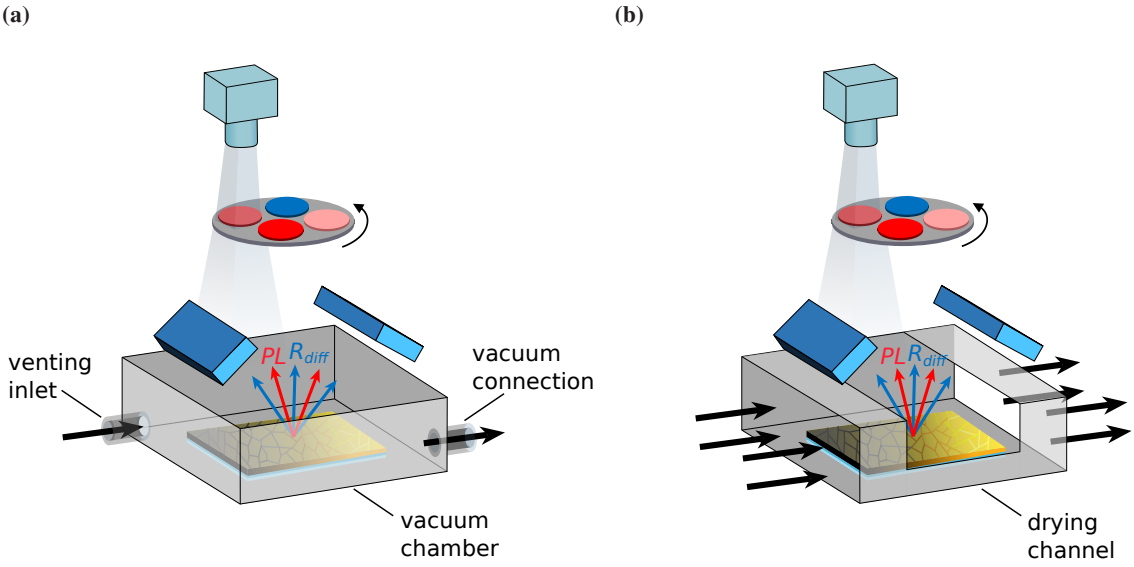

Figure 4.5: Schematics of the *in situ* monitoring setup integrated into two experimental quenching setups. The IPRDI system is used to *in situ* monitor the formation of blade-coated perovskite thin films. (a) During vacuum quenching, the setup is placed on a vacuum chamber that is evacuated, causing the wet film to dry and the perovskite thin film to form. (b) To monitor the laminar airflow quenching, the setup is placed on a drying channel where the solvents are extracted by the gas flow and the perovskite nucleation and crystallization take place (see Figure A.2a and Figure A.2b for photographs of the setup integrated into the vacuum quenching setup and the laminar gas flow channel).

4.3.1 Thin-film Formation during Vacuum Quenching

The demonstration of IPDRI's ability to monitor the perovskite thin-film formation during vacuum quenching was only made possible by previous work, in particular by Fabian Schackmar, who established the experimental setup for vacuum quenching in the LTI laboratory at KIT.[312–314, 413]

One strategy to achieve controlled crystallization is removing residual solvents by applying vacuum (see section 3.1.1.2 for more details on vacuum quenching)[303, 311–313]. While spectrally resolved *in situ* PL combined with light microscopy has been previously shown for vacuum quenching of perovskite thin films,[303] capturing spatially resolved PL through camera images is essential for obtaining information on the homogeneity of large-area thin films. Real-time monitoring of drying thin films with spatial resolution enables the detection of inhomogeneities or defects across large areas that are not discernible to the naked eye or through light microscopy.[313, 341] The large-area imaging capabilities with temporal resolution allow for multi-channel video capture of the DCP thin-film formation, as well as the ability to examine series of images taken at specific moments (see Figure 4.6). Like in the case of *ex situ* imaging (see Figure 4.2), spatial inhomogeneities and defects are already revealed during the thin-film formation process. In addition, the signal detected in the reflection and PL channels as well as the calculated PL peak wavelength change substantially with time during vacuum quenching of the blade-coated perovskite thin film. The diffuse reflection images show an increase in absorption during drying, followed by an increase in diffuse reflection due to increased surface roughness. The onset of the PL intensity indicates the initial formation of light absorbing and emitting material. The PL peak wavelength channel shows a redshift of the PL spectrum during the formation process of the perovskite thin film. The hypothesis that the redshift results from crystal growth and increased reabsorption is discussed in detail in the next section 4.3.2.
To investigate the transient behavior of the detected signals in more detail, the temporal changes of the spatial mean of the image patches corresponding to the PSCs' active areas (see Figure 2.8a for substrate layout) are examined (see Figure 4.7a). The characteristic signal transients can be attributed to the phases of (i) drying, (ii) nucleation,

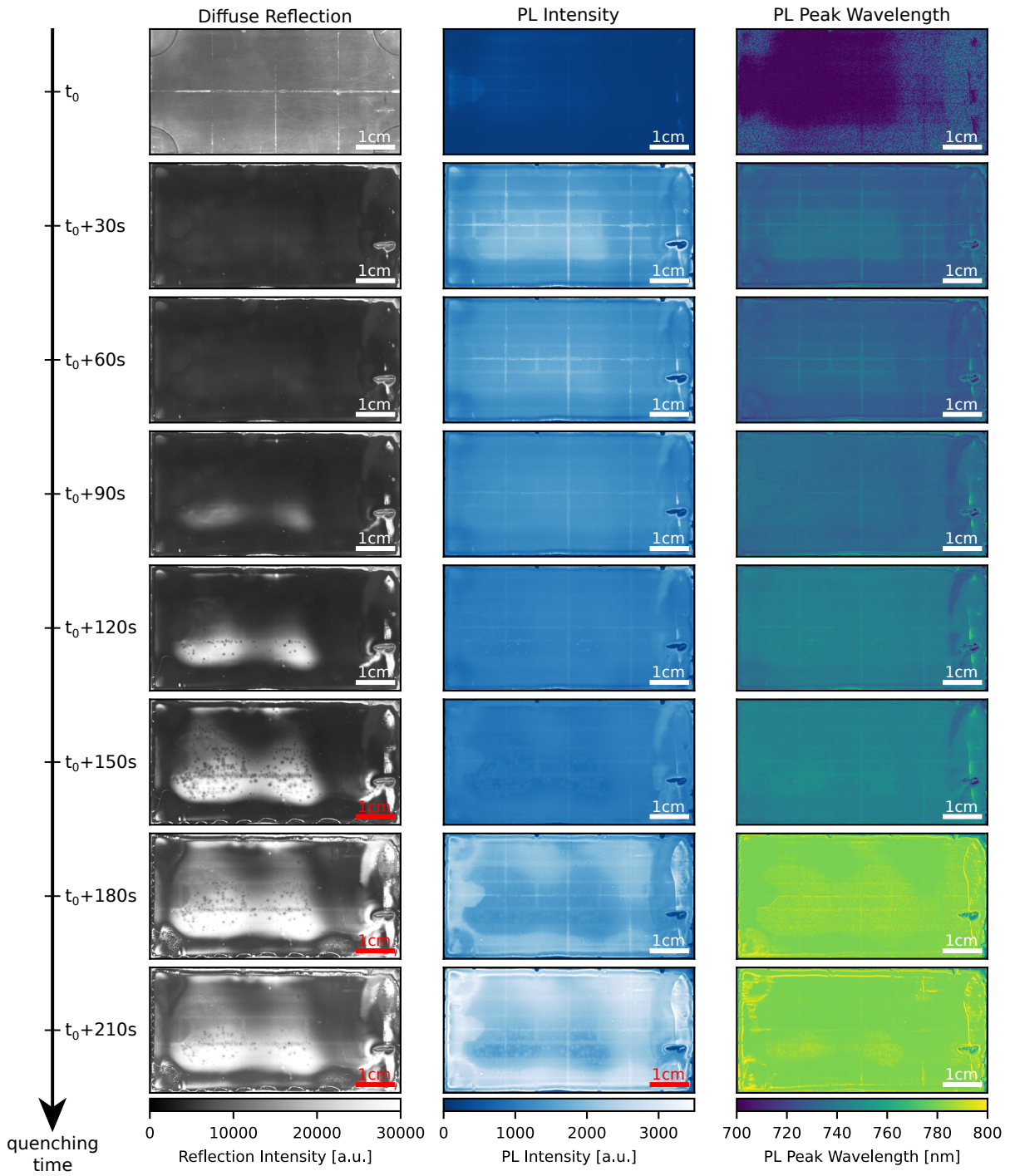

Figure 4.6: Exemplary *in situ* time series of multi-channel images capturing the DCP thin-film formation during vacuum quenching. Spatial inhomogeneities and defects in the absorber layer are already detected during the thin-film formation. The diffuse reflection images show an increase in the absorption of the thin film followed by increasing surface roughness. The PL intensity (shown here: 725 nm longpass channel) onset suggests the initial formation of light absorbing and emitting material and the PL peak wavelength channel reveals a redshift of the PL spectrum while the perovskite thin film is forming (see Figure A.3 for multi-channel time series of the MAPI thin-film formation during laminar airflow quenching).

(iii) crystallization/crystal growth, and an additional phase of (iv) surface morphology formation (see Figure 7.4 for correlating of formation phases with the acquired signals). (i) During drying (t≈0–30 s), the rapid evacuation

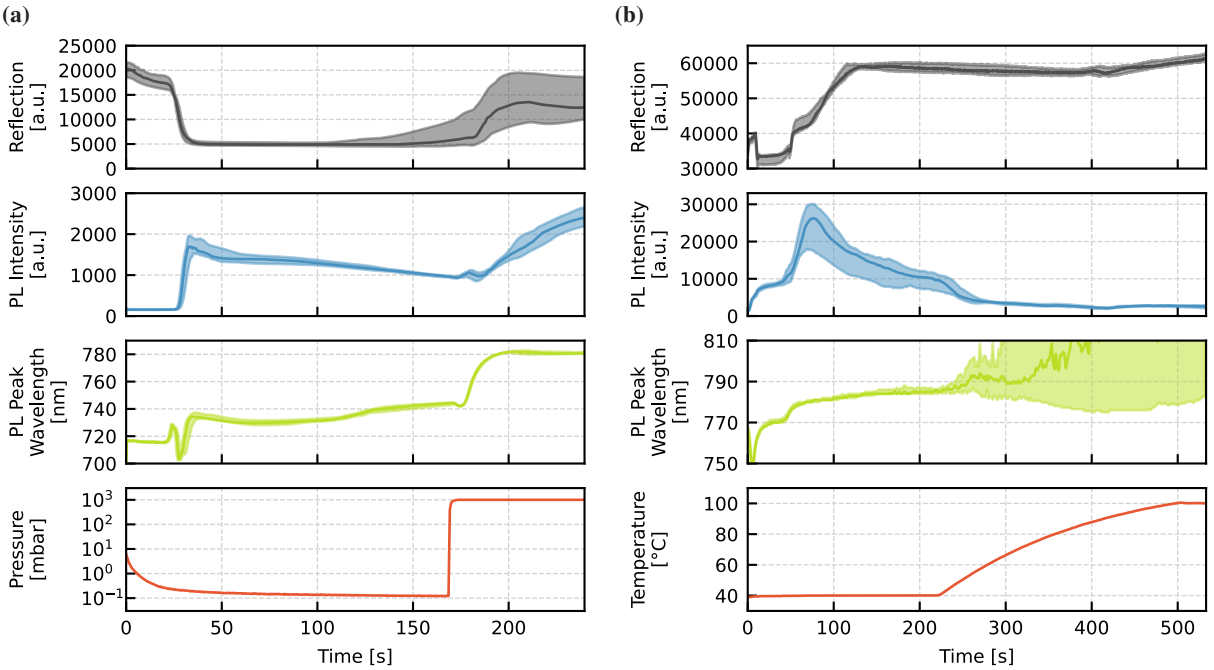

Figure 4.7: Transient *in situ* evolution of multi-channel signals during the perovskite thin-film formation. (a) During vacuum quenching of DCP thin films, the characteristic temporal changes can be attributed to the phases of drying, nucleation, crystallization, and surface morphology formation. The start of nucleation is indicated by a drop in reflection and the onset of PL, while the PL intensity decreases and the PL peak redshifts during crystallization. As the vacuum chamber is vented, the morphology forms, accompanied by an increase in all signals. (b) During laminar airflow quenching of MAPI thin films, nucleation and crystallization phases are identified by similar characteristics of the transients. Here, the start of annealing is shown resulting in a drop of PL intensity. (The solid lines indicate the median transient of each signal, and the shaded areas indicate the 25^{th} and 75^{th} percentiles of all transients obtained from numerous substrate locations).

of the vacuum chamber accelerates solvent evaporation, leading to a significant reduction in wet-film thickness, as deducted by changes in the reflection signal.[373] The reflection channel primarily indicates a change in absorption and surface roughness as the film dries. At this stage, no PL signal is detected, as the precursor materials remain dissolved and perovskite formation has not yet occurred. (ii) The nucleation starts after reaching a supersaturation state due to the precursor concentration in the wet film exceeding a critical threshold. The perovskite thin film changes to a brownish color and absorption increases as indicated by a significant drop in reflection intensity. The nucleation onset of perovskite crystallites is identified by a strong increase in PL intensity as perovskite nuclei and small grains start to emit a PL signal. Shortly after PL onset, the PL intensity peaks, indicating that the crystallite concentration reaches its maximum, while extraction of excited charge carriers may be hampered by residual solvents in the thin film. The timing of PL onset and the height of the initial PL peak are influenced by factors such as the evacuation rate of the vacuum chamber, solvent evaporation rate, wet-film thickness, and precursor concentration. (iii) During the crystallization phase, the crystallites grow and coalesce resulting in larger grains. It is hypothesized that crystal growth leads to improved charge carrier extraction and reduced radiative recombination, as indicated by the decreasing intensity of the emitted PL. (iv) Venting of the vacuum chamber (t≈170 s) determines the final surface morphology of the thin film. In some cases, the PL intensity and reflection show a brief oscillation as the valve is opened to vent, but in general, both reflection and PL signal intensity increase during venting. The presence and amplitude of the signal oscillation and the overall signal evolution are related to the amount of residual solvent present in the thin film at the time of venting.[304] However, the changes in PL signal during this phase are not yet fully understood but are hypothesized to correlate with the thin film's final morphology, particularly its surface roughness.[303]

The various phases of perovskite thin-film formation can also be identified in the calculated PL peak wavelength transients. During drying, no PL is detected resulting in unfeasible PL peak data. Upon PL onset, the PL redshifts from around 720 nm to 730-740 nm indicating nucleation and growth of the crystals. An additional strong redshift to the final PL peak wavelength of around 780 nm is observed when the vacuum chamber is vented with air (see [304] for additional details). The hypothesis that this redshift results from crystal growth and increased reabsorption is discussed in more detail in the next section, where it is observed again during the gas flow quenching process.
In summary, capturing the transient behavior of thin film properties during formation with temporal resolution, combined with IPDRI's large area imaging capabilities, allows identification of the critical phases of the perovskite thin-film formation process. It enables the tracking of the complex dynamics, which is critical to monitor, characterize, and control the fabrication process to obtain high-quality large-area perovskite thin films. This initial investigation lays the groundwork for more sophisticated data analyses of data obtained with *in situ* monitoring of vacuum quenching of blade-coated perovskite thin films in the following result chapters 5, 6, and 7.

4.3.2 Thin-film Formation during Laminar Gas Flow Quenching

The demonstration of IPDRI's ability to monitor the formation of perovskite thin films during gas flow quenching, in close collaboration with Simon Ternes, was only made possible by previous work that established the laminar gas flow quenching channel in the MZE laboratory at KIT.[373, 414]

In addition to vacuum quenching, another strategy to achieve controlled crystallization by removing residual solvents over large areas is gas flow quenching.[299, 308–310] Here, a gas flow, such as nitrogen or air, is used to accelerate the evaporation of precursor solvents after the coating process, which promotes fast saturation and induces rapid nucleation, resulting in high-quality perovskite thin films.[310] As previously demonstrated for monitoring the vacuum quenching process, the time-resolved large-area imaging capabilities allow multi-channel acquisition of the MAPI thin-film formation yielding time series of images, i.e., videos (see Figure A.3 for *in situ* image time series obtained during laminar airflow quenching). Although the reflection and PL signals change substantially with time during the quenching of the thin film, spatial inhomogeneities and defects are already revealed during the formation process, allowing a more sophisticated defect classification based on the temporal evolution of the signals acquired by IPDRI.
The formation of thin films during laminar airflow quenching is studied in more detail by examining the temporal evolution of the signals detected *in situ* from thin film patches associated with the active areas of the PSCs (see Figure 4.7b). As for the vacuum quenching case, the characteristic signal transients are in agreement with other publications on spotwise *in situ* characterization without spatial resolution[383, 415] and can be attributed to the different thin-film formation phases. Starting with nucleation, the absorption of the thin film starts to increase which is indicated by a decrease in reflection intensity. During crystallization, the remaining solvents are extracted from the film and its surface morphology begins to form. As the surface roughness increases, the detected diffuse reflection signal increases before remaining constant at a high level. In the PL channel, the start of nucleation is detected by the onset of the PL emission as small perovskite grains begin to emit PL. Shortly after PL onset, the intensity increases substantially and quickly reaches its peak as excited charge carriers are not extracted and recombine radiatively. During the crystallization phase, the intensity of the emitted PL decreases as the crystals grow and coalesce resulting in larger grains having improved charge carrier extraction and reduced radiative recombination.[374, 415] Increased reabsorption of PL can also contribute to a decrease in outcoupled PL.[327] As the temperature is increased, the PL intensity quickly drops below the camera noise level due to thermal quenching of the PL caused by a higher rate of nonradiative recombination.[328, 329]
During the thin-film formation process, the calculated PL peak wavelength shows a strong redshift to the final PL peak wavelength of around 780 nm. The shift can be attributed to the growth of the crystals, as the PL emission wavelength depends on the average perovskite grain size.[338, 416, 417] This dependence arises from quantum confinement in the nucleating perovskite crystals, which causes a decrease in the energy of emitted photons as

crystal size increases.[377] Also, thicker thin films lead to increased reabsorption of the photoluminescence which shifts the emitted PL to higher wavelengths[327] (see [341, 418] for additional details). As the PL emission fades with increasing temperature, the spread in the PL peak wavelength increases, indicating uncertainty in the calculated PL peak values due to the very low PL intensities used as input for the approximation. Also, the shift of the emission peak to longer wavelengths leads to exiting the wavelength interval for PL peak approximation which can be covered with the installed set of filters. The redshift as presented for vacuum and gas flow quenched perovskite thin films is also reported by other studies that perform *in situ* monitoring during the thin-film formation of solution-processed perovskite thin films.[357, 382, 415, 419] However, the redshift of the PL is also reported for the formation of evaporated perovskite thin films where the shift is also attributed to the gradual growth of individual crystallites.[420, 421]
In situ reflection and PL imaging enables monitoring of the perovskite thin-film formation and allows identification of the fundamental formation phases of drying, nucleation, and crystal growth. However, the reflection and PL intensity transients of both investigated quenching techniques (see Figure 4.7) are strongly affected by experimental variables such as process parameters and ambient conditions, e.g., temperature and humidity. Accordingly, the *in situ* monitoring technique can be used to distinguish process parameters based on the evolution of reflection and PL intensity (see section 4.3.2.1). In addition, IPDRI can be used to generate large datasets of *in situ* data, which can then be used for predicting material and device properties using machine learning (see chapters 5, 6, and 7).

4.3.2.1 Differentiating Process Parameters using *In Situ* Monitoring

To further investigate the information content of the data acquired with IPDRI, the transients obtained using different laminar airflow quenching parameters are compared (see Figure 4.8). It is showcased that differences in transient as well as spatial data can be attributed to and correlated with changes in processing conditions, namely the quenching parameters airflow velocity and temperature. Accordingly, the quenching parameters values of *nominal* airflow velocity and temperature (2.0 m/s, 40°C) are changed to investigate the changes introduced by *low temperature* (2.0 m/s, 20°C) and by *low airflow* (0.02 m/s, 40°C).[341]
In the reflection channel, the increase in absorption of the thin film and the formation of the surface morphology are studied. The *nominal* sample dries the fastest, producing a very high nucleation density and a generally smooth film. The increase in absorption during thin-film formation causes the reflection signal to decrease. The coalescence of the crystals leads to the formation of the surface morphology. The increased surface roughness compared to the wet film results in higher diffuse reflection. The *low temperature* sample dries slower and shows a delayed decrease in reflection due to increased absorption of the thin film. After crystallization, the average reflection intensity does not increase substantially because solution droplets are pushed by the airflow, resulting in streaks and strong inhomogeneities in the thin-film morphology caused by uneven drying. The *low airflow* sample also dries slowly and no decrease in reflection is observed, indicating that the absorption of the thin film has not increased significantly. Slow drying results in low nucleation density and a rough, uneven film surface with insufficiently covered areas.
In the PL intensity transients, the emergence of PL signals coincides with the onset of perovskite nucleation. The *nominal* sample shows the highest PL intensity, indicating better optoelectronic performance due to a lower probability of nonradiative recombination, probably due to its smoother, more homogeneous film with larger grains. In contrast, the *low airflow* sample, shows the lower PL intensity, reflecting poorer film quality with more defects. The *low temperature* sample shows maximum PL intensities comparable to *low airflow* sample, but a second peak is observed when the temperature is increased above 40°C, probably due to the removal of residuals that hinder crystallization. The differences in PL intensity between these samples highlight the significant influence of drying conditions on the optoelectronic properties of perovskite thin films.
The calculated transients of the PL peak wavelength also reveal differences between the different various quenching parameters. The PL peak of all three samples redshifts during formation. The *nominal* and the *low airflow* samples show similar transient behavior. The shift to slightly higher wavelengths of the *nominal* sample compared to the

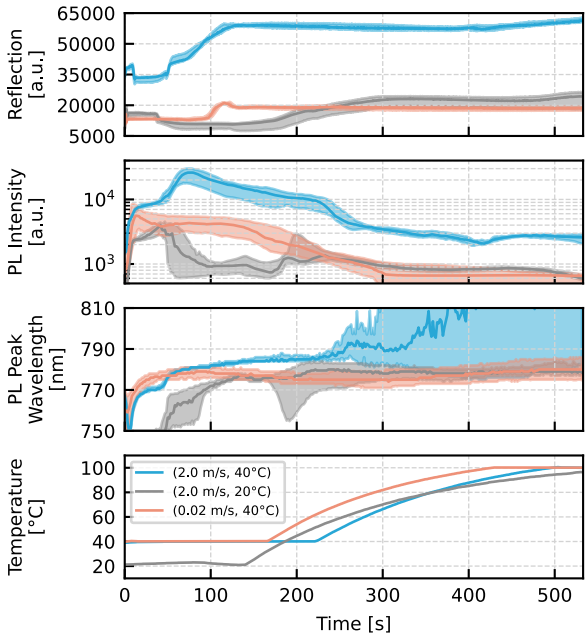

Figure 4.8: Discrimination of process parameters based on the characteristic *in situ* signal transients. Since reflection and PL intensity are affected by experimental variables, the *in situ* monitoring tool allows process parameters to be distinguished based on the signal transients. Here, deviations from *nominal* airflow velocity and temperature (2.0 m/s, 40°C) during laminar gas quenching of MAPI thin films are detected by substantial changes in PL and reflection transients. (Legend: quenching parameters (airflow velocity, temperature). The solid lines indicate the median transient of each signal, and the shaded areas indicate the 25^{th} and 75^{th} percentiles of all transients obtained from numerous substrate locations).

low airflow sample can be caused by stronger reabsorption due to a smoother surface of the *nominal* sample, which increases internal reflection and thus reabsorption leading to a stronger redshift of the PL. As for the increase in absorption indicated by the drop in reflection, the redshift of the *low temperature* sample is delayed and the shift is slower compared to the other samples.

In addition to time-resolved monitoring, IPDRI captures macroscopic large-area images that can be examined for differences in thin film uniformity of differently quenched samples. The reflection and PL images of the *nominal* sample are homogeneous and the PL intensity is high, yielding devices with PCEs mostly above 15%, outperforming the other two samples. The reflection images of the *low airflow* sample show that the absorption of the thin film is low. The PL intensity images also reveal spatial differences in the emitted PL due to crystalline islands, resulting in device PCEs mostly below 10%. The image of the *low temperature* sample shows strong inhomogeneities as solution droplets are pushed by the airflow resulting in streaks and waves. The difference in homogeneity leads to areas of homogeneous high PL and other areas showing low inhomogeneous PL, leading to two clusters of high and low PCE, respectively (see [341, 418] for images and additional details).

In summary, in addition to resolving spatial inhomogeneities in reflection and PL images, IPDRI enables the capturing of the transient evolution of these signals during thin-film formation. The technique allows the identification of different phases in the process and distinguishes between varying quenching parameters. The ability to detect subtle parameter differences can be used for feedback control in industrial production lines.

4.4 Summary

This chapter establishes *in situ* photoluminescence and diffuse reflection imaging as a novel imaging technique for large-area characterization of perovskite thin films with spatial, temporal, and spectral resolution and highlights its

application to *in situ* monitoring of perovskite thin-film formation from solution (research objective **I**, see section 1.2).

First, it is shown that IPDRI allows the detection and analysis of morphological inhomogeneities and defects, such as pinholes and absorber quality variations, because it is designed for large-area imaging characterization of perovskite thin films. These defects, which can significantly affect device performance, are identified prior to the final perovskite annealing step and correlated with PSC performance, showing that certain defects significantly reduce PCE. With a low false negative rate, IPDRI can be a valuable tool for the identification of potentially defective thin film regions. However, the high false positive rate indicates that more sophisticated data analysis is needed before potentially inferior thin films can be sorted out.

Second, the advantages of multi-channel imaging, which combines photoluminescence and diffuse reflection imaging with the calculation of PL peak wavelength images, are demonstrated. Multi-channel imaging provides a comprehensive insight into the quality and homogeneity of the perovskite thin films, as the signals captured in the different channels resolve different defects and thin film properties. Variations in absorber thickness and quality as well as local defects are more apparent in the PL images, while the reflection images reveal differences in surface roughness as well as voids between the perovskite thin film and the underlying hole transport layer.

In addition to PL imaging, the chapter discusses the complementary role of electroluminescence imaging, which detects electrical defects in fully fabricated devices and provides additional insight into the homogeneity of the entire device layer stack. Differences between EL and PL imaging are discussed, as PL probes optical properties of the absorber layer, which are influenced by crystal quality, non-radiative recombination centers, and surface roughness, whereas EL is most affected by resistive effects such as shunt and increased series resistance in the entire layer stack.

Next, after using the IPDRI setup for *ex situ* studies of deposited perovskite thin films, the ability of the system to *in situ* monitor perovskite thin-film formation is explored, taking advantage of the temporal resolution at a frame rate of three frames per second, effectively producing videos. The ability of the IPDRI system to monitor the dynamic processes during the complex thin-film formation phases of drying, nucleation, and crystal growth under different quenching conditions, i.e., vacuum and laminar airflow quenching, is highlighted. The identification of the critical phases in the signal transients enables the tracking of the complex dynamics, which is crucial for the monitoring and control of the process of fabricating high-quality large-area perovskite thin films. Furthermore, it is shown that IPDRI allows to discriminate between different quenching parameters, enabling process optimization and control in industrial production lines.

In conclusion, photoluminescence and reflection imaging is a powerful tool for advancing the *ex situ* characterization of perovskite thin films and *in situ* monitoring of the thin-film formation, which is crucial for both academic research and industrial applications. Due to its time-resolved large-area imaging capabilities, IPDRI can be used for in-line feedback, allowing immediate detection of thin film defects and inhomogeneities as well as identification and correction of unwanted variations in production parameters, which are revealed by differences in the characteristic PL and reflection transients.

5 Machine Learning for a Data-Driven Analysis of the Perovskite Thin-Film Formation

*This chapter explores the application of machine learning techniques to in situ photoluminescence data for enhanced analysis of perovskite thin-film formation. A comprehensive dataset of 1129 blade-coated perovskite solar cells is introduced, featuring in situ PL and diffuse reflection imaging data acquired during vacuum quenching (research objective **II**). The advantages of in situ monitoring over ex situ measurements are demonstrated by revealing stronger correlations between solar cell performance and features extracted from in situ PL data. Unsupervised ML, specifically k-means clustering, is applied to in situ PL transients, uncovering distinct data patterns, such as early PL onset and high PL maxima, that correlate with device performance. Transitioning from descriptive to predictive analysis, supervised ML models, specifically k-nearest neighbors, are used to predict perovskite thin film thickness and photovoltaic performance metrics before completing subsequent processing steps (research objective **III**). The models achieve substantial improvements in prediction performance over baseline human predictive capabilities, particularly for predicting thin film thickness. A comparison between several ML algorithms with different IPDRI channels as model input identifies the PL intensity channels as the most informative input and highlights the impact of model choice on prediction accuracy. The combination of ML and IPDRI improves process monitoring of the perovskite thin-film formation by facilitating early detection of fabrication defects and promises to enhance yield and reduce waste in industrial production lines.*

Parts of this chapter were published in the research article "Process Insights into Perovskite Thin-Film Photovoltaics from Machine Learning with In Situ Luminescence Data", *Solar RRL* 7.7 (2023), by *Felix Laufer (F.L.)*, *Sebastian Ziegler*, *Fabian Schackmar*, *Edwin Andres Moreno Viteri*, *Markus Götz*, *Charlotte Debus*, *Fabian Isensee*, and *Ulrich W. Paetzold*. This work is the result of collaborative research between Karlsruhe Institute of Technology, Helmholtz AI, Helmholtz Imaging and the German Cancer Research Center (DKFZ).[346] The dataset and the corresponding software code were made publicly available.[422, 423] Some figures in this chapter were adapted with permission from [346].
F.L. contributed to this project by co-conceptualizing the study, leading experimental investigations, dataset generation and curation, software implementation, formal analysis, and visualization, as well as writing the original draft of the manuscript. The contributions of all authors according to the CRediT system are listed in Table A.3.

5.1 Motivation

Scaling perovskite solar cells from laboratory to industrial production is challenging because maintaining high efficiency is difficult due to the complexities of large-area thin-film formation. The transition from small-area, spin-coated devices to large-area industrial fabrication methods results in a substantial drop in power conversion efficiency, with values dropping from over 26% for small-scale perovskite solar cells to 19.2% for 1027 cm^2 modules and 15.0% for 7906 cm^2 modules.[424] The drop in PCE is attributed to the difficulties in achieving high-quality, uniform perovskite thin films over larger areas due to the complex thin-film formation from solution, which involves the entangled process phases of drying, nucleation, and crystallization.[23, 27, 28] To fabricate high-quality, uniform perovskite thin films, it is crucial to accurately monitor and control the thin-film formation process. Advanced monitoring and control techniques become even more critical with increasing scale and are essential for the successful commercialization of perovskite photovoltaic technology.[232]

The *in situ* photoluminescence and diffuse reflection imaging system enables real-time, non-invasive monitoring of the perovskite thin-film formation over large areas with spatial, temporal, and spectral resolution (see chapter 4). The system's ability to capture high-resolution, multi-channel images over large areas with subsecond temporal resolution makes it an invaluable tool for investigating the scalable fabrication of perovskite solar cells. Although IPDRI captures valuable data, the challenge lies in effectively analyzing this complex, multidimensional information, as traditional methods are insufficient to fully exploit its potential. The previous chapter demonstrated that IPDRI combined with human expert image classification can effectively identify potentially defective thin film regions, but it suffers from a high false positive rate when relying on the conventional analysis technique of a human expert classifying images for thin film defects. This limitation underscores the need for more sophisticated data analysis methods to extract meaningful insights and hidden patterns from the information-rich but complex, multidimensional data provided by IPDRI.

Machine learning techniques provide a robust solution to these challenges.[143] ML not only enhances the ability to uncover hidden patterns in IPDRI data, but also enables the automation of defect detection with improved accuracy.[267, 425] By leveraging supervised learning for predictive modeling and unsupervised methods for data clustering, ML can significantly reduce the reliance on human experts and increase the reliability of thin-film quality assessments.[232] In recent years, ML has been successfully applied to various aspects of materials science[145, 146] and perovskite photovoltaics research, ranging from accelerated material discovery[174–177, 183, 187, 188, 231, 426] to high-throughput experimentation[195, 211, 216, 225, 241, 248, 252, 254, 427] (see section 2.4 for more details on the state of the art of ML for perovskite PV). The ability of ML algorithms to handle high-dimensional data and recognize patterns makes them particularly well-suited for analyzing the complex data generated by IPDRI. In addition to pattern extraction, ML can classify samples based on IPDRI data and its predictive capabilities allow assessing the quality of perovskite thin films. Accordingly, enhancing IPDRI data analysis with ML reveals insights that are not accessible through traditional methods, such as manual feature extraction based on predefined heuristics and rule-based classification using fixed criteria or predefined thresholds.

To leverage ML for investigating large-area perovskite thin-film formation, a suitably sized experimental dataset is essential. Building on the monitoring capabilities of IPDRI, a unique dataset was generated, containing IPDRI data acquired *in situ* during the vacuum quenching of 1129 blade-coated perovskite thin-film solar cells (research objective **II**).[422] This dataset is labeled with corresponding photovoltaic performance parameters, such as PCE and the perovskite thin film thickness. All solar cells were fabricated under constant experimental conditions, maintaining the same layer stack and materials. This controlled environment ensures that performance variations are attributable solely to fluctuations in the fabrication process, making it a unique resource for studying the large-area perovskite thin-film formation using ML.

Applying ML techniques to analyze the perovskite formation allows for the identification of unintended deviations during iterations of an optimized fabrication process.[346] In the conventional fabrication process, these deviations mostly go undetected until the entire layer stack is assembled into a fully fabricated device, requiring several additional processing steps after the perovskite thin film is deposited (see Figure 5.1). By establishing the relationship

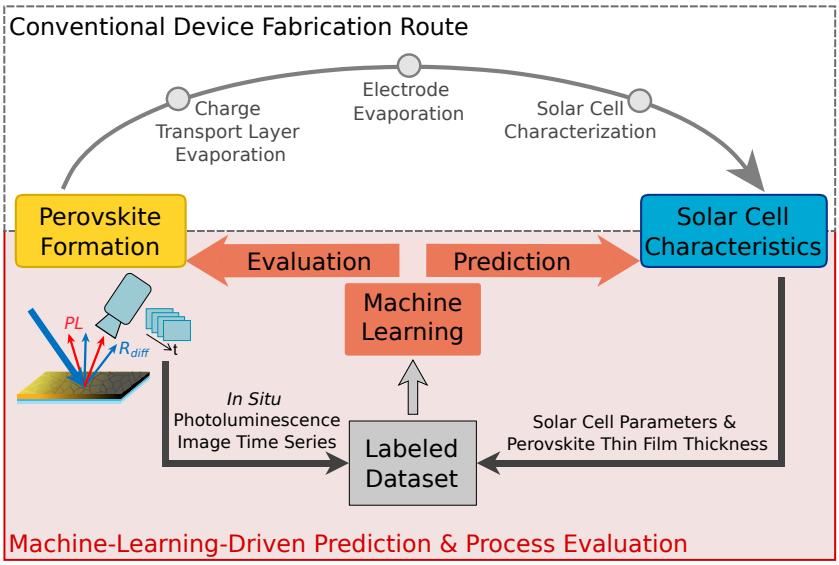

Figure 5.1: Schematic of the integration of machine learning (ML) into the conventional fabrication process of perovskite solar cells. In the conventional fabrication process (top), several additional steps follow the perovskite formation, including evaporation of charge transport layers and electrodes. The ML-enhanced process (bottom) leverages the dataset of *in situ* data obtained using IPDRI to directly predict solar cell characteristics without the need to complete the full conventional fabrication route. Moreover, ML facilitates the evaluation of perovskite formation by revealing data patterns extracted from the dataset, potentially leading to improvements in the fabrication process. Adapted with permission from [346].

between *in situ* imaged PL intensity during the perovskite deposition step and the final performance of solar cells, it becomes possible to predict PV performance before the solar cells undergo the remaining processing steps needed to finalize the devices. In an industrial production line, early detection of fabrication flaws reduces costs by saving time and minimizing material waste.

In this chapter, k-means clustering and k-nearest neighbors (kNN) are selected as complementary machine learning techniques for recognizing patterns in the *in situ* data and predicting device performance.[346] K-means clustering, an unsupervised learning technique, can identify distinct patterns in the IPDRI data without prior labeling, revealing clusters that might correlate with solar cell performance or perovskite thin film morphology. Meanwhile, kNN, a supervised learning method, is well-suited for regression tasks, such as predicting device performance based on the *in situ* data, enabling early detection of fabrication issues. The combination of these ML techniques enhances the evaluation of IPDRI-acquired data by addressing both exploratory analysis and predictive modeling needs. This chapter aims to use machine learning techniques to identify critical patterns in perovskite thin-film formation data, correlate them with device performance, and predict solar cell performance for early detection of fabrication problems (research objective **III**).[346] Achieving these goals will allow ML insights to be translated into practical improvements in fabrication processes of large-area perovskite solar cells.

In the following sections, machine learning for data-driven analysis of perovskite thin-film formation is established. First, a detailed description of the novel dataset obtained using IPDRI is given and the data preprocessing steps are discussed. Second, the advantage of acquiring *in situ* data is demonstrated by contrasting the correlation between PCE and *in situ* data versus *ex situ* data. After investigating the information content of human-selected data features, the potential of unsupervised ML techniques for data exploration is highlighted by demonstrating the correlation between clusters of PL transients, obtained by k-means clustering, and the performance of the fully fabricated devices. In addition, the heterogeneous thin-film quality is revealed by the spatial dependence of PL transients assigned to different clusters, indicating varying thin film properties across the large-area substrate due to unfavorable process mechanisms during perovskite formation. Next, based on slight sample-to-sample variations in *in situ* PL transients, the supervised ML technique kNN is applied to predict perovskite thin film thickness

and PV performance parameters of fully fabricated devices even before the solar cells are finalized in numerous remaining processing steps. Additionally, the predictive capabilities of the different IPDRI channels are compared by examining the prediction accuracy of kNN using different input data. Finally, the predictive performance of kNN is benchmarked by contrasting its error metrics with those of other classical supervised machine learning techniques. In summary, by combining the large-area monitoring capabilities of IPDRI with the analytical power of machine learning, this chapter explores the potential of the ML-enhanced characterization tool for in-line process monitoring to detect unwanted processing variations, improve process control, increase yield, and reduce waste in industrial production lines.

5.2 Experimental *In Situ* Photoluminescence Imaging Dataset for Blade-Coated Perovskite Photovoltaics

ML is a promising approach to enhance characterization of perovskite fabrication processes by quickly quantifying the homogeneity of the deposited thin films. Capturing *in situ* data allows monitoring the formation of the perovskite thin film enabling ML techniques to detect iterative and spatial process variations resulting in different perovskite thin film properties. However, for training ML models extensive datasets are required which accurately capture the complexities of the fabrication processes.

To address this need, a comprehensive dataset containing IPDRI data acquired during the vacuum quenching of blade-coated perovskite solar cells is introduced.[422] Aligned with industrial manufacturing, blade coating the perovskite precursor solution is a scalable deposition technique which allows fabricating large-area thin films (see section 3.1.1.1 for more details on blade coating). Vacuum quenching of the deposited wet film is advantageous for batch-to-batch quenching of large-area thin films since antisolvent quenching, like the thin-film deposition using spin coating, is mainly limited to small-area devices (see section 3.1.1.2 more details on vacuum quenching). Using only scalable fabrication techniques for all processing steps, 1129 solar cells were fabricated to generate the unique, novel dataset (see Figure 5.2). The dataset consists of *in situ* data obtained during fabrication and the corresponding performance metrics of fully fabricated solar cells, such as PCE, and the additional target variable perovskite

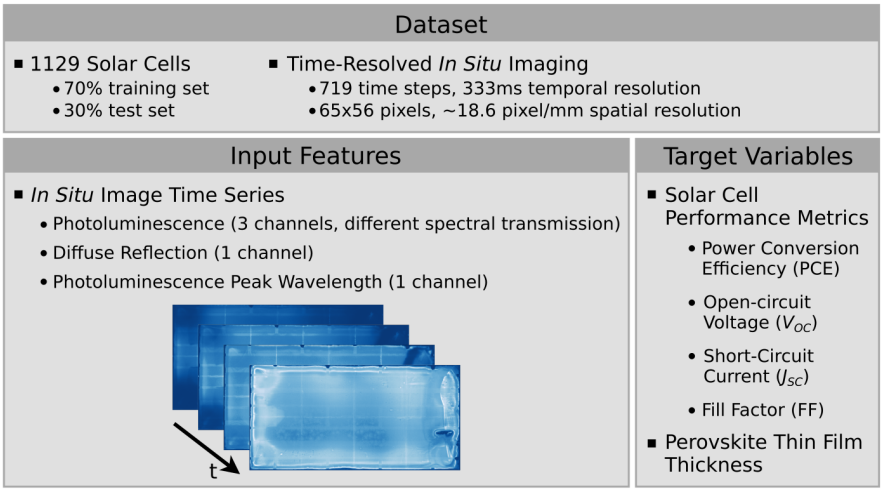

Figure 5.2: Experimental dataset containing 1129 blade-coated solar cells. For each solar cell, multi-channel *in situ* imaging data is obtained during the perovskite formation using vacuum quenching. Multi-channel imaging provides five different *in situ* image time series (i.e., videos) that capture photoluminescence (PL), diffuse reflection, and PL peak wavelength, which are used as input features. For all solar cells, solar cell performance metrics (e.g., power conversion efficiency) and perovskite thin film thickness are measured and added to the dataset as target variables (i.e., labels). The input features are used as input to ML models to predict the target variables. Adapted with permission from [346].

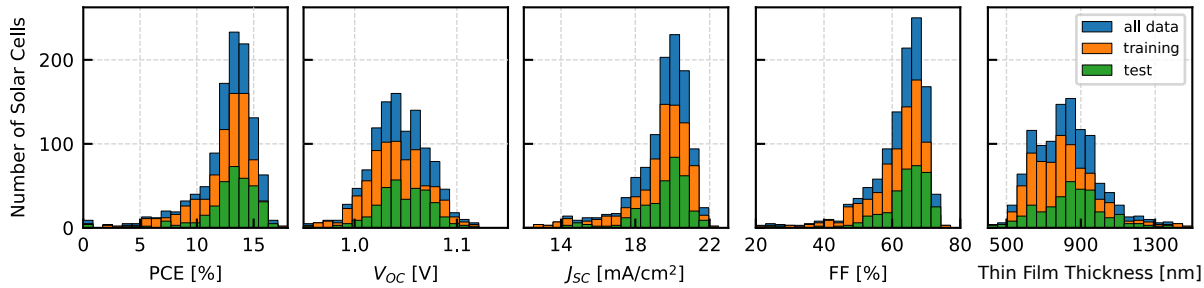

Figure 5.3: Distribution of the target variables, namely solar cell performance metrics and perovskite thin film thickness, for the full dataset, training set, and test set. The full dataset of 1129 solar cells is divided into training and test sets (70%/30%), containing 780 and 349 samples, respectively. Model training and hyperparameter optimization are performed on the training set, while unbiased evaluation of the models is performed on the test set with previously unseen data. For all target variables, the training and test set splits show good agreement between the two distributions, ensuring representative sampling for model training and evaluation.

thin film thickness. All solar cells contained the same layer stack and precursor materials and were processed under constant experimental conditions. Accordingly, variations in perovskite thin film thickness and solar cell performance are solely caused by fluctuations in the fabrication process itself.

The time-resolved *in situ* images were acquired using the IPDRI setup during the vacuum quenching of perovskite thin films, which initiates the drying and crystallization of the blade-coated wet films. The camera frame captures images of the entire $32 \times 64\,\mathrm{mm}^2$ substrate covered with the blade-coated perovskite thin film. The multi-channel acquisition of IPDRI yields time series of images, i.e., videos, with a temporal resolution of 333 ms showing the spatially resolved PL intensity (three channels) and the diffuse reflection (R_{diff}, one channel). The additional PL peak wavelength approximation channel is calculated from the three spectrally filtered PL channels using the method introduced by Chen et al.[340]

Since the target variables (such as PCE of the fully fabricated device) depend only on the perovskite thin film properties within the active area of the solar cells, the large-area images were cropped into 32 smaller patches (65×56 pixels each) in a data preprocessing step, resulting in image patches that represent only the active area (3.5 mm $\times$ 3 mm = 10.5 mm^2) of the 32 individual solar cells located on the large-area substrate (see Figure 2.8a for substrate layout). In addition to spatially matching the input features to the labels, i.e., target variables, the input data was also temporally aligned at the beginning of the vacuum chamber evacuation for all experimental iterations. Consequently, for all input features, the vacuum chamber was flooded with ambient air after 170 s (≈505 time steps) of evacuation before data acquisition was stopped after a total of 240 s, resulting in image time series of 719 time steps at three frames per second covering the drying and crystallization of the blade-coated perovskite thin films (see section 3.1.1.3).

After deposition of the double cation perovskite thin film (DCP, composition $Cs_{0.17}FA_{0.83}Pb(I_{0.91}Br_{0.09})_3$), all perovskite thin films were built to completion into fully fabricated, functional solar cells (entire device stack: glass, ITO, NiO_x, 2PACz, DCP, C_{60}, BCP, Ag; see section 3.1.3 for more details). To determine the metrics of interest to add as labels to the dataset, the performance of all solar cells was determined by measuring the current-density-voltage (j-v) curves. For each solar cell, the PV parameters (PCE, V_{OC}, J_{SC}, FF), obtained both from backward and forward voltage sweeps, were added to the dataset as target variables, i.e., labels. In the work in this chapter, the averages of the backward and forward sweep are used as target variables (see Figure 5.3). In addition to the PV performance parameters, the perovskite thin film thickness within the active area of each solar cell was experimentally measured and added as an additional label to the dataset. The thickness was obtained from the spatial average of three spatially offset profilometer scan lines. The dataset also contains supplementary information such as substrate IDs and the position of each solar cell within its substrate.

The full dataset contains data from 1129 solar cells. To evaluate the predictive capabilities of the ML models, the dataset was divided into training and test sets (70%/30%), containing 780 and 349 solar cell samples, respectively.

The training set is used for model training and hyperparameter optimization, while the test set allows an unbiased evaluation of the models using new, previously unseen data. The split was performed at the substrate level, ensuring that all solar cells (up to 32) from the same substrate were consistently assigned to either the training or test set. This approach allows the evaluations on the test set to be viewed as actual predictions on newly generated experimental data. Additionally, the training set was split into five subsets for fivefold cross-validation, with solar cells from the same substrate again consistently assigned to the same subset (see section 2.3.5 for more details).
The assembled dataset is a unique resource for studying large-area perovskite thin-film formation and can be used to apply ML techniques to improve process understanding[347], enable in-line performance prediction, monitor the fabrication process, and detect inferior perovskite thin-film quality due to variations between blade coating iterations. Since all solar cells were fabricated under constant conditions using the same materials, variations in solar cell performance can only be attributed to fluctuations in the fabrication process. In the work presented in this chapter, the dataset is used to train ML models to analyze the perovskite formation by identifying unintended deviations during iterations of the optimized fabrication process.[346] Conventionally, these deviations mostly go undetected until the layer stack is finalized in several additional processing steps into a fully fabricated device (see Figure 5.1). However, after learning the relationship between *in situ* data and the final properties of solar cells using this dataset, ML models are able to predict PV performance parameters before the solar cells undergo these remaining processing steps needed to finalize the devices. Early detection of fabrication flaws is critical for data-driven in-line process monitoring required in industrial perovskite production lines to reduce costs due to time loss and material waste. However, when using the dataset and evaluating trained models, it must be kept in mind that the target variables, i.e., the labels, are affected by all process steps, while the IPDRI data only provides information about the perovskite formation, excluding details about subsequent steps. Consequently, there may be cases where irregularities occur in other fabrication steps that adversely affect the PV performance parameters but are not included as information in the model's input data. The dataset and the corresponding software code are publicly available to the research community.[422, 423]
For the work presented in this chapter, domain expert knowledge on the importance of the temporal component of the thin-film formation is leveraged and emphasis is placed on the temporal sequence of the experiment. The IPDRI image frames showing the active area of the solar cells are aggregated via their spatial mean value for each time step. Accordingly, for each solar cell, the input feature consists of transients representing the temporal information of the spatial mean intensity of the five channels, namely $\mathrm{PL}_{LP\,725nm}$, $\mathrm{PL}_{LP\,780nm}$, $\mathrm{PL}_{SP\,775nm}$, R_{diff}, and PL Peak Wavelength (see Figure 5.4a). This dimensionality reduction (see section 2.3.8) decreases the complexity of the problem and facilitates the investigation of subtle differences in the material formation process between iterations, as revealed by variations in the temporal evolution of the IPDRI data. Consequently, the ML models are trained using the transient input features obtained by dimensionality reduction from the *in situ* imaging data. In the following sections on data exploration using unsupervised machine learning, the focus is initially on the transients of the 725 nm longpass-filtered PL ($\mathrm{PL}_{LP\,725nm}$), since it captures the entire PL spectrum of the DCP material with a bandgap of 1.59 eV. The supervised learning sections for PV performance prediction examine the $\mathrm{PL}_{LP\,725nm}$ transients as input features as well as data transients from all other IPDRI channels. In conclusion, this chapter focuses on the transient evolution of PL (and R_{diff}) intensity, while PCE and thin film thickness predictions using different data representations, including the entire image time series, are performed in section 7.2, and detailed analysis of spatial thin film uniformity, such as semantic segmentation, is left for future work.

5.3 Advantages of *In Situ* Monitoring over *Ex Situ* Measurements

Establishing a characterization setup capable of *in situ* monitoring is more complex than characterizing samples after the experimental process is complete and the sample can be transferred out of the confined processing environment into dedicated *ex situ* characterization setups. Therefore, considering the additional effort required for *in situ* measurements to integrate the characterization system into the experimental fabrication setup, the advantages

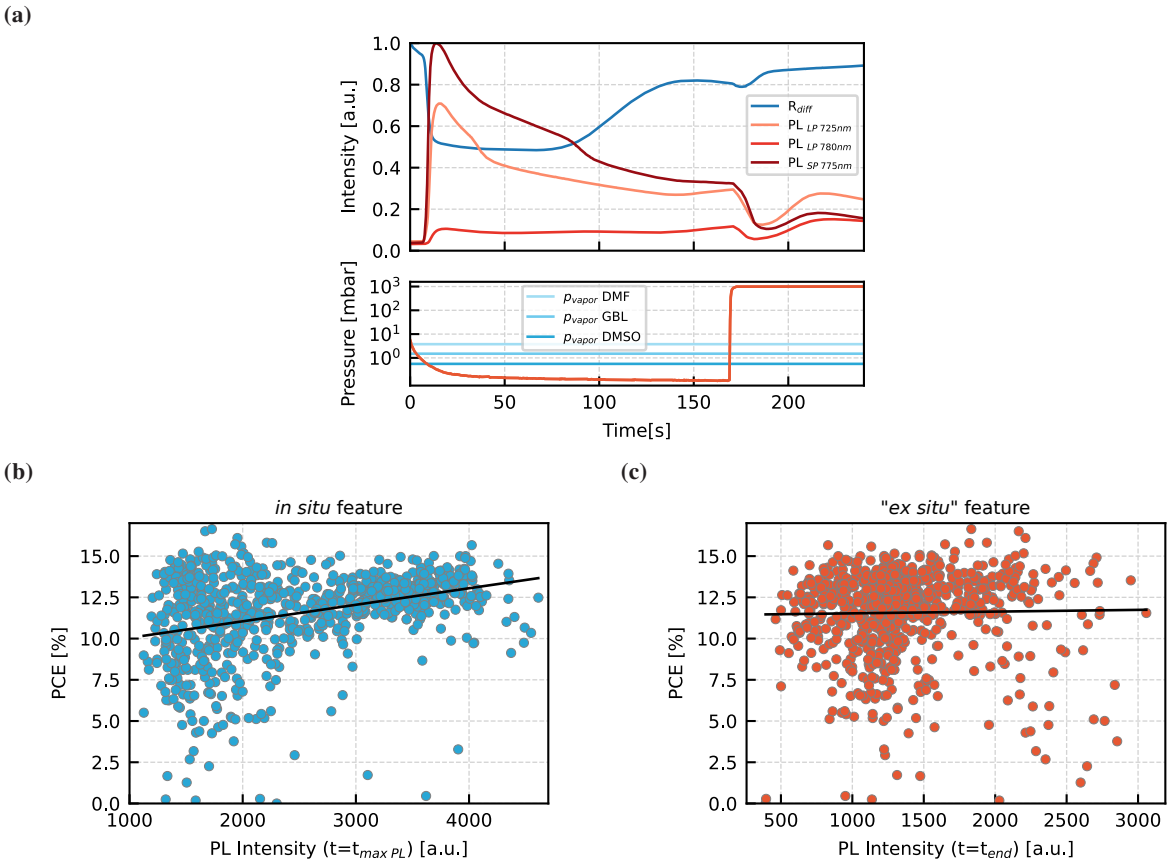

Figure 5.4: Highlighting the rationale for *in situ* monitoring by comparing *in situ* and *ex situ* features for PCE prediction. (a) Temporal evolution of photoluminescence (PL) and diffuse reflection (R_{diff}) intensity and chamber pressure during vacuum quenching (see sections 3.1.1.2 and 3.1.1.3 for more details). The different spectral transients (R_{diff}, $PL_{LP\,725nm}$, $PL_{LP\,780nm}$, $PL_{SP\,775nm}$) are obtained from the video data by dimensionality reduction through aggregating the images for each time step via their spatial mean value (see section 2.3.8 for more details). (b) Correlation of the power conversion efficiency (PCE) with the human-selected *in situ* feature, the maximum value of the initial $PL_{LP\,725nm}$ peak. (c) Correlation of PCE with the pseudo *ex situ* feature, human-selected as the last data point of the *in situ* transient. Linear regression fits (solid lines) for each feature highlight an advantage in predictive capability of *in situ* features over *ex situ* measurements. Partially adapted with permission from [346].

of acquiring data during the experimental process over obtaining only *ex situ* data points must be emphasized. To highlight the benefits of recording *in situ* data during the perovskite formation process, the correlation of solar cell performance with *in situ* versus *ex situ* PL features is compared.[346]

Accordingly, *in situ* and *ex situ* features are extracted from the transients obtained by dimensionality reduction from the IPDRI data (see Figure 5.4a). Using a simple, intuitive approach, for each sample the maximum PL value reached in the initial $PL_{LP\,725nm}$ maximum after nucleation onset is identified as the most prominent feature of the transient, which also varies with fabrication conditions and iterations. Consequently, the maximum $PL_{LP\,725nm}$ values, located at around 15 s in Figure 5.4a, are defined as the *in situ* features. Since no additional *ex situ* measurements were performed, the last $PL_{LP\,725nm}$ data point during *in situ* acquisition, located at 240 s in Figure 5.4a, is defined as the *ex situ* feature for each sample. These last data points of the transients can be considered as representatives of *ex situ* measurements since they were acquired in normal atmosphere after quenching was finished and the vacuum chamber was vented with ambient air.

After extracting *in situ* and *ex situ* parameters from the PL transients, these parameters are correlated with the solar cell performance. First, all samples in the training set are analyzed to determine the relationship between the

Table 5.1: Comparison of correlation metrics of *in situ* and *ex situ* features highlight a higher correlation between the *in situ* feature and the corresponding target variables. Bold values indicate higher correlation for given target variable. (for |r| and R^2: higher is better ↑, r: correlation coefficient, R^2: coefficient of determination, PCE: power conversion efficiency, V_{OC}: open-circuit voltage, J_{SC}: short-circuit current density, FF: fill factor)

Metric	Input Feature	Target Variable				
		PCE	V_{OC}	J_{SC}	FF	Thin Film Thickness
r	*in situ*	**0.34**	0.05	**0.17**	**0.42**	**–0.61**
	ex situ	0.02	**0.12**	–0.01	–0.03	**0.61**
R^2	*in situ*	**0.11**	0.00	**0.03**	**0.18**	**0.37**
	ex situ	0.00	**0.02**	0.00	0.00	**0.37**

extracted *in situ* or *ex situ* features and the final PCE of the fully fabricated solar cells. Investigating the *in situ* feature, it becomes evident that the PCE of the solar cell tends to increase with the maximum PL value of the PL transients, i.e., the *in situ* feature (see Figure 5.4b). For high maximum PL values, the corresponding PCEs are generally above 11%. However, as the maximum PL value decreases, the average PCE also decreases, and the distribution of PCEs broadens for lower values of the *in situ* feature. This suggests that while some solar cells with a low maximum PL value still achieve high solar cell performance, the proportion of low-performing solar cells (PCE $< 10\%$) increases as the value of the *in situ* feature decreases. When the data points are fitted using linear regression, the increasing slope of the fitted line underscores that the average PCE tends to increase with higher values of the *in situ* feature.

In contrast, the relationship between the *ex situ* feature, i.e., the last data points of the *in situ* PL transients, and the corresponding PCEs is substantially weaker. Compared to the *in situ* data, the *ex situ* data points are more dispersed (see Figure 5.4c) indicating that the *ex situ* feature encodes less information about the subsequently measured PCE of the solar cell than the *in situ* feature. The fitted line obtained by linear regression is nearly horizontal, suggesting no linear relationship between the *ex situ* feature and the corresponding PCEs.

Next, to quantify the relationship, the correlation coefficient (r) is used as a direct measure of the strength (and direction) of the linear relationship between the extracted feature and the corresponding target variables. Examining the differences between the correlation coefficients for the *in situ* feature and the *ex situ* feature reveals a stronger relationship between the target variables and the *in situ* feature (see Table 5.1).[346] Except for V_{OC}, the correlation between PCE, J_{SC}, and FF is stronger with the extracted *in situ* feature than with the *ex situ* feature. While $r_{V_{OC}} = 0.12$ (*ex situ*) and $r_{J_{SC}} = 0.17$ (*in situ*) generally indicate a weak linear relationship, a stronger correlation is found between the *in situ* feature and PCE ($r_{PCE} = 0.34$) as well as FF ($r_{FF} = 0.42$). The strongest linear relationship is found for thin film thickness, where the strength of the correlation is similar for both features, while the direction is opposite ($r_{thickness} = \pm 0.61$).

In addition, the coefficients of determination (R^2) are calculated using linear regression to fit the data points. R^2 describes the proportion of variance in the target variable that can be explained by the feature and indicates how well the linear model predicts the target variable based on the input feature. The (R^2) values confirm the higher correlation between the *in situ* feature and the target variables compared to the *ex situ* features (see Table 5.1). The highest R^2 values are determined for the target variable thin film thickness ($R^2_{thickness} = 0.37$), followed by $R^2_{FF} = 0.18$ and $R^2_{PCE} = 0.11$.

In general, the strongest linear relationship is found for perovskite thin film thickness, both for the *in situ* feature and *ex situ* feature. This is due to the dependence of the solar cell's performance on the quality of the entire device

stack, while the perovskite thin film thickness is fully determined during the process step represented in the *in situ* PL dataset. Other processing steps do not introduce uncertainty in the thin film thickness, while device performance can be affected by factors introduced in subsequent steps, resulting in a lower correlation between input features and device target variables such as PCE.
In summary, the *in situ* feature is considerably more insightful compared to the *ex situ* feature. Consequently, the acquisition of *in situ* data during the vacuum quenching process is highly advantageous over having access only to *ex situ* data. Although the choice of data point used as the input feature is sensitive and strongly influences the result, this simple, intuitive approach highlights the advantages of acquiring data during the experimental process over obtaining only *ex situ* data points. Accordingly, the integration of the characterization system into the experimental fabrication setup is worth the additional effort to leverage the correlation between *in situ* data and final device parameters for implementing predictive process monitoring.

5.4 Data Exploration with Unsupervised Machine Learning

Having established the advantages of obtaining *in situ* data over *ex situ* measurements, this chapter focuses on extracting meaningful patterns and insights from the complex data obtained during the perovskite formation process. While the previous comparative analysis relied on human-selected features from the PL transients, which can provide valuable information, the complexity of the data requires more sophisticated analytical approaches. Unsupervised machine learning techniques are powerful tools for data exploration and pattern extraction without relying on predetermined, human-selected features or labels. By applying these techniques, underlying structures and relationships can be revealed that may not be apparent through manual feature selection alone.
This section uses k-means clustering, a fundamental unsupervised learning algorithm, to explore the generated dataset by identifying clusters within the data that may not be apparent through manual analysis (see Figure 5.5). First, k-means clustering is applied to human-selected features, gradually increasing the number of features from one to three. By increasing the complexity of the input data, it is possible to visualize how additional features affect the clustering results. Next, k-means clustering is applied to the entire transients, exploiting all the available transient information of the *in situ* measurement data and bypassing the need for human feature selection. Minimizing the bias introduced by human feature selection, the full temporal information captured in the *in situ* measurements is

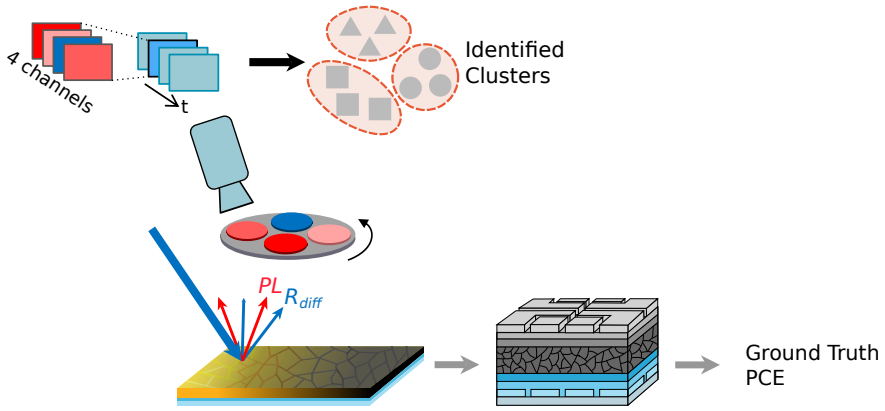

Figure 5.5: Schematic representation of the concept of correlating extracted *in situ* data patterns with the power conversion efficiency (PCE) of fully fabricated perovskite solar cells. Time-resolved multi-channel imaging channels, including photoluminescence and diffuse reflection, are captured during the perovskite thin-film formation. The acquired *in situ* data is investigated by identifying distinct clusters using the unsupervised machine learning method k-means clustering, which groups the solar cells based on similarities in the transient PL data. After building the perovskite thin films into functional devices, the PCE is measured experimentally, and the identified solar cell clusters are then correlated with the ground truth PCE.

used to discover potential correlations between *in situ* data and final solar cell performance. This stepwise approach allows comparing the effectiveness of human intuition in feature selection with the potential of unbiased, data-driven unsupervised learning to identify patterns in complex data. The potential of unsupervised ML techniques, such as k-means clustering, for data exploration is highlighted by demonstrating the correlation between clusters of PL transients and the performance of the fully fabricated devices. Finally, the heterogeneous thin-film quality is revealed by the spatial dependence of the PL transient clusters, indicating varying thin film properties across the large-area substrate due to unfavorable perovskite formation.
Using unsupervised machine learning techniques, the dataset is explored without the biased human feature selection, which is sensitive and strongly influences the result. It allows the identification of patterns inherent in the dataset that may not be immediately apparent using traditional analysis methods. However, these different patterns are indicators of unwanted variations in the experimental process that can be correlated to solar cell performance and therefore help to investigate the complex perovskite thin-film formation from precursor solution.

5.4.1 Clustering Human-Selected Data Features

The unsupervised ML technique of k-means clustering is used to explore and analyze the data by extracting patterns from the dataset that can then be interpreted by the researcher (see section 2.3.1.2 for more details on k-means clustering). To motivate the use of data-driven methods such as k-means clustering, the limitations of the traditional approach of human expert data analysis are highlighted by gradually increasing the number of features considered in the analysis until the human evaluation capacity is exceeded.
Initially, the visual representation of the features allows the examination of up to three human-selected features by plotting the data on up to three axes, combined with color coding the data points with respect to the corresponding PCE. However, because the visual examination by plotting is spatially limited to three dimensions, it is difficult to examine more than three features in this way (further differentiation is potentially possible by varying the color and symbol of the plotted data points). To illustrate the limitations of this approach, three prominent features are extracted from the $\mathrm{PL}_{LP\,725nm}$ transients, namely the maximum $\mathrm{PL}_{LP\,725nm}$, the time of the maximum $\mathrm{PL}_{LP\,725nm}$, and the local maximum $\mathrm{PL}_{LP\,725nm}$ after venting the vacuum chamber (see Figure 5.6a for *PL Intensity (t=*t_{maxPL}*))*, *Time (PL=*PL_{max}*)*, and *PL Intensity (t=*$t_{PL(localmax)}$*)*, respectively).
Plotting the features as data points on the respective axes in combination with the color coding allows to gain a qualitative intuition about the relationship between the values of the extracted features and the corresponding PCEs (see Figure 5.6b to 5.6d). While it is difficult to identify a clear correlation due to the lack of distinct color gradients in the feature space, areas within the scatter plots, i.e., intervals of feature values, can be identified where mostly light or dark-colored data points are located, indicating a stronger presence of low or high PCEs, respectively. For example, high maximum $\mathrm{PL}_{LP\,725nm}$ values are mostly associated with high PCEs (see top right corner in Figure 5.6b) and delayed time of maximum $\mathrm{PL}_{LP\,725nm}$ is mostly associated with low PCEs (see top left corner in Figure 5.6c).
Since the multidimensional representation of the successively increasing feature space combined with color coding is not sufficient to identify clear trends, k-means clustering is used to group data points within the feature space based on the extracted feature values. The k-means clustering algorithm divides the dataset into `k` clusters, placing data points with similar characteristics in the same subset (see section 2.3.1.2 for more details).[75] To facilitate comparison of the clustering results, the same number of clusters `k` is used for all clustering examples. Using the well-established elbow method[77], the number of clusters `k` = 4 is determined to be the most suitable for all presented examples (see Figure 5.7 for elbow plot when clustering the entire transients and supporting information of [346] for elbow plots when clustering human-selected features).
First, when clustering the maximum PL as a single input feature, k-means groups the data into four clusters by only determining three threshold maximum PL values that define the four clusters (see Figure 5.6e). The identified trend that the solar cells with high maximum PL are mostly associated with high PCEs and the samples with low maximum PL have a much broader PCE distribution is confirmed (see Figure 5.6h). Adding the time of the maximum PL as

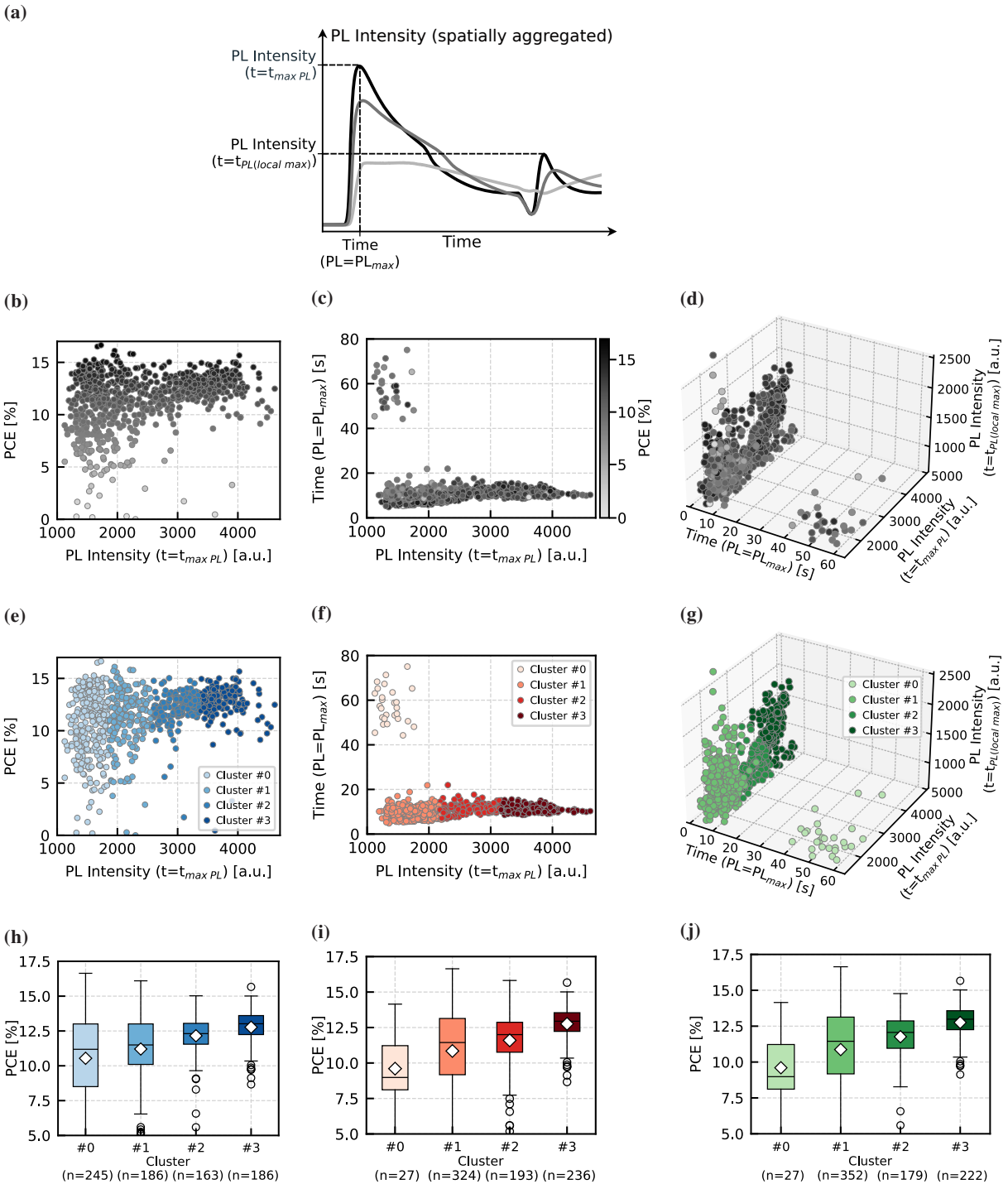

Figure 5.6: Clustering of human-selected features reveals correlations with solar cell performance. (a) Schematic showing $PL_{LP\,725nm}$ features gradually added to the input: initial peak maximum, peak time, and local maximum after venting. (b–g) Scatter plots and 3D visualization of power conversion efficiency (PCE) as a function of (b) one, (c) two, and (d) three input features (b-d), showing clusters identified based on similarities in human-selected PL features (e-g). (h-j) PCE distributions for each cluster with the same color-code as in (e-g). The analysis shows that PL features correlate with performance, but clustering results are highly sensitive to feature selection (see Figure A.4 and Figure A.5 for clustering of other human-selected features). Mean and median values are indicated by white diamonds and black lines, respectively. Partially adapted with permission from [346].

an additional second input feature identifies two distinct groups within the dataset, as a small number of solar cells have a substantially delayed maximum PL (see Figure 5.6f). The solar cells with delayed maximum PL are assigned to cluster *#0* (see Figure 5.6f) and generally display low solar cell device performance (see Figure 5.6i). Depending on the value of the maximum PL intensity, the remaining data points without delayed time of maximum PL are grouped into three clusters *#1* to *#3* and show increasing median and mean PCE (see Figure 5.6i). As in the case of single feature clustering, the best-performing cluster *#3* has low variance even though it has 228 solar cells assigned to it. Adding the local maximum PL after venting the vacuum chamber as a third feature to the value and time of the maximum PL potentially allows for more informative clustering of the data as the information contained in the input continues to increase. While the two identified distinct groups of data points are still evident, the introduction of the third feature adds further variance to the data points, as in particular the group without delayed PL maxima is spread out depending on the values of the local maximum PL (see Figure 5.6g). The boundaries between the clusters are placed similarly to the two-feature clustering case resulting in a similar cluster assignment of solar cells (see Figure 5.6j).
In summary, k-means clustering based on the different input features groups the solar cells into data clusters. It is shown that the clusters generated based on differences in the input data are associated with differences in the corresponding general solar cell performance. This makes it possible to distinguish between data features that are indicators of high and low PCEs, respectively, and facilitates the identification of favorable and unfavorable characteristics of the *in situ* PL transients. The PCE distributions show that even the simple approach of human data selection combined with unsupervised learning reveals information about the relationship between *in situ* PL feature and the corresponding solar cell device performance. However, this section also illustrates that the selection of the input features by a human is sensitive and strongly influences the clustering result. Even by gradually increasing the number of features from one to three, the additional features affect the clustering results as individual solar cell data points are assigned to different clusters changing the sizes of the clusters (see Figure 5.6h to 5.6j). In addition, when the human-selected input is modified by replacing the features with two (or three) different data points extracted from the PL transients, applying k-means leads to substantially different results in cluster assignment and PCE distributions (see Figure A.4 and Figure A.5). By selecting prominent features, the complex data is reduced into few values, making it easier for humans to interpret the data. However, gradually increasing the number of input features results in a more holistic representation of the entire data, but also leads to more complexity. The more complex the data, the more difficult it is for the human researcher to interpret, requiring the use of machine learning. As features with more than three parameters become increasingly difficult to represent and interpret qualitatively, automated methods such as unsupervised ML are needed to explore such high-dimensional feature spaces without losing information by reducing features to a few data points.

5.4.2 Clustering *In Situ* Photoluminescence Transients without Human Data Selection

While the previous section illustrated how human-selected features help to gain a qualitative intuition about the relationship between the input data and the corresponding target variables, it also revealed the limitations of manual feature selection, which leads to a simplification of the complex data. By reducing the entire transient into a small number of values, data interpretation is made easier for the human expert. However, potentially valuable information is removed by making the data human-readable, as the simplification potentially obscures subtle but important patterns in the full transient evolution of the perovskite thin-film formation.
Without selecting individual input features, meaningful human interpretation becomes more difficult, requiring more advanced, unbiased methods. Therefore, in this section, unsupervised ML is used to analyze the entire *in situ* PL transients. Without the need to identify the features of the transients with the highest potential information content, no prior selection is made by a human expert. By applying k-means clustering to the full temporal data of PL transients, bias is minimized, and the inherent complexity of perovskite formation is better represented, allowing

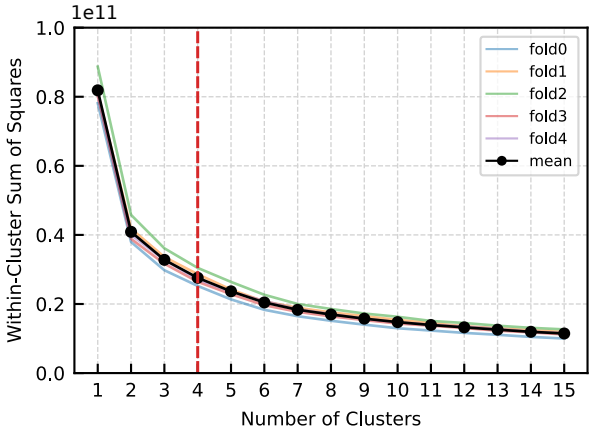

Figure 5.7: Determining the optimal number of clusters using the elbow plot. The heuristic plots the within-cluster sum of squared error as a function of the number of clusters for the five cross-validation folds. The optimal number of clusters is determined by the elbow point, indicated by the red dashed line, where the curves begin to flatten. This indicates a trade-off between minimizing variance within clusters and avoiding overfitting. The elbow point suggests that `k` = 4 clusters effectively capture the data patterns.

the algorithm to detect patterns and relationships that would otherwise stay hidden. Consequently, this approach enables a more holistic analysis of the perovskite formation process by revealing correlations between *in situ* PL data and solar cell performance.

In order to apply k-means clustering to identify *in situ* data patterns corresponding to differences in solar cell performance, the number of distinct clusters to be used must be determined. Using the heuristic elbow method[77] in combination with cross-validation on the training data, the number of clusters `k` = 4 is determined to be the most suitable for clustering the PL transients (see Figure 5.7 and section 2.3.1.2 for more details on the elbow method). Therefore, k-means clustering is applied and the samples of the training set are assigned to one of four clusters, each containing samples with similar PL transient characteristics. However, a comparison of the transients assigned to the different clusters shows that the clusters differ with respect to several characteristics of the transients. First, a temporal shift in the onset of the PL signal is observed when comparing the transients of the different clusters (see Figure 5.8a). The prominent shift in the PL onset time is evident as the transients assigned to cluster *#3* show an earlier onset of the PL signal than the transients in cluster *#0*. The temporal shift in the PL onset time is caused by differences in wet film thickness (see Figure 5.8c for boxplot of thin film thickness). For thicker wet films, the drying of the film by solvent evaporation takes longer and therefore the nucleation and consequently the PL signal onset is delayed compared to thinner wet films.[304]

Second, in addition to the onset time, the transients assigned to the different clusters also differ in the magnitude of the PL maxima just after the PL signal onset (see Figure 5.8b). The transients of cluster *#0* have low PL maxima, and the average maximum magnitude increases with cluster number so that cluster *#3* contains only transients with high PL maxima. Differences in the magnitude of the PL maxima are also caused by differences in wet film thickness, as PL intensity is negatively correlated with thin film thickness (see Figure 5.8c for boxplot of thin film thickness). In thicker wet films, the intensity of the outcoupled PL may decrease because the excitation light penetrates less deeply relative to the film's thickness, and the emitted PL undergoes stronger self-absorption.[304] The absolute PL intensity is also affected by differences in PL quenching, as the blade coating of the underlying 2PACz monolayer leads to spatially different non-radiative recombination due to non-uniform 2PACz layer thickness.

Third, beyond differences in absolute PL intensity, the four clusters show different relative temporal patterns (see Figure 5.8b). The transients in cluster *#0*, which have a low absolute PL intensity, show only a slight relative decrease over time, while higher cluster numbers, which are associated with higher absolute PL intensity, show increasingly steeper PL decreases after the initial maximum. Additionally, the clusters show a distinct behavior in the PL signal after venting the chamber after 170 s of vacuum quenching. In cluster *#0*, associated with thicker films, the signal generally increases after a brief oscillation. However, the magnitude of this signal increase decreases

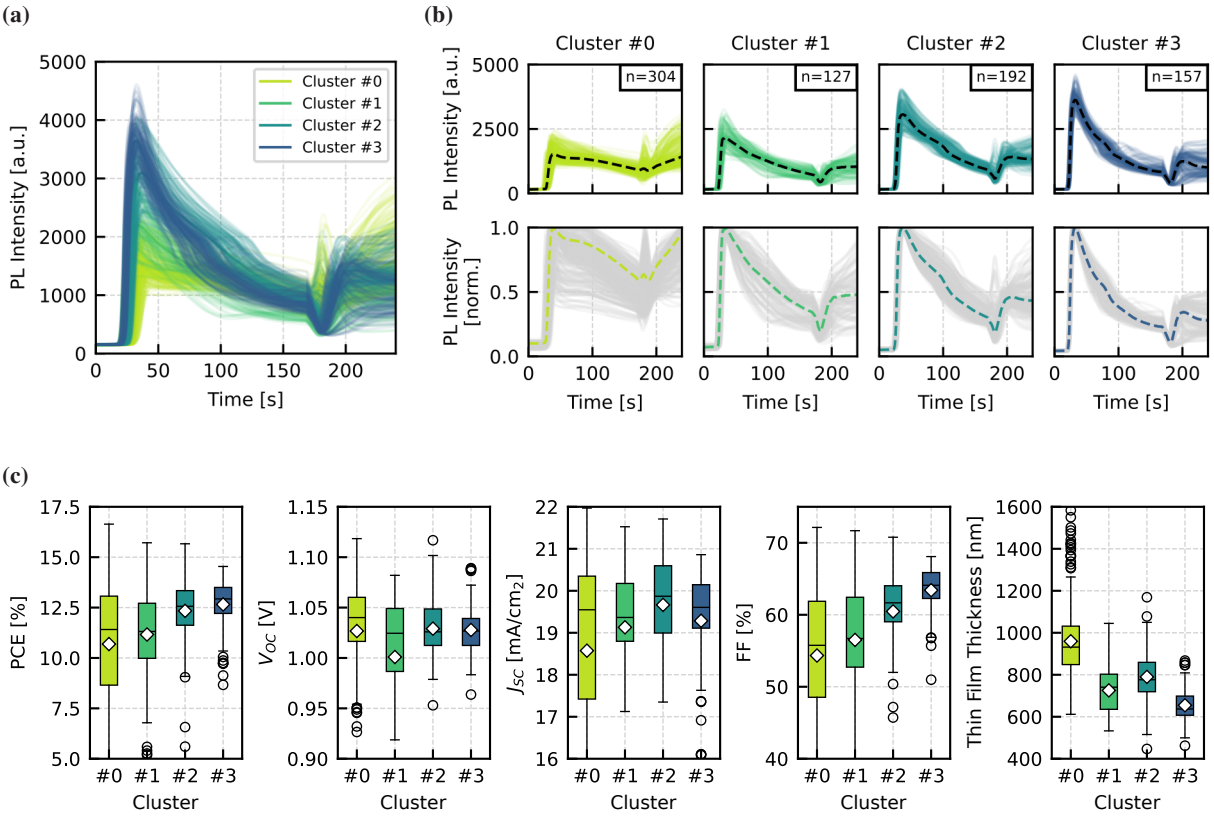

Figure 5.8: Clustering of photoluminescence (PL) transients without human feature selection. (a) $\mathrm{PL}_{LP\,725nm}$ transients of all training samples, color-coded with respect to the assigned cluster, show a temporal shift in the PL onset. (b) PL transients assigned to the four clusters, with the median transient curve of each cluster highlighted as the dashed black line, reveal differences in the magnitude of the PL maxima. Different relative temporal patterns are evident from the normalized PL transients assigned to the different clusters (the median transient curve of each cluster is the colored dashed line). (c) Distributions of power conversion efficiency (PCE), open-circuit voltage (V_{OC}), short-circuit current density (J_{SC}), fill factor (FF), and perovskite thin film thickness for each cluster reveal distinct correlations between the PL transients and the target variables, demonstrating the ability of clustering to extract meaningful data patterns. Mean and median values are indicated by white diamonds and black lines, respectively. Adapted with permission from [346]. Results of clustering transients of diffuse reflection and PL peak wavelength are discussed in Figure A.6 and Figure A.7.

with higher cluster numbers. In contrast, for transients in cluster *#3*, corresponding to thinner films, the signal decreases after a brief oscillation. This behavior is attributed to the outcoupling properties influenced by the final surface roughness of the thin film, which depends on the residual solvent content at the time of venting.[304, 347] Finally, after analyzing the differences in the transient characteristics, the clusters are evaluated in terms of the performance of the corresponding solar cells. The analysis confirms that clustering the entire PL transients effectively reveals data patterns that correlate with the performance of the fully fabricated devices. As the clusters are sorted, showing a gradual shift in the PL onset time and a gradual increase in the magnitude of the PL maxima, trends in the PV performance boxplots can be related to these changes in the PL transient characteristics. As described, changes in the PL transients are attributed to different wet film thicknesses, allowing the PL data to be correlated with the perovskite thin film thickness. However, trends in PV performance parameters are also observed with changing PL characteristics (see Figure 5.8c). In general, PCE and FF increase from cluster *#0* to cluster *#3*, corresponding to higher PL maxima and earlier PL onsets, indicating a correlation between PL onset time and PL maximum magnitude and the photovoltaic parameters PCE and FF. The general trend is reflected by the mean and median PCE increasing from cluster *#0* to cluster *#3*. Consistent with previous clustering examples, the variance in

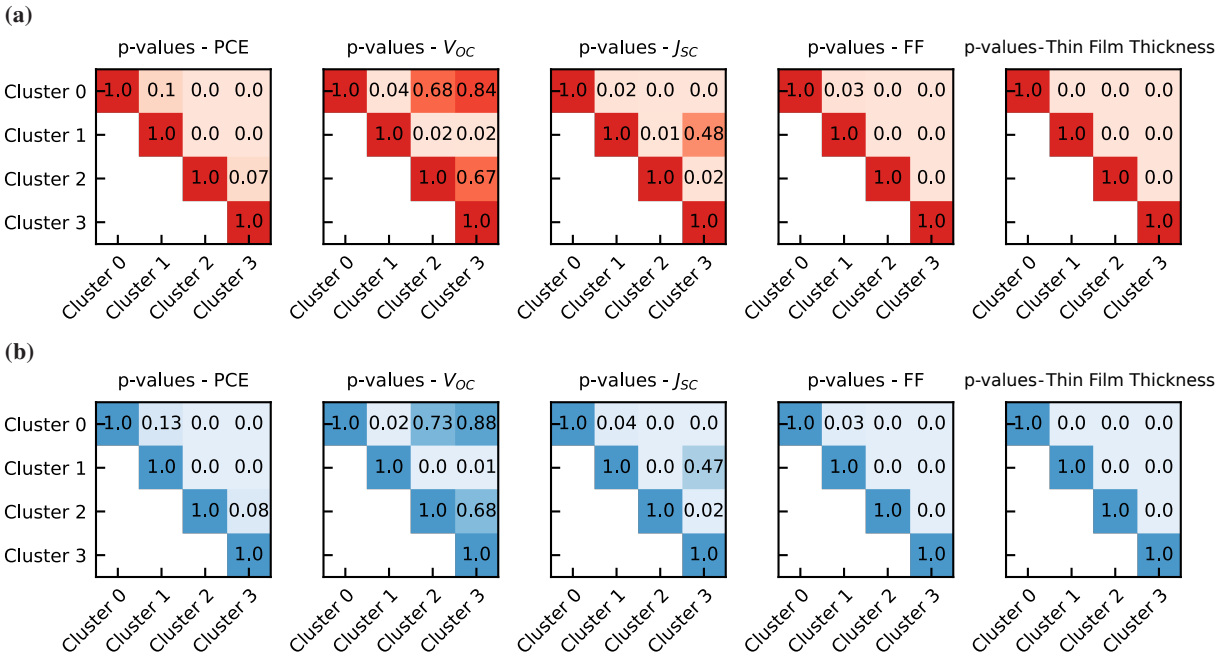

Figure 5.9: Statistical tests show the significance of the difference between the target variable distributions of the clusters. (a) p-values obtained from t-tests (*scipy.stats*[140]) for power conversion efficiency (PCE), open-circuit voltage (V_{OC}), short-circuit current density (J_{SC}), fill factor (FF), and perovskite thin film thickness. (b) p-values obtained from z-tests (*statsmodels*[141]) for the same metrics. p-values smaller than 0.05 indicate that the means of two clusters are significantly different. The z-test is appropriate for large sample sizes with known variances, while the t-test is used for smaller sample sizes or when variances are unknown. The results show that, with the exception of the V_{OC} distributions, the distributions of the clusters are significantly different, supporting the effectiveness of clustering *in situ* data for distinguishing solar cell characteristics.

PCE is low in the best-performing cluster, but increases as the mean PCE decreases across clusters. The analysis reveals distinct data patterns in cluster *#3* that result in predominantly high-performing solar cells, with very few low-performing samples. In particular, 87.3% of the solar cells in cluster *#3* have a PCE higher than the average of the training set ($\text{PCE}_{mean} = 11.6\%$), highlighting the above-average performance of solar cells in this cluster (see supporting information of [346]). A similar, even more pronounced trend is observed for FF. Mean and median FF increase from cluster *#0* to cluster *#3*, with 93.7% of solar cells in cluster *#3* having a higher FF than the dataset average ($\text{FF}_{mean} = 58.0\%$).

No clear trend is observed for V_{OC} and J_{SC}. The median V_{OC} decreases from cluster *#0* to cluster *#3*, with cluster *#1* as an outlier. This could indicate an inverse correlation between V_{OC} and both the magnitude of the PL maximum and the PL onset time. However, statistical tests (t-tests and z-tests) indicate no significant differences between the means of the V_{OC} distributions across clusters (see Figure 5.9). For J_{SC}, the mean increases from cluster *#0* to cluster *#2*, but this trend is interrupted by cluster *#3*. Statistical testing reveals significant differences in the means of J_{SC} across most clusters (see Figure 5.9), indicating a correlation between J_{SC} and the PL transients. Unlike the clear trend seen for PCE and FF, J_{SC} does not show a consistent increase from cluster *#0* to cluster *#3*, suggesting a more complex relationship that cannot be explained by gradual shifts in PL onset time or PL maximum magnitude alone.

In addition, applying k-means clustering to the other channels obtained from IPDRI reveals data patterns that correlate with the performance of fully fabricated devices. Clustering based on the PL peak wavelength transients shows similar trends in the distribution of PV parameters, particularly PCE and FF, suggesting a correlation between the observed data patterns and solar cell performance. As with the PL transients, no clear trend is found for V_{OC} and J_{SC} (see Figure A.7). When clustering samples based on diffuse reflection transients, no significant relationship is

observed between the transient data patterns and PV parameters. However, a clear correlation is found between the evolution of diffuse reflection transients and the final thin film thickness (see Figure A.6).
In summary, applying k-means clustering to the full *in situ* PL transients without human-selected input features reveals distinct data patterns. By analyzing the entire transient data, clusters are generated that differ regarding several characteristics, including the PL onset time and the magnitude of the PL maxima. It is shown that the data patterns assigned to the different clusters correlate with the performance of the fully fabricated devices. Early PL onset and higher PL maxima are associated with better-performing solar cells, as reflected in higher PCE and FF values. While trends are identified for PCE and FF, the clusters, which are assigned based on gradual shifts in PL onset time and PL maximum magnitude, show no clear trends regarding V_{OC} and J_{SC}. Furthermore, clustering based on other IPDRI channels demonstrates similar trends for PCE and FF when examining the PL peak wavelength transients, while clusters of diffuse reflection transients correlate with thin film thickness but not with the photovoltaic performance. Unsupervised machine learning allows investigation of the perovskite thin-film formation without obscuring subtle data patterns by simplifying the complex data through human feature selection. By applying k-means clustering to the entire *in situ* PL transients, this approach minimizes bias, uncovers hidden transient data patterns, and reveals relationships between PL data and solar cell performance, providing a more holistic analysis.

5.4.3 Spatial Distribution of Clusters Reveals Heterogeneous Thin-Film Quality

When analyzing the four PL transient clusters, it is evident that cluster *#0* has a notably larger variance in solar cell performance metrics compared to the other clusters (see Figure 5.8c). To investigate whether the PL patterns within cluster *#0* still correlate with solar cell performance or whether this subset lacks such a relationship, a subclustering analysis is performed on this subset of data. This additional clustering reveals finer distinctions in the PL transient patterns, suggesting that even within cluster *#0*, variations in the transients can be linked to differences in solar cell performance. Based on these findings, the spatial distribution of the clusters across the substrate is investigated to uncover potential process-related factors affecting performance. By examining the positioning of the solar cells during fabrication, spatial correlations between the PL transient patterns and solar cell performance are identified. It is observed that certain clusters, particularly those associated with poorer performance, are predominantly located in specific areas of the substrate. This spatial analysis reveals that process-related factors, such as material backflow and thickness deviations during blade coating, contribute to the heterogeneity in perovskite thin-film quality. Understanding these spatial variations provides valuable insights into detrimental process mechanisms and highlights areas for optimization in the fabrication process.
To determine whether the subset of samples in cluster *#0* still shows a correlation between PL data and solar cell performance despite the high variance, a second round of clustering (subclustering) is performed (see Figure 5.10a). The elbow method identifies $\mathtt{k}_{sub}$ = 3 as the optimal number of subclusters (see Figure 5.11a). Since the previous analysis has shown a correlation between PL onset time, PL maximum magnitude, and solar cell performance (see Figure 5.8), the PL transients are truncated for the subclustering step to minimize the influence of data collected after vacuum quenching was stopped at 170 s. To illustrate the reasoning behind subclustering, i.e., performing two consecutive rounds of clustering, a comparison of the cluster centroid transients from different approaches is presented. By comparing the centroids from two rounds of clustering with those from a single round of clustering (k = 6, for the same total number of clusters), using both untruncated and truncated transients, the differences in the identified data patterns become apparent (see Figure 5.11b). Subclustering divides the data more precisely into several low-intensity PL subclusters, while clustering with k = 6 in a single round produces less distinct divisions, particularly for low-intensity PL transients.
Consequently, subclustering reviews whether further resolving of the PL transients regarding PL onset time and PL maximum magnitude allows extending the correlation between PL data and solar cell performance to samples previously assigned to cluster *#0*. As the correlation holds, it is found that assigning the samples to three subclusters allows further differentiation between PL transient patterns associated with different solar cell performance. Like

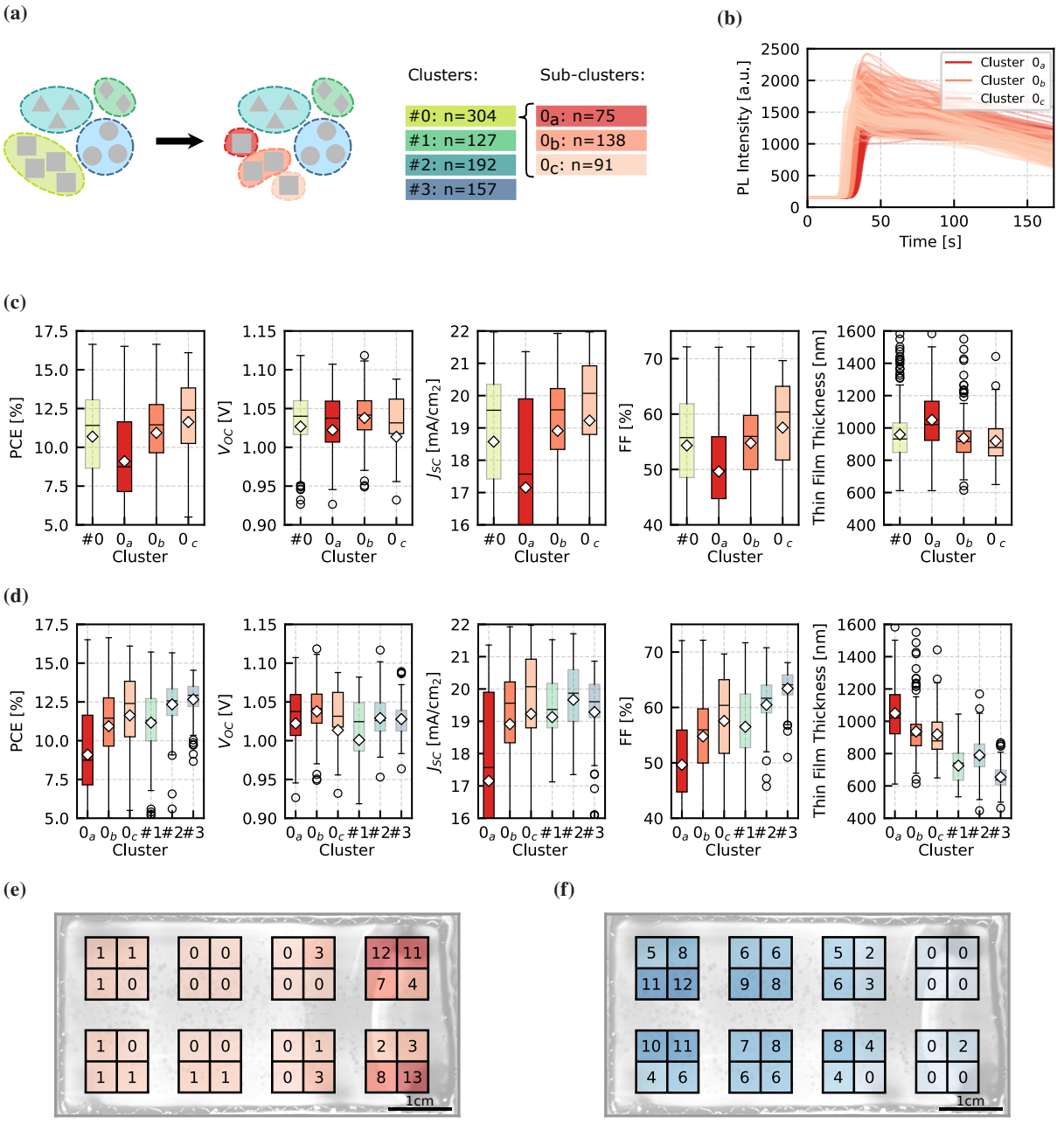

Figure 5.10: In-depth investigation of the clusters confirms the correlation with solar cell performance and shows distinct spatial distribution of the clusters. (a) Schematic of the subclustering process, where the original cluster *#0* is further divided into subclusters (*0_a*, *0_b*, *0_c*), revealing additional substructure within the data. (b) The PL transients previously assigned to cluster *#0*, are truncated and subclustered, showing distinct patterns in PL evolution over time. (c, d) Comparison of power conversion efficiency (PCE), open-circuit voltage (V_{OC}), short-circuit current density (J_{SC}), fill factor (FF), and perovskite thin film thickness distributions confirms the previously identified correlation between PL transients and target variables also for samples in the high variance cluster *#0*. Mean and median values are indicated by white diamonds and black lines, respectively. (e, f) Heatmaps showing the spatial distribution across the 32 possible locations on the large-area substrates of the worst-performing cluster, cluster *0_a* (e), and the best-performing cluster, cluster *#3* (f). The subclustering analysis demonstrates the ability to resolve finer distinctions within clusters that correlate with variations in solar cell performance. Partially adapted with permission from [346].

(a)

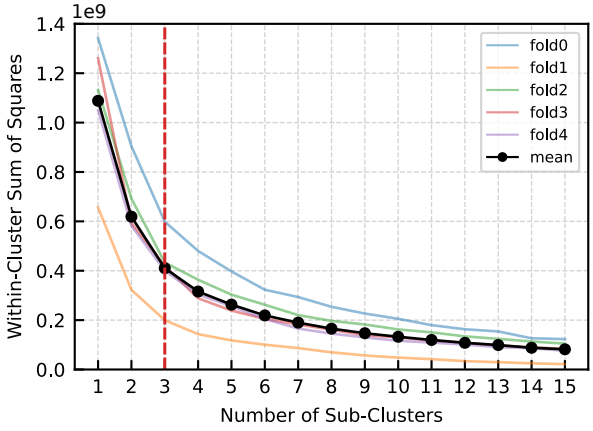

(b)

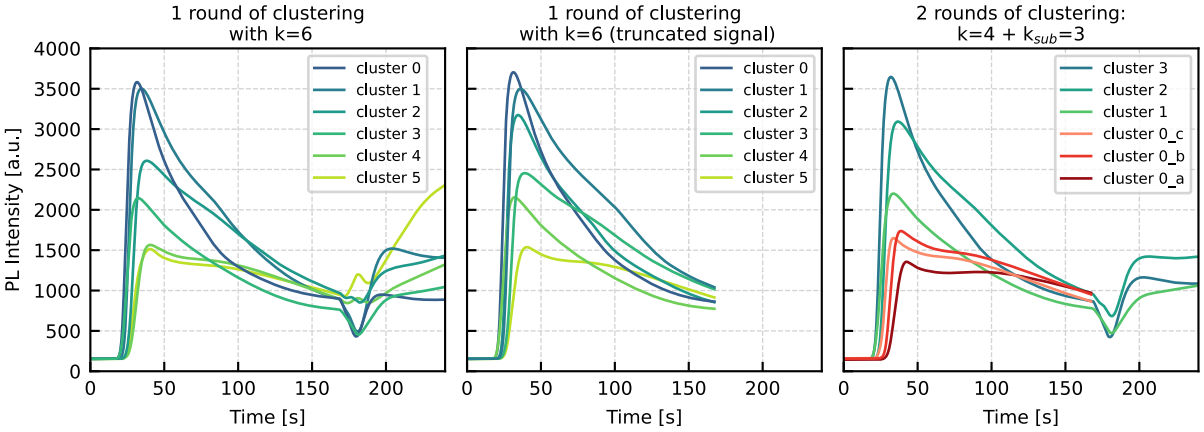

Figure 5.11: Comparison of clustering and subclustering approaches for photoluminescence (PL) transients. (a) Elbow plot for determining the optimal number of subclusters for cluster *#0*, showing the within-cluster sum of squares as a function of the number of subclusters. The red dashed line indicates k_{sub} = 3 as the optimal number of subclusters. (b) Comparison of centroid PL transients obtained using different clustering strategies: single-round clustering with k = 6 (left), single-round clustering with truncated PL transients and k = 6 (middle), and two-round clustering with k = 4 for the first round and k_{sub} = 3 for subclustering cluster *#0* (right). The analysis shows that subclustering provides a more refined division of PL transients within low-intensity clusters, facilitating the investigation of the correlation between PL data and solar cell performance for samples in cluster *#0*. Partially adapted with permission from [346].

in the first round of clustering, it is observed that the PL onset time as well as PL maximum magnitude have a profound impact on the subclustering result (see Figure 5.10b). Compared to the PCE distribution of the original cluster *#0*, solar cells in subcluster *0_a* have poorer average performance, while those in subcluster *0_c* have higher average PCEs (see Figure 5.10c). Both the mean and median PCEs differ across the three subclusters, indicating that the extracted PL transient patterns can be associated with differences in performance. Although no clear trend is observed for V_{OC} and thin film thickness, similar trends are evident for J_{SC} and FF distributions across the subclusters. In summary, subclustering confirms the previously identified correlation between PL transients and solar cell performance for samples in cluster *#0* (see Figure 5.10d).

After evaluating the clusters based on solar cell performance metrics, the position of each solar cell on the substrate during fabrication is introduced as an additional feature for further analysis. Incorporating this spatial information reveals distinct spatial patterns of PL transients associated with different clusters. Substantial differences in the spatial distribution of the clusters across the substrate are observed as certain PL transient patterns are predominantly

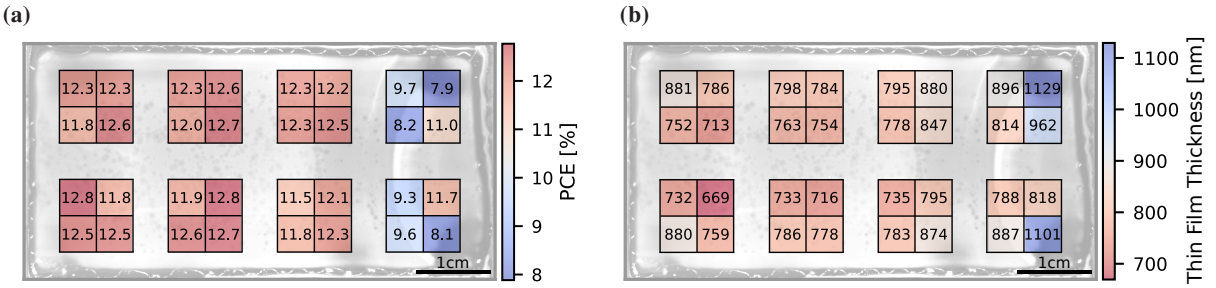

Figure 5.12: Spatial distribution of average PCE and thin film thickness across the substrate. Heatmaps showing the spatial distribution of (a) average power conversion efficiency (PCE) and (b) average perovskite thin film thickness for all training set solar cells across the 32 possible locations on the large-area substrates. Cells with higher PCE values are predominantly located in the left-central region of the substrate, corresponding to cluster *#3*. In contrast, cells in areas affected by solution backflow have lower PCE values. Along the right edge of the substrate increased thickness is observed due to material backflow during blade coating.

located in specific areas of the substrate. First, analyzing the spatial distribution of solar cells assigned to the poorest-performing cluster, cluster *0_a*, reveals a concentration of these cells along the right edge of the substrate (see Figure 5.10e). During fabrication, almost none of the solar cells in cluster *0_a* were positioned on the left side of the substrate, while over 80% were located in the rightmost quarter. To connect the extracted PL patterns with the experimental process, the morphology of the blade-coated perovskite thin films is investigated. Comparing the film morphology with the spatial distribution of cluster *0_a* indicates that the accumulation of low-performing cells results from an arc-shaped inhomogeneity caused by precursor solution backflow as the blade coating applicator is moved from left to right. This backflow causes spatial variations in material distribution, resulting in thin film thicknesses that deviate from the intended thickness. These spatial variations in perovskite thin film properties lead to altered PL transients, and based on these differences, unsupervised machine learning assigns these samples to a cluster containing predominantly low-performing solar cells.

Second, the solar cells assigned to the best-performing cluster, cluster *#3*, were also predominantly located in a specific area of the substrate. Unlike cluster *0_a*, almost none of the solar cells in cluster *#3* were positioned in the substrate area affected by solution backflow (see Figure 5.10f). The majority of these high-performing cells were located in the center of the leftmost quarter of the substrate. This spatial distribution results from thickness variations caused by a decreasing amount of solution available for blade coating as the applicator moves from left to right, as well as material flow toward the top and bottom edges of the substrate. Heatmaps of the original clusters reveal similar insights regarding their spatial distribution (see Figure A.8). Consequently, the extracted PL data patterns from the original clusters are not uniformly distributed but are also concentrated in specific areas of the substrate. Examining the spatial distribution of the average PCE of the solar cells further confirms that cells positioned in the substrate area affected by solution backflow generally exhibit poorer performance (see Figure 5.12a and Figure A.9). In addition, the spatial distribution of average thin film thickness highlights the increased perovskite thin film thickness along the right edge of the substrate due to solution backflow (see Figure 5.12b).

In summary, subclustering of the original PL transient cluster *#0* reveals that even within this group of high PV parameter variance, distinct PL transient patterns correlate with solar cell performance. By performing a second round of k-means clustering on the samples assigned to cluster *#0*, finer distinctions in PL onset time and PL maximum magnitude are identified, confirming that the correlation between PL transients and solar cell performance extends to this subset. Furthermore, incorporating the spatial position of each solar cell on the substrate into the analysis uncovers significant differences in the spatial distribution of the clusters. Solar cells assigned to poor-performing clusters, like subcluster *0_a*, are predominantly located along the right edge of the substrate, an area affected by solution backflow during blade coating. The backflow of material leads to thickness variations and inhomogeneities in the perovskite thin film, resulting in altered PL transients and reduced solar cell performance. In contrast, solar cells in the best-performing cluster, cluster *#3*, are mainly located in substrate areas with uniform thin

film thickness, unaffected by solution backflow. This section demonstrates that unsupervised machine learning not only uncovers hidden patterns in PL transients that correlate with solar cell performance but also reveals a spatial distribution of PL patterns indicative of poor solar cell performance related to detrimental process mechanisms. By identifying issues such as solution backflow and thickness variations, this approach provides valuable insights for improving the quality of perovskite thin films by optimizing the fabrication process.

5.5 Predicting Solar Cell Performance Prior to Device Completion using Supervised Machine Learning

Building on insights from unsupervised machine learning that revealed correlations between *in situ* PL transient patterns and solar cell performance, the focus is shifted from descriptive to predictive analysis using supervised machine learning. While clustering has identified PL patterns related to spatial inhomogeneities in perovskite thin-film formation, the ultimate objective is to predict solar cell performance before device completion. Early prediction of PV performance metrics, such as PCE, is crucial for improving process control, reducing material waste, and accelerating the commercialization of perovskite PV technology. Transitioning from descriptive to predictive analysis, ML-based process monitoring of the perovskite thin-film formation enables early detection of deviations from the intended experimental process and facilitates real-time process control.
To achieve early assessment of perovskite PV properties before the solar cells go through the subsequent fabrication steps required for experimental performance measurement, this section applies supervised machine learning to predict solar cell performance based solely on *in situ* PL data acquired during the vacuum quenching of blade-coated perovskite thin films. In supervised ML, the model learns a mapping between the input data features and the target variable, and when given new input data, the trained model predicts the corresponding target variable for the new sample (see section 2.3.1.1 for more details). For the initial investigation, the k-nearest neighbors algorithm[80] is chosen because it is a supervised ML method that is simple and effective without requiring extensive parameter tuning. Like unsupervised k-means clustering, kNN is distance-based and assumes that similar samples are close to each other in the feature space. To predict the target value of a new sample, kNN determines the `k` samples in the training set that are closest (most similar) to the new sample based on the Euclidean distance (see Figure 5.13).

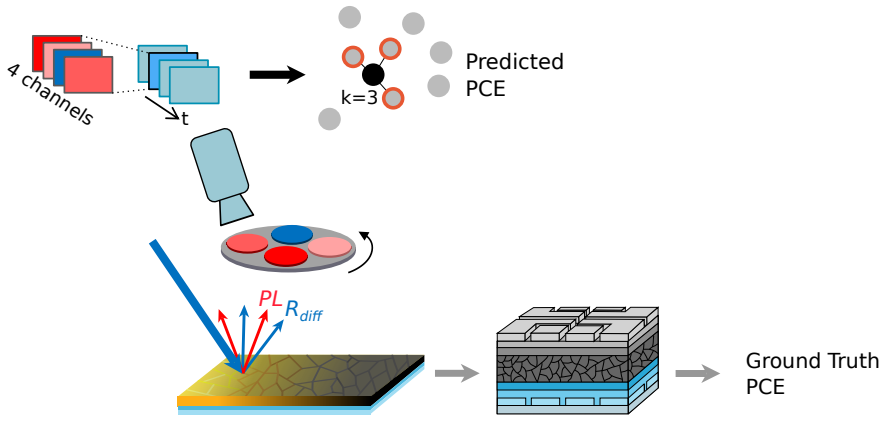

Figure 5.13: Schematic representation of the concept of predicting the power conversion efficiency (PCE) of perovskite solar cells using the k-nearest neighbors (kNN) algorithm prior to completion into fully fabricated devices. Time-resolved multi-channel imaging data, including photoluminescence and diffuse reflection, are captured during the perovskite thin-film formation. Using the acquired *in situ* data as model input, the supervised machine learning method kNN predicts the PCE based on similarity to neighboring samples in the feature space. After the perovskite thin films are fabricated into functional devices, the ground truth PCE is measured experimentally and compared with the predicted values to evaluate the prediction accuracy of the kNN model.

The mean of the k closest samples in the training set is then output as the prediction for the new sample.
To ensure an unbiased evaluation on the test set, the model is trained exclusively on the training set. The hyperparameter optimization, i.e., the determination of the number of neighbors k, is performed by fivefold cross-validation on the training set (see section 2.3.5 for more details). For each fold, the prediction accuracy is measured by the MAE, the average magnitude of the errors between the predicted values and the ground truth (lower is better). The overall model performance is then determined by averaging the MAE values across all five folds for different values of k. This approach allows the identification of the optimal value of k without using any data from the test set. A separate kNN model is trained for each target variable, resulting in distinct optimal values of the parameter k for the different target variables, including the PV performance parameters (PCE, V_{OC}, J_{SC}, and FF) as well as the perovskite thin film thickness.
To establish a benchmark for predictive performance, a simple baseline model is introduced as a reference for evaluating prediction improvements. This baseline model uses the mean value of the target variable (e.g., PCE) from all samples in the training set as the predicted value for each new sample. It represents the predictive ability of a human researcher without the help of machine learning methods. Without predictive tools, the researcher would likely assume that the results of new experiments (i.e., the test set) are comparable to the average results of previous experiments (i.e., the training set) because no experimental parameters or conditions have been changed. Thus, the baseline predicts the mean of the training set for all new samples.
To evaluate the predictive performance of the kNN models during cross-validation on the training set, the MAEs obtained by the kNN regression are compared to the baseline MAEs (see Table 5.2). For the initial investigation, only the $\mathrm{PL}_{LP\,725nm}$ transients are used as input to the prediction model, but the next section examines the differences in prediction results when the different IPDRI channels are used as input to the model (see section 5.6). Since lower MAE values indicate better performance, an improvement is observed for all target variables as the prediction error is reduced when comparing the kNN model to the baseline. For PCE, the kNN model achieves a substantial improvement, reducing the MAE from 1.90%$_{abs}$ to 1.54%$_{abs}$, which corresponds to a relative decrease of 18.8%$_{rel}$. Although the model shows only a modest improvement for V_{OC} with a decrease of 8.4%$_{rel}$ (from

Table 5.2: Reduction of prediction error using the k-nearest neighbors (kNN) regressor. The prediction result of the kNN model using the photoluminescence transient ($\mathrm{PL}_{LP\,725nm}$) as input is compared to a baseline model representing human predictive capabilities that predicts the training set mean. Bold values indicate prediction improvement on previously unseen data (test set). (for MAE: lower is better ↓, MAE: mean absolute error, kNN: k-nearest neighbors, k: number of neighbors, PCE: power conversion efficiency, V_{OC}: open-circuit voltage, J_{SC}: short-circuit current density, FF: fill factor)

	MAE – Cross-Validation			MAE – Test Set			
Target Variable	Baseline	kNN	Error Reduction	Baseline	kNN	Error Reduction	k
PCE [%]	1.90	1.54	$-18.8\%_{rel}$	1.94	1.52	**–21.7**%$_{rel}$	14
V_{OC} [V]	0.031	0.028	$-8.4\%_{rel}$	0.036	0.030	**–17.1**%$_{rel}$	24
J_{SC} [mA/cm^2]	1.43	1.25	$-12.7\%_{rel}$	1.37	1.14	**–17.0**%$_{rel}$	15
FF [%]	6.56	5.10	$-22.3\%_{rel}$	6.55	5.10	**–22.2**%$_{rel}$	14
Thin Film Thickness [nm]	137.93	79.29	$-42.5\%_{rel}$	139.80	67.68	**–51.6**%$_{rel}$	18

0.031 V to 0.028 V), it performs better for J_{SC}, reducing the MAE from 1.43 mA/cm^2 to 1.25 mA/cm^2, a decrease of 12.7%$_{rel}$. There is also a substantial improvement in the prediction of FF, as the MAE decreases by 22.3%$_{rel}$, from 6.56%$_{abs}$ to 5.10%$_{abs}$. The model performs particularly well in predicting the perovskite thin film thickness, where the MAE decreases from 137.93 nm to 79.29 nm, resulting in a substantial relative reduction of 42.5%$_{rel}$.
After determining the optimal value of `k` through cross-validation on the training set, the predictive capability of the kNN models is evaluated on previously unseen data in the test set. Compared to the baseline, which represents the human predictive ability, the kNN models show substantial improvements in prediction accuracy, as evidenced by lower MAEs (see Table 5.2). For PCE and FF, the MAE is reduced by 21.7%$_{rel}$ (from 1.94%$_{abs}$ to 1.52%$_{abs}$) and by 22.2%$_{rel}$ (from 6.55%$_{abs}$ to 5.10%$_{abs}$), respectively. Similarly, the MAE for V_{OC} decreases by 17.1%$_{rel}$ (from 0.036 V to 0.030 V) and for J_{SC} by 17.0%$_{rel}$ (from 1.37 mA/cm^2 to 1.14 mA/cm^2). Again, the largest improvement is observed for the prediction of thin film thickness, where the MAE is reduced by 51.6%$_{rel}$, from 139.80 nm to 67.68 nm.
To evaluate how accurately the models predict the target variables compared to the experimentally measured data (i.e., ground truth), parity plots are used to visually validate the performance of the kNN models. The results of the test set predictions clearly show that the kNN models outperform the baseline predictions (see Figure 5.14). The baseline, which uses the mean value of the training set as the prediction for each test sample, fails to accurately predict the target variables. This reflects the inherent limitations of a human researcher's predictive ability, which relies only on past experimental results without specific data-driven insights, and underscores the importance of introducing ML-based predictive capabilities into the experimental laboratory.
In contrast, the kNN models show substantially better agreement between the predicted and actual values, particularly for the perovskite thin film thickness. The parity plots confirm the quantitative results, highlighting the best prediction performance for perovskite thin film thickness (see Table 5.2). While a clear correlation between prediction and ground truth values is observed for thin film thickness, PCE, and FF, the models show less accuracy when predicting V_{OC} and J_{SC}. Interestingly, the parity plots indicate that the models tend to overestimate outliers with low ground truth values for all photovoltaic performance parameters (PCE, V_{OC}, J_{SC}, and FF). This may be due to the complex task of predicting PV performance metrics based solely on data acquired during the perovskite thin-film formation step, while the final performance of the solar cells is influenced by subsequent processing steps and the quality of the entire device stack.
While irregularities in the other fabrication steps can adversely affect solar cell performance, they are not captured in the input data used to train the models. Consequently, this limitation may contribute to discrepancies in model predictions. In contrast, since the perovskite thin film thickness is only determined during the thin-film formation step, and this process is fully represented in the *in situ* data, the parity plot for thin film thickness shows no data points in the top left corner. This suggests that the kNN model predictions for thin film thickness are unaffected by the complexities introduced by downstream processing steps, which can lead to deviations in solar cell performance that are not captured in the input data.
For a more comprehensive comparison of prediction accuracy across different target variables, additional error metrics, namely RMSE and R^2, are introduced alongside MAE to further evaluate the predictive performance of the kNN models (see Table 5.3). Similar to MAE, RMSE measures the magnitude of prediction errors (lower is better), but it penalizes larger errors more severely, providing a complementary metric of model accuracy. The kNN model achieves lower RMSE values for all target variables compared to the baseline, indicating fewer large deviations from the ground truth values. Notably, with an RMSE of 2.28% for PCE prediction, the model outperforms "the best models for PCE prediction based on literature databases which have achieved an RMSE of around three percent units", according to a recent review paper on machine learning in perovskite research [155].
The R^2 scores provide further evidence of the improved fit of the kNN models, measuring how well the predictions explain the variance in the data. Substantial improvements in R^2 (higher is better) are observed for PCE (from -0.03 to 0.24), J_{SC} (from -0.00 to 0.18), FF (from -0.05 to 0.21), and particularly for thin film thickness (from -0.04 to 0.74), indicating a strong correlation between predicted and ground truth values. However, for V_{OC}, the R^2 value remains low (0.008), indicating that this parameter is less predictable from the available input features,

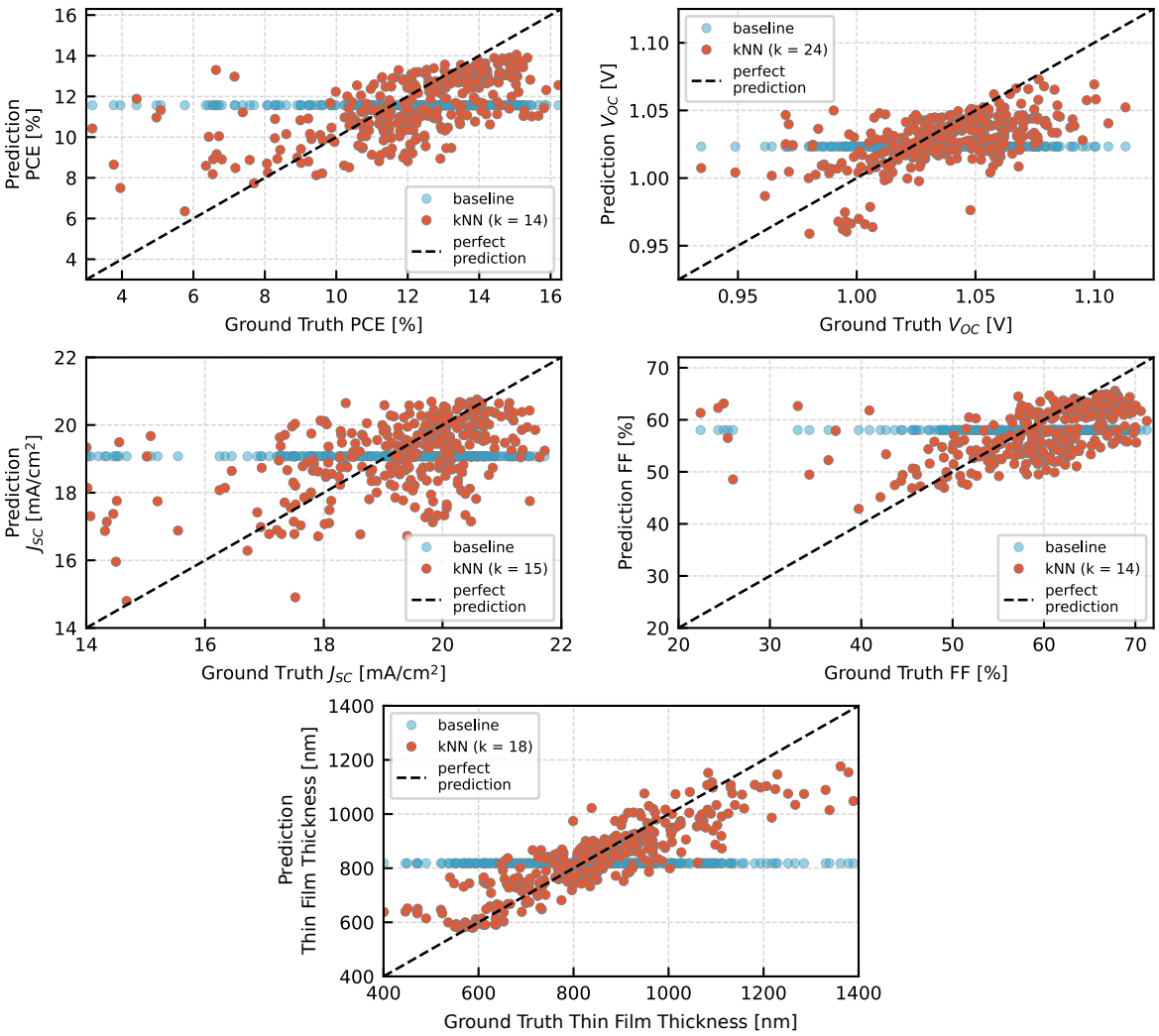

Figure 5.14: Parity plots of k-nearest neighbors (kNN) model predictions for solar cell performance metrics and thin film thickness. The parity plots compare the kNN model predictions using the photoluminescence transient ($PL_{LP\,725nm}$) as input against the ground truth values for power conversion efficiency (PCE), open-circuit voltage (V_{OC}), short-circuit current density (J_{SC}), fill factor (FF), and perovskite thin film thickness. The baseline predictions, which use the mean value of the training set as the prediction for each held-out test sample, show poor agreement with the ground truth, while the kNN models demonstrate a much closer fit to the perfect prediction line (black dashed line). The best prediction performance is observed for thin film thickness. For each target variable, the optimal number of neighbors `k` is determined using cross-validation on the training set. The parity plots reveal that kNN predictions tend to overestimate outliers with low ground truth values for all photovoltaic performance parameters, highlighting the challenges in predicting PV performance metrics based solely on *in situ* data from the thin-film formation step. Adapted with permission from [346].

highlighting potential limitations of the *in situ* PL data for accurate V_{OC} prediction, at least for this dataset. Overall, the additional error metrics further confirm the superior predictive capabilities of the kNN models compared to the baseline.

In summary, transitioning from descriptive analysis using unsupervised machine learning to predictive analysis by leveraging supervised ML, this section demonstrates that k-nearest neighbors regression can effectively predict solar cell performance metrics and perovskite thin film thickness based solely on *in situ* PL data acquired during the thin-film formation process. By training kNN models on PL transients, significant reductions in prediction error are achieved compared to a baseline model representing human predictive capabilities, which predicts the mean of

Table 5.3: Predictive performance of the k-nearest neighbors (kNN) model using the photoluminescence transient ($PL_{LP\,725nm}$) as input on the held-out test set measured in different error metrics. (for MAE and RMSE: lower is better ↓, for R^2: higher is better ↑, MAE: mean absolute error, RMSE: root mean square error, R^2: coefficient of determination, kNN: k-nearest neighbors, PCE: power conversion efficiency, V_{OC}: open-circuit voltage, J_{SC}: short-circuit current density, FF: fill factor)

	MAE		RMSE		R^2	
Target Variable	Baseline	kNN	Baseline	kNN	Baseline	kNN
PCE	1.94%	1.52%	2.65%	2.28%	–0.03	0.24
V_{OC}	0.036 V	0.030 V	0.100 V	0.100 V	–0.001	0.008
J_{SC}	1.37 mA/cm^2	1.14 mA/cm^2	2.12 mA/cm^2	1.92 mA/cm^2	–0.00	0.18
FF	6.55%	5.10%	8.64%	7.48%	–0.05	0.21
Thin Film Thickness	139.80 nm	67.68 nm	182.29 nm	91.35 nm	–0.04	0.74

the training set. The kNN models show substantial improvements in prediction accuracy, reducing the MAE for all target variables and achieving the highest relative improvement for perovskite thin film thickness. Additional error metrics, including RMSE and R^2, further validate the improved predictive capabilities of the kNN models. While the R^2 values indicate strong correlations between predicted and ground truth values for most target variables, the low R^2 value for V_{OC} highlights the challenges of predicting this parameter using *in situ* PL data alone. Parity plots visually confirm that the kNN models outperform the baseline predictions, especially for thin film thickness, PCE, and FF. However, for the PV performance metrics there is also a consistent overestimation of outliers with low ground truth values, possibly due to the influence of downstream processing steps not captured in the *in situ* data. This suggests that while kNN models can effectively capture the relationships between *in situ* PL transients and perovskite thin-film quality, the complexity of predicting PV parameters based solely on thin-film formation data is limited by the lack of information from other processing steps. Overall, the results highlight the potential of supervised machine learning to predict solar cell performance metrics prior to device completion, facilitating the detection of deviations from the optimal experimental process through data-driven process monitoring to increase yield and reduce material waste.

5.6 Prediction Accuracy of Various Machine Learning Algorithms using Different Input Data

The previous section demonstrated the potential of using the supervised ML method k-nearest neighbors to predict solar cell performance metrics and perovskite thin film thickness using only the $PL_{LP\,725nm}$ transients. However, one of the major benefits of the IPDRI setup is its ability to capture multiple imaging channels, each providing unique insights into the process through different signals. Therefore, this section investigates the predictive capabilities of these different IPDRI channels by comparing the prediction accuracy of kNN when using different input data. In addition, kNN is benchmarked against other classical supervised machine learning techniques by analyzing

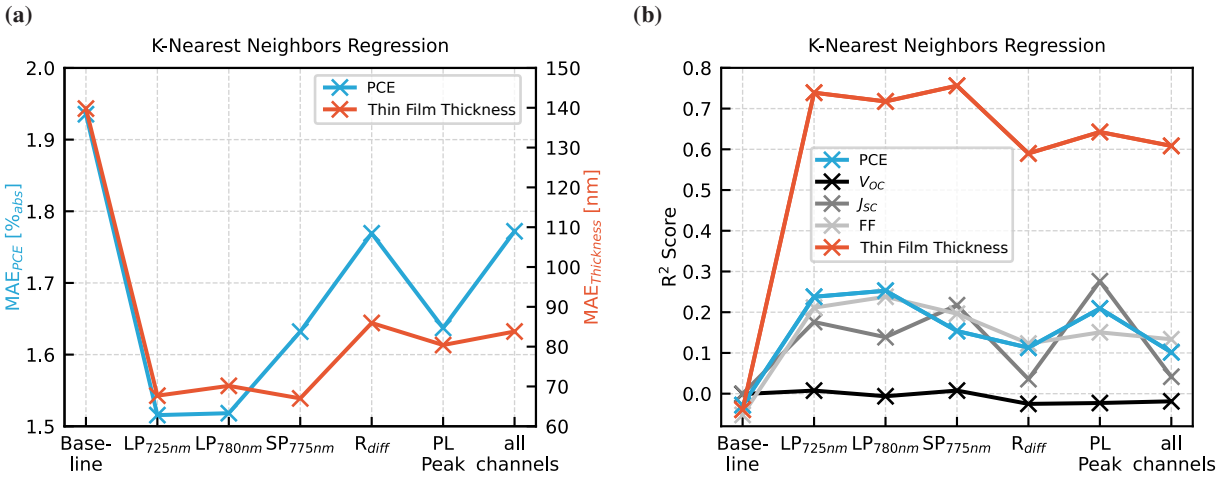

Figure 5.15: Prediction performance of k-nearest neighbors (kNN) on the held-out test set using different *in situ* channels as model input. (a) Mean absolute error (MAE) of kNN predictions for power conversion efficiency (PCE) and thin film thickness using different *in situ* signals as input. The baseline model, which uses the mean of the training set as the prediction for each test sample, has the highest MAE. The lowest errors for both PCE and thin film thickness are achieved using the photoluminescence (PL) intensity channels (LP_{725nm}, LP_{780nm}, and SP_{775nm}). (b) R^2 scores for kNN predictions of PCE, open-circuit voltage (V_{OC}), short-circuit current density (J_{SC}), fill factor (FF), and perovskite thin film thickness. The highest R^2 values for PCE, FF, and thin film thickness are observed with the PL intensity channels, while the PL_{peak} channel performs best for J_{SC} prediction and V_{OC} shows consistently low predictability across all channels.

and comparing their respective predictive performance.

Comparing the prediction results obtained with different input signals reveals substantial differences in the predictive performance between individual signals, suggesting that some channels are more informative than others when predicting different target variables (see Figure 5.15). Compared to predictions of the kNNs using any IPDRI channel as input, the baseline model consistently performs the worst, indicating that the use of these spectral *in situ* transients provides valuable information for solar cell performance predictions. Consistent with previous results, investigating the input-dependent test set prediction results, after parameter `k` optimization for each input-target-combination using cross-validation, confirms that thin film thickness is more predictable than other solar cell parameters, with consistently higher R^2 values. On the other hand, V_{OC} remains difficult to predict, regardless of the signals used.

Among the acquired signals, the three PL intensity channels, namely $PL_{LP\,725nm}$, $PL_{LP\,780nm}$, and $PL_{SP\,775nm}$ stand out as the generally best-performing individual predictors for both PCE and thin film thickness, achieving the lowest MAE and the highest R^2 scores. However, while for thin film thickness prediction, all three PL intensity channels ($PL_{LP\,725nm}$, $PL_{LP\,780nm}$, and $PL_{SP\,775nm}$ provide superior predictive performance with minimal variance compared to other signals, in the case of PCE, only the $PL_{LP\,725nm}$ and $PL_{LP\,780nm}$ signals yield the most accurate predictions with $PL_{SP\,775nm}$ performing noticeably worse. Regarding MAE and R^2, the kNNs trained on either R_{diff} or PL_{peak} show poorer performance in predicting PCE as well as thin film thickness compared to the results obtained by the models trained on the three PL intensity channels, indicating a lack of useful information for predicting these target variables (see Figure 5.15a and Figure 5.15b).

Predictions for J_{SC} also show variability in performance across different signals, but in contrast to PCE, FF, and thin film thickness, the PL_{peak} channel emerges as the best individual predictor for J_{SC} prediction, followed by the PL intensity channel $PL_{SP\,775nm}$. These results underscore the importance of using the IPDRI setup for multi-channel imaging, which allows the use of specific signals tailored to each target variable instead of relying on a single signal overall. However, for predicting V_{OC}, all models trained on the different channels perform poorly, suggesting that this parameter may be inherently difficult to predict based on these spectral measurements.

Interestingly, for all target variables, combining all acquired IPDRI channels as model input does not improve

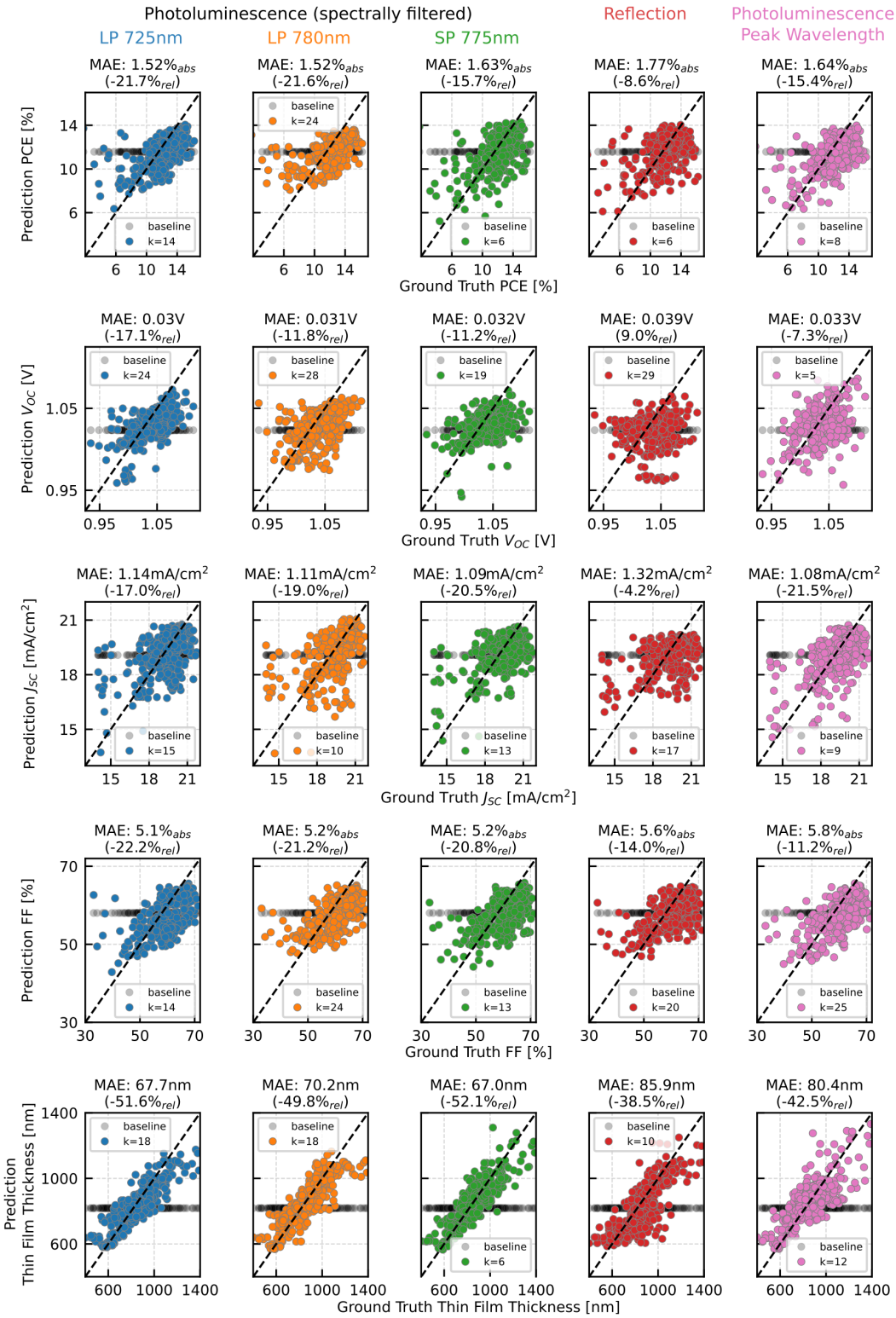

Figure 5.16: Parity plots of k-nearest neighbors (kNN) predictions using different *in situ* channels as input compare the predictions with ground truth values for power conversion efficiency (PCE), open-circuit voltage (V_{OC}), short-circuit current density (J_{SC}), fill factor (FF), and thin film thickness. Especially for thin film thickness and PCE, the kNN models show good agreement. For PCE, V_{OC}, J_{SC}, and FF, the models tend to overestimate values for low ground truth samples, reflecting the limitations of using only data from one process step to predict final device performance. (MAE: mean absolute error)

model performance and even decreases prediction accuracy. This suggests that certain signals introduce noise or redundant information that negatively affect the models' ability to generalize. While combining multiple channels can generally improve robustness, it is not beneficial to prediction accuracy, as evidenced by the drop in model performance when all signals are used to for predict PCE, thin film thickness, or any other target variable.
This analysis highlights the complexity of predicting solar cell parameters by revealing the significant variation in model performance between individual input signals. It suggests that some signals are more informative than others for a given prediction task, and therefore different channels are optimal for predicting different solar cell parameters. In general, it underscores the importance of acquiring *in situ* PL data compared to monitoring only diffuse reflection as the PL intensity channels ($\mathrm{PL}_{LP\,725nm}$, $\mathrm{PL}_{LP\,780nm}$, and $\mathrm{PL}_{SP\,775nm}$) provide the best overall predictive performance.
To evaluate the kNN predictions using different signals as input in more detail, all predictions are visually compared to the experimentally measured data to validate the performance of the models (see Figure 5.16). All kNN models outperform the baseline predictions, which fail to accurately predict all target variables, highlighting the poor predictive ability of human researchers. The kNN models show much better agreement between the predicted and actual values, particularly for the perovskite thin film thickness. Confirming the best prediction performance for the perovskite thin film thickness, the parity plots show clear correlations between predicted and ground truth values for thin film thickness, PCE, and FF, while the prediction accuracy is worse when predicting V_{OC} and J_{SC}.
As for the kNN predictions based on the $\mathrm{PL}_{LP\,725nm}$ channel, the parity plots show that for all photovoltaic performance parameters (PCE, V_{OC}, J_{SC}, and FF), the models tend to overestimate values for samples with low ground truth measurements. As discussed earlier, this is likely due to the fact that the models are trained only on perovskite thin-film formation data, while the final solar cell performance is influenced by other processing steps not captured in the input data. The overestimation is attributed to the models being trained solely on perovskite thin-film formation data, whereas the final solar cell performance is influenced by additional processing steps not captured in the input data. In contrast, the parity plots for thin film thickness show no such overestimation. Since thin film thickness is determined exclusively during the thin-film formation step, which is fully represented in the *in situ* data, the kNN models predict it more accurately and consistently. As the target variable directly linked to the process step represented in the training data is predicted more accurately, it underscores the importance of considering all process steps when predicting solar cell performance and highlights the limitations of models trained on partial process data.
To benchmark the prediction results obtained with kNN regressors, the predictive performance is compared with other classical supervised machine learning techniques. Since the PL intensity channel $\mathrm{PL}_{LP\,725nm}$ has been shown to be one of the generally best-performing individual predictors (see Figure 5.17) and its signal covers the entire PL spectrum of the investigated DCP material (bandgap of 1.59 eV), the $\mathrm{PL}_{LP\,725nm}$ transients are used as input to the models of several, mostly tree- and neighbor-based, supervised machine learning methods (see section 2.3.1.1 for more details). As with the previous optimization of the parameter `k` for kNN predictions, one essential hyperparameter is identified and optimized for each regression model during fivefold cross-validation on the training set (number of neighbors `k` for kNN, ensemble members `n_estimators` for random forest, regularization parameter `C` for support vector machine, maximum depth of the tree `max_depth` for decision tree, number of estimators `n_estimators` for gradient boosting, maximum number of iterations `max_iter` for histogram-based gradient boosting, number of estimators `n_estimators` for AdaBoost, and regularization strength `alpha` for ElasticNet).
Comparing the test set performance of different regression models using $\mathrm{PL}_{LP\,725nm}$ as input reveals substantial variation in the prediction accuracy for PCE and thin film thickness. Again, the baseline model consistently shows the worst performance, highlighting the general value of using machine learning models over the human prediction baseline. For PCE prediction, the support vector machine achieves the lowest MAE and the highest R^2 score, making it the best-performing model for this target variable, followed by kNN, gradient boosting, and random forest. In contrast, decision tree and AdaBoost show relatively poor performance for PCE prediction, with higher MAE values and lower R^2 scores. In the case of thin film thickness, all models perform well with consistently high R^2 scores and low MAE values, indicating that thin film thickness is more predictable compared to PCE. Among

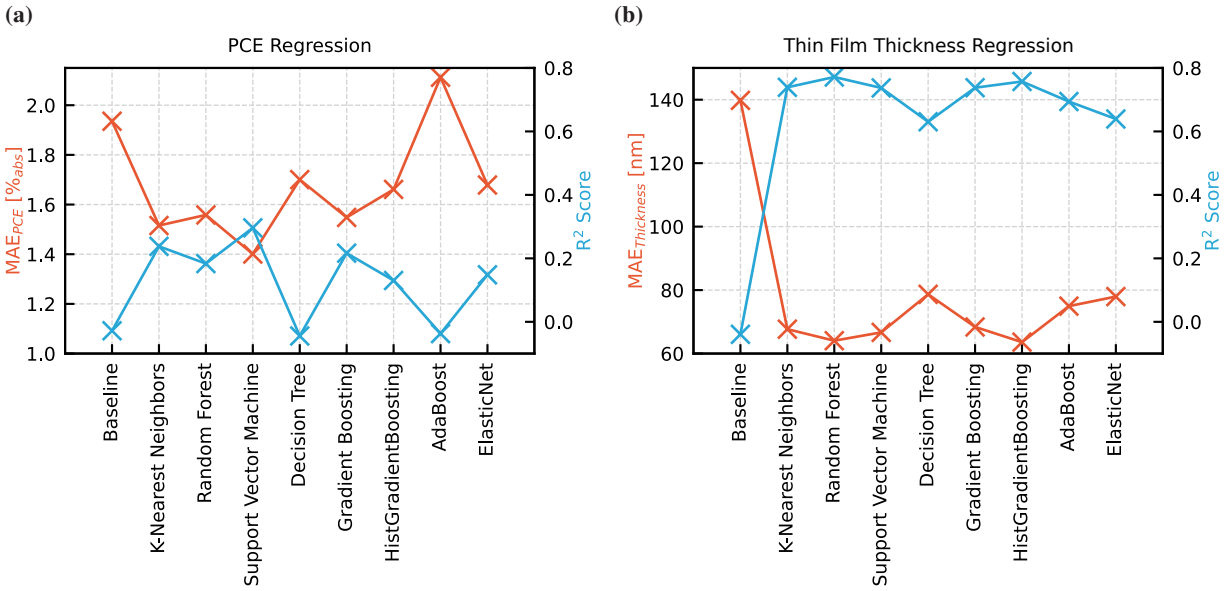

Figure 5.17: Comparison of prediction performance on the held-out test set for different supervised machine learning models using photoluminescence transients ($PL_{LP\,725nm}$) as input for predicting (a) power conversion efficiency (PCE) and (b) perovskite thin film thickness. Mean absolute error (MAE) and R^2 score are used as performance metrics. The support vector machine achieves the best performance for PCE prediction, followed by k-nearest neighbors, gradient boosting, and random forest. For thin film thickness prediction, random forest and histogram-based gradient boosting outperform the other models.

the models, random forest and histogram-based gradient boosting regression have the best predictive performance for thin film thickness, while decision tree, ElasticNet, and AdaBoost have slightly higher MAE values and lower R^2 scores. Overall, the tree-based models random forest and (histogram-based) gradient boosting, as well as support vector machine and kNN, generally outperform the other models. Support vector machine is particularly effective for PCE regression, although it is slightly outperformed by some tree-based models for predicting thin film thickness. Random forest, gradient boosting, and kNN show good performance for both target variables, while histogram-based gradient boosting performs particularly well for the thin film thickness regression task. Decision tree, ElasticNet, and AdaBoost achieve the lowest prediction accuracies for both target variables.

In summary, this section evaluates the predictive capabilities of different IPDRI channels and compares various classical supervised machine learning algorithms for predicting solar cell performance metrics and perovskite thin film thickness. The PL intensity channels emerge as the most informative inputs, providing the best accuracy for PCE and thin film thickness predictions, while V_{OC} remains difficult to predict regardless of the input signal. Notably, combining all IPDRI channels does not improve prediction accuracy and may introduce noise or redundancy. Benchmarking of different algorithms shows that support vector machines achieve the best performance for PCE prediction, while random forest and histogram-based gradient boosting predict thin film thickness best. Overall, random forest, (histogram-based) gradient boosting, support vector machine, and kNN outperform others, highlighting the importance of selecting appropriate ML models and input data tailored to specific prediction tasks. These results confirm the potential of using other supervised machine learning methods to improve prediction accuracy in perovskite photovoltaic fabrication further. By leveraging the informative *in situ* data and suitable machine learning models, ML-based process monitoring of the perovskite thin-film formation increases yield and reduces material waste by facilitating process optimization and real-time control.

5.7 Summary

This chapter explores the application of unsupervised and supervised machine learning techniques to *in situ* photoluminescence imaging data to enhance the analysis of the perovskite thin-film formation process. For such data-driven analysis of the complex thin-film formation from solution during vacuum quenching, a laboratory-scale experimental dataset of *in situ* PL and reflection data is generated using the IPDRI setup (research objective **II**, see section 1.2). The dataset is used to predict material and device properties, including perovskite thin film thickness and solar cell performance, based on PL and diffuse reflection measurements before subsequent processing steps are completed (research objective **III**).

First, a unique experimental dataset is introduced, comprising *in situ* PL data acquired during the vacuum quenching of 1129 blade-coated perovskite solar cells. All solar cells were fabricated under constant experimental conditions, ensuring that performance variations are solely due to unintended fluctuations in the fabrication process. The dataset was published as open source and serves as a valuable resource for applying machine learning techniques to investigate various research questions related to the complex perovskite thin-film formation process.

Second, to motivate the additional effort required for *in situ* measurements, the advantages of *in situ* monitoring over *ex situ* measurements alone are demonstrated. By showing a stronger correlation between solar cell performance and features extracted from *in situ* PL data compared to *ex situ* data, the importance of capturing data during the thin-film formation process is highlighted to enable more accurate predictions.

Third, unsupervised machine learning, specifically k-means clustering, is applied to the *in situ* PL transients without relying on human-selected features as they provide qualitative intuition but also highlight the limitations of manual feature selection, which oversimplifies the complex data. Clustering reveals distinct data patterns that correlate with the performance of fully fabricated devices. Clusters that differ in PL onset time and PL maximum magnitude are identified, with earlier PL onset and higher PL maxima associated with better-performing solar cells. In addition, incorporating the spatial distribution of the clusters reveals heterogeneous thin-film quality across the substrate due to process-related solution backflow during blade coating, resulting in thickness variations and inhomogeneities.

Next, transitioning from descriptive to predictive analysis, supervised machine learning is used to predict solar cell performance prior to device completion. K-nearest neighbors regression models are trained on *in situ* PL data to predict perovskite thin film thickness and photovoltaic performance metrics. The kNN models achieve a substantial reduction in prediction error compared to a baseline model representing human predictive capabilities, particularly in predicting thin film thickness. While the models effectively capture relationships between *in situ* PL transients and perovskite thin-film quality, limitations are noted in accurately predicting photovoltaic parameters due to the influence of other processing steps not captured in the input data.

Finally, the predictive performance of the different IPDRI channels used as model input are compared and the differences in prediction error obtained from various classical supervised machine learning algorithms are evaluated. Compared to diffuse reflection and PL peak wavelength, the PL intensity channels emerge as the most informative inputs, providing the best accuracy for predicting PCE and thin film thickness. Benchmarking of different supervised machine learning methods shows that support vector machines achieve the best performance for PCE prediction, and random forest and histogram-based gradient boosting models perform best for thin film thickness prediction, highlighting the impact of model choice and its input.

In conclusion, combining the monitoring capabilities of IPDRI with the analytical power of machine learning enhances process monitoring of the perovskite thin-film formation from solution. While ML models uncover hidden patterns in *in situ* data and enable predictions of solar cell performance at early fabrication stages, these predictions are inherently constrained by factors not captured in the input data, such as post-deposition processing steps. By detecting unintended fabrication defects early, ML-based process monitoring can still be used for in-line feedback in industrial production lines to improve yield and reduce waste. Although the final device performance remains influenced by subsequent processing steps, integrating ML with *in situ* monitoring represents a critical step in optimizing the production process and accelerating the commercialization of perovskite solar cell technology.

6 Deep Learning for Enhanced Monitoring of the Perovskite Thin-Film Formation

*This chapter demonstrates how deep learning enhances the analysis of perovskite thin-film formation by addressing critical challenges in transferring perovskite photovoltaics from laboratory to industrial scale. Building on the first dataset, a more diverse and extensive experimental dataset of in situ photoluminescence and diffuse reflection data is generated, containing 4448 thin films with varying material compositions and 2215 solar cells fabricated with systematically varied vacuum quenching times (research objective **II**). Neural networks are used for in situ material composition monitoring, detecting subtle variations in the perovskite precursor solution. Beyond ensuring material consistency during fabrication, DL models enable early in-line assessment of thin-film quality by predicting solar cell performance before complete device fabrication (research objective **III**). For both use cases, the DL models substantially exceed human baseline capabilities and outperform most classical machine learning models, showing superior scalability as the dataset size increases. Advancing from predictive to prescriptive analysis, a cascade of ML models is developed to provide in situ AI recommendations for process control by forecasting different quenching scenarios and their impact on device performance (research objective **IV**). Application of the methodology to large-area substrates demonstrates spatially resolved feedback for optimizing thin-film quality across multiple solar cells. The ability to transform complex experimental data into actionable recommendations underscores the essential role of DL in improving reproducibility, scalability, and quality control. The data-driven approach is particularly beneficial in high-throughput production, where large-scale data collection enables superior DL model performance.*

Parts of this chapter were published in the research article "Deep learning for augmented process monitoring of scalable perovskite thin-film fabrication", *Energy & Environmental Science* (2025), by *Felix Laufer (F.L.)*, *Markus Götz*, and *Ulrich W. Paetzold*. This work is the result of collaborative research between Karlsruhe Institute of Technology and Helmholtz AI.[352] The dataset and the corresponding software code were made publicly available.[428, 429] Some figures in this chapter were adapted with permission from [352].
F.L. contributed to this project by co-conceptualizing the study, leading methodology development, experimental investigation, data generation and curation, software implementation, formal analysis, and visualization, as well as writing the original draft of the manuscript. The contributions of all authors according to the CRediT system are listed in Table A.4.

6.1 Motivation

To advance the commercialization of perovskite PV technology, it is essential to improve long-term stability and reliability as well as scale up high-throughput fabrication to larger, industry-relevant areas. Recently, the perovskite research community has shown a rapidly growing interest in the application of artificial intelligence, particularly machine learning, as a powerful tool to address these challenges.[153–158, 163–167] ML applications in perovskite solar cell research can be broadly classified into three main areas[155]: (a) accelerated theoretical screening of new materials, (b) automated high-throughput experimentation and characterization, and (c) improved utilization and evaluation of experimental data.

One promising application of ML is to enhance perovskite thin-film characterization tools to extract additional insight from readily available data. For example, such ML-enhanced characterization tools have been used to forecast experimental data such as environment-dependent transmittance[217] and photoluminescence[235, 236] to perform accelerated stability testing. In addition, machine vision techniques have been explored to identify substrate coverage using white light photography.[232] Beyond research environments, ML techniques are increasingly needed to address the challenges of reliability, batch-to-batch reproducibility, and high fabrication yield, which are critical for scaling up production to industrial scale.[239] Ensuring consistent performance across different devices and batches, maintaining a stable baseline process, and quantitatively evaluating process fluctuations require the development of ML-enhanced *in situ* metrology and characterization methods.[156]

ML tools are also seen as essential for narrowing the performance gap between state-of-the-art, small-scale, spin-coated devices and large-area devices fabricated using scalable deposition methods.[156] The formation of perovskite thin films from solution is complex,[23, 27, 28] and the probability of defects increases with larger areas, often leading to shunting of entire cells due to a single defect.[341, 343, 355] The integration of ML with spatially resolved imaging methods can help address challenges that arise when scaling to larger areas, such as identifying spatial inhomogeneities and detecting temporal fluctuations. This integration enables the prediction of how observed changes and inconsistencies in monitoring data will affect the quality of perovskite thin films and the overall performance of PSCs. Critically, ML enables predictions that are potentially impossible through human analysis alone. For example, electrical conductance was predicted from dark-field microscopy images using ML, despite no recognizable patterns in the images that could be interpreted by humans.[163] Also, the use of ML is not limited to passive monitoring and prediction tasks, but ML-enhanced metrology can be extended to make active decisions about process control. Despite these advances, the integration of ML into experimental research laboratories has been gradual and has yet to be fully adopted by experimentalists who could benefit from these tools, particularly in enhanced data analysis of experimental results (see section 2.4 for more details on the state of the art of ML for perovskite PV).

To detect thin film defects on large areas early in the fabrication process, previous chapters introduced the *in situ* photoluminescence and diffuse reflection imaging system, which allows monitoring of the perovskite thin-film formation with spatial, temporal, and spectral resolution (see chapter 4). Building on this progress, data-driven analysis using ML has shown great potential for exploring the complex data generated by IPDRI (see chapter 5), since human analytical capabilities are inherently limited. Classical ML techniques, namely unsupervised k-means clustering and supervised k-nearest neighbors, can be applied to investigate the relationship between *in situ* data and device performance under controlled, constant experimental conditions. While this approach has provided valuable insights into the correlation between perovskite thin-film properties and device performance, its applicability is limited when faced with varying process conditions, a scenario often encountered in real-world research and industrial settings. Building on the previous results, this chapter extends the research setup in several substantial ways: (1) introduction of a more extensive dataset, (2) use of more sophisticated ML methods, and (3) transition from descriptive and predictive to prescriptive analysis.

To increase the capabilities of ML-enhanced imaging techniques, an appropriate experimental dataset generated from experiments with systematically varied process conditions is essential. Using the monitoring capabilities of IPDRI, a new dataset was generated containing IPDRI data acquired *in situ* during the industry-relevant vacuum

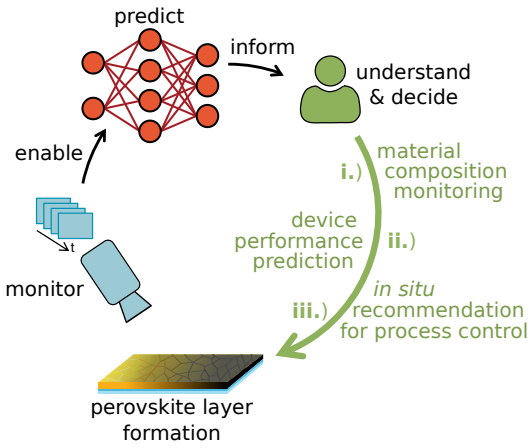

Figure 6.1: Schematic representation of the integration of AI-driven monitoring and prediction into the perovskite thin-film formation process. Using the *in situ* monitoring data acquired during the perovskite thin-film formation as model input, a neural network performs various tasks to inform the human researcher. To demonstrate the versatility of the characterization setup enhanced with machine learning, three increasingly complex use cases are addressed, which are difficult to solve with standard data analysis: (i) material composition monitoring, (ii) device performance prediction, and (iii) *in situ* recommendations for process control. Adapted with permission from [352].

quenching process[430–432] of 2215 blade-coated perovskite thin-film solar cells (research objective **II**).[428] This dataset is labeled with corresponding photovoltaic performance parameters, such as PCE. In contrast to the first dataset where all solar cells were fabricated under constant experimental conditions, maintaining the same layer stack and materials, this second dataset includes solar cells with perovskite thin films fabricated with a range of different vacuum quenching times, ranging from 20 s to 600 s. In addition to the IPDRI data corresponding to performance metrics of fully fabricated solar cells, the dataset also includes *in situ* data acquired from 4448 solar cell active areas with different perovskite material compositions, namely precursor molarity and molar ratio. Using the newly introduced dataset, this chapter demonstrates the transformative potential of enhancing *in situ* metrology with ML-driven data analysis by converting photoluminescence and diffuse reflection imaging data into early predictions of material composition and device performance. Investigation of this *in situ* data allows early qualitative assessment of the complex, large-area thin-film formation process where traditional human analysis is limited by the complexity and high dimensionality of the data.

In addition to examining a novel, more comprehensive dataset, potential limitations caused by ML model selection are addressed by introducing advanced deep learning techniques, in particular neural networks, to model complex, non-linear relationships within the data. The incorporation of DL methods potentially enables more accurate predictions and insights compared to classical ML approaches. Despite its potential to transform data into meaningful predictions of critical target parameters, DL has not yet been widely used to analyze complex experimental data in PSC research laboratories. To fully harness the power of machine learning, this study leverages DL, a sophisticated ML subcategory, by training artificial deep neural networks to learn complex, non-linear correlations within large datasets.

This chapter demonstrates the impact of DL-enhanced metrology by addressing three increasingly complex use cases that are difficult to solve with human analysis alone (see Figure 6.1). These use cases encompass key challenges in perovskite research, ranging from process reliability and batch-to-batch reproducibility to process optimization and control. Detecting small unwanted changes in material composition, quantitatively predicting PSC performance, or forecasting experimental scenarios and their corresponding PCE is nearly impossible for a human researcher. However, DL-enhanced characterization methods enable tackling these challenges in experimental data analysis. Artificial deep neural networks are trained on the novel, unique experimental dataset to learn the underlying mappings between *in situ* monitoring data and target variables. The first use case focuses on (i) material composition monitoring by classifying material target variables, namely precursor concentration and precursor

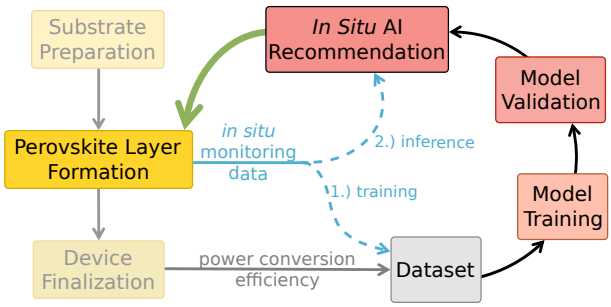

Figure 6.2: Sequential workflow for the generation of the experimental *in situ* dataset. After acquiring the *in situ* monitoring data during vacuum quenching of the perovskite, the thin films are completed into functional solar cells, and performance metrics such as power conversion efficiency (PCE) are measured. The dataset linking the acquired monitoring data and PCE is then used for model training and validation before the model can be used for testing and inference. Adapted with permission from [352].

ratio. Successful learning of these correlations demonstrates that DL-enhanced *in situ* imaging methods can detect precursor inconsistencies at the material level and discriminate between small variations, thereby ensuring the consistency of materials used in PSC fabrication. The second use case extends the predictive capabilities from the material level to the device level by enabling (ii) device performance prediction. The ability to predict holistic device performance before the completion of all fabrication process steps facilitates early assessments of thin-film quality and device performance, thereby enhancing the decision-making process during production. For both use cases, (i) material composition monitoring and (ii) device performance prediction, the prediction performance of deep neural networks is benchmarked against various classical ML methods, and the impact of training set size on model performance is systematically evaluated. The final use case advances the methodology from predictive to prescriptive analysis by combining *in situ* forecasting of monitoring data with performance prediction to provide (iii) actionable *in situ* recommendations for process control. This approach makes it possible to forecast various experimental scenarios and to predict the corresponding solar cell performance for each scenario, providing scientists with data-driven insights to guide experimental procedures in the laboratory. This prescriptive analysis enables the transition from passive predictive analysis to active data-driven process control, further improving PSC fabrication. In summary, by addressing these use cases, this chapter explores the potential of DL-enhanced metrology in PSC research, moving beyond descriptive and predictive analysis to prescriptive analysis for active process optimization. This approach provides a foundation for integrating DL methods into experimental research, ultimately paving the way for more efficient characterization methods that enable intelligent process control in PSC research and large-scale production.

6.2 *In Situ* Photoluminescence Dataset for Exploring Material and Processing Variabilities in Blade-Coated Perovskite Photovoltaics

To further advance the study of the perovskite thin-film formation process and to extend the capabilities of ML-enhanced characterization, a new dataset with systematically varied process parameters is introduced. While the first dataset focuses on a constant set of fabrication conditions[422], this second dataset is designed to capture the effect of different process variables, specifically precursor compositions and vacuum quenching times.[428] These variations enable a more comprehensive analysis of the fabrication process and a deeper insight into how different conditions affect the resulting thin-film quality and PV performance.

Like the first dataset, the second dataset contains *in situ* PL and diffuse reflection imaging data acquired during vacuum quenching of blade-coated perovskite solar cells (see Figure 6.2). To address industrial manufacturing requirements for scalability and ability to produce large-area thin films, blade coating was used to deposit the

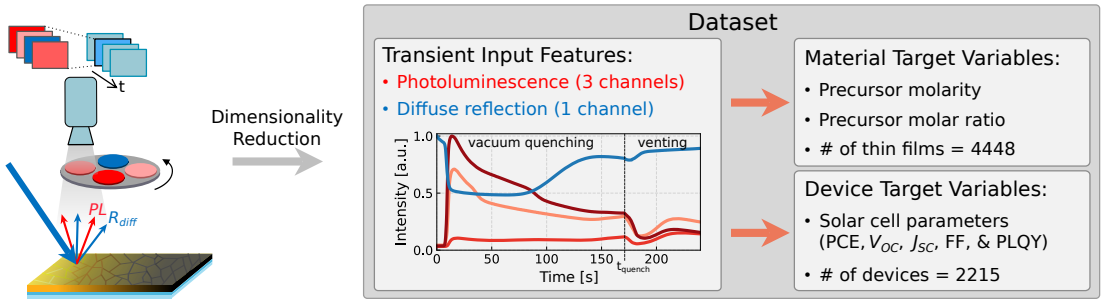

Figure 6.3: Description of the second generated dataset consisting of *in situ* monitoring data and material and device target variables. The setup captures multi-channel imaging data, including photoluminescence (PL) and diffuse reflection (R_{diff}), during the perovskite formation process. Dimensionality reduction is performed by feature aggregation, which calculates the spatial mean value at each time step, resulting in four transients that are used as input features. The dataset contains 4448 thin films with different perovskite material compositions, namely precursor molarity and molar ratio, and 2215 functional solar cells fabricated under systematically varied vacuum quenching times. The transient input features are used as input to neural networks to predict the target variables. Adapted with permission from [352].

perovskite precursor solution (see section 3.1.1.1 for more details on blade coating) and vacuum quenching was used to initiate the drying and crystallization of the blade-coated wet films (see section 3.1.1.2 for more details on vacuum quenching).

The *in situ* data was acquired using the IPDRI setup during the vacuum quenching process (see Figure 6.3). The camera captures images of the entire $32 \times 64\,\mathrm{mm}^2$ substrate with a temporal resolution of 333 ms, resulting in time series of images (i.e., videos) that provide spatially resolved PL intensities across three channels and one channel showing R_{diff}. Thus, the dataset captures the dynamic evolution of the perovskite thin films during the formation process. In a data preprocessing step, the large-area images were cropped into smaller patches corresponding to the active areas of individual solar cells, similar to the approach used in the first dataset (see section 5.2 and Figure 2.8a for substrate layout). The input data was temporally aligned at the beginning of the vacuum chamber evacuation, and due to the different quenching times resulting in image time series of different lengths, the input features had to be preprocessed by padding zeros to the end so that they all had the same length.

After deposition of the perovskite thin film, 2215 thin films were built to completion into fully fabricated, functional solar cells using the same layer stack as in the first dataset (glass, ITO, NiO_x, 2PACz, double cation perovskite layer, C_{60}, BCP, Ag; see section 3.1.3 for more details). The performance of all solar cells was determined by

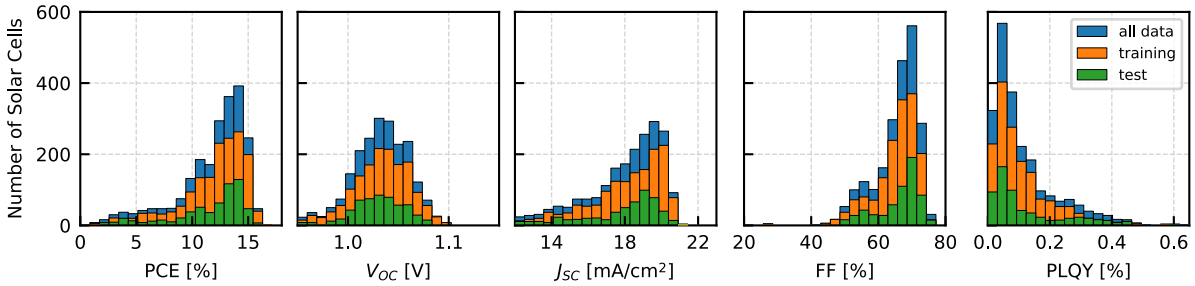

Figure 6.4: Distribution of solar cell performance metrics used as device target variables for the full dataset, training set, and test set. The full dataset of 2215 solar cells is divided into training and test sets (72.5%/27.5%), containing 1606 and 609 samples, respectively. The 2215 solar cells were fabricated under systematically varied vacuum quenching times, with the reference cells incorporating perovskite thin films quenched for 180 s (see Figure 6.5b for the device quenching time distribution). Model training and hyperparameter optimization are performed on the training set, while unbiased model evaluation is performed on previously unseen data in the test set. For all target variables, the distributions of the training and test sets show good agreement, ensuring representative sampling for training and testing.

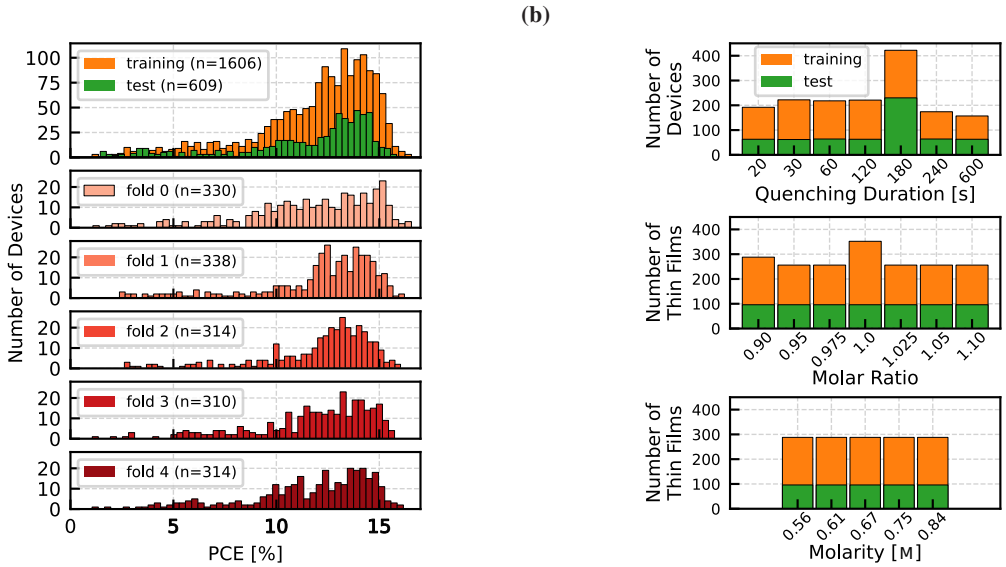

Figure 6.5: Dataset distribution and fivefold cross-validation setup for predicting power conversion efficiency (PCE) and classifying precursor properties. (a) Histograms of PCE values show the distribution across the training (n = 1606) and test (n = 609) sets, with the training data further divided into five folds for cross-validation. The stratification based on substrate level ensures a consistent and representative evaluation of the models. (b) Histograms illustrating the distribution of training and test samples for the different process parameters quenching time, precursor molar ratio, and precursor molarity. The dataset includes 2215 fully fabricated solar cell devices with quenching times distributed as follows: 192, 222, 218, 221, 422, 174, and 157 samples in the training set, and corresponding samples in the test set: 63, 62, 64, 63, 230, 64, and 63. The molar ratio subset consists of 288, 256, 256, 352, 256, 256, and 256 training samples for each class, with 96 test samples per class. The molarity subset contains 288 training samples and 96 test samples per class. 46 samples overlap between the molar ratio and molarity subsets, resulting in 4448 unique thin films. Adapted with permission from [352].

measuring the current-density-voltage curves, and key PV parameters such as PCE, V_{OC}), J_{SC}, and FF were added to the dataset as target variables (see Figure 6.4). When evaluating models trained on either of the two datasets, it is crucial to remember that the solar cell device target variables are influenced by all fabrication steps, while the IPDRI data only captures information related to the perovskite formation process and lacks insight into other fabrication steps. As a result, any irregularities that occur in other process steps that negatively impact PV performance are not reflected in the model input data. The dataset and the corresponding software code are publicly available to the research community.[428, 429]

To evaluate the predictive performance of ML models trained on the dataset, the data was split into a training set and a test set (75%/25%) (see Figure 6.5a). The data was split at the substrate level, ensuring that all samples originating from the same substrate were always assigned to either the training or test set. This method enables evaluations on the test set to be regarded as predictions on newly generated experimental samples. For model training and hyperparameter optimization, fivefold cross-validation was applied on the training set, with samples from the same substrate assigned to the same fold (see section 2.3.5 for more details).

In general, both datasets share the common goal of improving process understanding and performance prediction of perovskite thin-film solar cells using *in situ* data. They both use the scalable blade coating technique and vacuum quenching process for thin-film deposition, making them suitable for large-area fabrication. In addition, both datasets were acquired using the IPDRI setup, which captures time-resolved images of PL and R_{diff}, providing a detailed temporal and spatial characterization of the perovskite thin-film formation. Moreover, in both cases, the solar cells were fabricated using the same layer stack and precursor materials, with PV performance metrics as target variables for predictions by ML models. Despite these similarities, the second dataset introduces systematic variations in vacuum quenching times and precursor compositions (see Figure 6.5b). By including systematic variations in critical

process parameters, the dataset captures a broader range of process-related differences, allowing ML models to learn more complex relationships between *in situ* data and final thin-film quality and solar cell performance. In contrast, the first dataset was generated under constant experimental conditions, allowing the investigation of the impact of unwanted variations on material properties and device performance. Furthermore, the second dataset is larger in size, containing *in situ* data corresponding to 2215 solar cells and data corresponding to 4448 thin films (same dimensions and locations as the active areas of the solar cells) fabricated with different precursor compositions, compared to 1129 solar cells in the first dataset (see Figure A.10). These differences make the second dataset more complex and comprehensive, allowing a broader exploration of the relationship between *in situ* data, process parameters, thin-film quality, and solar cell performance.

In this chapter, domain knowledge of the importance of the temporal aspect in thin-film formation is leveraged, emphasizing the temporal progression of the experiment. As a result, the IPDRI image frames corresponding to the active areas of the solar cells are aggregated by calculating the spatial mean value at each time step. Consequently, the input feature for each solar cell consists of transients capturing the temporal evolution of the spatial mean intensity over four channels ($PL_{LP\,725nm}$, $PL_{LP\,780nm}$, $PL_{SP\,775nm}$, and R_{diff}). By applying this dimensionality reduction, the problem's complexity is reduced, making it easier to analyze subtle differences in the material formation process across various iterations and processing conditions, as reflected by changes in the temporal evolution of the IPDRI data (see section 2.3.8 for more details on dimensionality reduction).

In summary, this second dataset provides a richer and more diverse set of experimental data, potentially allowing for an improvement in the capabilities of ML-enhanced imaging techniques. By including systematic variations in vacuum quenching times and precursor compositions, the dataset allows ML models to learn from a wider range of conditions, facilitating the application of ML techniques to monitor the fabrication process, detect material or process variations, enable in-line performance prediction, and improve process control.

6.3 Detecting Material Composition Inconsistencies

Achieving precise stoichiometry, the ratio of elements in the crystal structure, during the fabrication of PSCs is essential to achieve reproducible results and ensure optimal device performance and stability.[433, 434] Small deviations from the target stoichiometric ratios can significantly affect the crystallization kinetics, phase stability, morphology, and defect density of the resulting films. These changes directly influence the electronic properties, PV performance, and long-term stability of PSCs.[350, 435–440] Especially when using scalable, non-rotating deposition techniques such as blade and slot-die coating, the properties of the precursor solution have a substantial impact on the final thin-film quality.[23, 441, 442] Consequently, due to the low tolerance against small compositional variations, precise control over the stoichiometry of the precursor solution is essential to ensure reproducibility and consistent device performance, key factors for advancing perovskite technology toward commercialization.[443]

This section addresses these challenges by implementing *in situ* material composition monitoring (use case (i)) by leveraging DL to detect subtle variations in precursor molarity and molar ratios during the fabrication process.[352] By distinguishing between small unintended deviations from the target precursor composition based on time-resolved PL and R_{diff} data, the approach enables early identification of process inconsistencies that might otherwise go unnoticed (see Figure 6.6). This allows for tighter control of material quality in PSC research and contributes to improved reproducibility and reliability of industrial PSC production through automated in-line material composition monitoring.

Reference thin films with the composition $Cs_{0.17}FA_{0.83}Pb(I_{0.91}Br_{0.09})_3$ were fabricated using a precursor solution with a molarity of 0.67 M and a molar ratio (Pb/A-cation ratio) of 1.0 (see section 3.1.3 for more details). To investigate the effect of variations in material composition on the *in situ* PL and R_{diff} data, the molar ratio was varied between 0.9 (lead deficiency) and 1.1 (lead excess) by changing the (CsI:FAI):($PbBr_2$:PbI_2) ratio in the precursor solution (see Figure 6.7). To obtain different molar ratios, base solutions corresponding to molar ratios of 0.9, 1.0, and 1.1 were prepared by weighing the corresponding amounts of precursors. Intermediate molar ratios were

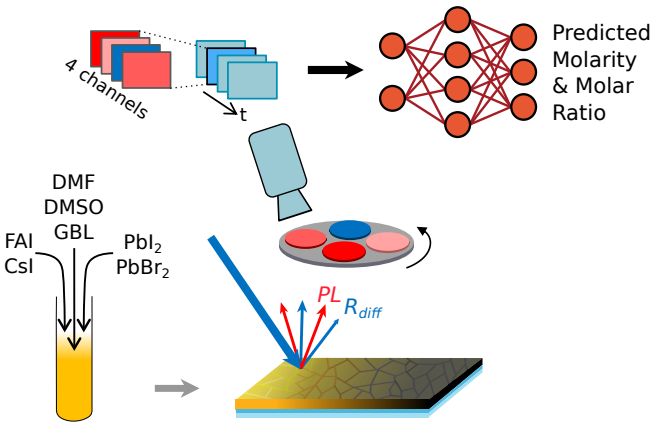

Figure 6.6: Schematic representation of material composition monitoring using the *in situ* characterization setup and deep learning. The setup captures multi-channel imaging data of the perovskite thin-film formation process, including photoluminescence (PL) and diffuse reflection (R_{diff}), which serve as input to the model. A neural network model then uses the acquired *in situ* data to predict variations in precursor molarity and molar ratio, enabling the detection of unwanted variations in material composition. Adapted with permission from [352].

obtained by mixing these base solutions in a 1:1 volume ratio. Similarly, the precursor molarity was varied between 0.56 M and 0.84 M by changing the amount of solvent added (see Figure 6.8). To vary the precursor molarity, starting from the standard molarity of 0.67 M, the total solvent volume, consisting of a mixture of ((DMF:DMSO 4:1 ($\%_{vol}$)):GBL 2:1 ($\%_{vol}$)), was decreased or increased by 10$\%_{vol}$ and 20$\%_{vol}$, respectively. Reducing the solvent volume increased the molarity to 0.75 M and 0.84 M, while increasing the solvent volume decreased the molarity to 0.61 M and 0.56 M.

To enhance time-resolved *in situ* PL and diffuse reflection process monitoring with DL, neural network classifiers are trained to differentiate between variations in the data caused by material composition inconsistencies (see Figure 6.7 and Figure 6.8). Feedforward neural networks with five fully connected hidden layers are used to classify input features based on precursor molarity or molar ratio (see Figure 6.6). Unlike recurrent neural networks, the feedforward architecture allows information to move in a single direction without feedback loops. For the given classification tasks, the models use five output neurons for molarity classification and seven output neurons for molar ratio classification, instead of a single neuron as in the regression case (see section 6.4). The models are trained using fivefold cross-validation on the training set. The average performance over the five folds is used to select hyperparameters for retraining the model on the entire training set (`cross-entropy loss`, `Adam optimizer`, `learning rate`: 10^{-4}, `weight decay`: 10^{-4}, `batch size`: 512). The ability of the models to distinguish subtle variations in these parameters is evaluated on the held-out test set by comparing the predicted target values, represented as discretized classes, with the actual ground truth labels using confusion matrices, along with metrics such as accuracy and top-2 score to quantify the prediction performance (see Figure 6.9a and Figure 6.9b).

The confusion matrices show that the models perform well in predicting both the molar ratio and the precursor molarity based solely on PL and R_{diff} data acquired during the thin-film formation.[352] Correctly classified samples are located along the diagonal, where the predicted values match the ground truth, while incorrectly classified samples appear as off-diagonal entries, representing instances where the model predictions deviate from the actual values. However, the model exhibits some misclassifications with noticeable confusion between closely related classes. More frequent misclassifications between neighboring classes suggest challenges in discriminating fine variations in experimental conditions (e.g., molar ratios of 0.975, 1.0, and 1.025; or molarities of 0.56 M and 0.61 M). However, inspection of the input data underscores the complexity of the task of distinguishing data from these neighboring classes (see Figure 6.7 and Figure 6.8).

In addition to the qualitative analysis of neural network predictions on the test set using confusion matrices, a quantitative evaluation is performed. Predictive performance is measured using two metrics, namely accuracy,

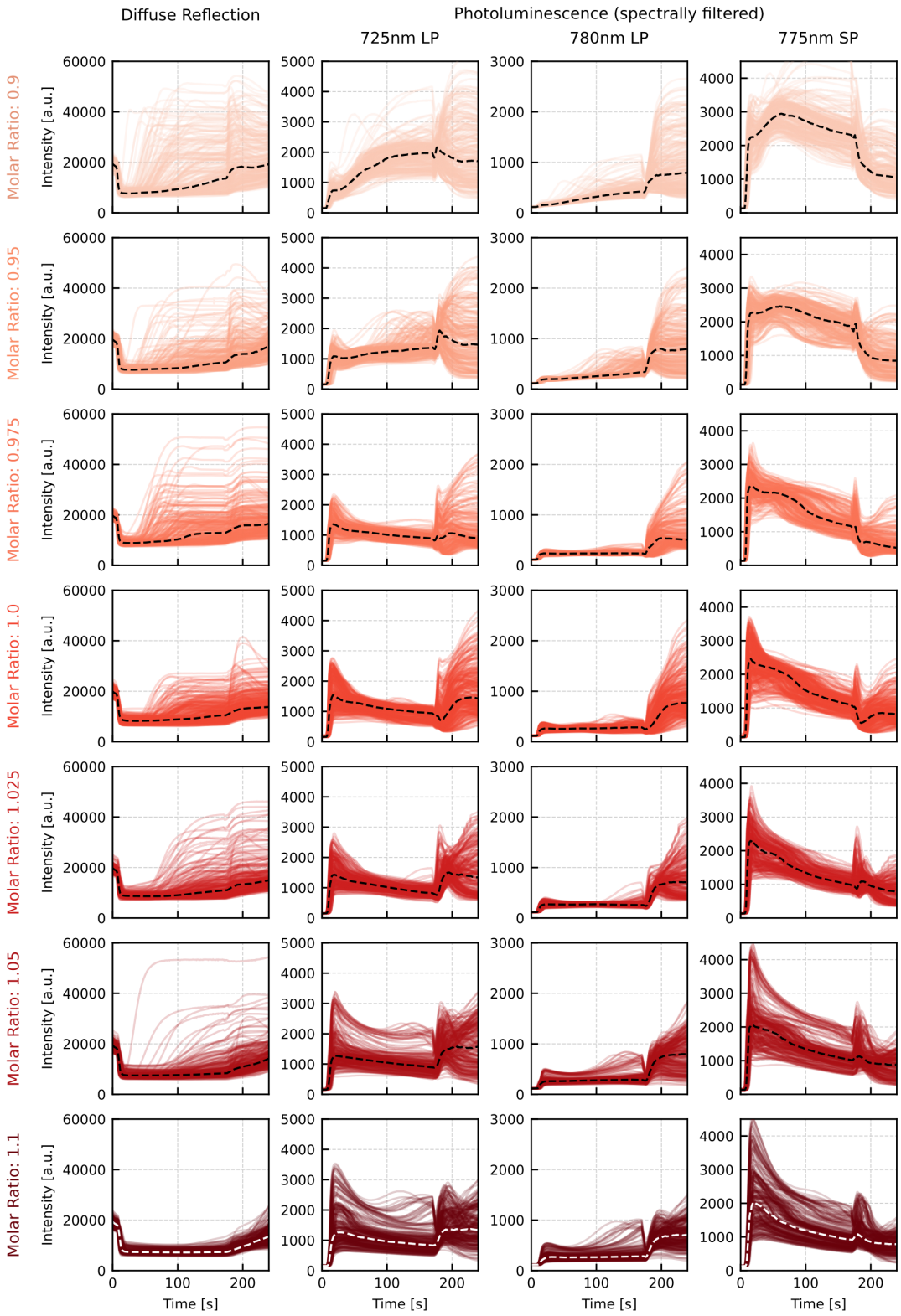

Figure 6.7: Transients of the monitoring data for different molar ratio classes (dashed line indicates the median). The transients, derived by spatially averaging the active area at each time step, illustrate the complexity of discriminating between different molar ratios. Distinguishing adjacent classes is difficult for human analysis, highlighting the need for machine learning methods to detect these subtle variations. Adapted with permission from [352]. (LP: longpass, SP: shortpass)

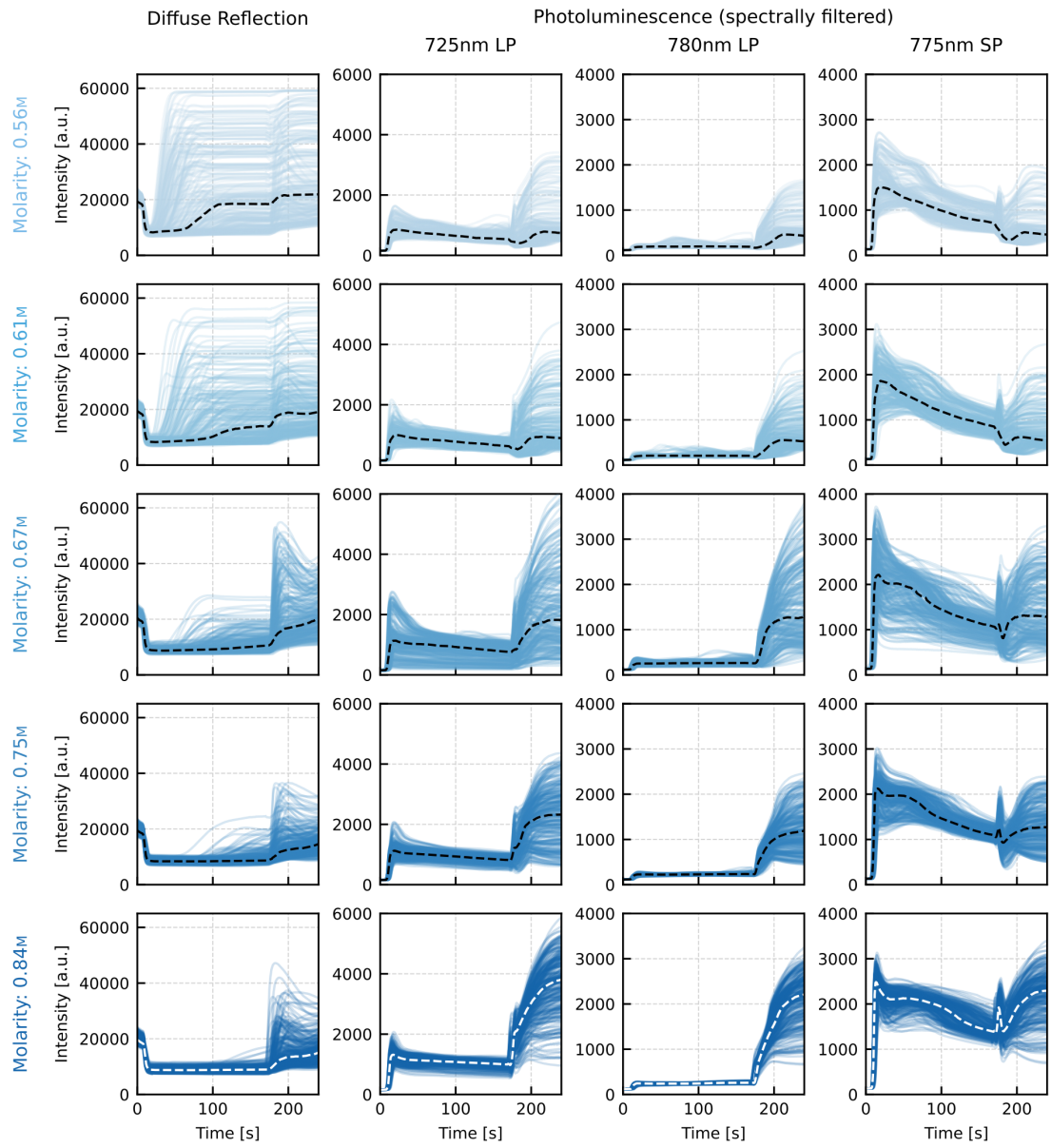

Figure 6.8: Transients of the monitoring data for different molarity classes. The sample transients (dashed line indicates the median), derived by spatially averaging the active area at each time step, illustrate the complexity of distinguishing different molarity classes. It is hardly possible for a human researcher to detect subtle changes in molarity during the experiment by visually inspecting the perovskite thin-film formation. Given the monitoring data, human analysis may be able to distinguish between large differences in molarity (e.g., 0.56 M vs. 0.84 M), but differentiating between neighboring classes (e.g., 0.56 M vs. 0.61 M) is difficult. While there are some noticeable differences in *in situ* transients, individual observations of different classes can be very similar and thus difficult to classify for both human and machine learning models). Adapted with permission from [352]. (LP: longpass, SP: shortpass)

which reflects the proportion of correctly predicted observations out of the total, and top-2 score, which counts a prediction as correct if the true class label is among the two classes with the highest predicted probabilities. For accuracy and top-2 score, higher values indicate better performance, with both metrics ranging from 0 to 1. The neural network models achieve accuracy scores of 0.61 for molar ratio classification of the test set samples and 0.83 for molarity classification. When considering the top-2 score, the performance increases to 0.86 for molar ratio classification and 0.96 for molarity classification on previously unseen test data.

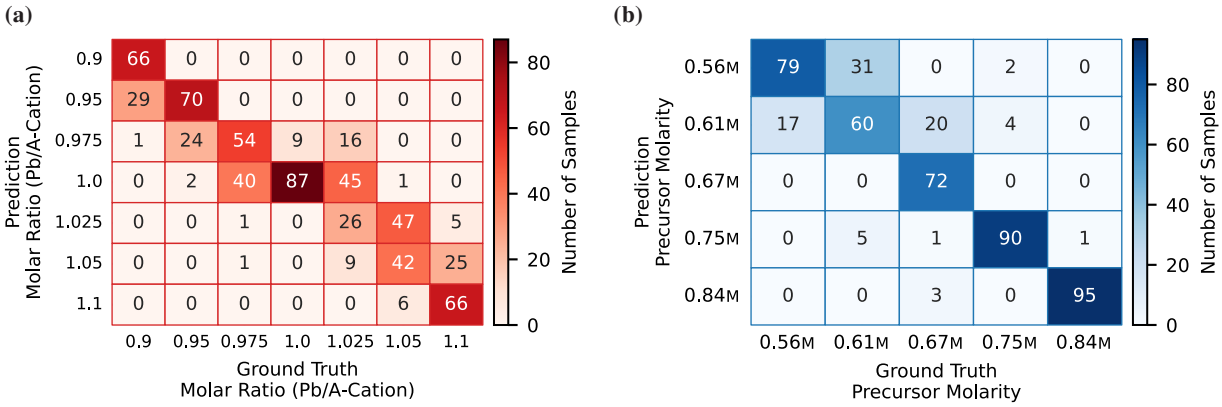

Figure 6.9: Confusion matrices for predicting molar ratio (a) and precursor molarity (b) using deep neural networks based on *in situ* monitoring data acquired during thin-film formation. Correct classifications are shown along the diagonal, indicating instances where predictions match the ground truth, while off-diagonal entries represent misclassifications. Although there is confusion between some neighboring classes (e.g., molar ratios of 0.975, 1.0, and 1.025, and molarities of 0.56 M and 0.61 M), the models perform well overall given the complexity of the task (see Figure 6.7 and Figure 6.8). Adapted with permission from [352].

To benchmark the DL results for molar ratio and molarity prediction, the predictive performance of neural networks is compared to classical ML classifiers such as random forest and k-nearest neighbors (see Figure 6.10). The comparison between DL models and the best-performing classical ML classifiers reveals that neural networks perform comparably well, with slight variations depending on the use case and evaluation metric, matching the performance of the best classical methods in most cases and outperforming several other classical models as well as the human baseline. Among the evaluated methods, the histogram-based gradient boosting classification tree achieves the highest overall performance, closely followed by the neural network, random forest models, and the ensemble of all classical ML methods. For molarity classification, the neural network shows high accuracy (0.83), just slightly behind the best-performing ML methods HGB (0.86) and RF (0.84). In addition, the neural network achieves a top-2 score of 0.96, closely rivaling the scores of HGB (0.98) and RF (0.99). In the more challenging task of molar ratio classification, the neural network outperforms random forests, achieving an accuracy of 0.61 and a top-2 score of 0.86, compared to RF's 0.53 accuracy and 0.80 top-2 score. While HGB performs slightly better in accuracy (0.64), its top-2 score of 0.82 is lower than that of the neural network. Compared to the limited hyperparameter optimization for neural networks, the classical ML classifiers are trained with fixed parameters (`strategy`='uniform' for baseline (=DummyClassifier), `solver`= 'liblinear' and `max_iter`=1000 for logistic regression, `n_estimators`=100 for random forest, none for Naive Bayes, `n_neighbors`=10 for k-nearest neighbors, `kernel`='rbf' and `probability`=True for support vector machine, `max_depth`=4 for decision tree, `n_estimators`=100 and `learning_rate`=1.0 and `max_depth`=1 for gradient boosting, `max_iter`=100 for histogram-based gradient boosting, `n_estimators`=100 for AdaBoost, `estimators`=[*all the classifiers mentioned above*] and `voting`='soft' for ensamble (=VotingClassifier)). However, even after hyperparameter optimization, the performance improvements remain modest. For example, optimizing the number of ensemble members in the random forest on the training set using fivefold cross-validation does not substantially improve performance (see Figure A.11). While the simple baseline, which generates predictions uniformly for each class, is likely to provide a lower-bound estimate, actual human predictive performance may be slightly better, although not by a large margin given the complexity of the data. In many cases, data in one class is barely distinguishable from data in the neighboring class (see Figure 6.7 and Figure 6.8). Overall, the neural networks prove to be highly competitive, outperforming many classical ML models and significantly surpassing the human predictive capabilities.

The performance comparison between DL models and classical ML methods highlights that neural networks are competitive, as they perform comparable to the two best ML classifiers and outperform most of the investigated classical ML models. However, to fully realize the potential of DL in complex tasks such as molar ratio and molarity

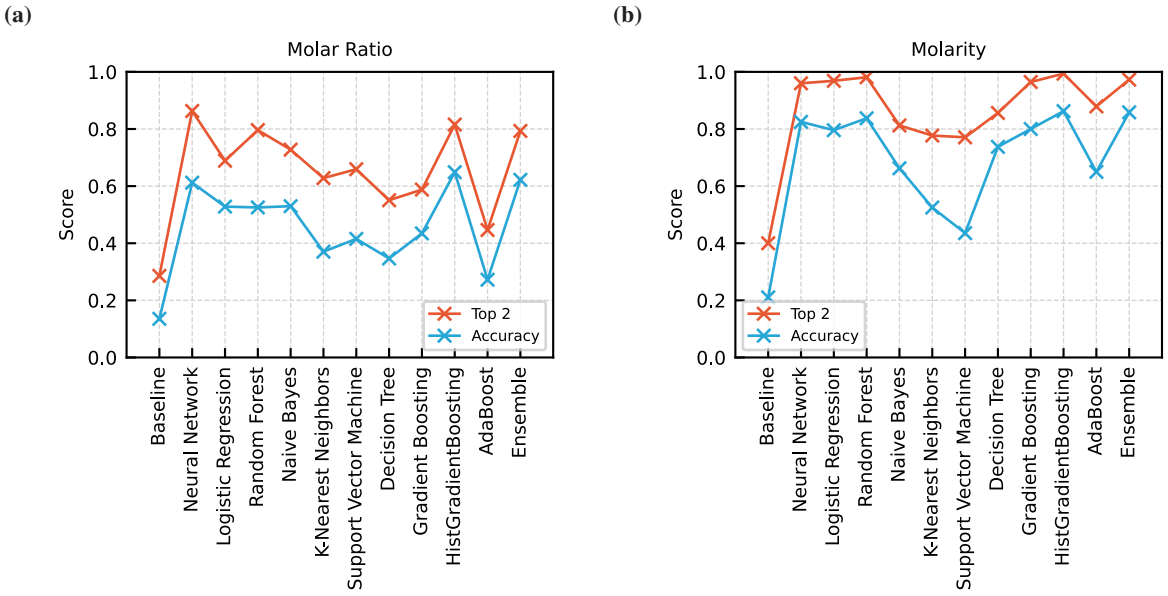

Figure 6.10: Comparison of deep learning and classical machine learning (ML) models for predicting molar ratio (a) and precursor molarity (b). The neural network (NN) is benchmarked against several classical ML classifiers, with random forest (RF) and histogram-based gradient boosting (HGB) emerging as the best-performing classical models. For molar ratio classification, the NN substantially outperforms the RF, while HGB achieves slightly higher accuracy but a lower top-2 score than the NN. For molarity prediction, the NN shows a high accuracy and top-2 score, closely matching the scores of HGB and RF. Overall, the NNs perform comparably to the best classical models and substantially outperform the human baseline and other classical ML models. Adapted with permission from [352].

classification, the impact of scaling up the dataset needs to be considered. Larger datasets could unlock substantial improvements, particularly for DL models, as demonstrated by neural scaling laws, which suggest that more data generally leads to better predictive performance.[444–446]

To assess the impact of available training data, the model performance on the held-out test set is systematically evaluated by using gradually larger subsets of the training data for model training (see Figure 6.11 and Figure A.12). For molarity classification, the neural network shows a notably faster improvement in accuracy with increasing dataset size compared to the two best-performing classical ML methods, RF and HGB (see Figure 6.11b). While the performance of the neural network still lags slightly behind the best classical models when trained on the full dataset, its rate of improvement per additional 100 training samples is the highest for most data intervals (see Table A.6). Further increases in dataset size, from 100% to 125%, are linearly extrapolated and shown as shaded areas in Figure 6.11. These extrapolations are based on the slopes calculated between the 100% data point and each preceding data point (10%, 20%, ..., 90%). However, since accuracy scores cannot exceed one, these linear extrapolations should be considered upper-bound estimates. In reality, the model's performance would likely approach one asymptotically, as perfect accuracy is improbable due to uncertainties in the actual ground truth composition, as the actual molarity or molar ratio may sometimes lie between two class labels.

In the case of molar ratio classification, all models perform similarly poorly with small training sets, but the neural network initially shows a stronger rate of improvement, outperforming HGB as more data is added (see Figure 6.11a). The performance of the neural network begins to plateau at medium dataset sizes, and HGB eventually outperforms it. However, once the dataset reaches 90% of the available training data, the performance of the neural network improves again to nearly match that of HGB, while showing a more pronounced trend of improvement.

For both target variables, the general trend shows that more data consistently improves the predictive performance for all models. RF and HGB show a continuous improvement in prediction accuracy as the size of the training dataset increases. Neural networks, on the other hand, struggle with small datasets and experience a plateau in

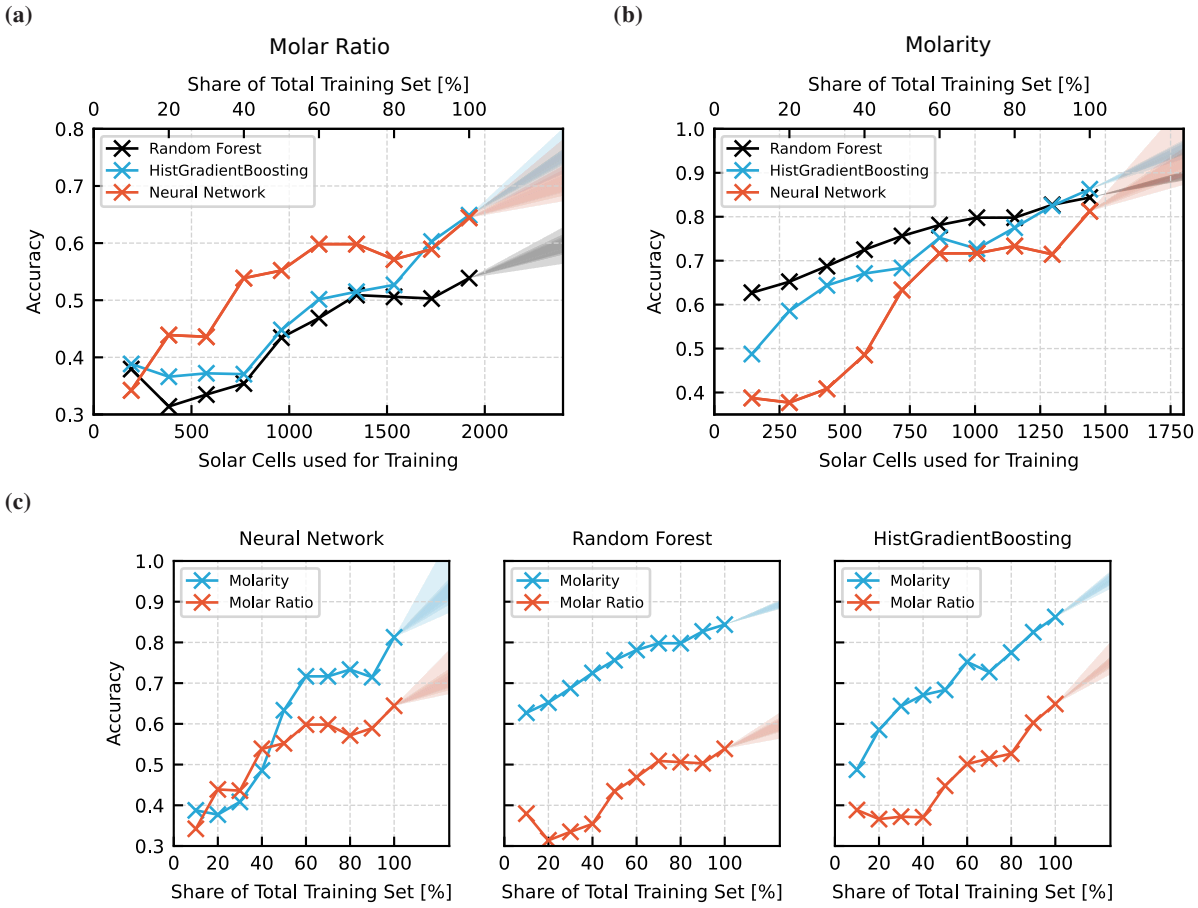

Figure 6.11: Impact of training dataset size on model performance for molar ratio (a) and molarity (b) classification, and performance comparison (c) between neural network (NN), random forest (RF), and histogram-based gradient boosting (HGB) models. Prediction accuracy improves as larger subsets of training data are used. For molarity prediction, the NN shows a faster rate of improvement compared to RF and HGB as the dataset size increases. For molar ratio classification, all models perform similarly with small datasets, the NN shows the fastest initial improvement but plateaus at medium dataset sizes, eventually matching HGB's performance as the dataset approaches full size. The extrapolated performance (shaded areas) suggests further gains if the dataset size were increased beyond the current size. The results highlight the importance of dataset scaling, particularly for DL models, which benefit from larger datasets according to neural scaling laws. Adapted with permission from [352].

performance when trained on medium-sized datasets. However, with access to larger datasets, the neural networks begin to show notable gains in accuracy, improving at a faster rate than the other methods (see Figure 6.11c and Table A.6). This trend is consistent with established results from DL literature, where scaling laws show that neural networks continue to improve with additional data.[444–446]

In industrial applications, such as in-line material composition monitoring, there is considerable potential to generate much larger datasets. The ability to continuously collect large amounts of data from production processes could enable further improvements in DL performance, making neural networks an increasingly attractive option in these settings. As more data becomes available, especially in industrial environments, the performance of DL models is expected to continue to scale, potentially outperforming classical models and enabling highly accurate, automated material composition monitoring.

In summary, the application of DL to *in situ* material composition monitoring shows promise for improving the reproducibility of perovskite solar cell fabrication.[352] The predictive *in situ* technique, enhanced by both ML and DL, detects subtle changes in precursor molarity or molar ratio using only time-resolved PL and reflection

data, which would be difficult, if not impossible, for a human researcher to observe during thin-film formation (see Figure 6.7 and Figure 6.8). While neural networks initially lag behind classical methods with smaller datasets, they show superior rates of improvement as the amount of training data increases. This suggests their potential for improved performance on larger datasets. Expanding the dataset to include intermediate values between the current discrete molarity and molar ratio classes could enable regression models to predict continuous material parameters in future work, as even small undetected differences (<1%[443]) could affect the stability, device performance, and other key properties of perovskite solar cells.[350, 435, 436, 438, 443] This highlights the need for predictive monitoring tools that can detect unwanted variations early, not only in laboratory research but also in industrial-scale fabrication processes. Particularly with the potential for real-time, large-scale data collection in industrial settings, DL is positioned to become a powerful tool for ensuring consistent, high-quality material composition in perovskite solar cells.

6.4 Predicting Holistic Device Performance with Varying Process Parameters

Accurately predicting the performance of PSCs is crucial for optimizing fabrication processes and ensuring consistent device quality, as small variations in process parameters during fabrication can result in significant variations in device performance. Therefore, early assessment of device performance, even before the completion of the entire solar cell device stack, is essential to achieve reproducibility in the fabrication of high-performance, scalable PSCs.[352] Predictive methods based on *in situ* characterization and deep learning offer a promising solution to assess performance indicators early in the fabrication process.

Therefore, after demonstrating the ability of neural networks to detect subtle variations in material composition, the predictive capabilities of PL characterization enhanced with DL are extended from material-level analysis to device-level predictions. Deep neural networks are used to monitor the quality of perovskite thin films by predicting solar cell performance based on *in situ* imaging data captured during the vacuum quenching of perovskite thin films. Device performance prediction (use case (ii)) is achieved by training DL models to map time-resolved *in situ* data to solar cell performance metrics, allowing early assessment of the final performance of PSCs, enabling

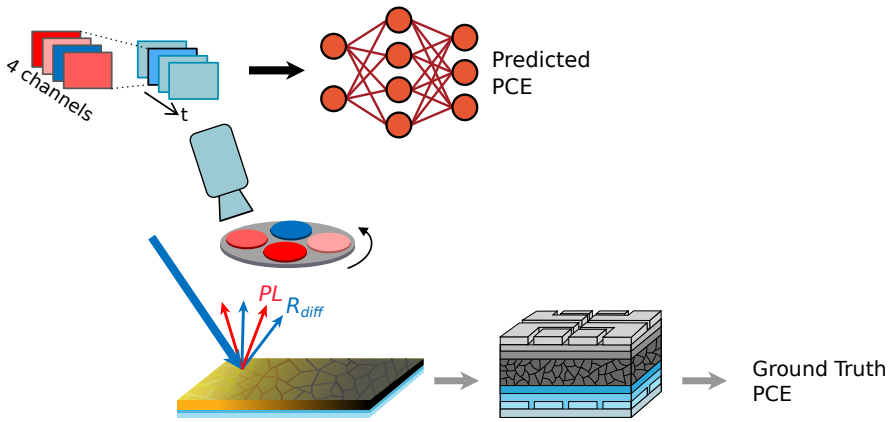

Figure 6.12: Schematic representation of device performance prediction using an *in situ* characterization setup and deep learning. The predictive approach is extended from the material to the device level by predicting device performance even before perovskite thin films are completed into functional solar cells. The *in situ* imaging data acquired during vacuum quenching of perovskite thin films is fed into a deep neural network to predict the power conversion efficiency (PCE). Ground truth PCE values are measured only after full device fabrication and used to validate the predictions. This approach allows early assessment of perovskite thin-film quality and facilitates reproducible fabrication by identifying performance variations early in the process. Adapted with permission from [352].

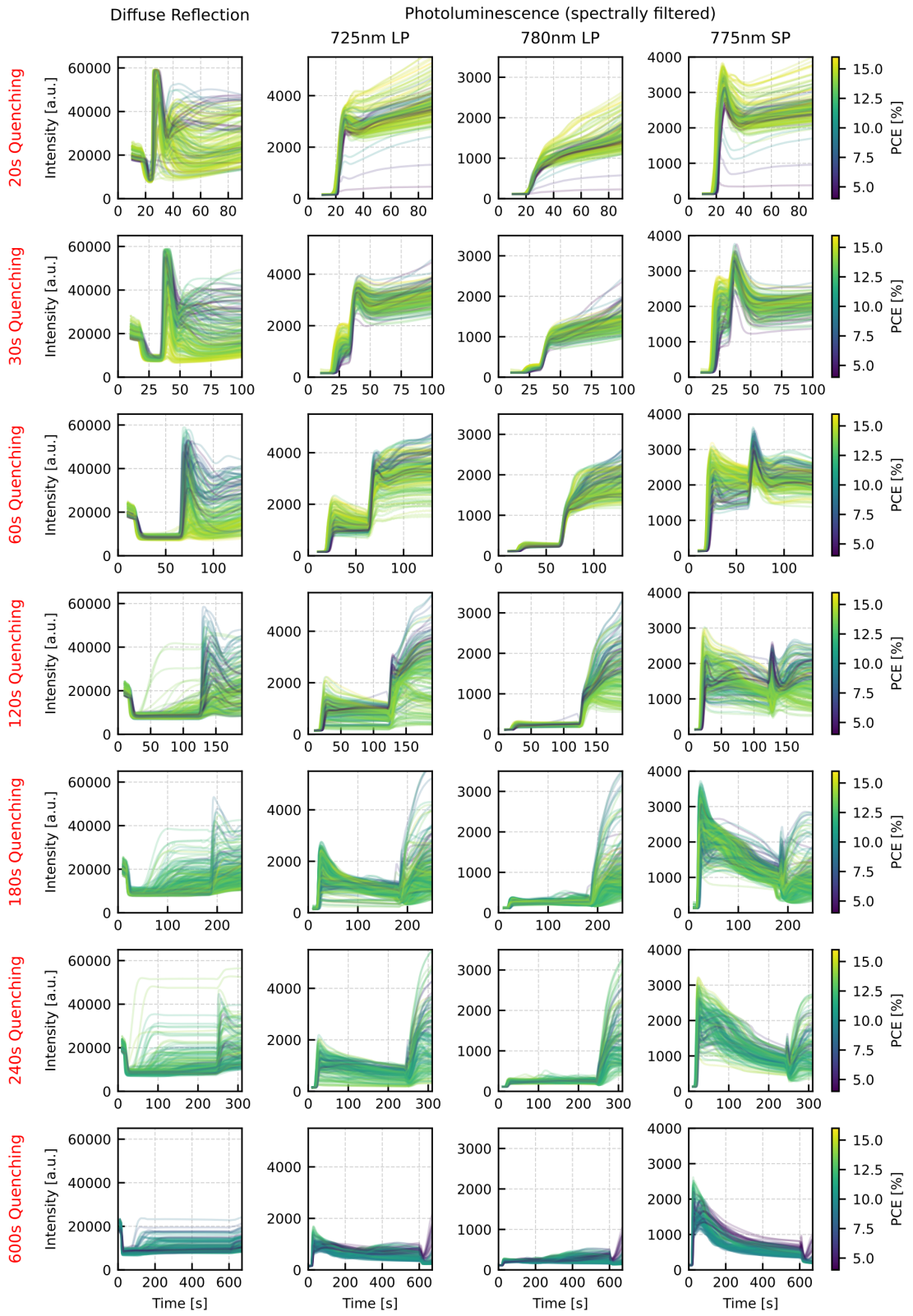

Figure 6.13: Transients of the monitoring data for different quenching times, color-coded by power conversion efficiency (PCE). Given the transients (derived by spatial averaging at each time step), human analysis might be able to categorize high and low PCE samples. But accurate PCE prediction requires machine learning to detect small variations in the monitoring data. Adapted with permission from [352].

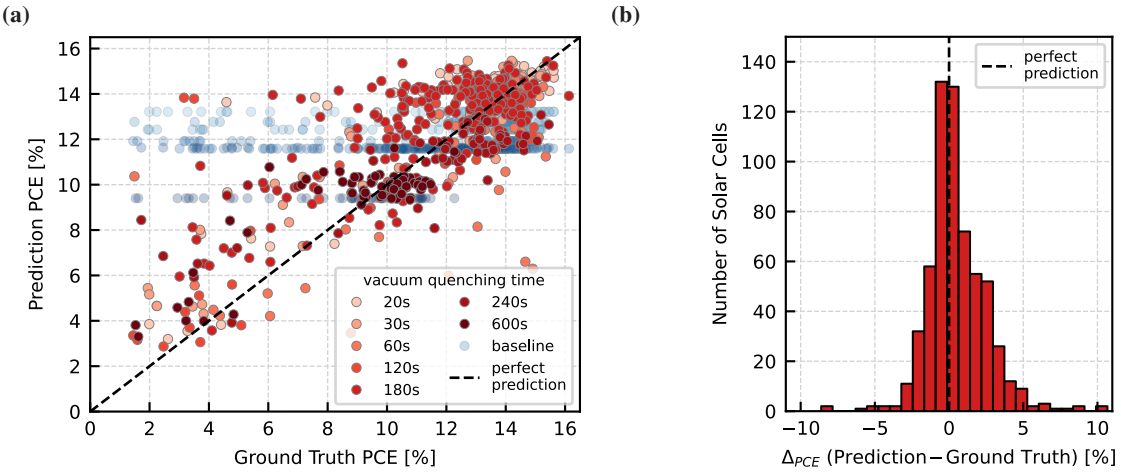

Figure 6.14: Comparison of predicted and ground truth power conversion efficiency (PCE) values for the test set. (a) The parity plot shows the correlation between predicted and actual PCE values. Model and baseline predictions are resolved for different vacuum quenching times. While the model generally captures the relationship between *in situ* monitoring data and device performance, it tends to overestimate low PCE values. (b) The histogram of residuals (prediction - ground truth) confirms this tendency, as evidenced by a wider distribution for positive residuals. This behavior may be caused by irregularities during unmonitored fabrication steps that affect the final PCE but are not captured in the *in situ* data. Adapted with permission from [352].

quantitative evaluations prior to the completion of the numerous processing steps required before for experimental device characterization (see Figure 6.12). This early prediction capability provides an invaluable tool for assessing device quality during fabrication, enabling accelerated optimization of the fabrication process.

Unlike the first dataset, where all solar cells were fabricated under constant conditions using the same layer stack and precursor materials, this second dataset introduces systematic variations in vacuum quenching times. With the reference process being 180 s, the quenching times ranged from 20 s to 600 s, allowing a broad exploration of the effects of quenching time on thin film morphology and device performance (see Figure 6.13). These variations result in diverse perovskite thin film morphologies and solar cell performance results, providing a broader dataset for evaluating the influence of quenching time on device performance. For device performance prediction (use case (ii)), all other processing parameters, including precursor composition and deposition conditions, were kept constant to isolate the effect of quenching time on the PCE of the resulting devices. This controlled variation of vacuum quenching time ensures that any observed differences in device performance can be attributed solely to changes in the duration of the vacuum quenching process, providing a robust dataset for predictive modeling in device performance prediction.

To enable early device performance prediction before the remaining fabrication process steps are completed, a deep neural network regressor is trained to leverage variations in the input data for PCE prediction (see Figure 6.13). A feedforward neural network with five fully connected hidden layers and a single output neuron is used to predict device performance based on the *in situ* PL and R_{diff} data used as input features (see Figure 6.12). The model is trained on the training set using fivefold cross-validation and the average performance over the folds is used to select hyperparameters for retraining the neural network regressor on the entire training set (`L1 loss`, `Adam optimizer`, `learning rate`: 10^{-4}, `weight decay`: 10^{-4}, `batch size`: 128). On the held-out test set, the predictive performance of the model is evaluated by comparing the predicted PCE values with the actual ground truth PCE labels using parity plots and quantitative metrics such as MAE, RMSE, and R^2.

Comparison of the model's predicted PCE values and the ground truth PCE values for all devices in the test set demonstrates that the model successfully captures the underlying relationship between the *in situ* monitoring data and the corresponding device performance (see Figure 6.14a). When examining the predictions for different subsets of the test data corresponding to different vacuum quenching times, the model shows consistently strong predictive

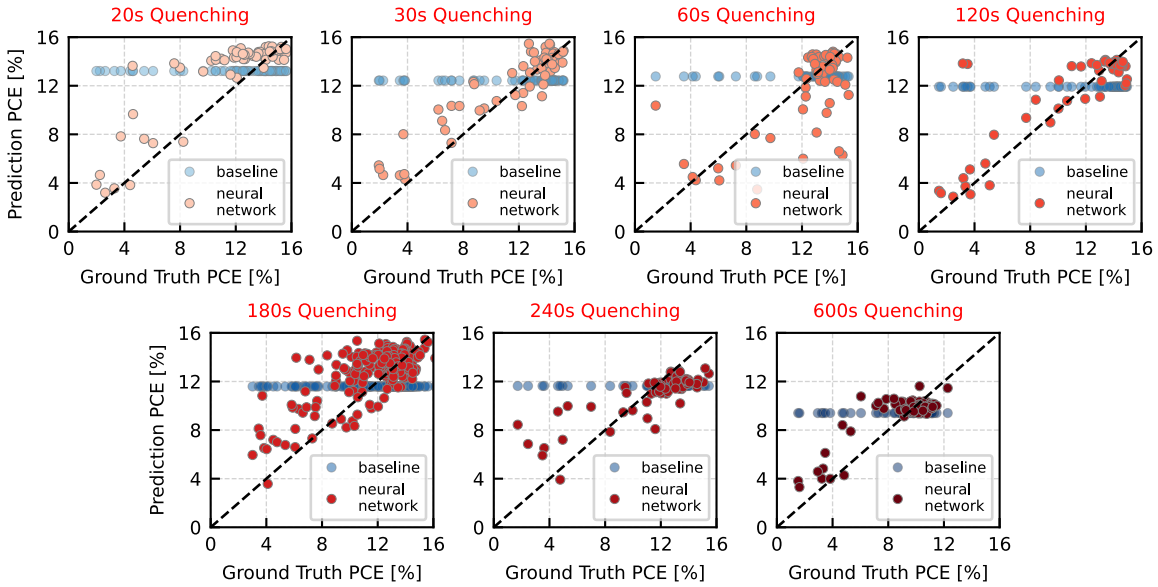

Figure 6.15: Parity plots showing predicted versus ground truth power conversion efficiency (PCE) for different vacuum quenching times in the test set. The neural network model accurately predicts the PCE for various quenching times, including both shorter (e.g., 20s) and longer (e.g., 600s) durations, with minimal prediction error. This consistent performance across different process conditions underscores the robustness of the model in predicting device performance based on *in situ* monitoring data. For each sample, the baseline model predicts the average PCE of all devices in the training set with the same quenching time. Adapted with permission from [352].

performance (see Figure 6.15). However, while showing a clear correlation between the predicted and ground truth PCE values, the parity plots and the residuals histogram reveal that the model tends to overestimate outliers with low ground truth PCE (see Figure 6.14b, Figure 6.14a and Figure 6.15). This overestimation, which results in more data points in the top left corner of the parity plots and a wider shoulder in the distribution of positive residuals, could be due to the complexity of predicting PCE based on data acquired during only one step of the fabrication process. Since the PCE is measured on the fully fabricated solar cell and is influenced by the entire device stack, irregularities during other fabrication steps may affect the final PCE but are not reflected in the *in situ* data and therefore remain unrepresented in the model input.

After a qualitative analysis of the predictions of the neural network on the test set using parity plots, a quantitative evaluation is performed. For an initial benchmarking of the performance of the neural network, a baseline is computed. For the baseline, the average PCE of all devices with a given quenching time from the training set is used to predict the PCE for each corresponding case with the same quenching time in the test set. Although the baseline is simple, it reflects the predictive approach of a human researcher working without advanced methods. In experimental work, it is often assumed that the outcomes of new experiments (test set) will closely match the results of previous experiments conducted under the same parameters and conditions (training set). Therefore, the baseline predicts the mean PCE from the training set for each quenching time subset, as no other variables were changed.

Model performance is measured quantitatively using three metrics. MAE describes the average magnitude of errors between predicted and actual values, while RMSE emphasizes larger errors by squaring the difference before averaging and taking the square root and R^2 quantifies how well the model predictions explain the variance in the actual values. For MAE and RMSE, lower values indicate better performance (lower is better), while R^2 typically ranges from 0 to 1, with higher values suggesting a better fit (higher is better). Negative R^2 values reveal that model predictions are worse than simply using the mean of the test data as a constant prediction.

A comparison of the prediction results shows that the neural network significantly outperforms the baseline for all metrics (see Table 6.1). For the entire test set, the neural network achieves an MAE of 1.44%$_{abs}$, considerably

Table 6.1: Predictive performance of the neural network for predicting power conversion efficiency (PCE) for different vacuum quenching times. For all metrics, the neural network outperforms the baseline, demonstrating substantial improvements and highlighting the need for data-driven methods to accurately predict PCE based on *in situ* monitoring data across different processing conditions. (for MAE and RMSE: lower is better ↓, for R^2: higher is better ↑, MAE: mean absolute error, RMSE: root mean square error, R^2: coefficient of determination)

	MAE [%]		RMSE [%]		R^2	
Vacuum Quenching Time	Baseline	Neural Network	Baseline	Neural Network	Baseline	Neural Network
All (= Entire Test Set)	2.55	1.44	3.39	2.07	-0.01	0.62
20s	2.95	1.68	3.86	2.39	0.00	0.62
30s	3.10	1.18	3.92	1.62	–0.01	0.83
60s	2.43	1.56	3.12	2.55	–0.04	0.30
120s	3.30	1.22	4.23	2.21	–0.01	0.73
180s	2.05	1.51	2.67	2.03	0.00	0.42
240s	2.28	1.66	3.33	2.12	–0.02	0.59
600s	3.06	1.11	4.02	1.45	–1.35	0.70

lower than the baseline of 2.55%$_{abs}$, and an RMSE of 2.07%$_{abs}$, compared to the baseline of 3.39%$_{abs}$. The R^2 score of the neural network improves to 0.62, while the baseline fails to accurately predict PCE, as reflected by its near-zero R^2 score (-0.01). The deep neural network clearly outperforms the baseline, which reflects the predictive ability of a human researcher without advanced methods and highlights the need for predictive tools in experimental laboratories. Furthermore, this performance trend holds for individual quenching times, where the neural network consistently shows lower error rates and higher R^2 values, indicating its superior ability to accurately predict PCE even as the quenching time varies.

By achieving an RMSE of 2.07%$_{abs}$, the neural network outperforms the "best models for PCE prediction" based on literature databases, which have achieved RMSE values around 3%$_{abs}$[116, 178, 203, 204], according to a recent review on machine learning in perovskite solar cell research[155]. Also, compared to other studies predicting PCE based on literature databases, as highlighted in another review on machine learning for perovskite photovoltaics[159], the neural network in this work demonstrates strong performance. While some studies reported better prediction accuracy[116, 185], others showed comparable[447] or worse performance[178, 184, 204]. However, these studies are meta-analyses of published experimental data, aggregating experimental results into cross-study datasets, rather than using *in situ* monitoring data for PCE prediction as done here. This fundamental difference in study design must be considered when comparing the results of literature-based PCE prediction approaches with the *in situ* prediction technique used for DL-enhanced characterization of perovskite fabrication processes.

Compared to previous studies on the first dataset, the neural network shows high accuracy over all quenching times. In prior work on the similar first dataset with constant processing parameters, PCE predictions were made using a k-nearest neighbors regressor[346] and a ResNet model[347], achieving MAEs of 1.52%$_{abs}$ and 1.58%$_{abs}$, respectively, on the test set. Notably, in terms of R^2 scores, the neural network applied to the second dataset (0.62) significantly outperforms k-nearest neighbors (0.24) and other classical ML regressors applied to the first dataset(see Table 5.3 and Figure 5.17a).

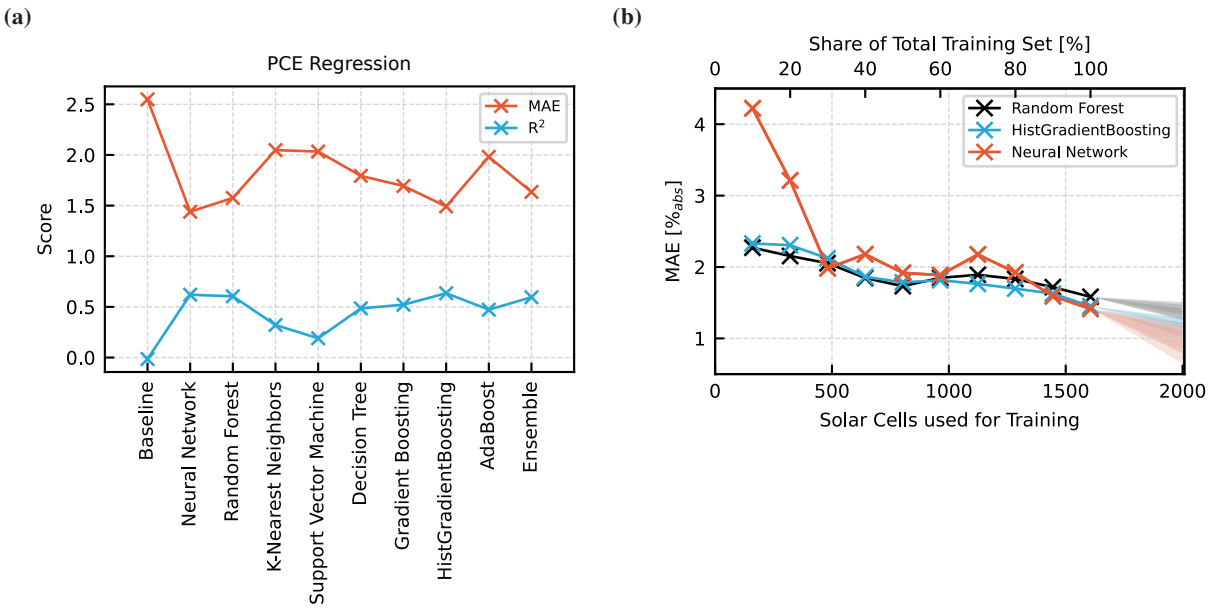

Figure 6.16: Comparison of predictive performance for power conversion efficiency (PCE) prediction using different machine learning (ML) models and the effect of training dataset size on model accuracy. (a) The neural network (NN) is benchmarked against several classical regressors, with random forest (RF) and histogram-based gradient boosting (HGB) emerging as the best-performing classical ML regressors. NN shows competitive performance, outperforming RF and HGB in terms of mean absolute error (MAE) and achieving comparable R^2 values. (b) All models (NN, RF, HGB) benefit from larger datasets, as the MAE of the three best models decreases with a larger training dataset size. While RF and HGB show steady improvement, the NN exhibits a slower start but improves substantially as the dataset grows, eventually outperforming the other models in MAE. The shaded areas indicate extrapolated performance gains with further dataset scaling, highlighting the potential, particularly of NN, for improved PCE prediction with larger training sets.

To further benchmark the performance of the DL model in predicting PCE, it is compared with classical ML regressors (see Figure 6.16a). The comparison shows that the neural network matches the performance of the best classical models while outperforming several other models and the human baseline. Similar to the molar ratio and molarity classification results, the neural network, histogram-based gradient boosting, and random forest regressors provide the best performance for PCE prediction. While the R^2 values for the three best models are close (neural network: 0.62, HGB: 0.63, RF: 0.60), the neural network achieves a slightly lower MAE of $1.44\%_{abs}$ compared to HGB ($1.49\%_{abs}$) and RF ($1.58\%_{abs}$). The classical ML regressors are trained with fixed parameters (`strategy`='mean' for baseline (=DummyRegressor), `n_estimators`=100 for random forest, `n_neighbors`=10 for k-nearest neighbors, `kernel`='rbf' for support vector machine, `max_depth`=4 for decision tree, `n_estimators`=100 and `learning_rate`=1.0 and `max_depth`=1 for gradient boosting, `max_iter`=100 for histogram-based gradient boosting, `n_estimators`=100 for AdaBoost, `estimators`=[*all the regressors mentioned above*] for ensamble (=VotingRegressor)). However, even when optimizing the hyperparameters, the performance improvements remain modest, since performance does not improve substantially when the number of ensemble members in the RF or the learning rate of the HGB are optimized using fivefold cross-validation on the training set (see Figure A.13). Overall, the neural network outperforms most classical ML models and significantly surpasses the baseline, which reflects human predictive capabilities.

Benchmarking shows that the performance of the neural network is highly competitive, outperforming most classical models. To fully exploit the potential of DL for complex prediction tasks, scaling up the dataset is crucial, as scaling laws suggest that larger datasets can significantly improve predictive performance, especially for DL models.[444–446] To evaluate how training dataset size affects predictive accuracy when predicting PCE based on *in situ* data, the performance of the three best regressors (neural network, RF, and HG) is systematically evaluated using progressively

larger subsets of the training data (see Figure 6.16b). For all models, more data improves predictive performance. The RF and HGB regressors steadily improve as the training set size increases, although there is a slight plateau at medium dataset sizes. In contrast, the neural network performs poorly when trained on a small dataset, even showing negative R^2 values (see Figure A.14). After plateauing at medium dataset sizes, the performance of the neural network improves substantially when more than 70% of the data is used for training. When trained on the full dataset, the neural network outperforms the RF and surpasses the HGB in terms of MAE, while nearly matching the HGB in terms of R^2. Further increases in dataset size, from 100% to 125%, are linearly extrapolated based on the slopes calculated between the 100% data point and each preceding data point (10%, 20%, ..., 90%) and shown as shaded areas in Figure 6.16b. However, even with very large datasets perfect prediction accuracy is unlikely because irregularities in other fabrication steps may affect the PCE but are not represented in the model input.
In general, the analysis shows that more data improves the performance of all models. However, while RF and HGB improve more continuously in prediction accuracy with increasing amounts of training data, the neural network performs poorly on small datasets but then improves substantially with more data for training (see Figure A.15). This observation is consistent with the literature, where scaling laws describe that neural networks continue to improve with additional data.[444–446] The higher rates of improvement per additional 100 training samples of the neural network compared to RF and HGB suggest a more substantial benefit from increasing the training data size for the DL model (see Table A.6). As perovskite PV technology transitions to large-scale production, much larger and more comprehensive datasets will be generated, which may facilitate further improvements in DL model performance. With continuously improving predictive performance at scale, neural networks will enable highly accurate, automated in-line PCE prediction for early device quality assessment in industrial fabrication.
In summary, deep neural networks effectively predict the PCE of perovskite solar cells based on data collected during fabrication, which is hardly possible for a human researcher process (see Figure 6.13). The model's predictive performance improves significantly with larger training datasets, highlighting the importance of data scaling in DL applications. The results demonstrate that integrating deep learning with *in situ* characterization enables early and accurate assessment of device performance, which is critical for optimizing fabrication processes and ensuring consistent quality in industrial production.

6.5 From Passive Analysis to Active *In Situ* AI Recommendation

Building on the capability of neural networks to accurately predict device performance, the approach is advanced from predictive to prescriptive analysis, where DL-driven insights are used to predict outcomes and to actively inform and optimize experimental processes. By combining *in situ* forecasting of monitoring data with performance prediction, the DL-enhanced characterization method provides actionable recommendations for process control (use case (iii)).[352] The approach enables forecasting various experimental scenarios and predicting the corresponding solar cell performance for each scenario, providing scientists with data-driven insights to guide experimental procedures in the laboratory. The prescriptive approach informs researchers of the plausible expected experimental scenarios, transitioning from passive predictive analysis to active data-driven process control for improved control over thin-film quality characteristics facilitated by AI recommendations (see Figure 6.17).
To implement the DL-driven *in situ* recommendation system, the overarching goal of recommendation generation is split into three subtasks (see Figure 6.17 and Figure 6.18). To perform the subtasks, various ML models are used in a cascade, where the output of one model serves as the input for the next. The designated subtasks are (a) *in situ* forecasting the monitoring data, (b) predicting the PCE using a regression model based on the forecasted monitoring data, and finally (c) approximating a continuous function from predicted PCE data points for discrete times. Particularly for subtasks (a) and (b), it is critical that the models achieve high prediction accuracies in order to implement a robust *in situ* feedback loop. Accordingly, subtask (a) requires that the neural network effectively learns the mapping between the input monitoring data and the corresponding PCE. Considering the results from the parity plots, the evaluation of various error metrics, and the comprehensive comparison between DL and ML results

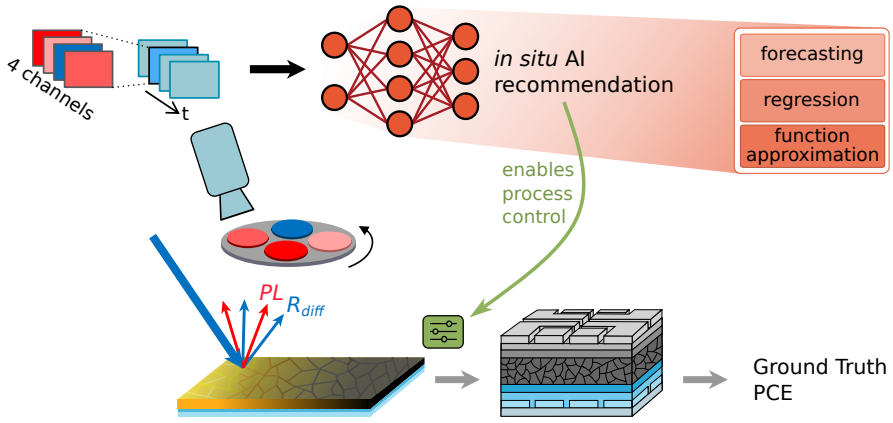

Figure 6.17: Schematic representation of *in situ* AI recommendations for process control in perovskite solar cell fabrication. Machine learning (ML) is used to predict power conversion efficiency (PCE) based on *in situ* monitoring data and to provide actionable recommendations for process optimization. By combining forecasting, regression, and function approximation, a cascade of ML models provides AI-driven insights that help guide the experimental process and enable active control of thin-film quality. Adapted with permission from [352].

in section 6.4, the prediction accuracy of the neural network is considered sufficient to perform subtask (b) of use case (iii). The *in situ* forecasting of monitoring data related to subtask (a) is discussed in the following sections.

6.5.1 *In Situ* Data Forecasting and Device Performance Prediction

As demonstrated in section 6.4, the trained neural network can successfully predict the PCE of solar cells quenched for various specific time intervals and is therefore used for subtask (b), which predicts the PCE based on forecasted monitoring data. However, since the neural network was trained with input data corresponding to specific vacuum quenching times (20 s, 30 s, 60 s, 120 s, 180 s, 240 s, and 600 s), it only makes reasonable predictions if it is provided with input features from these previously seen quenching times.
To facilitate this, random forest regressors, ML models that require less training data than neural networks, are used for *in situ* forecasting of the monitoring data (subtask (a)).[352] These regressors generate synthetic monitoring data corresponding to the feasible quenching times that the neural network can process (20 s, 30 s, ..., 600 s). At any

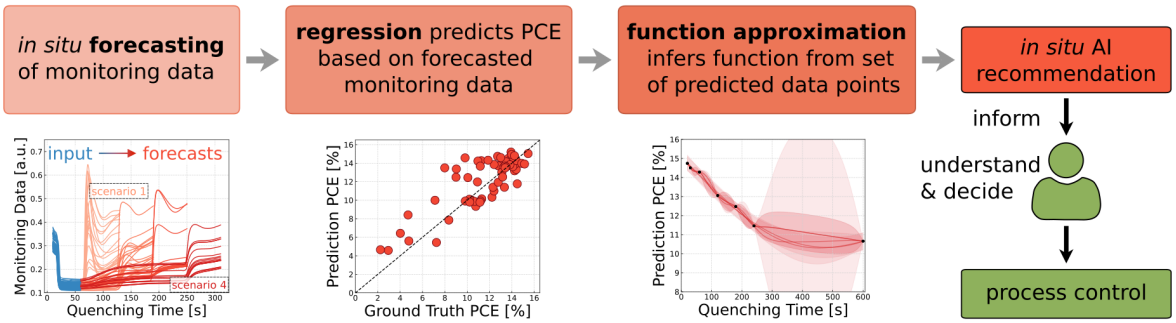

Figure 6.18: Workflow of the AI-driven *in situ* recommendation system for process control. The overarching goal of generating recommendations is split into three subtasks: (a) *in situ* forecasting of monitoring data, (b) prediction of power conversion efficiency (PCE) using a regression model based on forecasted monitoring data, and (c) approximation of a continuous function from the predicted PCE data points for discrete times. The cascade of models forecasts plausible monitoring data progression scenarios and subsequently predicts the PCE for each scenario. This prescriptive approach transitions from predicting outcomes to influencing and optimizing fabrication processes to improve overall fabrication consistency and quality. Adapted with permission from [352].

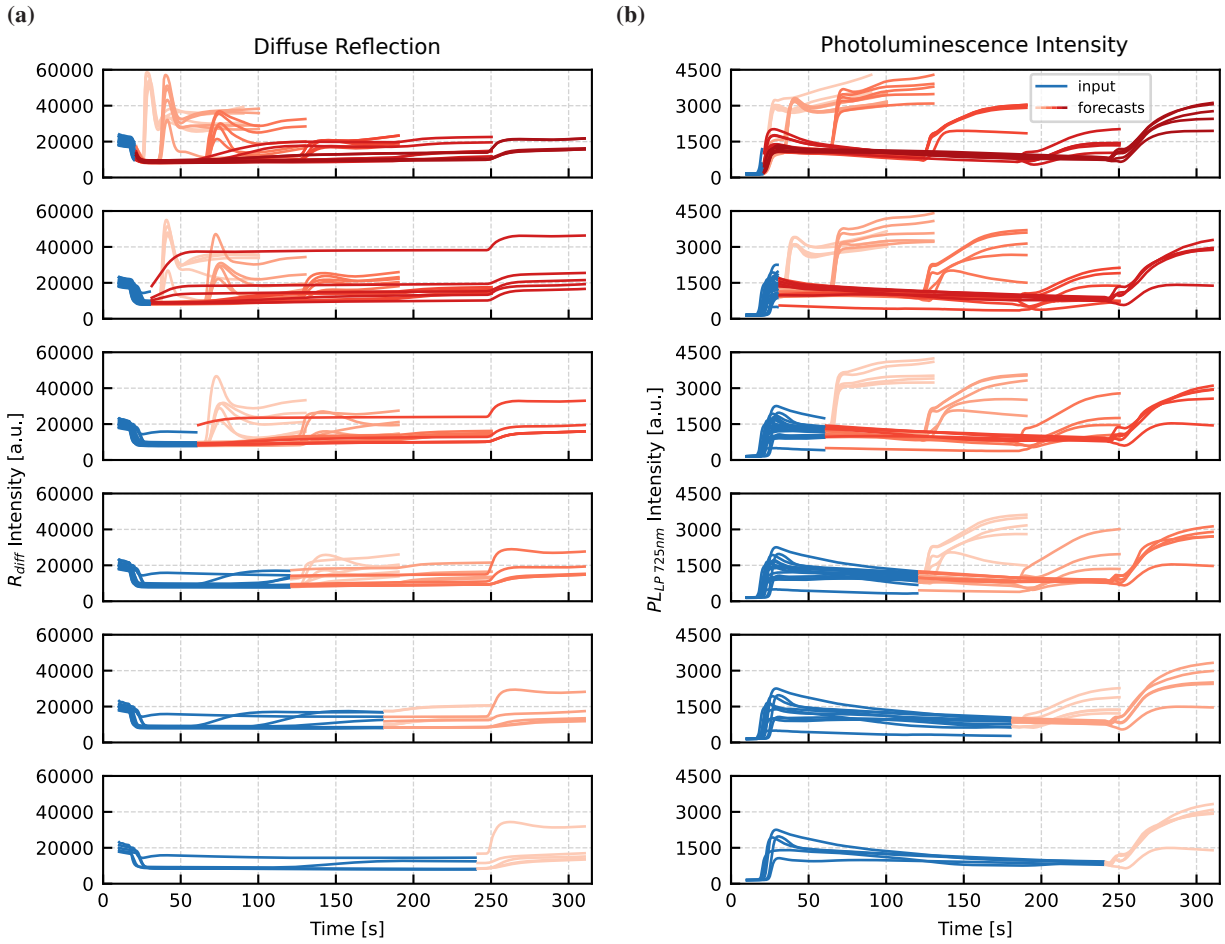

Figure 6.19: Forecasting different vacuum quenching scenarios using random forest regressors. For ten exemplary test set samples, the monitoring data (blue) of (a) diffuse reflection and (b) photoluminescence ($PL_{LP\,725nm}$) is used to forecast its progression (red) for different quenching times up to 240 seconds (scenarios with 600 s quenching times not shown for clarity). The forecasts are generated based on monitoring data collected up to specific time points (20 s, 30 s, ...) and predict the data progression when quenching is stopped at subsequent intervals. As the experiment progresses, more data is accumulated (blue) and the forecasts (red) are updated based on the newly collected data. This approach enables *in situ* forecasting, providing synthetic data as input to the neural network to predict the power conversion efficiency (PCE) under different scenarios. Adapted with permission from [352].

given time point, the monitoring data collected up to that moment is used to forecast its future progression. The initial forecasted scenario represents the outcome if the vacuum quenching is stopped immediately, while additional scenarios forecast what will happen if the quenching continues and is stopped at subsequent time points. For example, data acquired during the first 20 seconds is used to forecast the monitoring data progression under seven different scenarios: stop immediately after a total quenching time of 20 s, stop after an additional 10 seconds (total of 30 s), or continue for total quenching times of 60 s, 120 s, 180 s, 240 s, or 600 s, respectively (see Figure 6.19). The same approach is applied to the data collected during the first 30 seconds, resulting in forecasts for six different quenching times. This method is repeated for subsequent intervals (60 s, 120 s, . . .), producing a decreasing number of forecasted scenarios down to a single forecast for data acquired during 600 seconds of quenching.

To implement the forecasting capability, multiple combinations of input feature lengths (i.e., time already elapsed) and total quenching times (i.e., time remaining until quenching is stopped) must be addressed. With seven different quenching times in the dataset, this results in 28 unique forecasting scenarios. Since forecasting is required for all

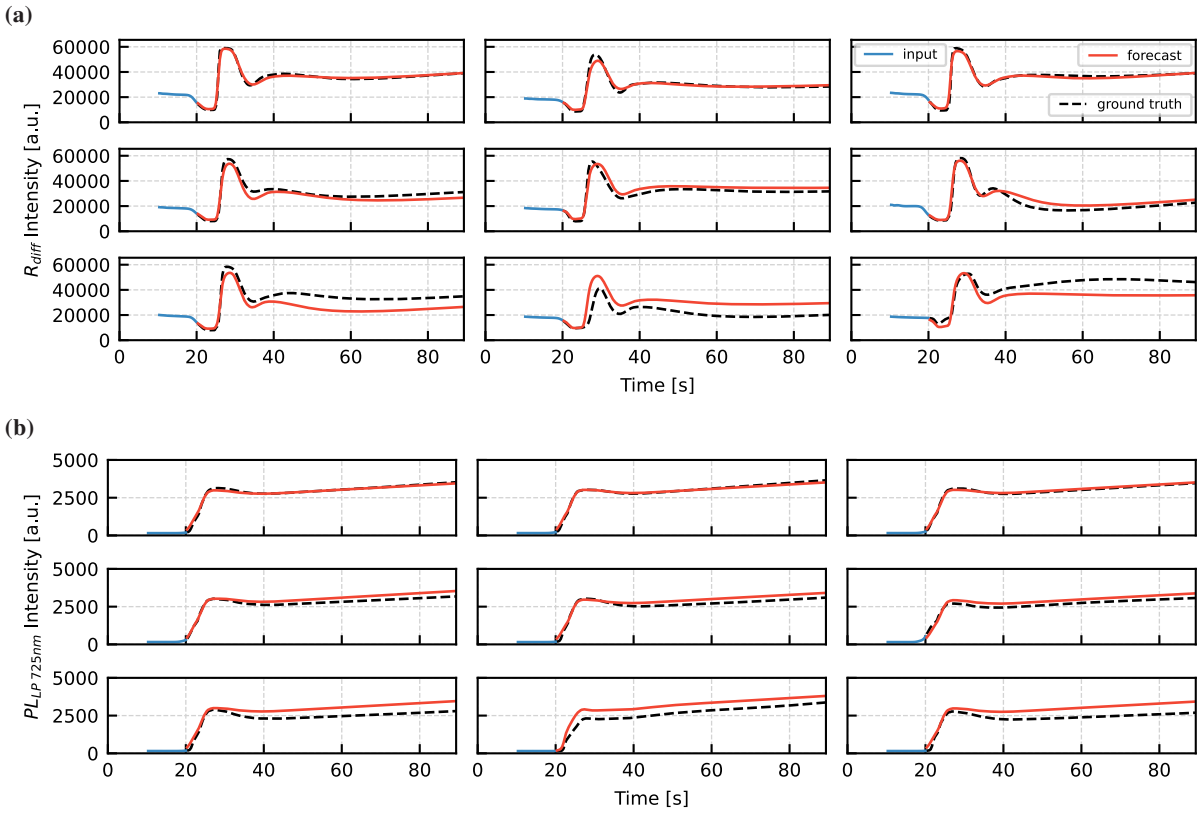

Figure 6.20: All random forest models are trained to optimize forecasting accuracy. Hyperparameter optimization is performed on the training set using grid search with threefold cross-validation to ensure optimal forecasting performance for all 112 random forest models forecasting the monitoring data of the four channels and covering 28 forecasting scenarios. As shown here for (a) diffuse reflection (R_{diff}) and (b) photoluminescence ($PL_{LP\,725nm}$) after 20 s of data acquisition, the forecasted data progression (red) of nine different samples is compared to the ground truth data (dashed black). The prediction error is minimized during hyperparameter optimization with cross-validation. Adapted with permission from [352].

four IPRDI channels, a total of 112 forecasting models (28 scenarios $\times$ 4 channels) are required. Each forecasting model is trained on a small subset of the training data relevant to its specific combination of input length and total quenching time, making random forest regressors an appropriate choice due to their ability to perform well with limited data compared to neural networks. The input feature for each model is the ground truth monitoring data collected up to the forecasting point (i.e., the elapsed time). The model output is the forecasted monitoring data from the forecasting point to the end of quenching (i.e., the remaining time) (see Figure 6.19).

Hyperparameter optimization for all 112 random forest models is performed using grid search. The following parameters are varied to find the optimal settings: `n_estimators` (varied between 20 and 200), `max_features` (set to "sqrt", "log2", or "None"), `max_depth` (set to 2, 4, or None), `min_samples_split` (set to 2 or 5), `min_samples_leaf` (set to 1 or 2), and `bootstrap` (set to True or False). Due to the smaller datasets available for each scenario, threefold cross-validation is used. Comparison of the forecasted progression of the monitoring data with the ground truth monitoring data on the test set shows a high agreement, as evidenced by a low forecasting error (see Figure 6.20) Successful data forecasting is also demonstrated by comparing the ground truth PCE with the predicted PCE based on the forecasted data progressions (see Figure 6.21 and Figure 6.22). In summary, 112 random forest models are used to perform subtask (a), forecasting the monitoring data for the 28 scenarios described above across all four IPRDI channels. Each model is trained on the training dataset using grid search to identify the best-performing hyperparameters that optimize forecasting performance.

The cascaded use of random forest models and a neural network allows (a) generating *in situ* forecasts by producing

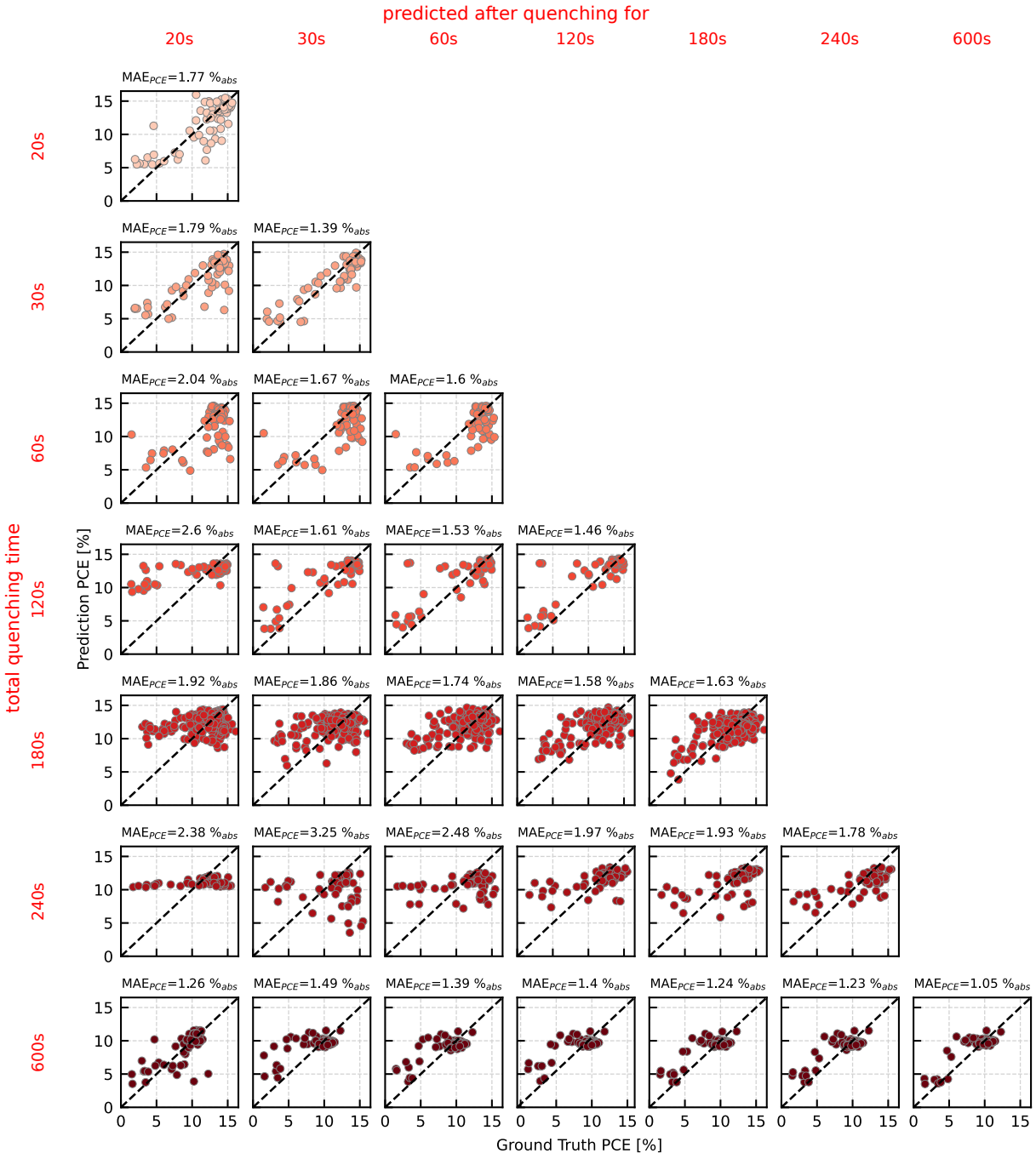

Figure 6.21: Parity plots illustrate the agreement between predicted and ground truth power conversion efficiency (PCE) for various combinations of total actual quenching time (rows) and time of the data forecasting and PCE prediction (columns). The performance of the cascade of models used for data forecasting and PCE prediction is validated by comparing the predicted PCE to the ground truth PCE of the test set solar cells. For all total quenching times, predictive performance improves as the prediction is made later in the process when more monitoring data is accumulated and used as input to the model. Adapted with permission from [352].

synthetic monitoring data progressions, and (b) predicting PCE values for all forecasted scenarios (see Figure 6.18). Due to experimental constraints, each laboratory sample undergoes only a single quenching time, resulting in one unique ground truth PCE per solar cell which is measured and associated with the corresponding quenching time. Determining ground truth PCE values for hypothetical what-if scenarios is impossible because each cell follows a

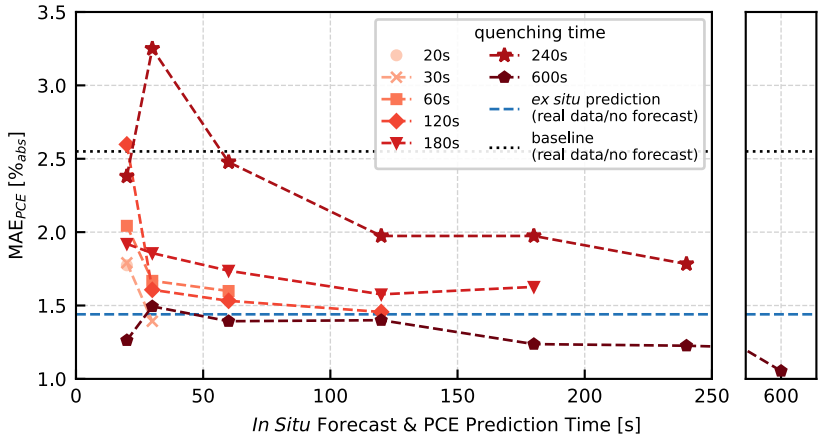

Figure 6.22: Mean absolute error (MAE) when predicting power conversion efficiency (PCE) as a function of *in situ* forecast and prediction time for different quenching times. The MAE decreases as the time of prediction shifts later in the quenching process, indicating that predictive accuracy improves with more accumulated data. The results are compared to human baseline predictions and neural network predictions based on actual ground truth monitoring data without forecasting. Since the MAE is below $2\%_{abs}$ in 23 of 28 total scenarios and for predictions made after 30 seconds or longer, 16 of the 21 scenarios achieve an MAE of less than $1.8\%_{abs}$, the effectiveness of the model cascade in predicting PCE values *in situ* is demonstrated, allowing for early intervention and optimization during thin-film formation. Adapted with permission from [352].

singular process path, resulting in only one ground truth PCE. To validate the forecasting and prediction capabilities of the cascade of ML models, the monitoring data is forecasted to the individual actual quenching time for each sample, and the predicted PCE values for that quenching time are then compared to the respective ground truth measurements.

When evaluated for all devices in the test set, the predicted PCE values show good agreement with the measured ground truth (see Figure 6.21). There is a consistent trend of better agreement as the total quenching time progresses. The MAE of the prediction decreases for all quenching times as the point of prediction is shifted later in the process, suggesting that predictive performance improves as more data is accumulated during the quenching process (see Figure 6.22). This supports the conclusion that more input data leads to enhanced predictive accuracy. To benchmark the predictive accuracy, the prediction error of the model cascade is compared to the human baseline and the neural network predictions generated "*ex situ*" based on the real monitoring data without forecasting (see Table 6.1). In 23 of the 28 scenarios, the MAE is less than $2\%_{abs}$, representing a substantial improvement over the baseline predictions. In scenarios where predictions are made after 30 seconds of quenching or later, the MAE falls below $1.8\%_{abs}$ in 16 of the remaining 21 cases. These results indicate that the cascade of random forests and the neural network can predict final PCE values *in situ* during the quenching process, providing a valuable opportunity to influence material formation based on early data-driven predictions.

The predictive *in situ* capability is further extended by forecasting hypothetical what-if scenarios, that explore the outcome of stopping or continuing quenching for longer times. This allows researchers to visualize multiple scenarios for different quenching times to make data-driven decisions to refine control over the experimental process (see Figure 6.18). While prediction accuracy is validated by forecasting to the actual quenching time and using the known ground truth PCE as reference, the ML cascade also generates quantitative predictions for other hypothetical quenching times by forecasting the monitoring data to any of the valid time steps (20 s, 30 s, ...) and then predicting the corresponding PCE. This approach allows the prediction of the PCE as a function of quenching time, which is updated as the experimental process continues and more monitoring data accumulates over time (see Figure 6.23a and Figure 6.23c). When compared to the measured PCE values at the actual vacuum quenching time, the model predictions agree well, as evidenced by data from specific samples such as the 240-second and 180-second cases in Figure 6.23c and Figure 6.23a, respectively. All other data points, before and after the actual quenching time,

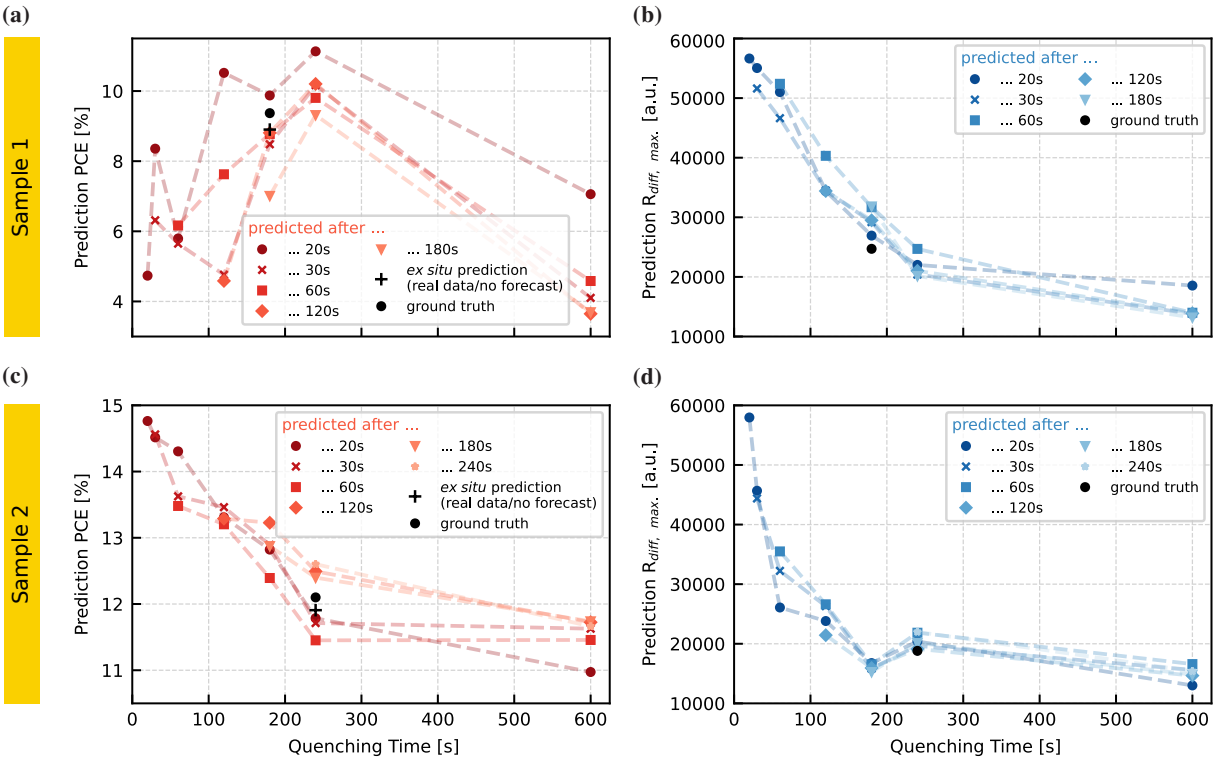

Figure 6.23: *In situ* forecasting and performance prediction for two solar cell samples with different perovskite thin film thickness. (a, c) The cascade of random forest and neural network visualizes the expected PCE as a function of quenching time. As more monitoring data is collected during the experiment, the predictions are updated. This allows recommendations on whether continued quenching is likely to increase the PCE (a) or whether early termination of quenching is beneficial as the PCE is expected to decrease with continued quenching (c). (b, d) The intensity of the diffuse reflection is forecasted as a qualitative indicator of the resulting thin film roughness. The decrease in diffuse reflection is correlated with a decrease in thin film surface roughness, which is slower for some thin films (b) compared to other thin films that show a rapid intensity decrease (d). This approach enables data-driven recommendations for optimization of quenching protocols based on *in situ* forecasting. Adapted with permission from [352].

represent hypothetical scenarios that are accessible only through the predictive *in situ* approach.

These predictions make it possible to generate recommendations on whether early stopping the quenching may be beneficial or whether extending the process would result in a better PCE. For example, for the sample shown in Figure 6.23c, stopping quenching early may be advantageous since continued quenching is predicted to decrease the PCE, while for the sample in Figure 6.23a, extending the quenching time appears beneficial since the PCE is expected to increase. The variation in quenching strategies for different samples is primarily attributed to spatial inhomogeneities in the perovskite thin film properties, which are influenced by the blade coating deposition process. The deposited wet film thickness varies across the substrate, resulting in different behavior during quenching. Sample 2 (see Figure 6.23c) is from a region with a thinner wet film, which allows for rapid solvent removal, favoring shorter quenching times. In contrast, sample 1 (see Figure 6.23a) is from a thicker wet film region that requires longer solvent extraction. This variability highlights the need for customizable quenching protocols, supported by forecasting hypothetical scenarios to realize data-driven recommendations that optimize PCE based on *in situ* predictions.

This *in situ* forecasting and prediction approach can be further refined by updating the forecasts more frequently based on the increasing accumulation of monitoring data, resulting in more prediction curves in Figure 6.23. However, the neural network is trained only on monitoring data corresponding to fixed quenching times (20 s, 30 s,

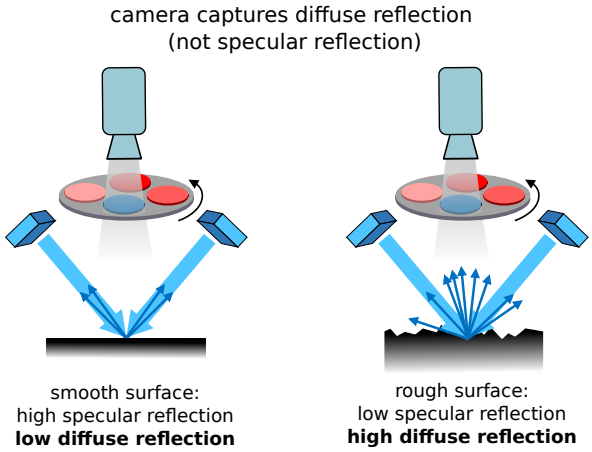

Figure 6.24: Schematic representation of diffuse reflection monitoring for thin film surface roughness assessment. The relationship between thin film morphology and diffuse reflection intensity is used to assess additional perovskite thin film properties using the characterization setup. While a smooth surface results in high specular reflection and low diffuse reflection, a rough surface shows increased diffuse reflection as captured by the camera system. The experimental setup exploits this correlation by using *in situ* diffuse reflection measurements as a qualitative indicator of thin film roughness, enabling morphology forecasting through deep learning-enhanced metrology. Adapted with permission from [352].

...), which means that predictions become unreliable when using out-of-distribution input features that differ from these predefined times. Since the number of possible quenching times is limited, each prediction curve is also constrained to a discrete number of data points (see Figure 6.23). Extending the method to continuous quenching times requires subtask (c), the approximation of a function from the discrete PCE data points produced by the neural network (see Figure 6.18). Linear interpolation or Gaussian processes can be used for this purpose, the latter being a more sophisticated approach to capture potential underlying relationships (see Figure A.16). Extending the model cascade by approximating a continuous prediction function from discrete data points provides researchers with more comprehensive insights into expected PCE trends and a finer granularity for decision-making.

6.5.1.1 Perovskite Thin Film Morphology Forecasting

Building on the predictive capabilities used to forecast PCE, the same methodology is used to forecast the morphological characteristics of the thin film, specifically the surface roughness. The predictive *in situ* approach is applied to assess the device performance and to qualitatively forecast the roughness of the perovskite thin film surface under different scenarios.[352] High surface roughness in perovskite films is detrimental, leading to increased non-radiative recombination, poor interface quality, and stability issues, as rough surfaces are more vulnerable to environmental degradation, including moisture, oxygen, and thermal stress.[299, 322, 448]
To achieve morphology forecasting, DL-enhanced metrology takes advantage of the relationship between thin film roughness and diffuse reflection intensity. A smoother film results in a higher specular reflection and lower diffuse reflection, while a rougher surface leads to higher diffuse reflection. This correlation allows the use of the experimental imaging system that detects diffuse reflection as a qualitative indicator of perovskite thin film roughness (see Figure 6.24). The existing random forest models that forecast monitoring data for different quenching times to predict PCE are now repurposed to forecast how diffuse reflection intensity changes based on different quenching scenarios.
Instead of using the forecasted monitoring data as input for the PCE prediction, the effect of quenching time on the changes in R_{diff} intensity after stopping the quenching process is investigated for the different scenarios (see

Figure 6.19a). For all investigated perovskite thin films, the predicted maximum R_{diff} intensity after quenching decreases with increasing quenching time, implying that longer quenching results in smoother surfaces (see Figure A.17).[304] However, this behavior varies between thin films. For some samples, the decrease in diffuse reflection is observed within the first tens of seconds (see Figure 6.23d), while for others, the reduction is significantly delayed, indicating a delayed decrease in thin film surface roughness (see Figure 6.23b). This variability is primarily due to spatial inhomogeneities in wet film thickness introduced during blade coating. For thinner films, solvent removal is faster, leading to a faster reduction in diffuse reflection intensity corresponding to decreased surface roughness, while thicker films require more time before the diffuse reflection diminishes due to slower solvent extraction.

As with the PCE predictions, the model's forecasts for maximum R_{diff} show good agreement when compared to ground truth values at corresponding quenching times. For example, the predicted diffuse reflection values match well with the experimentally measured values for the 240-second and 180-second cases in Figure 6.23d and Figure 6.23b, respectively. This indicates that the model is able to accurately capture changes in morphology *in situ*, allowing researchers to assess surface roughness and make informed decisions during the material formation process. All other hypothetical scenarios represented by the data points before and after the actual quenching time are accessible only through the predictive approach. In summary, by using the predictive approach for morphology prediction, it becomes possible to gain early insight into both the optoelectronic performance and physical properties of perovskite thin films. The ability to predict roughness *in situ* enhances process control to achieve better interface quality and improved stability in final devices. This dual capability of forecasting both PCE and morphology highlights the versatility of the DL-enhanced predictive methodology, providing a powerful tool for optimizing perovskite solar cell fabrication.

6.5.2 *In situ* AI recommendation system

By using a time-resolved imaging approach, the system benefits from both spatial resolution and temporal information, which allows monitoring data to be collected for multiple locations on a large-area substrate. This makes it possible to perform *in situ* forecasts and predictions of final device PCEs and maximum R_{diff} for multiple regions across the substrate, revealing spatial variations in thin-film quality and corresponding device performance.[352]

The experimental setup includes structured ITO glass substrates with 32 individual perovskite solar cells per blade-coated thin film, arranged in two rows of four small-area samples, each containing four solar cells. *In situ* forecasts and PCE predictions are made for each of the 32 cells, revealing thin film inhomogeneities on the large-area substrate that result in spatial differences of forecasted PCE and morphology. To provide researchers with a more intuitive representation, the quantitative predictions generated by the AI are translated into qualitative recommendations for each of the 32 solar cells (see Figure 6.25). The implementation of such an AI recommendation system *in situ* would enable early, informed assessments of the expected final device performance and morphological properties of the perovskite thin films.

For example, after 20 seconds of quenching, the AI system indicates that five of the 32 solar cells could benefit from continued quenching, while 17 are expected to maintain their current quality and ten are predicted to be adversely affected by further quenching. In terms of the predicted maximum R_{diff}, the AI forecasts that all 32 thin films will experience a significant decrease in surface roughness with continued quenching. When the quenching time reaches 60 seconds and more *in situ* data is available, the updated model predictions lead to adjustments in the AI recommendation. It suggests that roughness would improve for 18 solar cells if quenching continues, while no significant effect is expected for the other 14. Regarding PCE, the system forecasts a detrimental effect for nine solar cells, advises to stop quenching for 13 cells, and anticipates an improvement for the remaining ten cells with longer quenching times. After 180 seconds of quenching, the AI predicts that no further improvement in PCE is possible, categorizes all 32 cells as "quenching stopped too late", and no substantial improvement in surface roughness is expected. This example is consistent with a trend of generally decreasing PCE with increasing quenching time, while at the substrate edges, especially in areas with thicker wet films, this trend is different as the PCE for these

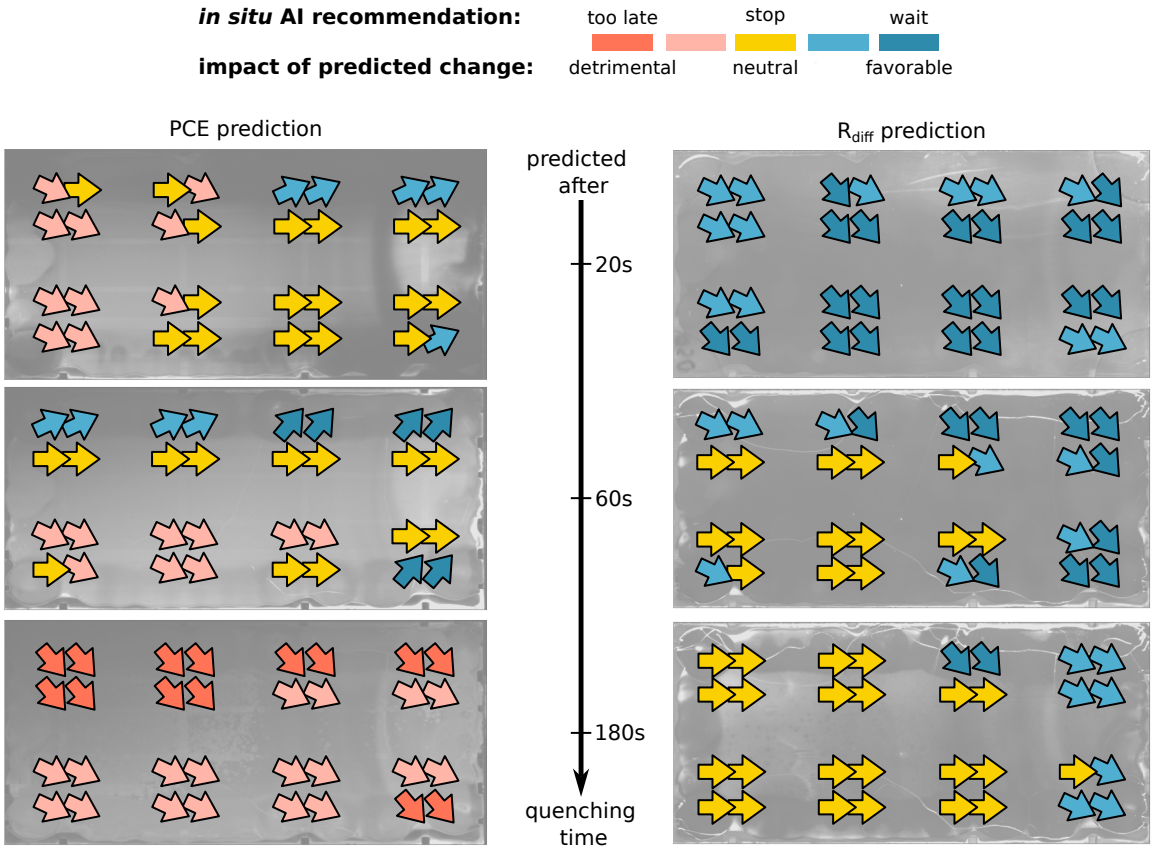

Figure 6.25: *In situ* AI recommendation system for predicting power conversion efficiency (PCE) and morphology on large-area perovskite substrates. Time-resolved imaging is used to generate predictions of PCE (left) and diffuse reflection (R_{diff}) intensity (right), a qualitative indicator of thin film roughness, for multiple locations on the same large-area substrate. The system translates the quantitative predictions into qualitative AI recommendations for each of the 32 individual solar cells, indicating whether stopping the quenching process would be favorable (blue), neutral (yellow), or detrimental (red) based on the forecasted PCE and R_{diff} intensity. This approach allows for location-specific assessments, improving control over large-area thin-film quality and device performance. Adapted with permission from [352].

substrate areas either remains constant or increases with longer quenching (see Figure A.18).

These results demonstrate the ability of the AI recommendation system to provide clear and actionable guidance based on DL-enhanced characterization, which enables a superior level of control over the complex quenching process. By providing early indications of the optimal quenching time, the AI-driven system helps researchers balance multiple objectives, such as maximizing the spatial average PCE on the large-area substrate or achieving the best individual champion solar cell performance. In addition, the intuitive visualization of the multiple potential experimental scenarios (see Figure A.19 and Figure A.20) enables easy qualitative interpretation of the *in situ* recommendations, making it possible to spatially represent predictions of material properties and device efficiencies. In summary, the implementation of this DL-enhanced metrology, combined with clear visualization, provides an early, intuitive, and predictive capability applicable to both academic research and industrial production. It enhances in-line monitoring of process variations and helps to make informed decisions, contributing to consistent and high-quality perovskite solar cell fabrication.

6.6 Summary

This chapter extends the application of ML techniques in experimental research by integrating DL methods into the characterization of the perovskite thin-film formation, enabling early, in-line quality assessments that are otherwise challenging to obtain. By introducing a second, more extensive, and diverse experimental dataset of *in situ* PL and reflection data (research objective **II**, see section 1.2), three increasing complex use cases are addressed that exceed the capabilities of human analysis and require advanced data-driven analysis. To enhance the monitoring of the thin-film formation, DL is used to detect material composition inconsistencies and predict holistic device performance (research objective **III**). In addition, DL is used to implement an *in situ* AI recommendation system for process control (research objective **IV**). The integration of DL enables deeper insights into the fabrication process, facilitating both improved detection of variations in fabrication and active control for optimization.

First, a more comprehensive laboratory-scale dataset of *in situ* PL and diffuse reflection data is generated, including 2215 solar cells fabricated under systematically varied vacuum quenching times. In addition to the fully fabricated solar cells, the new dataset includes 4448 thin films with different perovskite material compositions, namely precursor molarity and molar ratio. This larger and more diverse dataset captures a wider range of process-induced variations, allowing the training of DL models to learn the complex, non-linear relationships between *in situ* monitoring data and the quality of the resulting thin films and solar cell devices.

Second, advanced DL techniques, specifically neural networks, are used to implement *in situ* material composition monitoring to detect subtle variations in precursor molarity and molar ratios to ensure the consistency of materials used for fabrication. The neural networks substantially surpass the human baseline in detecting unwanted precursor variations and outperform most investigated classical ML methods. While the best-performing classical ML model performs slightly better on the current dataset, the neural networks show a faster rate of improvement with increasing amounts of training data, suggesting their potential for superior performance in industrial settings as larger datasets become available.

Third, the application of DL is extended from material-level analysis to device-level prediction, allowing early assessment of thin-film quality and prediction of solar cell performance even before completion into fully fabricated devices. The neural network shows a substantial improvement over previous studies on the first dataset, outperforming the human baseline and most models for PCE prediction reported in the literature, and matching the performance of the best classical ML model while outperforming several other models, especially when trained on larger datasets.

Next, the DL-enhanced approach is advanced from predictive to prescriptive analysis, where DL is used to predict outcomes and to actively inform and optimize the experimental process. By combining forecasting of monitoring data with performance prediction, a cascade of ML models is used to generate actionable *in situ* AI recommendations for improved process control. By forecasting different quenching scenarios and predicting their impact on solar cell performance, the model provides a basis for improved control over thin-film quality through data-driven decision-making during solar cell fabrication.

Finally, the AI recommendation system is applied to large-area substrates generating predictions and recommendations for multiple solar cells. By combining time-resolved imaging data with advanced DL techniques, the system provides spatially resolved feedback for optimizing thin-film quality and device performance across the substrate. This approach demonstrates the versatility of DL in transforming experimental data into actionable recommendations, improving process control, and paving the way for high-throughput production in industrial settings.

In conclusion, deep learning enhances the capabilities of *in situ* characterization of the perovskite thin-film formation, transforming complex experimental data into early in-line quality assessments. The demonstrated ability to detect variations in material composition, predict device performance, and provide recommendations represents a substantial advance in process monitoring required for improved reproducibility and quality control in both research and industrial settings. The superior scaling behavior of neural networks with increasing dataset size suggests particular promise for industrial applications where large-scale data collection is possible. Ultimately,

DL-enhanced monitoring capabilities are critical to the successful commercialization of perovskite PV technology, enabling scalable, high-throughput fabrication with consistently high quality.

7 Enhanced Understanding of the Perovskite Thin-Film Formation through Explainable AI

This chapter demonstrates how explainable artificial intelligence enhances the understanding of perovskite thin-film formation and investigates its impact on solar cell performance. Deep learning models learn the complex relationship between in situ photoluminescence and diffuse reflection data and target variables such as power conversion efficiency and perovskite thin film thickness. XAI is used to render the black-box predictions of these models humanly understandable (research objective ***V****). By comparing different data representations, the importance of temporal versus spatial information is explored, revealing that temporal progression contains crucial information for predicting target variables. Complementary XAI methods are used to not only identify which data features are important but also to explain why they are important. Feature attribution identifies distinct time intervals that are critical for prediction, highlighting nucleation onset as a key factor for accurately predicting PCE and thin film thickness. Counterfactual explanations further elucidate these findings by demonstrating how specific changes in PL intensity during critical phases affect predictions. Insights gained from XAI analysis are translated into actionable recommendations, such as increasing chamber evacuation rates to maximize PL intensity at the onset of nucleation, leading to higher device performance. The iterative feedback loop connecting experimental research with XAI refines the understanding of thin-film formation and accelerates process optimization. In addition to advancing perovskite photovoltaic technology, this framework underscores the broader value of XAI in translating complex model predictions into scientific insights that guide improvements in materials processing.*

Parts of this chapter were published in the research article "Discovering Process Dynamics for Scalable Perovskite Solar Cell Manufacturing with Explainable AI", *Advanced Materials* 36.7 (2024), by *Lukas Klein (L.K.)*, *Sebastian Ziegler (S.Z.)*, *Felix Laufer (F.L.)*, *Charlotte Debus*, *Markus Götz*, *Klaus Maier-Hein*, *Ulrich W. Paetzold (U.W.P.)*, *Fabian Isensee (F.I.)*, and *Paul F. Jäger (P.F.J.)*. *L.K.* and *S.Z.* as well as *U.W.P.*, *F.I.*, and *P.F.J.* contributed equally to this work. This work is the result of collaborative research between Karlsruhe Institute of Technology, Helmholtz AI, Helmholtz Imaging and the German Cancer Research Center (DKFZ).[347, 449] Some figures in this chapter were adapted with permission from [347].
F.L. contributed to this project by leading the experimental materials science investigations, generating and curating the dataset, analyzing the applicability and transfer of explainable AI methods to experimental tasks, and revising visualizations. Additionally, *F.L.* led the writing of the materials science sections of the original draft and the review of the machine learning sections of the manuscript. The contributions of all authors according to the CRediT system are listed in Table A.5.
The computational work published in the research article was conducted by *L.K.* and *S.Z.*, while validation and experimental interpretation were carried out by *F.L.* in collaboration with *L.K.* and *S.Z.*. Building on the published article[347], the evaluations shown in this thesis were performed by *F.L.* using the model weights from the original publication[450].

7.1 Motivation

Interest in machine learning is growing rapidly in the perovskite solar cell research community, as it is considered a powerful tool to accelerate progress toward commercialization of the technology.[153–158, 163–167] However, while ML methods, especially DL models, are capable of making highly accurate predictions, the reasoning behind these predictions is embedded in complex model parameters, obscuring the decision-making process. As a result, these AI methods are often viewed as black boxes, since it is not explained how outputs are generated and which inputs are critical in determining the outputs.[107, 108] However, since scientific understanding is one of the main goals of science, researchers want to understand how the models make their predictions.[269] The black-box nature of the models not only reduces user confidence in scientific applications but also limits their applicability in many real-world use cases where model results must be understood before implementation.

The use of explainable AI enables understanding of the decision-making process of complex models, thereby increasing trust and confidence in AI systems and their outputs.[451] In addition to increased confidence in predictions, understanding the reasoning behind those predictions is essential to validate whether the model is learning meaningful patterns or exploiting spurious correlations due to artifacts in the data.[110] XAI is also used to identify potential biases, errors, or limitations in the model, improving the reliability and robustness of AI models.[452] For human-in-the-loop applications where decisions are not fully delegated to AI systems, XAI supports human decision-making by providing insight into the model's reasoning.[453]

By revealing new insights from complex data patterns, XAI can enhance knowledge discovery, aid hypothesis generation, and advance understanding in scientific research areas.[269, 454] Explainability of AI models is also critical in research to ensure that the models not only provide accurate predictions, but also meaningful insights that can accelerate scientific progress. By presenting AI predictions in an interpretable way, XAI methods can lead to new ideas and concepts.[269]

The benefits of XAI also make it an invaluable additional tool in perovskite solar cell research, as it can elucidate complex relationships between material properties, process parameters, and target variables such as device performance or stability. By enabling researchers to understand which features are most influential to the model's predictions, XAI provides insight into how specific process parameters or material properties affect the target variable. Accordingly, by improving the understanding of the fundamental factors that drive perovskite solar cell performance or stability, XAI can guide efforts to improve fabrication techniques and optimize material composition. However, the application of XAI in perovskite solar cell research has only recently begun to emerge. Current implementations predominantly rely on Shapley additive explanations (SHAP)[112] for feature attribution, which quantifies the contributions of individual features to model predictions.[114–117] While SHAP provides valuable insight into model behavior, its effectiveness is limited when used as the sole interpretability method, particularly due to its underlying assumption of feature independence[112, 118], which can be contradictory to use cases that show complex interdependencies, such as material properties and processing parameters in perovskite research.

Therefore, this chapter uses a comprehensive approach using multiple complementary XAI techniques, which is favorable because it provides deeper insights into model behavior and more reliable interpretations of the complex relationships in perovskite systems.[347, 449] After training DL models to find patterns in complex experimental data, multiple XAI methods are used to render the identified patterns into human-understandable concepts. Translating these concepts into actionable recommendations based on the interpretations made by the human researcher enables data-driven knowledge discovery, capable of finding evidence for or against existing hypotheses but also capable of uncovering insights that lead to new hypotheses.

Using multiple XAI methods, this chapter examines the first of the two generated datasets containing time-resolved multi-channel imaging data, i.e., videos, capturing *in situ* photoluminescence and diffuse reflection during the perovskite thin-film formation using vacuum quenching (see section 5.2).[422] Since all solar cells were fabricated under constant conditions using the same materials, the process parameters are nominally identical. Although variations in solar cell performance are unintended, they result in a dataset that captures real-world process conditions that reflect fluctuations in the fabrication process as it unfolds in reality. By including all potential real-world

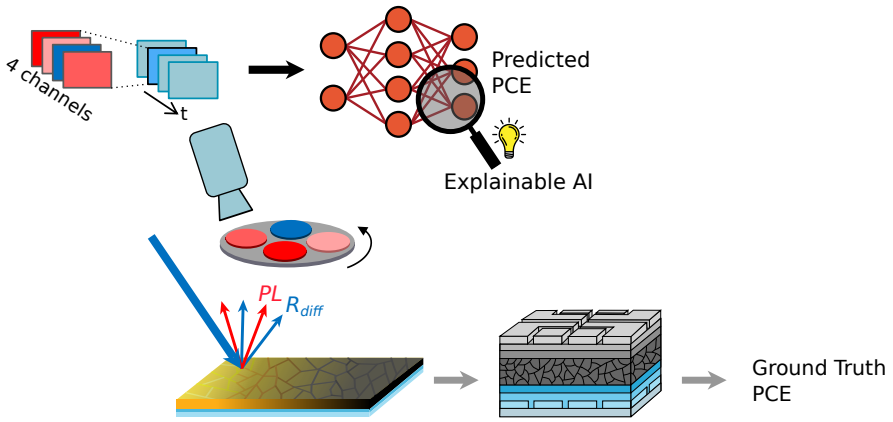

Figure 7.1: Schematic representation of applying explainable AI (XAI) to render model predictions humanly understandable. The imaging setup captures time-resolved multi-channel data, including photoluminescence (PL) and diffuse reflection (R_{diff}), which is used as input to deep neural network models to predict power conversion efficiency (PCE) and perovskite thin film thickness. XAI methods are then applied to analyze the trained model, elucidating the complex correlations between the *in situ* monitoring data and the target variables, providing insight into the underlying process.

parameters that affect the process, without relying on prior assumptions about high- and low-impact process parameters, this approach allows broad, unbiased discovery of optimization pathways. By enabling the identification of distinct process parameters that yield similar results, this methodology supports flexible process optimization, as the thin-film formation process can be influenced by different actions, each suited to specific experimental setups.[347] While there was sparse literature using single XAI methods on tabular perovskite solar cell data[116, 117, 270, 455], at the time of publication, there were no publications using a comprehensive approach of multiple XAI methods in perovskite PV research and no application of XAI addressing complex, non-tabular, high-dimensional data.[347] In the following sections, DL and XAI are used to investigate which factors drive solar cell performance by rendering the complex relationships between perovskite thin-film formation and target variables, such as PCE and thin film thickness, humanly understandable (research objective **V**).[347] By revealing the relative importance of different input features, XAI provides insight into how specific parameters affect final device performance and enables targeted optimization of critical parameters accelerating traditional, incremental scientific progress. First, deep neural networks are trained on different representations of the high-dimensional data, revealing that the temporal progression of *in situ* monitoring data contains more information about final device performance and perovskite thin film thickness than individual images. Next, to elucidate the complex correlations, the trained models are investigated using multiple XAI methods to understand the mappings between the monitoring data and the target variables (see Figure 7.1). To understand which data features are important for the models to predict device performance and thin film thickness, attribution methods[109, 119] are used to compute importance scores for each input feature. After identifying which parts of the input are important using feature attribution, counterfactual explanations[121–123] are used to provide a data-driven explanation of why they are important. Finally, these insights, which are generated only by analyzing the dataset without performing additional laborious experiments, are translated into actionable recommendations for optimizing perovskite thin-film fabrication. In summary, based on neural networks that have learned the mapping between *in situ* monitoring data and target variables, multiple XAI methods render these relationships humanly understandable. The findings are distilled into actionable recommendations that enable targeted optimization and accelerate traditional, incremental scientific progress.

7.2 Importance of Capturing Temporal *In Situ* Data

To systematically investigate which aspects of the video data contain the most relevant information for predicting PCE and perovskite thin film thickness, different approaches to representing the input data are compared. Each data

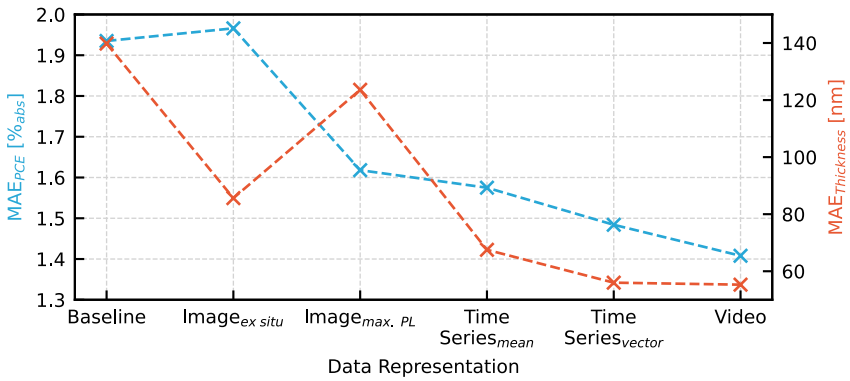

Figure 7.2: Mean absolute error (MAE) for power conversion efficiency (PCE) and thin film thickness predictions using different data representations as model input. Models trained on the *video* representation, which preserves both temporal and spatial information, outperform models using reduced representations. Models trained on data representations that preserve temporal information (*video* and *time series*) show superior performance to those based only on spatial information (*image*), regardless of whether the image captures the maximum PL intensity or the final state after quenching (see Figure A.21 for standardized MAE). Adapted with permission from [347].

representation not only affects the performance of the model but also provides different possibilities for interpretation through its unique way of capturing the information of the video data. Using the different data representations, it becomes possible to isolate the specific temporal and spatial features that influence model predictions, as each representation captures different aspects of the original time-resolved multi-channel imaging data (see section 5.2 for more details on the dataset).[422] The *video* representation captures all spatial and temporal information, while the image representations focus on specific moments of interest and contain only spatial information. The $image_{max.\,PL}$ representation shows the single most prominent *in situ* image, which shows the highest mean PL and the $image_{ex\,situ}$ contains the last image, which emphasizes the final state of the thin film after quenching. In contrast, the time series representations preserve the temporal behavior while reducing spatial complexity. The *time series* $_{mean}$ shows the general temporal dynamics during the thin-film formation because it contains only the temporal information by aggregating each image frame via its spatial mean. The *time series* $_{vector}$ aggregates each frame only in the dimension of the width of the image, resulting in a representation that contains both temporal and some spatial information. Investigating which of these representations performs best is a first step in understanding the complex relationship between the perovskite thin-film formation and solar cell device performance, as it reveals which aspects of the video data are most informative.[347]

For the different data representations, several neural network architectures are explored and the best-performing models are selected based on fivefold cross-validation on the training set. The ResNet[94] architectures perform best for low-dimensional data, using ResNet-152 with 1D convolutions for time series representations and ResNet-18 with 2D convolutions for image-based representations. For the more complex video data, the SlowFast[456] architecture is used, which uses two specialized branches to efficiently process static (slow) and dynamic (fast) information (see [347, 449] for more details on data representations and neural network training).

Evaluation of model performance on the test set shows that models trained using the *video* representation, which combines temporal and spatial information, outperform those using reduced representations (see Figure 7.2). This superior performance suggests that the temporal evolution of spatial features contains important information that is lost in reduced representations, demonstrating the value of preserving both spatial and temporal information. For most data representations, thin film thickness predictions are more accurate than PCE predictions, as only PCE is negatively affected by additional processing steps not captured in the input data (see Figure A.21). Interestingly, models trained on representations that preserve temporal information (*video* and *time series*) outperform those trained on spatial information only (*image*), regardless of whether the image captures the moment of maximum PL or the final state after quenching. This observation suggests that the temporal evolution of features contains critical information about the underlying physical processes that cannot be captured in the single-image analysis. It

suggests that this temporal evolution of features contains the most relevant information for prediction, rather than individual spatial patterns at specific time steps.[347] When the temporal dimension is removed by limiting the input data to a single frame in the *image* representations, the prediction performance is substantially affected by the chosen time step. Consistent with the investigation of the predictive capabilities of *in situ* and *ex situ* features (see section 5.3), thin film thickness prediction is more accurate using the $image_{ex\ situ}$ representation, while the *in situ* representation $image_{max.\ PL}$ is better for PCE prediction.
However, the choice of representation also introduces a trade-off between model performance and other practical considerations. While using all available data in the *video* representation yields the best prediction accuracy, this approach leads to increased computational cost due to the larger training dataset size. Along with the number of model parameters, large training dataset sizes are one of the major contributors to the computational and environmental cost of deep learning.[457, 458] These results demonstrate that while the unreduced *video* representation provides superior performance, rather than defaulting to using all available data, thoughtful reduction of data complexity preserves much of the predictive power while substantially improving computational efficiency, reducing AI's carbon footprint[459–462] and consumption of water[463–465] and electricity[466, 467].
Overall, the trained models show good performance in predicting the general trends, highlighting the successful learning of non-trivial relationships, which is a prerequisite for reliable XAI analysis. In summary, by reducing the high-dimensional data into different data representations that emphasize specific temporal or spatial aspects, this analysis underlines the value of selective data inclusion for model interpretability. It is emphasized that the temporal dimension provides critical information for understanding the perovskite thin-film formation, as the timing of different formation phases is not represented in individual images. Accordingly, the acquisition of single, static *in situ* images is not sufficient, as capturing the temporal dimension is critical for representing the quality of the perovskite thin-film formation when predicting PCE and thin film thickness. Investigating the information content of the different data representations allows distinguishing between temporal and spatial dynamics within the perovskite thin-film formation process and lays the foundation for the subsequent in-depth application of XAI techniques in the following sections.

7.3 Insights into the Thin-Film Formation From Explainable AI

With the various data representations established, several XAI methods are applied to provide robust and reliable insights that elucidate the perovskite thin-film formation process. First, feature attribution[109, 119] is used to compute importance scores for the input features, revealing which data features are most important for the models to predict device performance and thin film thickness. Second, counterfactual explanations[121–123] are generated to understand why these specific input features are considered important by the models.
While the following sections focus on the findings derived from the $time\ series_{mean}$ data representation, the published research article[347, 449] provides a comprehensive overview of the deep learning and XAI results across the different data representations, labels, and XAI methods. By showcasing the key insights, this chapter demonstrates the ability of XAI to improve the data-driven understanding of complex experimental processes.

7.3.1 Feature Attribution

Building on the trained models, XAI is used to render the mapping learned by the ML model between the input data and the target variables humanly understandable. To understand which aspects of the *in situ* monitoring data are most important for the deep learning models to predict PCE and thin film thickness, feature attribution techniques are applied. These methods compute importance scores for the input features, revealing which parts of the input data the model considers most important for its prediction (see section 2.3.7 for more details on XAI methods).
The visualization of the attribution scores for the $time\ series_{mean}$ data representation computed using the expected

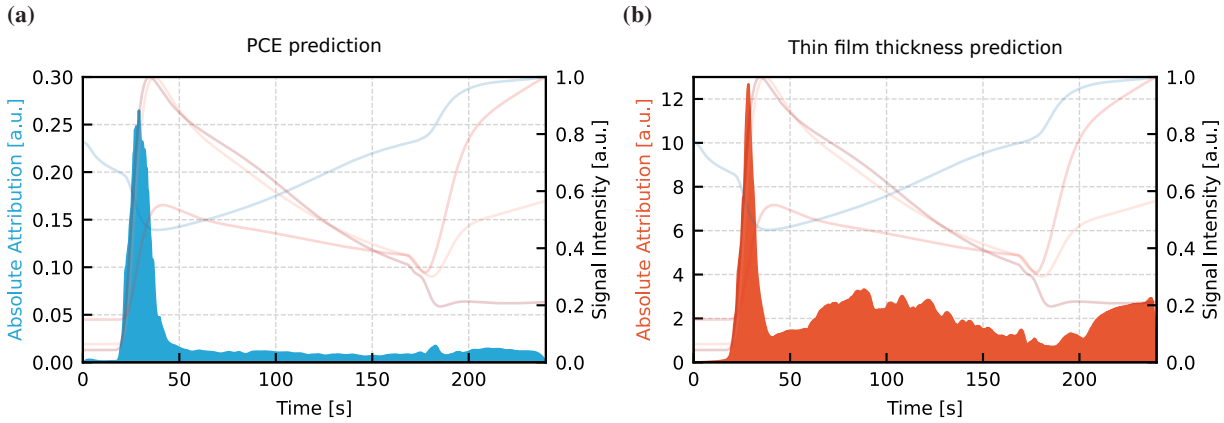

Figure 7.3: Feature attribution for prediction of (a) power conversion efficiency (PCE) and (b) thin film thickness based on the *time series*$_{mean}$ data representation using the expected gradients method. The attribution scores (here: local explanations) indicate time intervals of high importance within the perovskite thin-film formation process rather than isolated time steps. Both models show a peak in attribution around 30 seconds, corresponding to the onset of nucleation. For thickness predictions, the model shows additional importance of data features capturing subsequent process phases. Adapted with permission from [347].

gradients method[120] highlights the importance of different input features for the prediction of PCE and thin film thickness (see Figure 7.3). The analysis of local explanations, i.e., the explanation of the model prediction on a single observation, shows that the models do not identify individual dominant time steps, nor do they consider each time step as equally important. Rather, the analysis highlights distinct time intervals of high importance for the PCE and thickness prediction models. Interestingly, the same time intervals are also highlighted when analyzing the *video* representation, while no noticeable patterns are detected in the spatial attribution in the frames.[347]
The models focus on time periods that coincide with specific phases of the perovskite thin-film formation. Both models show the strongest attribution to the time interval around 30 seconds (see Figure 7.3a and Figure 7.3b), which corresponds to the onset of nucleation and crystallization of the perovskite material, indicated by the onset of PL emission as the first crystals form (see phase II in Figure 7.4; see section 3.1.1.3 for more details on the thin-film formation). For PCE prediction, the model mainly leverages information from this phase to successfully distinguish between nucleation and crystallization monitoring data resulting in high- or low-performing solar cell devices.
For thin film thickness prediction, the model shows great importance of the nucleation onset as well as attribution to other phases of the perovskite thin-film formation (see Figure 7.3b). In addition to considering features containing crystallization information as relevant for thickness prediction (see phase III in Figure 7.4), a substantial attribution is assigned to the final surface morphology formation after quenching is completed at 170 s (see phase IV in Figure 7.4). This suggests that the crystallization and the dynamics after 170 s during the venting phase are important for accurately predicting the thin film thickness. In contrast, the PCE prediction model shows only a small attribution peak at the end of the quenching process at 170 s, indicating that the details of the venting phase are less informative for predicting the device performance compared to the nucleation and crystallization dynamics. Global explanations, i.e., explanations of general patterns obtained by averaging over 100 observations, confirm the findings of the local explanations and emphasize the increased importance of phase IV for thickness prediction.[347]
Further analysis of the feature importance of the individual IPDRI channels reveals that the photoluminescence data is more important than the reflection signal for predicting PCE and thin film thickness. To avoid confirmation bias and unfaithful explanations, several other attribution methods are used to confirm the attribution results to ensure the trustworthiness and robustness of the findings, as diverse techniques may capture complementary perspectives (see [347, 449] for a comprehensive overview of all feature attribution results).
In summary, the models focus on distinct time intervals that contain the most relevant information for the deep

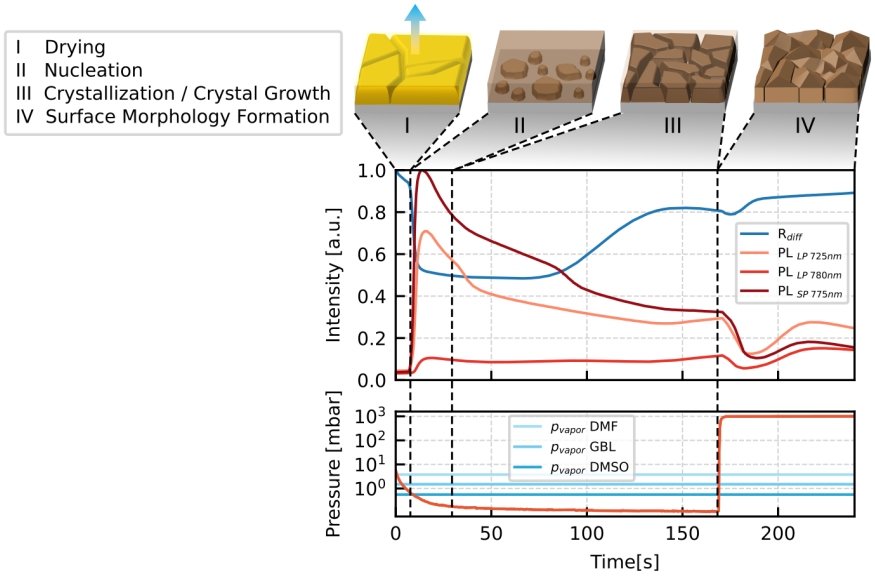

Figure 7.4: Phases of perovskite thin-film formation visualized by characteristic photoluminescence (PL) and diffuse reflection (R_{diff}) transients in the *time series*$_{mean}$ data representation. Vacuum quenching initiates the thin-film formation process, which includes four phases[28]: (I) accelerated drying due to decreasing chamber pressure, (II) onset of nucleation characterized by an initial PL signal as perovskite crystallites form, (III) crystallization characterized by grain coalescence leading to a reduction in PL intensity, and (IV) formation of final surface morphology during venting of the vacuum chamber after vacuum quenching is complete (see section 3.1.1.3 for more details on the thin-film formation). Adapted with permission from [347].

learning models to accurately predict PCE and thin film thickness. The time intervals of high importance coincide with specific phases of the perovskite thin-film formation, with the nucleation onset being the most important for the models. The attribution methods provide guidance on which aspects of the *in situ* monitoring data are most informative for the prediction tasks, informing future experimental design and data collection efforts.

7.3.2 Counterfactual Explanations

By indicating the importance of individual input features, feature attribution highlights which aspects of the perovskite thin-film formation process are most relevant to the models for predicting PCE and film thickness. However, the attributions alone cannot reveal the underlying causal mechanisms leading to the importance scores. To explain the underlying model behavior attributing importance to certain input features, counterfactual explanations (CEs)[121–123] are used (see section 2.3.7 for more details on XAI methods).

CEs generate what-if scenarios by altering input observations to achieve specific counterfactual outcomes. Generating these alternative, hypothetical scenarios provides insight into how the input features would need to change to increase or decrease the model's predictions significantly. By showing the changes required to produce a specific shift in prediction, CEs provide an understanding of the relationship between feature values and target variables. The genetic counterfactuals (GeCo) algorithm[468] is used to generate plausible and feasible CEs.

The counterfactuals are leveraged to visualize how the input would need to change for the model to predict substantially higher or lower values for PCE and thin film thickness compared to the ground truth (see Figure 7.5). The CEs reveal that an increase in the height of the $PL_{LP\,725nm}$ peak coinciding with the onset of nucleation (see phase II in Figure 7.4) leads to higher PCE predictions, confirming that early nucleation dynamics are critical for predicting device performance (see Figure 7.5a). For lower PCE predictions, the height of the nucleation onset peak is reduced and the PL onset time is substantially delayed (see Figure 7.5b).

In contrast, when predicting thin film thickness, the reduced PL intensity at the onset of nucleation and the delayed

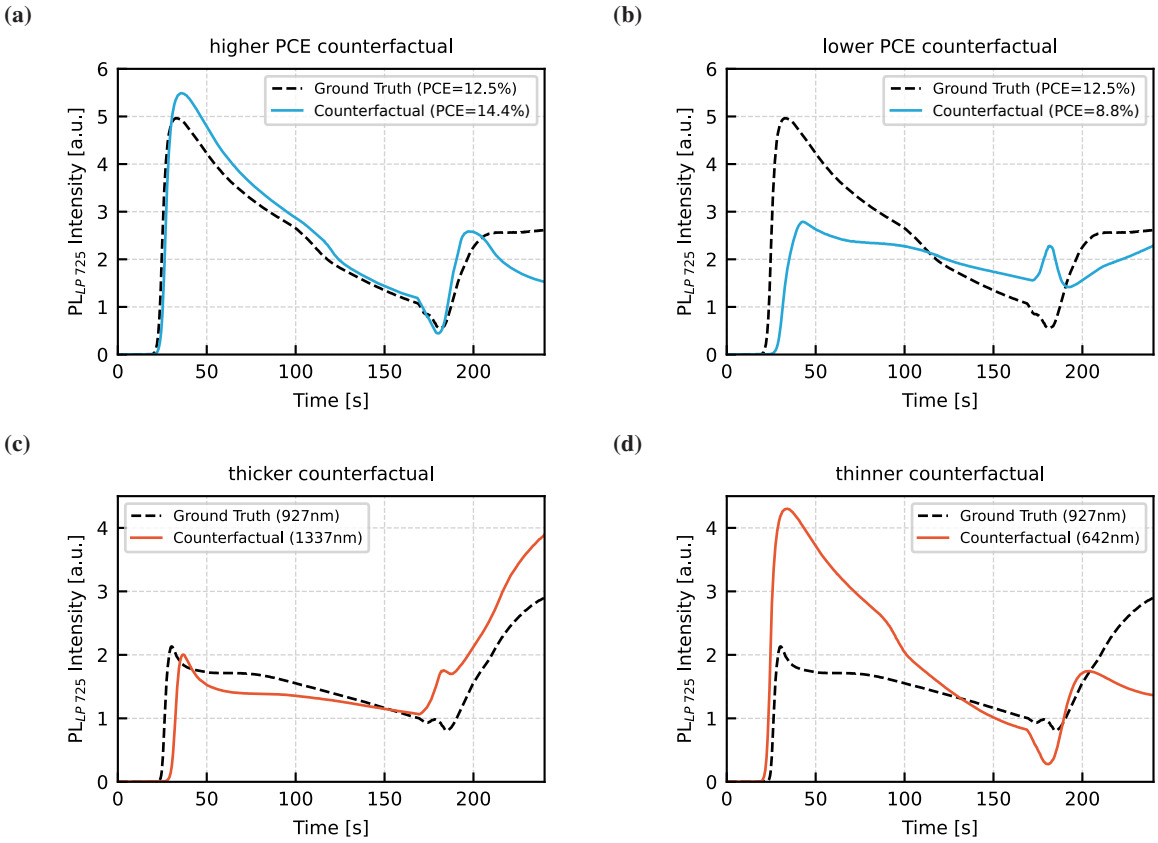

Figure 7.5: Counterfactual explanations for model predictions of power conversion efficiency (PCE) and thin film thickness based on the $\mathrm{PL}_{LP\,725nm}$ intensity channel highlight specific input adjustments required to shift model predictions. (a) Higher PCE counterfactual shows increased PL peak intensity at the onset of nucleation, suggesting that early nucleation dynamics are critical for improved device performance. (b) Lower PCE counterfactual with reduced nucleation peak height and delayed PL onset, indicating lower predicted efficiency. (c) Thicker film counterfactual with reduced PL intensity at nucleation and delayed onset time, and increased PL intensity after quenching is complete. (d) Thinner film counterfactual, with earlier PL onset and increased intensity during nucleation, but reduced PL intensity after quenching. Adapted with permission from [347].

PL onset time result in a higher predicted thin film thickness (see Figure 7.5c). Since feature attribution for thickness prediction considers not only the nucleation onset as important (see Figure 7.3b), the increased PL intensity of the CE at the end of quenching is also relevant for predicting high thickness values. Low-thickness predictions require an earlier PL onset and a substantial increase in PL intensity during nucleation, while the PL intensity at the end of quenching is reduced for the thinner counterfactual (see Figure 7.5d). The analysis is further substantiated by generating counterfactuals for the other IPDRI channels and all other data representations (see [347, 449] for a comprehensive overview of all counterfactual results).

To further support the conclusions drawn from the CEs, testing with concept activation vectors (TCAV)[124] can be used. TCAV provides a more nuanced understanding of model behavior by testing the influence of specific concepts included in the data on model layers responsible for PCE and thickness predictions. Based on the CE analysis, the concepts of high and low nucleation peaks are introduced and their importance is tested for high and low PCE observations. The TCAV results are consistent with the CE-based analysis, showing that the high peak concept is more important for predicting high PCE values, while the concept of low peak is more important for predicting low PCE observations. The published research article[347, 449] provides a comprehensive analysis of all results obtained using TCAV, highlighting the synergies between CE and TCAV investigations.

In summary, counterfactual explanations reveal why the models focus on distinct time intervals for predicting PCE

and thin film thickness. The analysis shows that increasing the early nucleation peak is critical for achieving higher PCE, while variations in PL intensity during the final phase of thin-film formation have a greater impact on thickness predictions. By exploring the importance of identified concepts, TCAV confirms the CE-based findings. By revealing why certain input features are important for predicting PCE and thin film thickness, these XAI methods render the black-box predictions of the neural networks humanly understandable, resulting in increased confidence in the model predictions.

7.4 From XAI Findings to Data-Driven Recommendations for Experimental Research

Applying XAI methods provides deeper insight into the perovskite thin-film formation. It allows these data-driven insights to be translated into actionable recommendations, offering new ways to optimize the fabrication process and improve device performance.[347] An iterative feedback loop facilitates a structured approach to experimentation in which each phase, from experimental research to data collection, model training, XAI analysis, scientific interpretation, and generation of actionable recommendations, complements and informs the next, promoting continuous learning and data-driven refinement of experimental strategies (see Figure 7.6). After elucidating the thin-film formation, the specific insights revealed by XAI are translated into targeted recommendations for optimizing the fabrication process to improve perovskite thin film properties. As several XAI methods are used to avoid confirmation bias, multiple findings are revealed. These insights are interpreted by domain scientists concerning the underlying experimental phenomena and used to generate recommendations for improving the fabrication process. The first finding, that temporal data significantly improves predictive performance, suggests that temporal dynamics are essential for understanding the sequence of different phases during thin-film formation. Consequently, the importance of temporal information underscores the need for comprehensive, *in situ* temporal data acquisition during experiments to ensure that no critical phase of the thin-film formation process is missed. By capturing the full temporal data, researchers gain a more nuanced view of the process dynamics that static measurements cannot provide, underscoring the advantage of time-resolved *in situ* monitoring setups.
The second finding highlights the importance of a pronounced PL peak observed during phase II (see Figure 7.4),

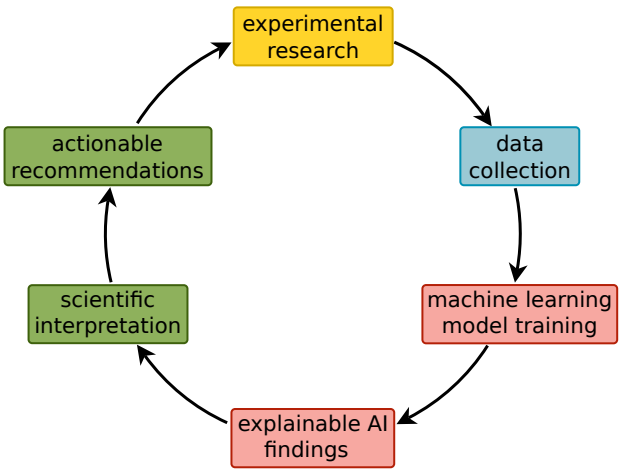

Figure 7.6: Iterative feedback loop connecting experimental research with explainable AI (XAI) for data-driven optimization of the experimental process. Findings revealed by the XAI analysis are scientifically interpreted and translated into actionable recommendations to optimize the experimental process. The structured, cyclical approach enables continuous, data-driven improvement of perovskite thin-film properties, with each cycle informing the next, accelerating scientific progress. Adapted with permission from [347].

as it correlates with high-performing solar cells, suggesting that this phase is critical for device efficiency. This peak is indicative of the nucleation and initial crystallization phases, where the quality of the thin films is largely determined. Since higher peaks lead to improved solar cell performance, the objective is to maximize the PL peak height during nucleation by optimizing process parameters. The scientific interpretation links this observation to the evacuation rate of the vacuum chamber, which affects the PL onset and peak intensity during vacuum quenching, and ultimately also the thin film morphology.[304] Based on this insight, an actionable recommendation to improve nucleation is to increase the chamber evacuation rate during phase II to maximize the PL peak and thereby improve the overall quality of the perovskite thin film.

The third finding emphasizes that the thin film thickness is not only correlated with the nucleation step but also with the crystallization and post-quenching dynamics, which are important to accurately predict the thickness. The scientific interpretation links the measured thickness to the surface roughness of the perovskite thin film, which is affected by the timing of the venting step (see Figure A.17). After quenching, high PL signals during venting are correlated with rougher thin films, which is attributed to residual solvents within the thin film leading to increased surface roughness, resulting in increased PL outcoupling.[304] In contrast, for fully dried perovskite thin films, the morphology does not change during venting, resulting in no substantial change in PL. Since lower PL intensity correlates with smoother thin films, the objective is to minimize the PL intensity during vacuum chamber venting by optimizing process parameters. Therefore, one recommendation is to increase the quenching time, which allows for complete solvent extraction, to prevent high PL signals during venting, resulting in smoother surfaces and mitigating thin film roughness and thickness variation. However, subsequent experiments revealed a detrimental effect of prolonged quenching time on PCE (see Figure A.18a), highlighting the need to optimize the process by implementing a trade-off between a smooth perovskite thin film and the ability to build high-performance solar cells from these thin films (see section 6.5.2).

While this section provides recommendations for improving the experimental process, it also highlights the limitations of XAI methods. The XAI insights are limited by the dataset as there may be process parameters that are not captured in the dataset but still affect the target variables. However, as the dataset contains the monitoring data of the actual thin-film formation itself, it captures the resulting interplay of all parameters affecting the process, thereby minimizing the likelihood of significant unobserved factors. In addition, XAI primarily reveals correlations rather than causal mechanisms, leaving final causal explanations to domain scientists. However, because the interpretation of XAI results is performed by human experts, the reliability of recommendations derived from XAI is increased by the collaborative approach. Furthermore, the approach used here should be considered as a generalizable framework for experimental materials research, as the XAI methods are not limited to perovskite solar cells, but can be adapted to other fabrication processes within materials science. As research progresses, XAI-based approaches are likely to become invaluable tools for the data-driven generation of process understanding needed to further optimize experimental protocols and accelerate scientific discovery across materials science.

In summary, XAI highlights the importance of input features around the PL onset when perovskite nucleation begins. It underscores the impact of nucleation dynamics early during the thin-film formation on overall device performance and suggests that a focus on optimizing this phase could lead to superior device performance. The integration of XAI findings into experimental practice completes a feedback loop in which each cycle of experimentation and analysis informs subsequent experiments. This iterative process enables actionable, data-driven insights that not only improve current fabrication methods, but also provide a transferable framework for advances in other areas of perovskite research and materials science.

7.5 Summary

This chapter investigates the application of explainable AI techniques to improve the understanding of the perovskite thin-film formation process and its impact on solar cell performance. After training deep learning models using photoluminescence and diffuse reflection data, XAI is used to render the complex relationships between *in situ*

monitoring data and target variables humanly understandable (research objective **V**, see section 1.2). Multiple XAI techniques are used to reveal the critical phases during thin-film formation that most influence device performance and perovskite thin film thickness.

First, the importance of capturing the temporal evolution of perovskite thin-film formation is highlighted by comparing the predictive accuracy of different representations of the high-dimensional data. Models trained on data representations that include temporal information outperform those trained on spatial information alone. The analysis highlights the importance of capturing the full temporal progression of the thin-film formation, rather than relying solely on spatial information from single images, as the temporal data provides essential information for predicting device performance.

Next, multiple XAI methods are used to elucidate the insights hidden in the trained deep learning models by interpreting the predictions by the models. Feature attribution is used to identify the specific time intervals that are most important for the predictions. The analysis shows that the onset of perovskite nucleation and crystallization is the most critical phase for the models to predict solar cell performance and thin film thickness accurately. For the prediction of perovskite thin film thickness, the input features that include information on crystallization and post-quenching dynamics also have significant predictive power. To further understand why the input features of these specific phases are important, counterfactual explanations are generated. The counterfactuals show that maximizing PL intensity during nucleation onset is critical for achieving higher device performance. Variations in PL intensity after quenching have a large impact on thickness predictions. By combining multiple XAI methods, this chapter not only explains which data features are important for predicting the target variable but also provides data-driven insights into why these features are important.

Finally, the findings revealed by the XAI analysis are interpreted by human experts and translated into actionable recommendations to optimize the experimental thin-film formation process. These include suggestions to increase the chamber evacuation rate to maximize the nucleation PL peak for higher solar cell performance, as well as using longer quenching times to minimize post-quenching PL intensity, thereby reducing surface roughness and variations in thin film thickness.

In conclusion, the application of XAI techniques renders the complex relationship between *in situ* monitoring data and target variables humanly understandable. By transforming black-box predictions of DL models into interpretable predictions, critical factors in the perovskite thin-film formation process are identified. The insights revealed from XAI enable a deeper understanding of how the perovskite thin-film formation affects solar cell performance and are translated into actionable recommendations for optimizing perovskite thin-film formation. The iterative feedback loop between experimental research, data collection, machine learning, XAI analysis, and the generation of data-driven recommendations enables data-driven optimization of the perovskite thin-film fabrication process, ultimately accelerating scientific progress in perovskite photovoltaics research.

8 Conclusion

8.1 Summary

The commercialization of perovskite photovoltaics requires scaling the technology from laboratory settings to industrial-scale production. However, transitioning from fabrication of small-scale devices to large-area modules introduces critical challenges, including spatial inhomogeneities in absorber quality, increased probability of defects and reduced reproducibility, requiring advanced characterization methods for process monitoring. To address these challenges, this work develops a methodology that combines *in situ* imaging and machine learning to monitor, analyze, predict, and optimize the perovskite thin-film fabrication process.
A large-area imaging technique is introduced, which enables detection of morphological inhomogeneities and defects, such as pinholes and absorber quality variations. Leveraging the temporal resolution, the imaging system is used to monitor the dynamic processes during the thin-film formation consisting of the entangled phases of drying, nucleation, and crystal growth. As the data complexity exceeds the limits of human analysis, the monitoring setup is used to generate two extensive experimental datasets needed for data-driven analysis with ML. The datasets serve as a foundation for analyzing relationships between the thin-film formation and the solar cell performance. To enhance the monitoring of the thin-film formation, machine learning models are applied to detect material composition inconsistencies and predict holistic device performance of individual solar cells. By providing AI-driven recommendations, the methodology enables process optimization while explainable AI is used to elucidate the complex relationship between *in situ* monitoring data and device performance.
As the thesis is structured around five research objectives, the results addressing each of them are discussed (see section 1.2):

I: Novel imaging technique for large-area characterization. To address the need for advanced large-area characterization in perovskite photovoltaics, the *in situ* photoluminescence and diffuse reflection imaging technique is developed in this work. This multi-channel imaging approach combines photoluminescence and diffuse reflection measurements, enabling a comprehensive assessment of thin-film quality and homogeneity by capturing different types of defects and properties in each channel. The system allows the detection of morphological inhomogeneities and defects such as pinholes and variations in absorber quality, which can significantly affect device performance metrics like PCE, before the annealing step. While PL imaging probes optical properties related to crystal quality and non-radiative recombination, the complementary use of electroluminescence imaging provides additional insight into electrical defects in fully fabricated devices.
With a temporal resolution of three frames per second, the IPDRI system enables real-time monitoring, capturing the dynamic processes of drying, nucleation, and crystal growth that occur during perovskite thin-film formation from solution. Identification of these critical phases enables tracking of process dynamics, which is essential for fabricating high-quality perovskite thin films. The integration of large-area imaging capabilities with high temporal resolution makes IPDRI an ideal tool for detecting and correcting process variations, facilitating in-line quality assessment and feedback essential for industrial production. The versatility and utility of IPDRI have been demonstrated in numerous research investigations at KIT.[304, 314, 326, 341, 343–352]

II: Laboratory-scale experimental datasets. To enable data-driven machine learning analysis of perovskite thin-film formation, this work introduces two laboratory-scale experimental datasets from *in situ* monitoring. The

complexity of the perovskite thin-film formation process, with its entangled phases that are influenced by multiple parameters, makes it unsuitable for traditional quantitative or qualitative human analysis. Data-driven ML methods are therefore essential to uncover hidden relationships between the formation process, material properties, and device performance, which requires the generation of suitable comprehensive datasets. To address this need, two extensive datasets are generated using the IPDRI setup.
The first dataset consists of *in situ* PL and reflection data from 1129 blade-coated solar cells fabricated under constant experimental conditions. In addition to PV performance metrics measured experimentally on the finalized solar cell devices, this dataset includes thin film thickness labels for all samples, which are obtained through additional experimental characterization. By limiting variations in solar cell performance to unintended fluctuations during fabrication, this dataset enables the investigation of unwanted process-induced variations in thin-film quality, both across large-area substrates and between different fabrication batches. Building on this, a second, more diverse dataset is generated, including *in situ* monitoring data from 2215 solar cells fabricated with systematically varied vacuum quenching times, as well as 4448 thin films with diverse material properties, such as variations in precursor molarity and molar ratios.
In contrast to datasets that allow general or theoretical PCE predictions based on tabular data of different material properties and device stacks extracted from literature or simulations, the introduced experimental datasets enable PCE prediction of individual solar cells using characterization data. This capability enables real-time feedback and optimization during fabrication. It is demonstrated that *in situ* monitoring is essential, as the correlation between *in situ* data and target variables, such as PCE, is stronger than the correlation achieved using only *ex situ* data acquired after thin-film formation. Unsupervised k-means clustering of *in situ* PL transients reveals distinct data patterns that correlate with device performance, linking earlier PL onsets and higher PL maxima to better PV performance, while spatial analysis of the clusters uncovers process-induced thin film inhomogeneities. To accelerate progress in the field and to enable other researchers to investigate research questions related to the complex perovskite thin-film formation process, both datasets have been published as open-access resources and are publicly available.

III: Material and device property prediction. This work demonstrates the ability of ML to predict precursor material properties, thin film characteristics, and solar cell performance from *in situ* PL and reflection data, enabling early evaluation prior to device completion. At the material level, the methodology predicts precursor molarity and molar ratios, ensuring material consistency by detecting subtle variations. At the thin film level, it accurately predicts thickness, identifying spatial inhomogeneities caused by the blade coating process as well as batch-to-batch variations. Extended to the device level, the models predict key device performance metrics such as PCE, enabling a holistic assessment of thin-film quality prior to subsequent processing steps.
The first dataset is used to compare the performance of various classical supervised ML models for both PV performance metric and thickness predictions, highlighting the importance of model selection and the choice of monitoring channels as model input. The analysis demonstrates the superiority of PL intensity channels, which provide the best accuracy for predicting both thin film thickness and PCE, while underscoring the value of multi-channel data acquisition. With the second dataset, the predictive capabilities are further enhanced by incorporating neural networks in addition to classical models. The neural networks demonstrate scalability advantages, achieving predictive accuracies that match or exceed the best-performing classical methods and show superior improvement with increasing dataset size. This trend underscores their promise for industrial applications, where large-scale data collection enables superior performance. Across all tasks, the ML models substantially outperform baselines representing human predictive capabilities. Compared to the literature, the neural network outperforms most reported use cases, even though PCE prediction in the literature is primarily based on tabular data from cross-study databases rather than experimental characterization data of individual samples.
The ability to predict device performance prior to fabrication completion represents a substantial advance in process monitoring for perovskite PV fabrication. However, challenges remain in predicting holistic PV parameters due to the complexity of device performance, which is influenced by other processing steps that are not captured in the model input data. Despite these limitations, ML substantially enhances *in situ* characterization by transforming

complex experimental data into early in-line quality assessments. This capability allows the detection of material inconsistencies, identification of thin film variations, and prediction of device performance, enabling monitoring for improved quality and reproducibility in both research and industrial applications.

IV: Enhanced experimental data analysis. In addition to improving experimental data analysis, this work demonstrates the essential role of ML in providing actionable *in situ* recommendations to improve control over experimental processes. By moving from predictive to prescriptive analysis, models are used to actively inform and optimize the fabrication process. An AI-driven recommendation system is developed to optimize experimental vacuum quenching parameters. This system uses a cascade of ML models that first forecasts IPDRI monitoring signals as a function of quenching time and then predicts the corresponding expected device performance.
This approach allows for data-driven decision-making during fabrication, enabling process control through dynamic adjustments to optimize thin-film quality and device performance. Applied to large-area substrates, the recommendation system generates spatially resolved predictions and recommendations for multiple solar cells, addressing spatial variations inherent in scalable fabrication. By transforming complex experimental data into actionable recommendations, the system uses ML to provide comprehensive feedback that enhances process control and optimization beyond traditional predictive analytics.

V: Insights into thin-film formation. Explainable AI techniques are applied to make the complex correlations between *in situ* monitoring data and the target variable PCE and thin film thickness relationships humanly understandable. The analysis highlights the importance of capturing the temporal evolution of thin-film formation, as opposed to relying solely on spatial information from single images. Multiple XAI methods are used to reveal the insights hidden in the trained black-box neural networks. Feature attribution analysis identifies critical phases during the formation process, with the onset of perovskite nucleation emerging as particularly important for predicting device performance, while post-quenching dynamics in the monitoring data show a substantial impact on thin film thickness. To gain a deeper understanding of the formation dynamics, counterfactual explanations are generated that provide insights into why the input features of these specific phases are important and how they influence the prediction results. These data-driven insights are translated into actionable recommendations for optimizing the fabrication process, including increasing the chamber evacuation rate to enhance the nucleation PL peak and adjusting the quenching time to minimize post-quenching PL intensity to reduce surface roughness and thickness variations. The iterative feedback loop between experimental research and data-driven insights uses XAI findings to guide process modifications, resulting in improved thin-film formation. More broadly, explainable AI has great potential to uncover hidden relationships learned by models from complex datasets, providing deeper understanding and enabling targeted optimizations that further advance perovskite PV research and commercialization.

In summary, the results presented in this work represent significant progress toward achieving the scalable, reproducible perovskite thin-film fabrication required for industrial production. By integrating advanced *in situ* imaging techniques, comprehensive experimental datasets, machine learning, and explainable AI, this work demonstrates novel approaches for process monitoring, material and device property prediction, and actionable process optimization. These advances address critical challenges in thin-film quality, defect detection, and reproducibility. Long-term stability remains the primary barrier to the widespread adoption of perovskite PV technology. Advanced *in situ* monitoring and machine learning techniques are powerful tools to address this challenge by enabling early detection of degradation processes and supporting data-driven strategies to improve material and device durability. The following section provides an outlook on the next steps needed to overcome these challenges and further advance the scaling of perovskite PV technology.

8.2 Outlook

Provided that the challenge of long-term stability can be overcome, perovskite PV technology is poised to play a key role in meeting the planet's growing demand for sustainable electrical energy. This immense potential underscores the need for continued innovation in scalable manufacturing processes, advanced monitoring techniques, and ML-based optimization. Building on the progress made in this work, this outlook explores the critical next steps and examines how ML can help address remaining challenges and drive further advances in perovskite PV research.

***In situ* monitoring limitations.** While *in situ* monitoring provides insight into the perovskite thin-film formation process, a fundamental limitation of the current approach is its inability to capture information about previous or subsequent processing steps in the device stack that also affect device performance metrics. For example, irregularities that occur during substrate handling or during the deposition of subsequent layers, such as transport layers or electrodes, can significantly affect the final device performance but are not accounted for in the current input data. As a result, predictions that are accurate for the perovskite thin film may not capture the holistic behavior of the entire device.
To address these limitations, future efforts could combine *in situ* monitoring with *ex situ* characterization after key process steps. For example, additional PL and reflection imaging *ex situ* after the device has undergone all fabrication steps would provide a dataset that includes the effects of all processes. This complementary approach could provide a more complete understanding of device performance and improve the accuracy of predictions for metrics that are influenced by interactions within the entire layer stack.
In addition, extending the imaging capabilities of IPDRI to monitor the fabrication of other layers in the stack could be a transformative step. This could involve using UV excitation to achieve photon energies above the bandgap of these layers, thereby enabling the capture of photoluminescence signals. In cases of insufficient luminescence, alternative data sources such as reflection or absorption measurements could provide valuable insights. Combined, these improvements would broaden the applicability of *in situ* monitoring and contribute to a more integrated understanding of perovskite photovoltaic device fabrication.

Temporal and spatial data aggregation. This work focuses on the analysis of the transient evolution of PL intensity during perovskite formation, leaving the detailed study of spatial inhomogeneities, such as pinholes and other material defects, to future investigations. To fully exploit the rich data provided by IPDRI monitoring, future research should aim to unify temporal and spatial analysis in a predictive framework. Spatial information on defects and inhomogeneities could complement temporal evolution data, providing valuable insights into the interplay between local material properties and overall device performance. Integrating both temporal and spatial dimensions could improve prediction accuracy and provide a deeper understanding of the relationship between thin-film formation and device quality.
Dimensionality reduction techniques like autoencoders could play a key role by compressing spatial data into low-dimensional latent representations that preserve essential features, such as spatial homogeneity and defect patterns. These latent representations balance the need to maintain critical information contained in the video data with the computational efficiency required for high-dimensional data. Tracking the temporal change of these compressed spatial features could enable powerful predictive modeling, providing new insight into the relationship between local material properties and overall device performance. In addition, not all time steps during thin-film formation are equally informative for prediction. Methods such as feature attribution help identify the most critical phases for prediction, reducing data complexity while improving model accuracy.

Defect detection through segmentation and classification. As perovskite PV transitions to industrial-scale production, advanced defect detection is essential to maintain consistent device quality and high production yields. The combination of segmentation and classification techniques enables comprehensive defect analysis, enabling early detection of pinholes, cracks, and inhomogeneities.

Semantic segmentation creates pixel maps of thin-film irregularities, capturing the spatial distribution of defects such as pinholes and thickness variations. These maps provide valuable insight for process monitoring and optimization. Classification complements segmentation by categorizing defects based on type, severity, and potential impact on device performance, distinguishing minor inhomogeneities from critical defects like pinholes that significantly reduce device performance. ML improves defect detection by identifying subtle patterns and early indicators of defect formation that may not be visually apparent to human inspection, enabling proactive intervention during fabrication. Explainable AI techniques further provide insight into why specific features are flagged as defects and how they contribute to performance losses, helping to investigate the underlying causes of defect formation.
Advanced, automated defect detection is particularly relevant for large-scale production and high-throughput experimentation, where traditional human inspection is not feasible. Integrating these methods into real-time monitoring systems could enable immediate detection and classification of defects during high-throughput production, supporting rapid process adjustments to maintain quality standards. Linking defects to device performance establishes a feedback loop that optimizes fabrication processes to minimize defects, reduce waste, and increase yield.

Multimodal ML-based monitoring. While the IPDRI system has demonstrated the value of *in situ* monitoring, advancing perovskite PV manufacturing will require the integration of multiple complementary characterization techniques. Multimodal datasets combining imaging, spectroscopy, and environmental parameters provide a holistic view of how fabrication conditions affect material properties and device performance. By providing deeper insight into process-parameter relationships, these datasets can support effective optimization strategies.
Integrating such diverse data streams requires ML frameworks capable of processing and correlating information from multiple sources. Combining data from IPDRI with environmental sensor readings (e.g., temperature, humidity), deposition rate measurements, and additional *in situ* techniques could enable more robust process control. These multimodal ML-based approaches increase predictive power and interpretability, making them essential for industrial-scale production.
A comprehensive monitoring framework could incorporate high-resolution *ex situ* methods alongside production-friendly *in situ* techniques. While high-resolution methods such as scanning electron microscopy, atomic force microscopy, and whitelight interferometry provide detailed insights into surface morphology and layer thickness, they are limited in their applicability in production settings because they are time-consuming and often destructive. Instead, non-destructive and fast techniques that are well-suited for real-time characterization in production lines are likely to complement imaging systems such as IPDRI. These include *in situ* point probe measurements such as X-ray diffraction for crystal structure analysis, spectroscopic ellipsometry for thickness monitoring, and spectral measurements that combine photoluminescence, reflection, absorption, and transmission data for comprehensive optical characterization.
The development of ML models capable of handling diverse data types, temporal resolutions, and spatial scales is key to processing and interpreting these multimodal streams. Such systems would enable sophisticated quality control by exploiting the complementary strengths of different characterization techniques, ultimately supporting industrial-scale monitoring and optimization.

Broadening ML capabilities in thin film analysis. While this work has demonstrated the potential of ML for predicting PCE based on *in situ* monitoring data, future developments can extend these capabilities to a broader range of thin-film properties critical to perovskite solar cells. Multi-task learning frameworks could improve accuracy by simultaneously predicting related properties. Efforts could focus on target properties such as photoluminescence quantum yield (PLQY) and absorption, for which labeled datasets can be generated with limited effort due to simple measurement techniques. In particular, PLQY offers a valuable alternative for evaluating thin-film quality because, unlike PCE, it does require complete device fabrication. More complex but important targets, such as grain size and long-term stability metrics, also hold promise for ML-based prediction. Although generating training labels for these properties requires more extensive characterization efforts, their successful prediction during fabrication using early *in situ* data would be highly valuable for accelerating material and process

optimization.
To ensure robustness, ML models need to generalize across different perovskite compositions and processing methods. Transfer learning could enable models to adapt between fabrication methods such as blade coating, slot-die coating, and inkjet printing, or extend pre-trained models to new material systems. Incorporating uncertainty quantification into ML frameworks would add confidence metrics to predictions and help identify areas for improvement. Integrating these ML-based monitoring capabilities with high-throughput manufacturing systems is particularly promising. Robotic automation can generate large datasets that can be used to train more sophisticated models to drive process optimization. Extending the explainable AI approaches demonstrated in this work to interpret material composition predictions could further uncover relationships between processing and material properties.

The advances presented in this work are part of the rapidly growing field of machine learning applications for perovskite photovoltaics. With its versatility and ability to tackle complex tasks, ML is becoming an indispensable tool for materials researchers and is driving extensive efforts to address diverse challenges in perovskite PV research (see section 2.4). Looking ahead, the synergy of global experimental research on long-term stability and large-area upscaling, accelerated by the predictive power and optimization capabilities of ML, holds great promise for overcoming barriers to perovskite PV commercialization.

Appendix

A.1 Resources, Funding, and Tools

All experimental work was performed within the laboratory infrastructure of the Light Technology Institute (LTI) at the Karlsruhe Institute of Technology (KIT), primarily provided by Prof. Dr. Ulrich W. Paetzold and Prof. Dr. Uli Lemmer. A detailed description of the experimental tools used for this work can be found in Chapter 3.

This PhD thesis and the associated research were only made possible by funding secured by Prof. Dr. Ulrich W. Paetzold from various funding agencies, including the *Helmholtz Association* (program-oriented funding phase IV, MTET Topic 1, Code: 38.01.05 / project AI-INSU-PERO, ZT-I-PF-5-106 / project AutoPeroSol, ZT-PF-3-020 / Solar Technology Acceleration Platform (Solar TAP) / HYIG of U.W.P., VH-NG-1148), the *German Federal Ministry for Economic Affairs and Climate Action (BMWK)* (project CAPITANO, 3EE1038B / project SHAPE, 03EE1123A), the *German Federal Ministry of Education and Research (BMBF)* (PRINTPERO, 03SF0557A), and the *Karlsruhe School of Optics & Photonics (KSOP)*.

This work relied heavily on free and open-source software libraries, as well as access to high-performance computing (HPC) resources. Machine learning applications were implemented using *Python* and several key libraries, including *scikit-learn*, *PyTorch*, and *pandas*. A complete list of all *Python* packages and their respective versions is provided in section 2.3.9. Computational experiments were performed on the HPC clusters *bwUniCluster 2.0* and *Helmholtz AI computing resources (HAICORE)@KIT*, supported by the *state of Baden-Württemberg through bwHPC* and the *Helmholtz Association Initiative and Networking Fund on the HAICORE@KIT partition*. Version control and collaborative development were managed using *Git* and *GitHub*, while *Zenodo* was used for open access sharing of the generated datasets.
Additional software tools were used to facilitate various aspects of data processing and documentation. *ImageJ* was used for quick inspection of raw images, while all graphs were generated using *Python*. Figures with sketches were created with *Inkscape*. References were managed using *Mendeley* and *JabRef*. The thesis was written in *LaTeX* with the editor *TeXstudio*.
AI-assisted technologies were used as writing aids to check spelling and suggest grammatical improvements. These tools were strictly used to improve readability and grammar and did not contribute to the creation of the scientific content. The author reviewed and edited all AI-based suggestions and takes full responsibility for the content of the work. The AI-based tools used include *ChatGPT 4/4o*, *Grammarly*, *DeepL*, and *Claude 3.5 Sonnet*.

A.2 Author Contributions According to CRediT System

When publishing within collaborative research projects, *CRediT (Contributor Roles Taxonomy)* is a taxonomy that allows for a high-level description of 14 roles played by contributors in the research process. It informs about individual author contributions to the research project and reduces disagreements between collaboration partners.[469]

Table A.1: Overview of the categories used in this work to identify the contributions of different authors according to the contributor role taxonomy (CRediT) by Brand *et al.*[469]

Category	Definition
Conceptualization	Ideas; formulation or evolution of overarching research goals and aims
Methodology	Development or design of methodology; creation of models
Investigation	Conducting a research and investigation process, specifically performing the experiments, or data/evidence collection
Data Curation	Management activities to annotate (produce metadata), scrub data and maintain research data (including software code, where it is necessary for interpreting the data itself) for initial use and later reuse
Software	Programming, software development; designing computer programs; implementation of the computer code and supporting algorithms; testing of existing code components
Formal Analysis	Application of statistical, mathematical, computational, or other formal techniques to analyze or synthesize study data
Validation	Verification, whether as a part of the activity or separate, of the overall replication/reproducibility of results/experiments and other research outputs
Writing – Original Draft	Preparation, creation and/or presentation of the published work, specifically writing the initial draft (including substantive translation)
Writing – Review & Editing	Preparation, creation and/or presentation of the published work by those from the original research group, specifically critical review, commentary or revision – including pre- or post-publication stages
Visualization	Preparation, creation and/or presentation of the published work, specifically visualization/data presentation
Project Administration	Management and coordination responsibility for the research activity planning and execution
Funding Acquisition	Acquisition of the financial support for the project leading to this publication
Resources	Provision of study materials, reagents, materials, patients, laboratory samples, animals, instrumentation, computing resources, or other analysis tools
Supervision	Oversight and leadership responsibility for the research activity planning and execution, including mentorship external to the core team

A.2.1 Correlative In Situ Multichannel Imaging for Large-Area Monitoring of Morphology Formation in Solution-Processed Perovskite Layers

The research article "Correlative In Situ Multichannel Imaging for Large-Area Monitoring of Morphology Formation in Solution-Processed Perovskite Layers" was published in *Solar RRL* by *Simon Ternes (S.T.)*, *Felix Laufer (F.L.)*, *Philip Scharfer (P.S.)*, *Wilhelm Schabel (W.S.)*, *Bryce S. Richards (B.S.R.)*, *Ian A. Howard (I.A.H.)* and *Ulrich W. Paetzold (U.W.P.)*. *S.T.* and *F.L.* contributed equally to this work.[341]

Table A.2: Author CRediT – Correlative In Situ Multichannel Imaging for Large-Area Monitoring of Morphology Formation in Solution-Processed Perovskite Layers

Category	Authors	Details
Conceptualization	*S.T.* & *I.A.H.*	Conceptualization of imaging setup
Methodology	***F.L.***, *S.T.*, *I.A.H.* & *U.W.P.*	Application of system on the drying channel at different drying parameters
Investigation	***F.L.*** & *S.T.*	Conducting of experiments by *F.L* and *S.T.*, chemical engineering of devices by *S.T.*
Data Curation	***F.L.*** & *S.T.*	Creating of 'database' and detection of trends by *F.L.*, defect analysis by *S.T.*
Software	***F.L.*** & *S.T.*	Camera operation, filter wheel control via microcontroller, data post-processing
Formal Analysis	***F.L.*** & *S.T.*	Data evaluation and interpretation
Validation	*S.T.* & ***F.L.***	Comparison with spectral one-point probe PL setup by *F.L.*, comparison with literature by *S.T.*
Writing – Original Draft	*S.T.*	-
Writing – Review & Editing	***F.L.***, *B.S.R.*, *I.A.H.* & *U.W.P.*	-
Visualization	***F.L.***, *S.T.*, *B.S.R.*, *I.A.H.* & *U.W.P.*	Original figures by *F.L.* & *S.T.*, revised by *B.S.R.*, *I.A.H.* & *U.W.P.*
Project Administration	*I.A.H.* & *U.W.P.*	-
Funding Acquisition	*W.S*, *B.S.R.* & *U.W.P.*	-
Resources	*I.A.H.*, *P.S.* & *W.S*	-
Supervision	*P.S.*, *W.S*, *B.S.R.*, *I.A.H.* & *U.W.P.*	-

A.2.2 Process Insights into Perovskite Thin-Film Photovoltaics from Machine Learning with In Situ Luminescence Data

The research article "Process Insights into Perovskite Thin-Film Photovoltaics from Machine Learning with In Situ Luminescence Data" was published in *Solar RRL* by *Felix Laufer (F.L.)*, *Sebastian Ziegler (S.Z.)*, *Fabian Schackmar (F.S.)*, *Edwin Andres Moreno Viteri (E.A.M.V.)*, *Markus Götz (M.G.)*, *Charlotte Debus (C.D.)*, *Fabian Isensee (F.I.)* and *Ulrich W. Paetzold (U.W.P.)*.[346]

Table A.3: Author CRediT – Process Insights into Perovskite Thin-Film Photovoltaics from Machine Learning with In Situ Luminescence Data

Category	Authors	Details
Conceptualization	***F.L.*** & *U.W.P.*	-
Methodology	*F.S.*	Application of *in situ* monitoring during vacuum quenching
Investigation	***F.L.***, *F.S.* & *E.A.M.V.*	Performing experimental lab work to generate the dataset
Data Curation	***F.L.*** & *S.Z.*	Dataset generation, maintenance, and publication
Software	***F.L.*** & *S.Z.*	Writing code for machine learning evaluation by *F.L.*, review and validation by *S.Z.*
Formal Analysis	***F.L.*** & *S.Z.*	Data evaluation and interpretation by *F.L.*, review and validation by *S.Z.*
Validation	*S.Z.*, *M.G.*, *C.D.* & *F.I.*	-
Writing – Original Draft	***F.L.***	-
Writing – Review & Editing	*S.Z.*, *F.S.*, *M.G.*, *C.D.*, *F.I.* & *U.W.P.*	-
Visualization	***F.L.***	-
Project Administration	*M.G.*, *C.D.*, *F.I.* & *U.W.P.*	-
Funding Acquisition	*M.G.*, *C.D.*, *F.I.* & *U.W.P.*	-
Resources	*M.G.*, *F.I.* & *U.W.P.*	-
Supervision	*C.D.*, *F.I.* & *U.W.P.*	-

A.2.3 Deep learning for augmented process monitoring of scalable perovskite thin-film fabrication

The research article "Deep learning for augmented process monitoring of scalable perovskite thin-film fabrication" was published in *Energy & Environmental Science* by *Felix Laufer (F.L.)*, *Markus Götz (M.G.)*, and *Ulrich W. Paetzold (U.W.P.)*.[352]

Table A.4: Author CRediT – Deep learning for augmented process monitoring of scalable perovskite thin-film fabrication

Category	Authors	Details
Conceptualization	***F.L.*** & *U.W.P.*	-
Methodology	***F.L.***	-
Investigation	***F.L.***	-
Data Curation	***F.L.***	-
Software	***F.L.***	-
Formal Analysis	***F.L.***	-
Validation	*M.G.* & ***F.L.***	-
Writing – Original Draft	***F.L.***	-
Writing – Review & Editing	*M.G.* & *U.W.P.*	-
Visualization	***F.L.***	-
Project Administration	*U.W.P.*	-
Funding Acquisition	*M.G.* & *U.W.P.*	-
Resources	*M.G.* & *U.W.P.*	-
Supervision	*U.W.P.*	-

A.2.4 Discovering Process Dynamics for Scalable Perovskite Solar Cell Manufacturing with Explainable AI

The research article "Discovering Process Dynamics for Scalable Perovskite Solar Cell Manufacturing with Explainable AI" was published in *Advanced Materials* by *Lukas Klein (L.K.)*, *Sebastian Ziegler (S.Z.)*, *Felix Laufer (F.L.)*, *Charlotte Debus (C.D.)*, *Markus Götz (M.G.)*, *Klaus Maier-Hein (K.M.H.)*, *Ulrich W. Paetzold (U.W.P.)*, *Fabian Isensee (F.I.)* and *Paul F. Jäger (P.F.J.)*. *L.K.* and *S.Z.* as well as *U.W.P.*, *F.I.*, and *P.F.J.* contributed equally to this work.[347]

Table A.5: Author CRediT – Discovering Process Dynamics for Scalable Perovskite Solar Cell Manufacturing with Explainable AI

Category	Authors	Details
Conceptualization	*L.K.*, *S.Z.*, *F.I.* & *P.F.J.*	-
Methodology	*L.K.* & *S.Z.*	Training neural networks by *S.Z.* and applying various explainable AI methods by *L.K.*
Investigation	*L.K.*, *S.Z.* & ***F.L.***	Machine learning focused investigation by *L.K.* and *S.Z.*, experimental material science focused investigation by *F.L.*
Data Curation	***F.L.*** & *S.Z.*	Work based on dataset generated and maintained by *F.L.*
Software	*L.K.* & *S.Z.*	Training neural networks by *S.Z.* and applying various explainable AI methods by *L.K.*
Formal Analysis	*L.K.*,*S.Z.* & ***F.L.***	Analysis of investigated neural networks and XAI results by *L.K.* and *S.Z.*, analysis of applicability and transfer to experimental materials science task by *F.L.*
Validation	***F.L.***, *C.D.*, *M.G.*, *K.M.H.*, *U.W.P.*, *F.I.* & *P.F.J.*	-
Writing – Original Draft	*L.K.*, *S.Z.* & ***F.L.***	Focus on machine learning parts by *L.K.* and *S.Z.*, focus on experimental material science parts by *F.L.*
Writing – Review & Editing	***F.L.*** , *C.D.*, *M.G.*, *K.M.H.*, *U.W.P.*, *F.I.* & *P.F.J.*	-
Visualization	*L.K.*, *S.Z.* & ***F.L.***	Original figures by *L.K.* & *S.Z.*, revised by *F.L.*
Project Administration	*U.W.P.*, *F.I.* & *P.F.J.*	-
Funding Acquisition	*M.G.*, *C.D.*, *F.I.* & *U.W.P.*	-
Resources	*M.G.*, *K.M.H.*, *P.F.J.*, *F.I.* & *U.W.P.*	-
Supervision	*U.W.P.*, *F.I.*, & *P.F.J.*	-

A.3 Photoluminescence Versus Electroluminescence

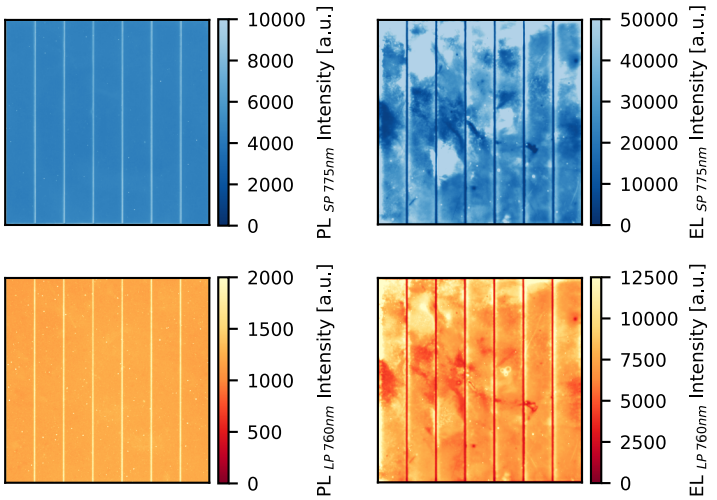

Figure A.1: PL and EL imaging of all-perovskite tandem solar mini-modules. The PL response (left column) is captured using a 760 nm longpass filter to image the bottom subcell ($E_G \approx 1.26$ eV) and a 775 nm shortpass filter (combined with a 665 nm longpass) to image the top subcell ($E_G \approx 1.78$ eV). PL images show high uniformity of the layer stack. However, the EL response (right column) of both subcells displays large-area diffuse homogeneities. Solar mini-modules provided by [314].

A.4 *In Situ* Imaging Setup – Applications

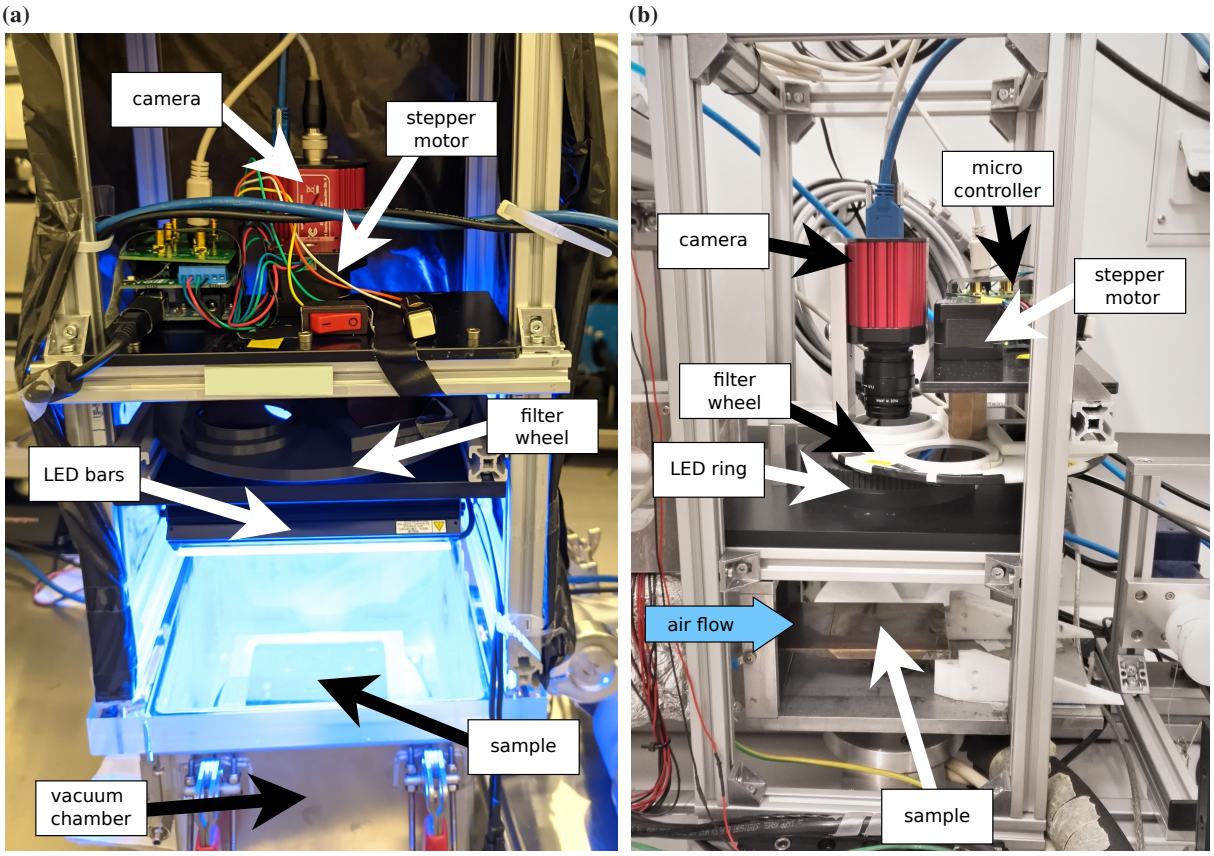

Figure A.2: Photograph of IPDRI integrated into experimental setups. (a) Photograph of IPDRI integrated into the vacuum quenching setup. IPDRI is placed on top of the transparent lid of the vacuum quenching chamber, which is evacuated, causing the wet film to dry and the perovskite thin film to form. During the formation, the samples are excited with blue LED bars, and the signals (emitted PL and diffuse reflection) are detected with a camera. By synchronizing the camera trigger with the rotation of the wheel carrying different spectral filters, *in situ* multi-channel videos of the perovskite thin-film formation are obtained. Adapted with permission from [346]. (b) Photograph of IPDRI integrated into the laminar airflow channel. IPDRI is placed on top of the drying channel above the sample which is exposed to a laminar airflow, causing the wet film to dry and the perovskite thin film to form. During the formation, the samples are excited with a blue LED ring, and the signals (emitted PL and diffuse reflection) are detected with a camera. By synchronizing the camera trigger with the rotation of the wheel carrying different spectral filters, *in situ* multi-channel videos of the perovskite thin-film formation are obtained.[341, 342, 418]

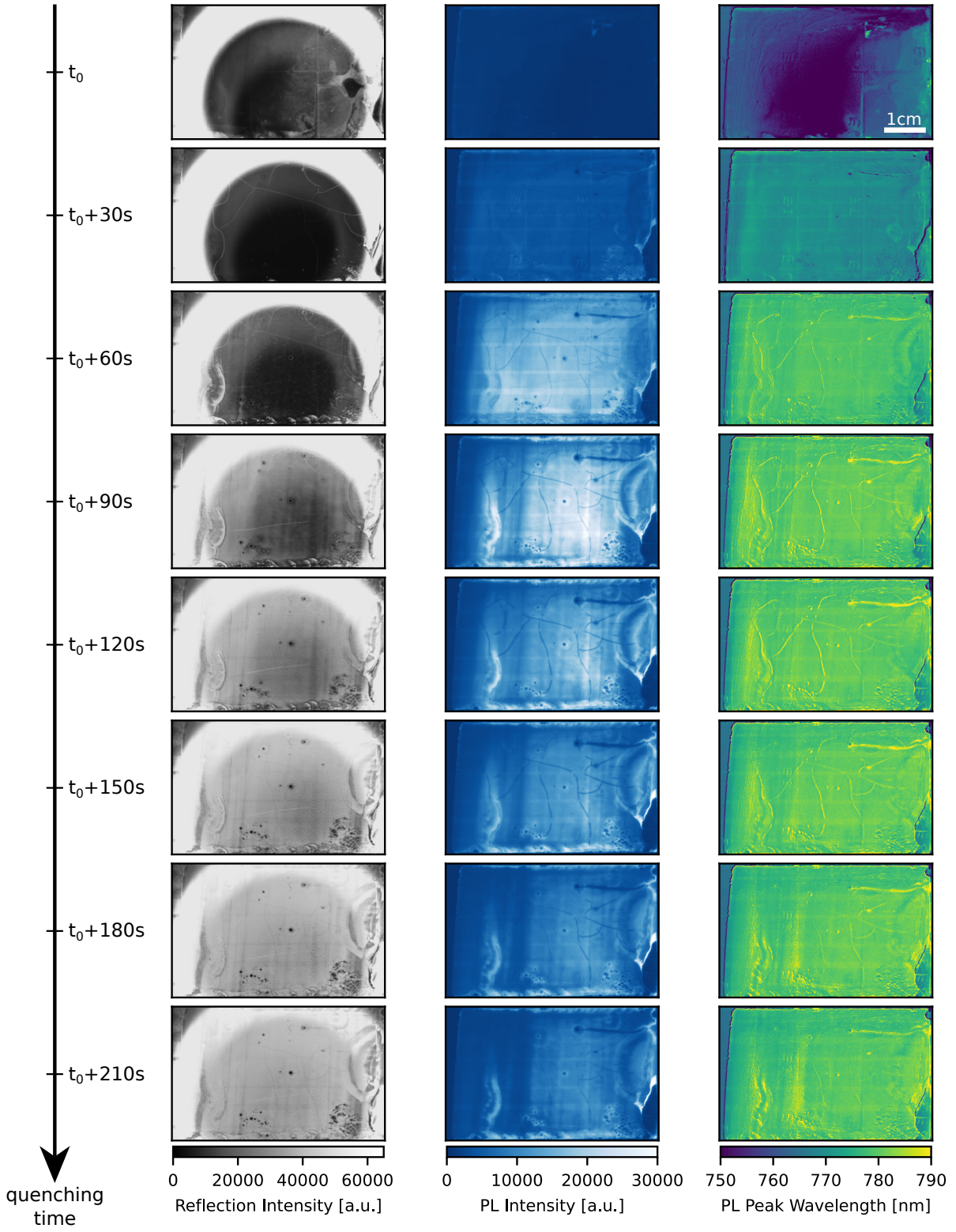

Figure A.3: *In situ* time-series of multi-channel images capturing the MAPI thin-film formation during laminar airflow quenching. The diffuse reflection images show an increase in the absorption of the thin film followed by increasing surface roughness, which is indicated by increasing diffuse reflection intensity. The ring-shaped artifacts are caused by the reflection of the LED ring (HPR2-100BL, CCS Inc.), which was replaced by two tilted LED bars for more homogeneous illumination for subsequent measurements. The onset of PL intensity (shown here: 725 nm longpass channel) indicates the formation of light absorbing and emitting material, and a redshift of the PL spectrum is revealed in the PL peak wavelength channel during the formation of the perovskite thin film.[341, 418]

A.5 Exploration of *In Situ* Imaging Data

A.5.1 Clustering Human-Selected Features

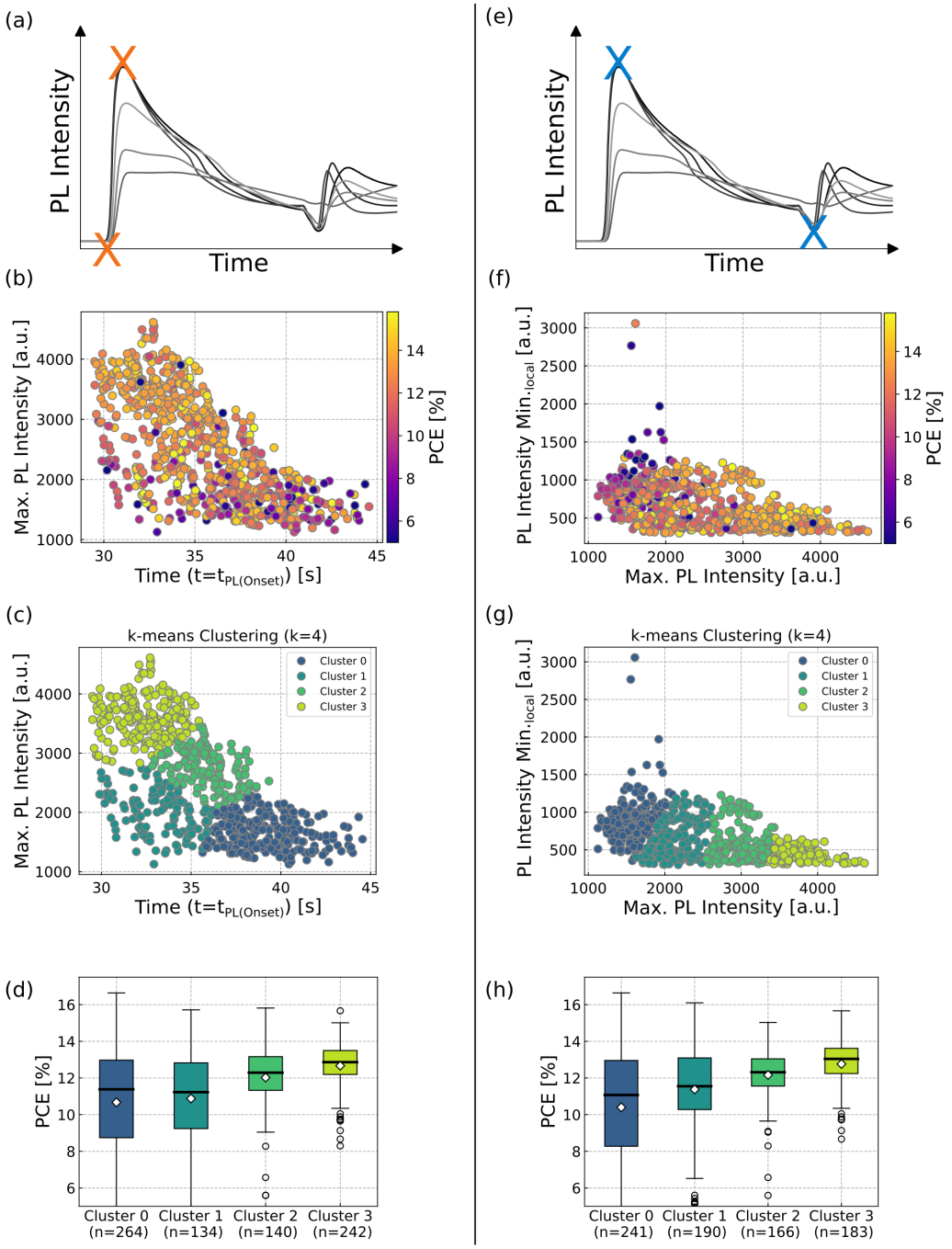

Figure A.4: Additional examples of clustering two human-selected features. Photoluminescence (PL) onset time and initial maximum $PL_{LP725nm}$ (left column), or local minimum $PL_{LP725nm}$ after vacuum chamber venting and initial maximum $PL_{LP725nm}$ (right column), are used as input features for k-means clustering. Power conversion efficiency distributions of the solar cells assigned to the corresponding cluster confirm that meaningful patterns are extracted from the data. However, the clustering result is sensitive and strongly affected by feature selection. Reproduced with permission from [346].

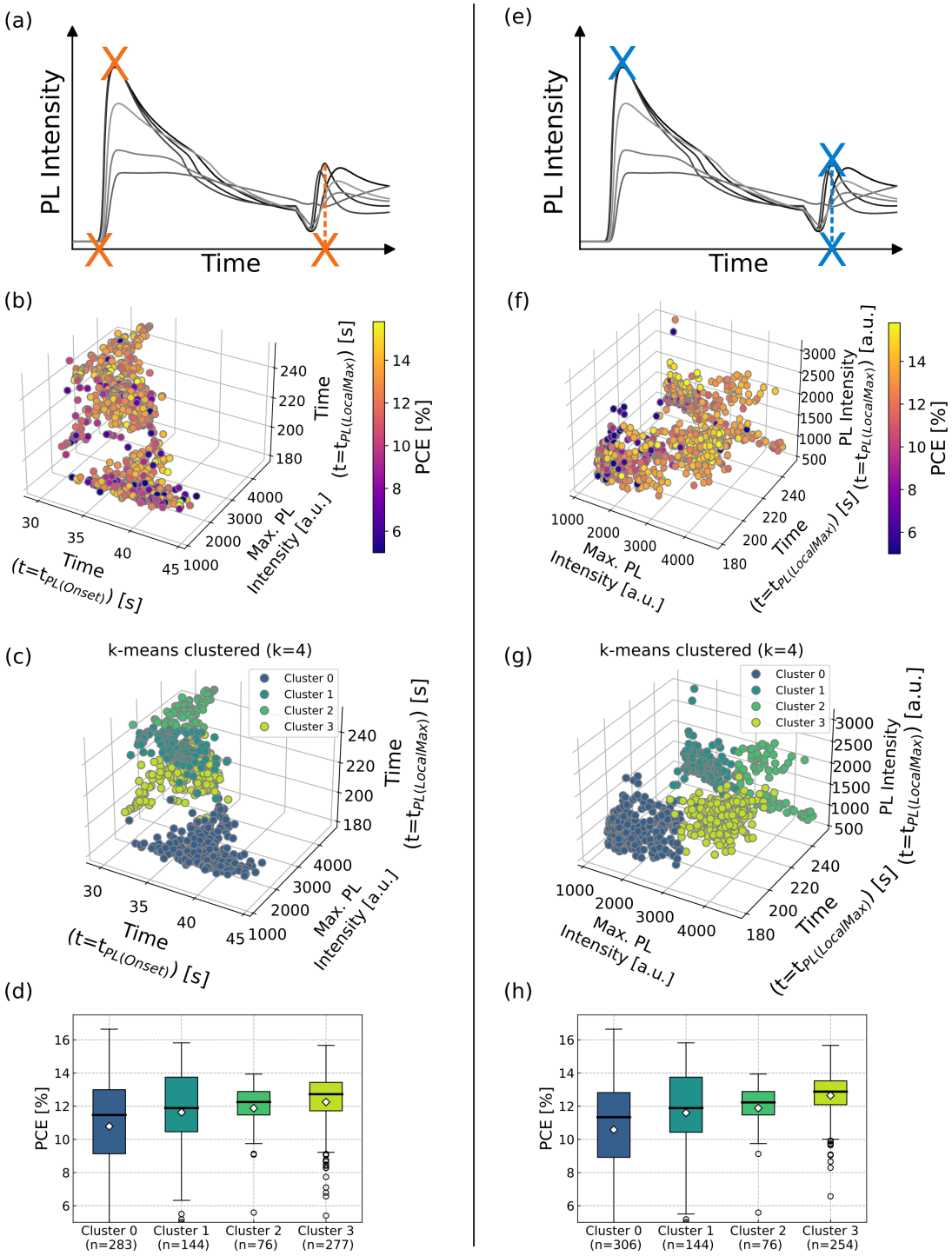

Figure A.5: Additional examples of clustering three human-selected features. Photoluminescence (PL) onset time, initial maximum $\mathrm{PL}_{LP725nm}$, and time of local maximum $\mathrm{PL}_{LP725nm}$ after vacuum chamber venting (left column), or initial maximum $\mathrm{PL}_{LP725nm}$, time and magnitude of local maximum $\mathrm{PL}_{LP725nm}$ after vacuum chamber venting (right column), are used as different input features for k-means clustering. Power conversion efficiency distributions of the solar cells assigned to the corresponding cluster confirm that meaningful patterns are extracted from the PL data. However, the clustering result is sensitive and strongly affected by feature selection. Reproduced with permission from [346].

A.5.2 Clustering Transients of Diffuse Reflection and Photoluminescence Peak Wavelength

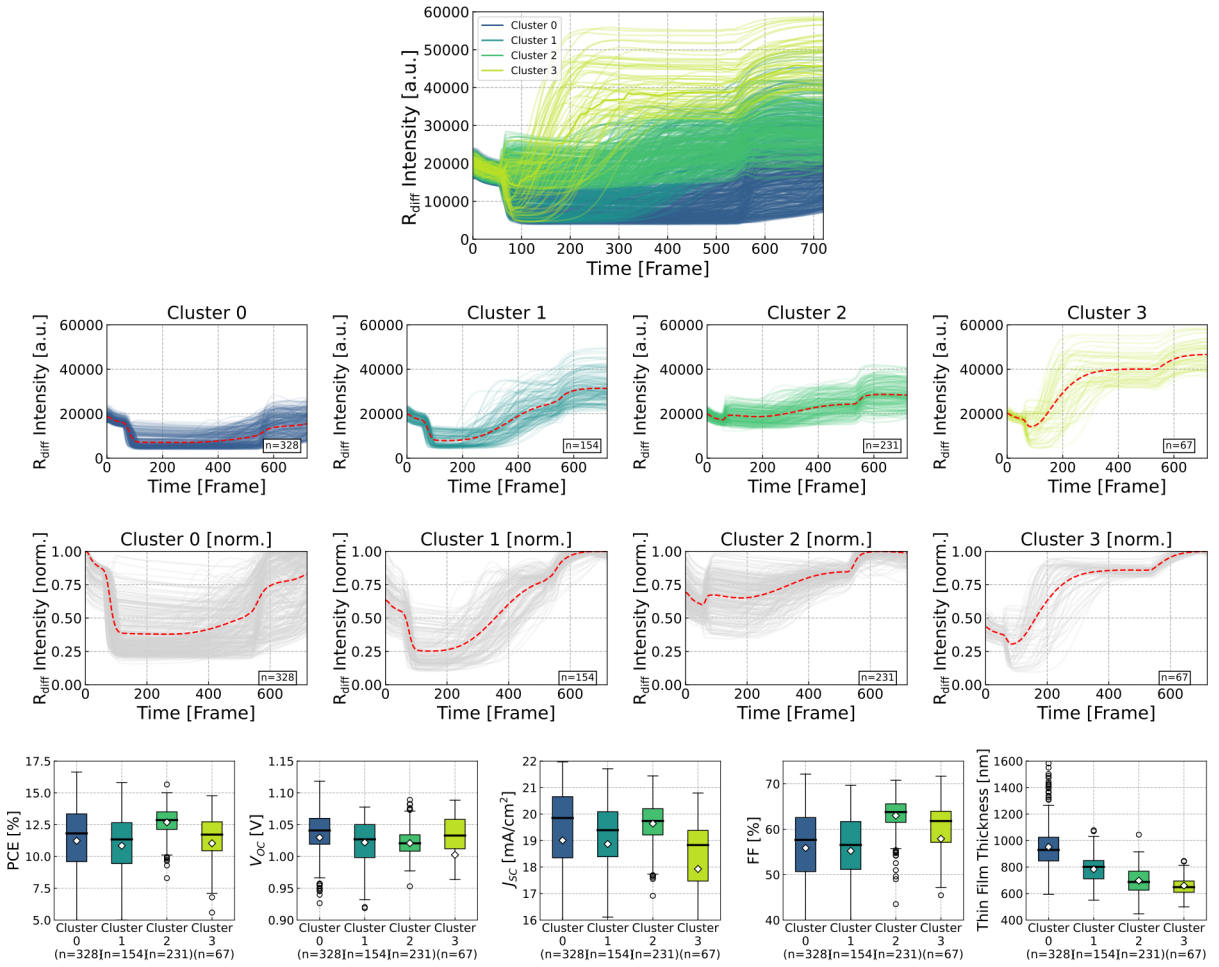

Figure A.6: Clustering of diffuse reflection (R_{diff}) transients without human feature selection. R_{diff} transients assigned to the four clusters, with the mean transient curve of each cluster highlighted as the dashed red line, show differences in the evolution of the R_{diff} signal. Different relative temporal patterns are evident from the normalized R_{diff} transients assigned to the different clusters (the mean transient curve of each cluster is the dashed red line). The distributions of power conversion efficiency (PCE), open-circuit voltage (V_{OC}), short-circuit current density (J_{SC}), fill factor (FF), and perovskite thin film thickness for each cluster reveal no significant relationship between the R_{diff} transients and photovoltaic parameters. However, a clear correlation is found between the evolution of R_{diff} transients and the thin film thickness. Mean and median values are indicated by white diamonds and black lines, respectively. Reproduced with permission from [346].

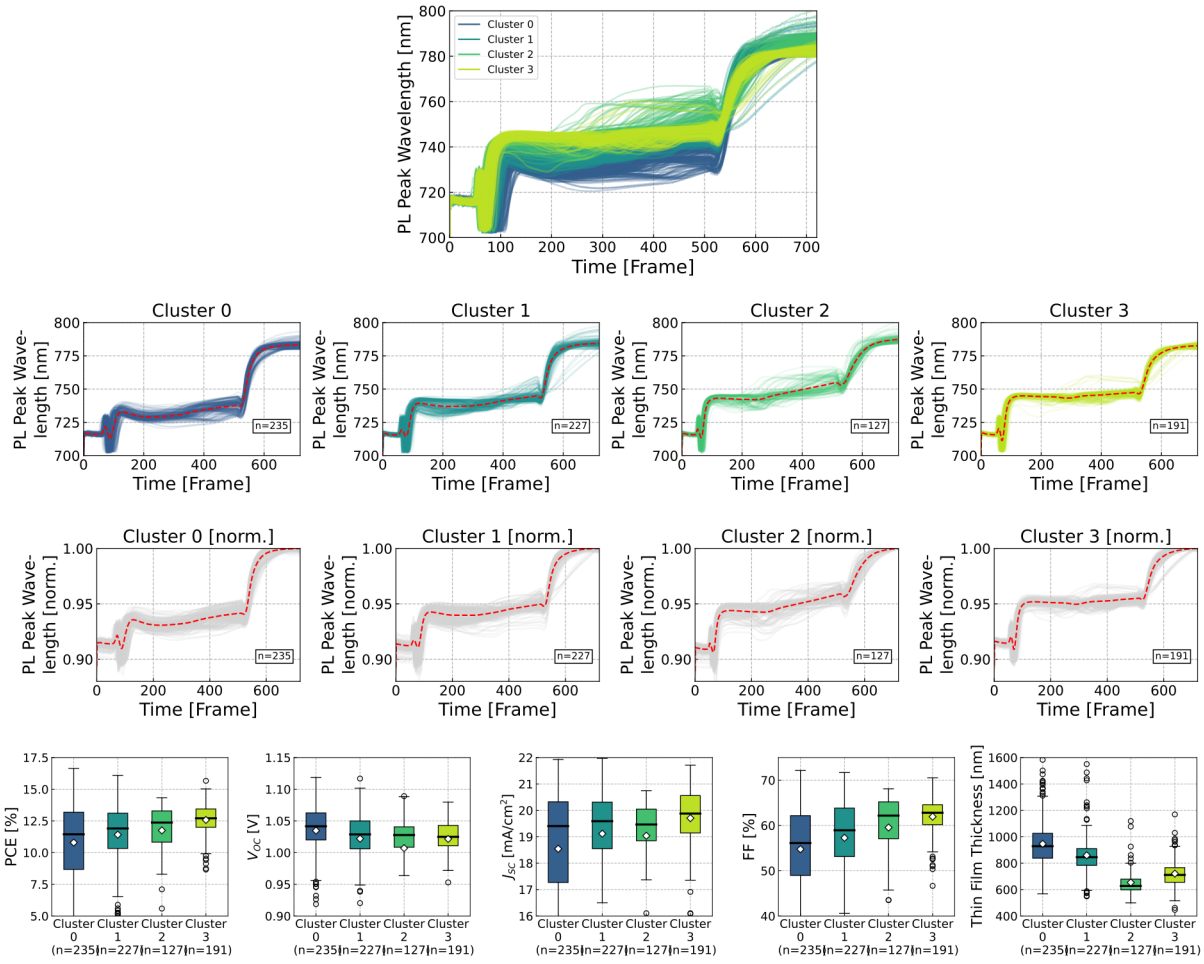

Figure A.7: Clustering of photoluminescence (PL) peak wavelength transients without human feature selection. The PL peak wavelength transients assigned to the four clusters, with the mean transient curve of each cluster highlighted as the dashed red line, show differences in the evolution of the PL peak wavelength signal. Different relative temporal patterns are evident from the normalized PL peak wavelength transients assigned to the different clusters (the mean transient curve of each cluster is the dashed red line). The distributions of power conversion efficiency (PCE), open-circuit voltage (V_{OC}), short-circuit current density (J_{SC}), fill factor (FF), and perovskite thin film thickness for each cluster suggest a correlation between the observed data patterns and PCE as well as FF. However, as with the PL transients, no clear trend is found for V_{OC} and J_{SC}. Mean and median values are indicated by white diamonds and black lines, respectively. Reproduced with permission from [346].

A.5.3 Spatial Distribution of Clusters and Subclusters

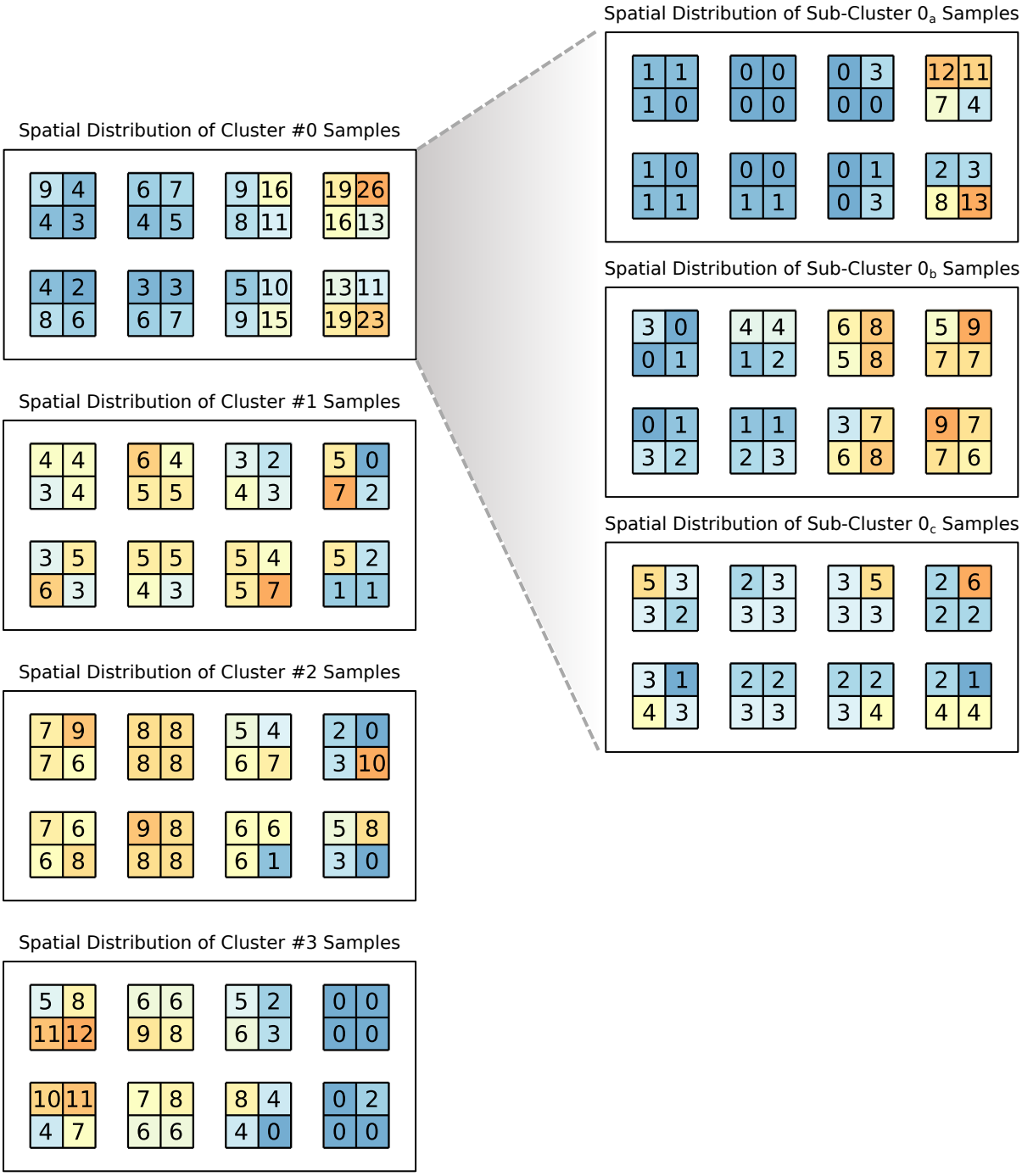

Figure A.8: Heat maps showing the spatial distribution of solar cells assigned to all clusters and subclusters generated by clustering the *in situ* photoluminescence (PL) transients. In addition to the original clusters, cluster *#0* to cluster *#3*, the subclusters are obtained by further dividing *#0* into subclusters (*0_a*, *0_b*, *0_c*). While the solar cells assigned to the poor-performing clusters are concentrated along the right edge of the substrate area affected by solution backflow, most of the solar cells assigned to better-performing clusters are located in the center of the leftmost quarter of the substrate. The blade coating applicator is moved from left to right. Reproduced with permission from [346].

A.5.4 Solar Cell Performance Dependent on Substrate Location

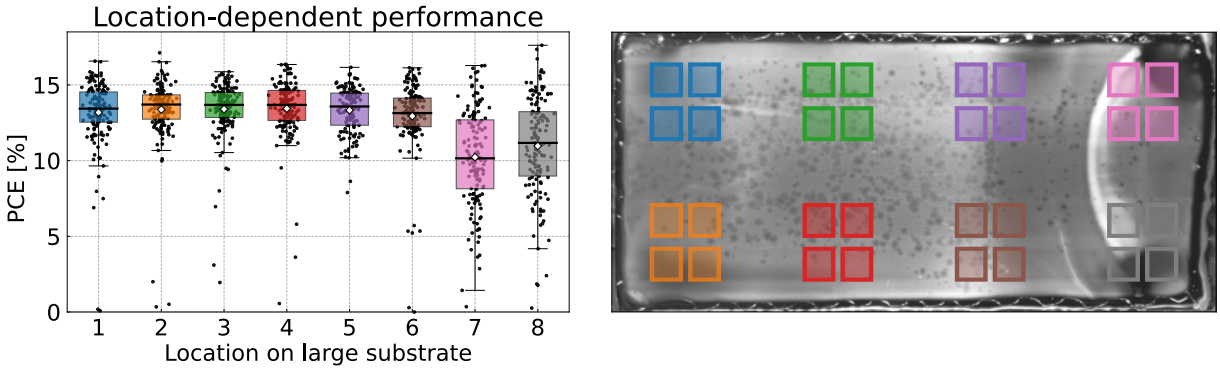

Figure A.9: Analysis of location-dependent power conversion efficiency (PCE) on large-area substrates. (Left) Boxplot showing the variation in PCE for cells located in different regions (1-8) on the substrate. Solar cells positioned in areas affected by solution backflow (i.e., regions 7 and 8) exhibit significantly lower PCE values, indicating reduced performance. (Right) Heatmap of the substrate with colored regions corresponding to the boxplots covering the 32 possible solar cell locations, highlighting the spatial distribution of solar cell performance. Poorer-performing cells are concentrated along the right edge of the substrate, which is affected by solution backflow during the blade coating process.

A.5.5 Solar Cell Performance Dependent on Date for Both Datasets

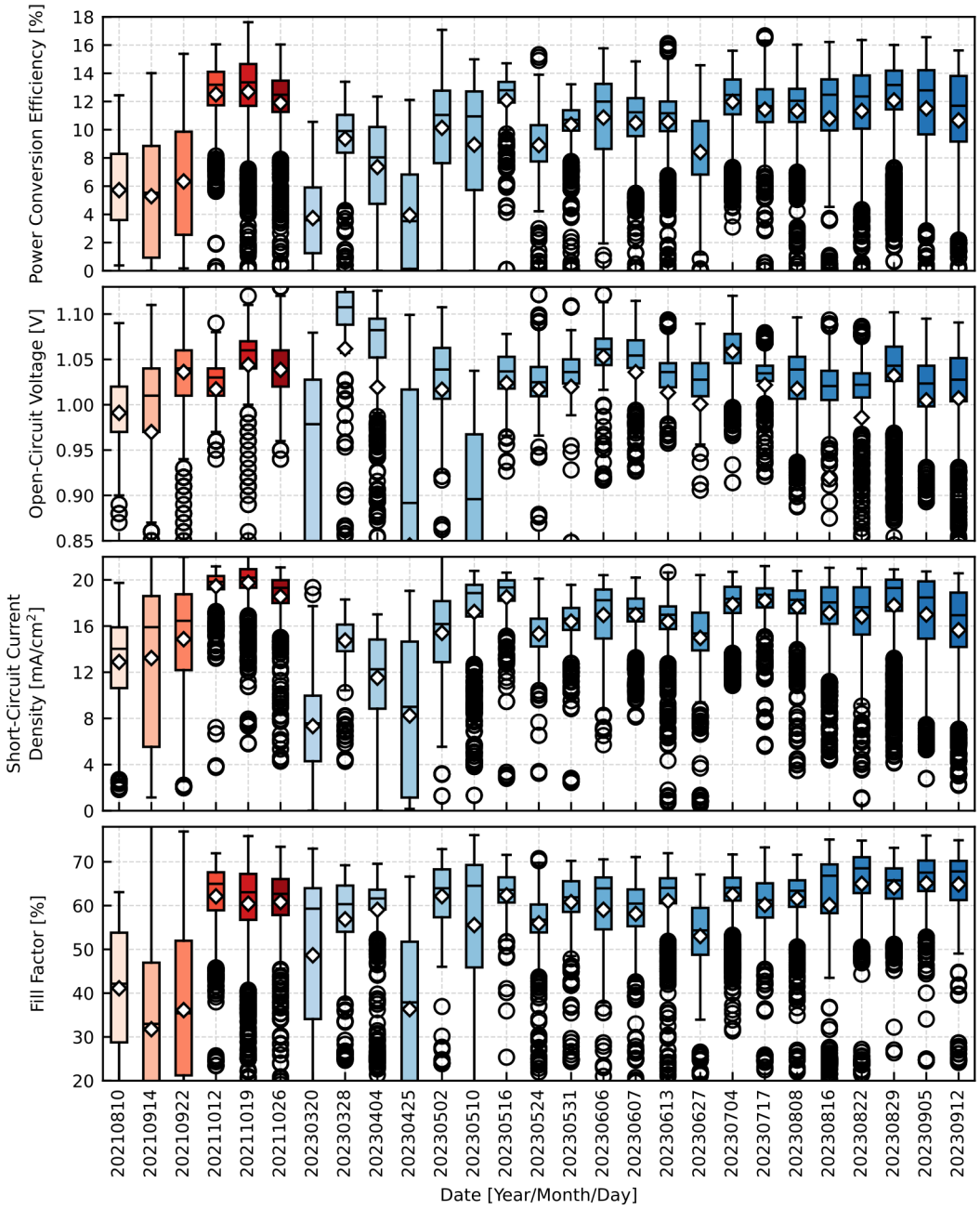

Figure A.10: Solar cell performance over time for the two different experimental datasets. Boxplots showing the evolution of solar cell performance over time for the two generated datasets. The experiments performed to generate the first dataset are indicated by red boxplots, while the experiments performed to generate the second dataset are shown as blue boxplots. Due to experimental problems caused by processing layers other than the perovskite thin films, a significant number of batches were not included in the datasets, as process fluctuations in unmonitored process steps make it impossible to predict device performance based only on data acquired during the perovskite formation. Accordingly, the device data included in the first dataset spans from 2021-10-12 to 2021-10-26, and the device data included in the second dataset spans from 2023-08-08 to 2023-09-12. While all solar cells for the first dataset were fabricated under constant conditions, the experimental parameters for the second dataset were varied (see Figure A.18 for quenching-time-dependent performance).

A.6 Material Classification and PCE Regression

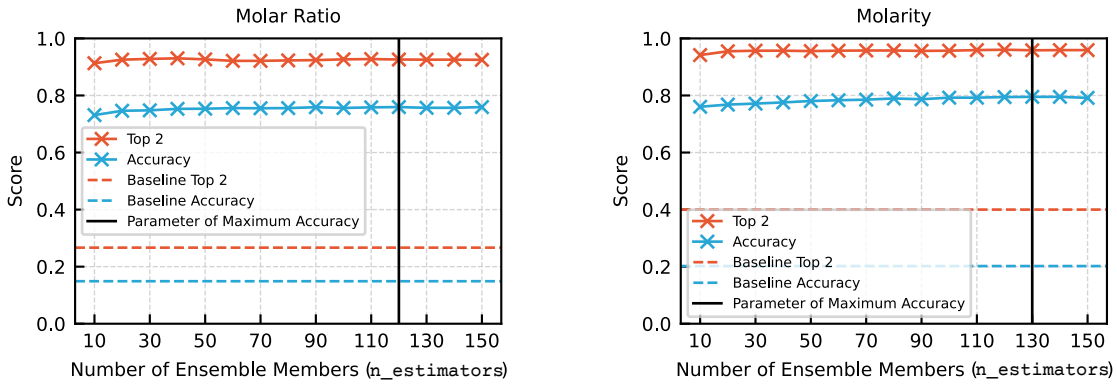

Figure A.11: Effect of the number of ensemble members (`n_estimators`) on the classification accuracy for molar ratio (left) and molarity (right). The accuracy and top-2 scores of the random forest model are evaluated for different numbers of ensemble members using fivefold cross-validation. Despite optimizing the number of ensemble members, the performance improvement remains minimal, with the optimal number of members determined to be 120 for molar ratio classification and 130 for molarity classification. The performance of the models shows limited improvement despite hyperparameter tuning, but they substantially outperform the baseline, which predicts each class with equal probability. Adapted with permission from [352].

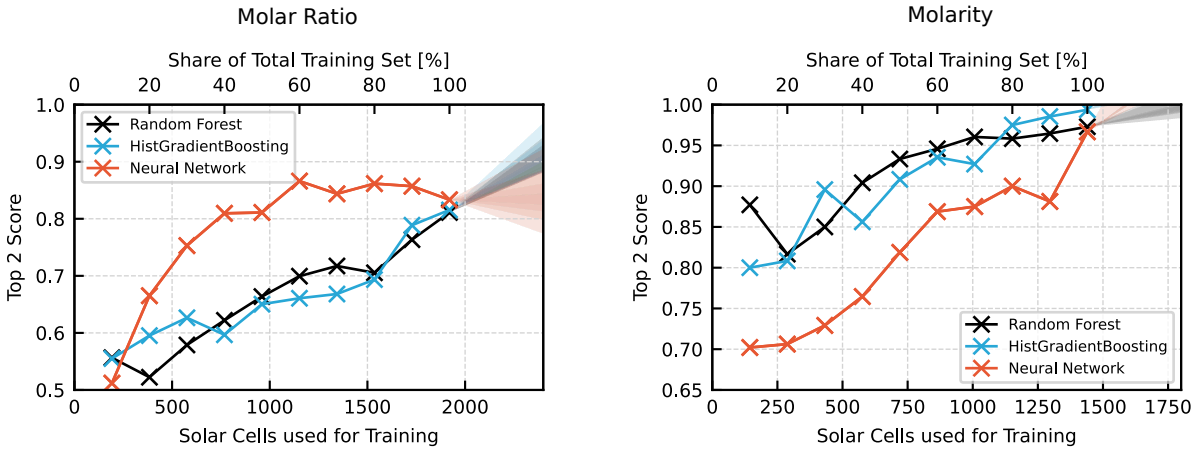

Figure A.12: Top-2 score performance of models for molar ratio (left) and molarity (right) classification as a function of training dataset size. The random forest (RF), histogram-based gradient boosting (HGB), and neural network (NN) models are trained on progressively larger subsets of the training data, and their performance is evaluated on the test set. For molar ratio classification, the NN initially shows the fastest improvement, but plateaus at medium dataset sizes, allowing the RF and HGB to minimize the difference in top-2 scores. For molarity prediction, the NN initially performs worse than the two best classical models but improves rapidly as the training dataset size increases and almost matches RF and HGB when trained on the full-size training set. The shaded areas indicate extrapolated performance trends, highlighting the potential for further improvement with larger datasets. Adapted with permission from [352].

Table A.6: Rate of improvement per 100 additional training samples for random forest (RF), histogram-based gradient boosting (HGB), and neural network (NN) models over various data intervals and metrics. For different data intervals, model performance changes as more training data is added and the rate of improvement is normalized to show the change per 100 additional training samples. In particular, when the entire data interval (10%-100%) is examined and when the dataset size is expanded beyond 90%, the NN shows a stronger increase in performance for all target variables and metrics. The color coding indicates the magnitude of the improvement, with fully saturated colors representing the highest improvement rates. Adapted with permission from [352]. (MAE: mean absolute error, R^2: coefficient of determination)

Rate of Improvement / 100 Additional Training Samples		Data Interval for Rate Calculation			
		10–100%	50–100%	70–100%	90–100%
Molarity [Accuracy]	RF	0.017	0.012	0.011	0.012
	HGB	0.029	0.025	0.031	0.026
	NN	0.033	0.025	0.022	0.068
Molar Ratio [Accuracy]	RF	0.009	0.011	0.005	0.019
	HGB	0.015	0.021	0.023	0.024
	NN	0.017	0.010	0.008	0.029
PCE [MAE]	RF	-0.048	-0.019	-0.064	-0.084
	HGB	-0.061	-0.041	-0.065	-0.109
	NN	-0.194	-0.063	-0.0158	-0.11
PCE [R^2]	RF	0.024	0.007	0.026	0.032
	HGB	0.027	0.017	0.027	0.044
	NN	0.16	0.033	0.083	0.05

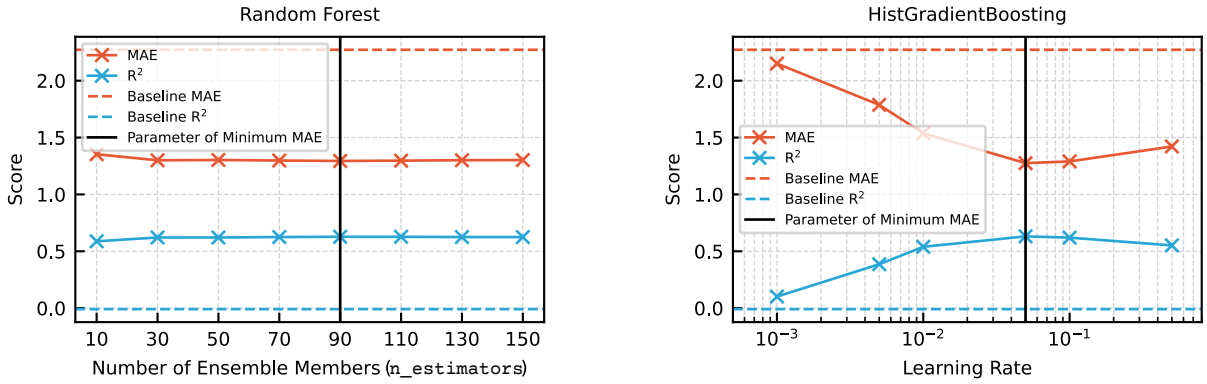

Figure A.13: Hyperparameter optimization for random forest (RF) and histogram-based gradient boosting (HGB) models for power conversion efficiency (PCE) regression. The impact of varying the number of ensemble members (`n_estimators`) for RF, with the optimal parameter determined to be 90 for minimizing the mean absolute error (MAE), is shown to be small. The effect of the parameter `learning_rate` on HGB performance is stronger, with an optimal learning rate of 0.05 identified using fivefold cross-validation. However, despite hyperparameter tuning, improvements in MAE and coefficient of determination (R^2) remain modest, suggesting limited gains from further optimization. Adapted with permission from [352].

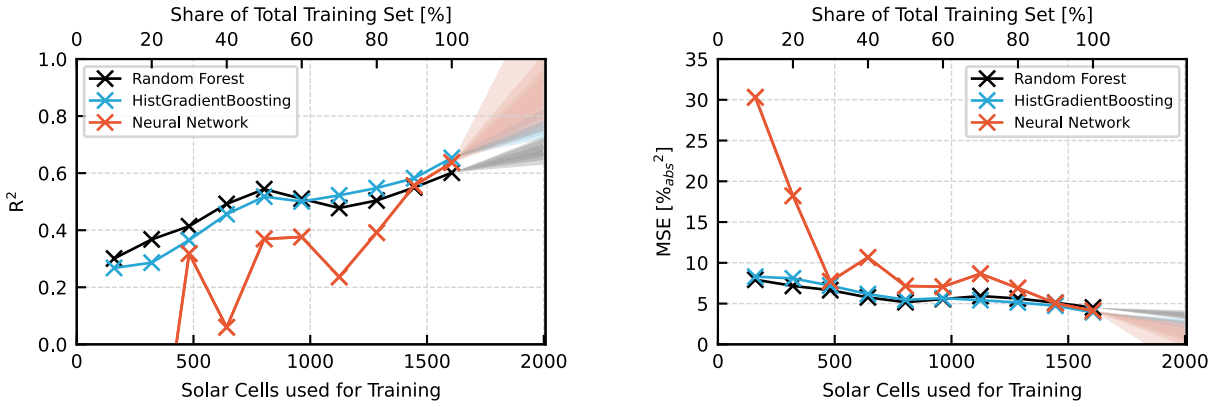

Figure A.14: Performance of random forest (RF), histogram-based gradient boosting (HGB), and neural network (NN) models for power conversion efficiency (PCE) regression as a function of training dataset size. RF and HGB show a steady improvement in coefficient of determination (R^2) and mean squared error (MSE) as more training data is used. In contrast, the NN performs poorly with small datasets, initially showing negative R^2 values and plateauing between 30% and 70% of the data. However, the NN demonstrates substantial improvement when trained on more than 70% of the dataset, eventually outperforming the RF and closely rivaling the HGB model. Extrapolation suggests that performance, especially for the NN, may continue to improve with even larger datasets. Adapted with permission from [352].

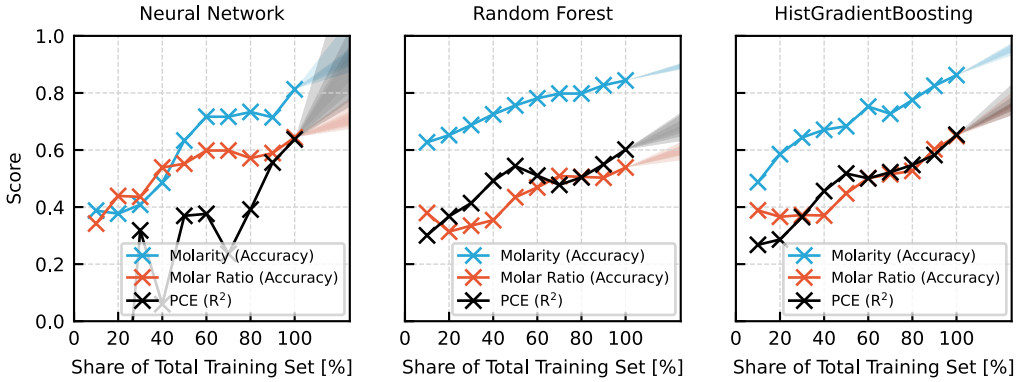

Figure A.15: Performance comparison of neural network (NN), random forest (RF), and histogram-based gradient boosting (HGB) models for molarity, molar ratio, and power conversion efficiency (PCE) prediction as a function of training dataset size. Both RF and HGB show steady improvement with increasing training dataset size. The NNs perform poorly with smaller datasets and plateau with medium-sized datasets but show rapid improvement when the dataset exceeds 70% of its total size, suggesting that additional data could further improve NN performance. The shaded areas indicate extrapolated performance trends, highlighting potential improvement with further dataset scaling. Adapted with permission from [352].

A.7 Generating *In Situ* AI Recommendations

A.7.1 Function Approximation by Interpolation with Gaussian Processes

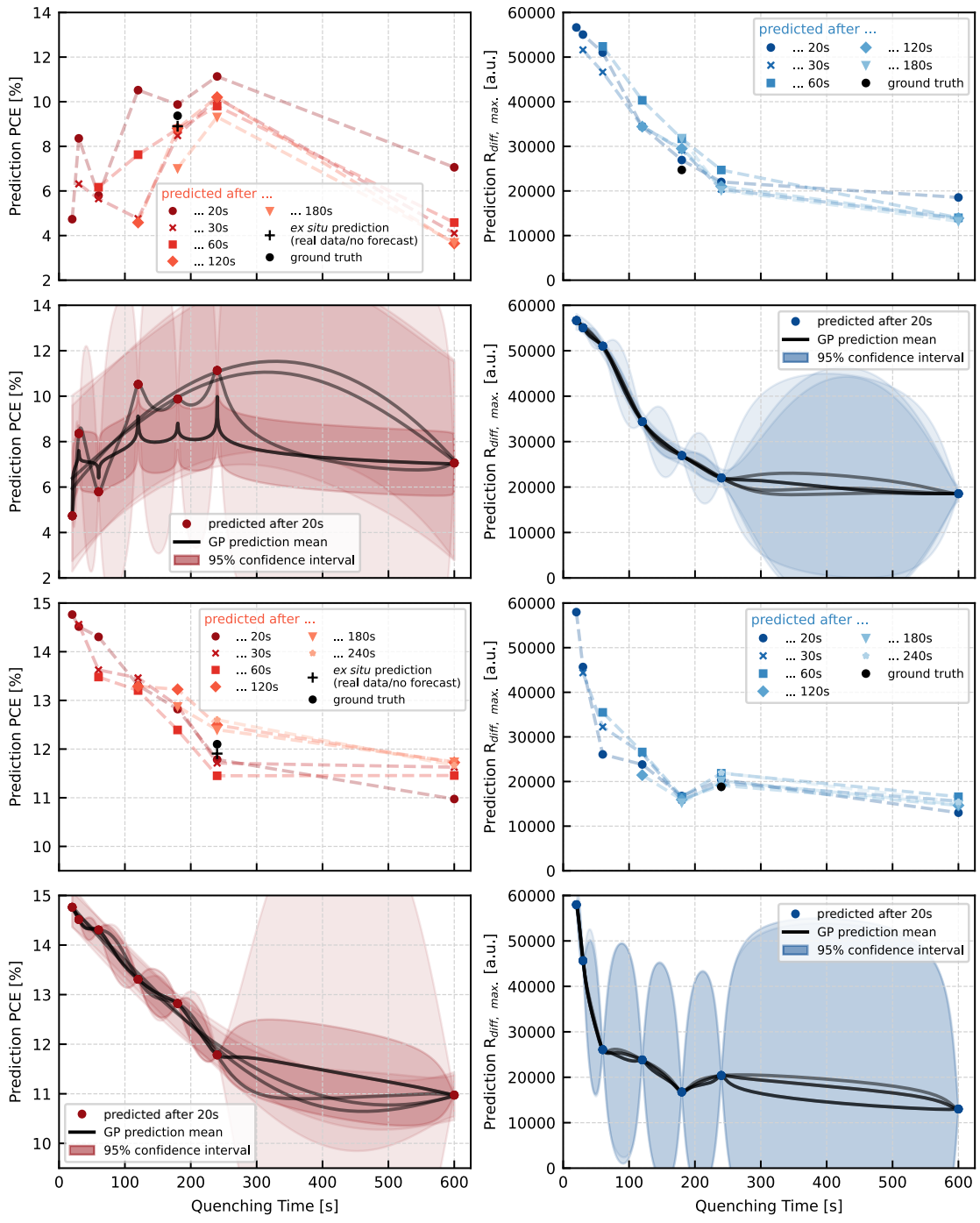

Figure A.16: Gaussian process (GP) approximation of continuous functions for power conversion efficiency (PCE) and diffuse reflection (R_{diff}) intensity forecasts. The GPs infer a continuous function from the set of discrete data points and allow the plotting of the mean function $\pm$ 1.96 standard deviations. The GPs capture the underlying relationships in the data and help overcome the limitation of model predictions being valid only for discrete times. Adapted with permission from [352].

A.7.2 Quenching-Time-Dependent Thin Film Morphology

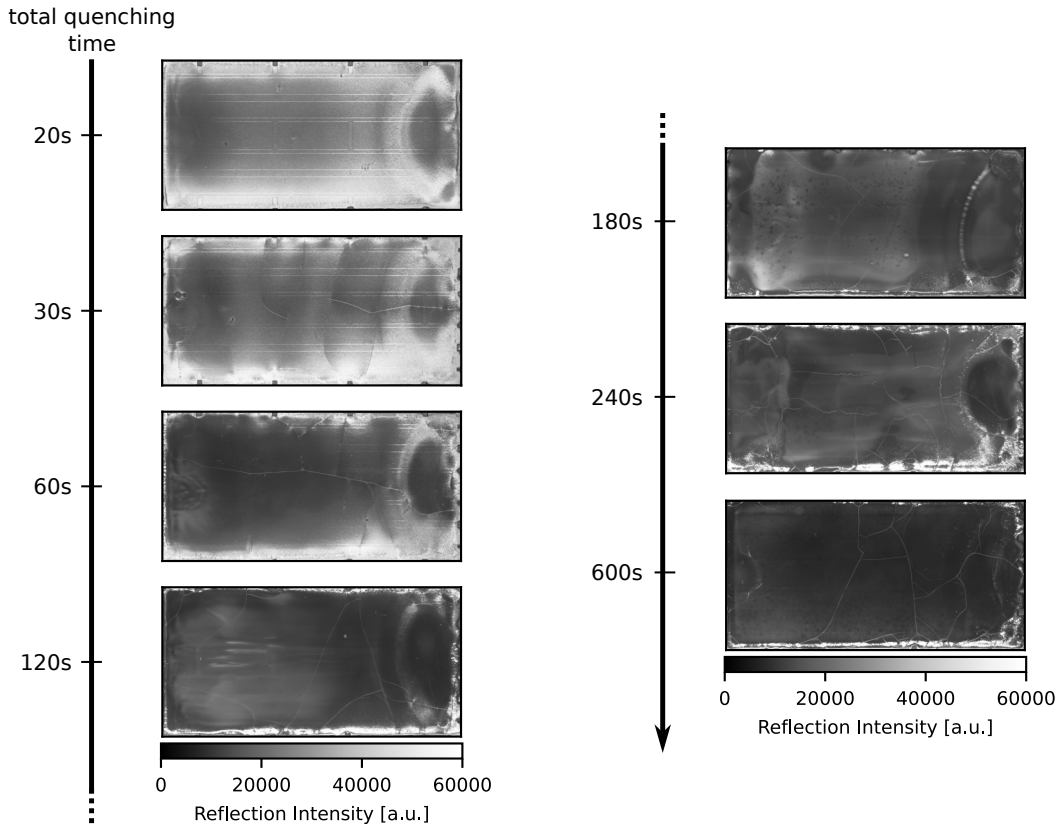

Figure A.17: *Ex situ* images of perovskite thin films quenched for different time intervals showing variations in reflection intensity. The images capture the surface morphology of thin films quenched from 20 seconds to 600 seconds. Due to the relationship between the diffuse reflection intensity (R_{diff}) and the surface roughness of the thin film, the R_{diff} intensity is a qualitative indicator of the surface roughness of the perovskite thin film. The intensity of R_{diff} decreases with increasing quenching time, indicating a reduction in surface roughness, resulting in smoother thin films at longer quenching times.[304] Adapted with permission from [352].

A.7.3 Quenching-Time-Dependent Power Conversion Efficiency

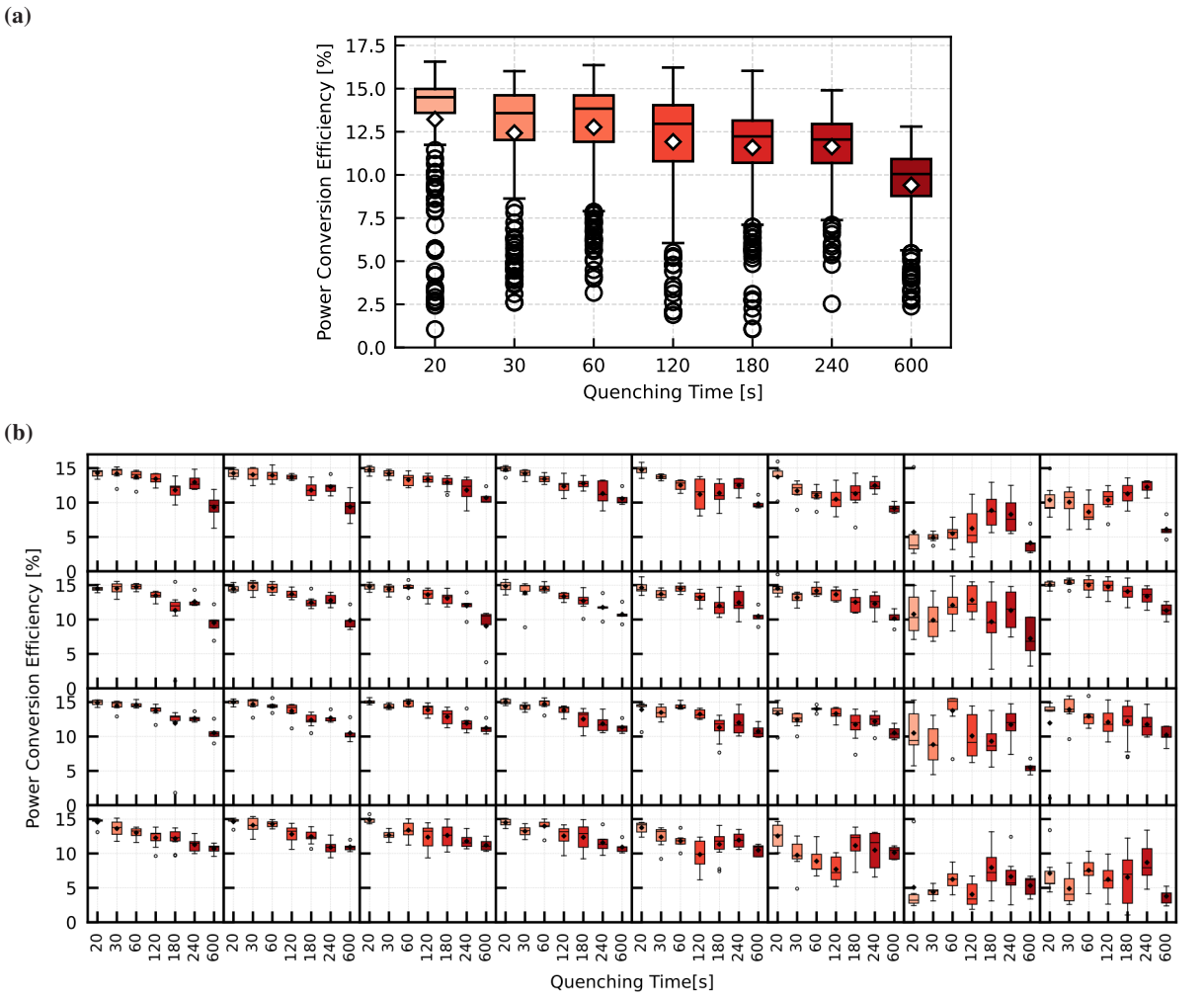

Figure A.18: Quenching time-dependent power conversion efficiency (PCE) of perovskite solar cells. (a) The distribution of PCE values for different quenching times highlights the general trend of decreasing PCE with longer quenching times. (b) Detailed PCE distributions over different regions of the substrate are shown by 32 subplots representing the 32 solar cell locations on the large-area substrate (see Figure 2.8a for substrate layout). During blade coating, the applicator moves from left to right, creating spatial variations in wet film thickness with increased wet film thickness at the substrate edges, especially at the right substrate edge (see Figure 5.12 for the spatial distribution of thin film thickness). The spatial variation in wet film thickness leads to variations in PCE behavior, particularly at the substrate edges, where thicker wet films result in either stable or increasing PCE with longer quenching. This spatial dependence highlights the influence of wet film thickness on quenching. Adapted with permission from [352].

A.7.4 Spatially-Resolved Forecasting and Predictions

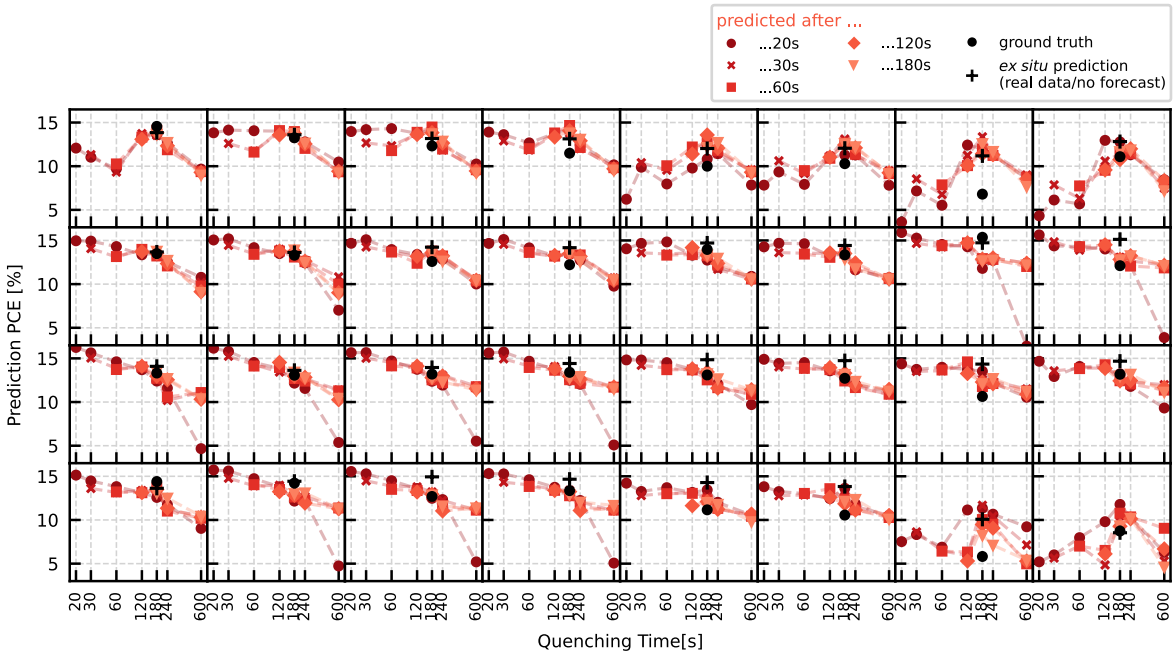

Figure A.19: Forecasting and predicting PCE for different substrate locations. The figure shows spatially resolved PCE forecasts for each of the 32 solar cell locations on the large-area substrate, with each subplot corresponding to a specific substrate location. The local *in situ* imaging data is used as input to the model cascade to forecast PCE values under different quenching scenarios. During the blade coating process, the applicator moves from left to right, resulting in spatial variations in wet film thickness, with thicker films at the substrate edges, especially on the right (see Figure 5.12 for the spatial distribution of thin film thickness). This spatial distribution influences the measured PCEs (see Figure A.18) and is therefore also noticeable in the PCE forecasts. For locations with thin wet films (e.g., middle left), the PCE is forecasted to decrease rapidly as the quenching occurs much faster than for thicker wet films (e.g., top right and bottom right). This spatially resolved forecasting is only possible using imaging techniques that provide spatial information in contrast to single-spot measurements.

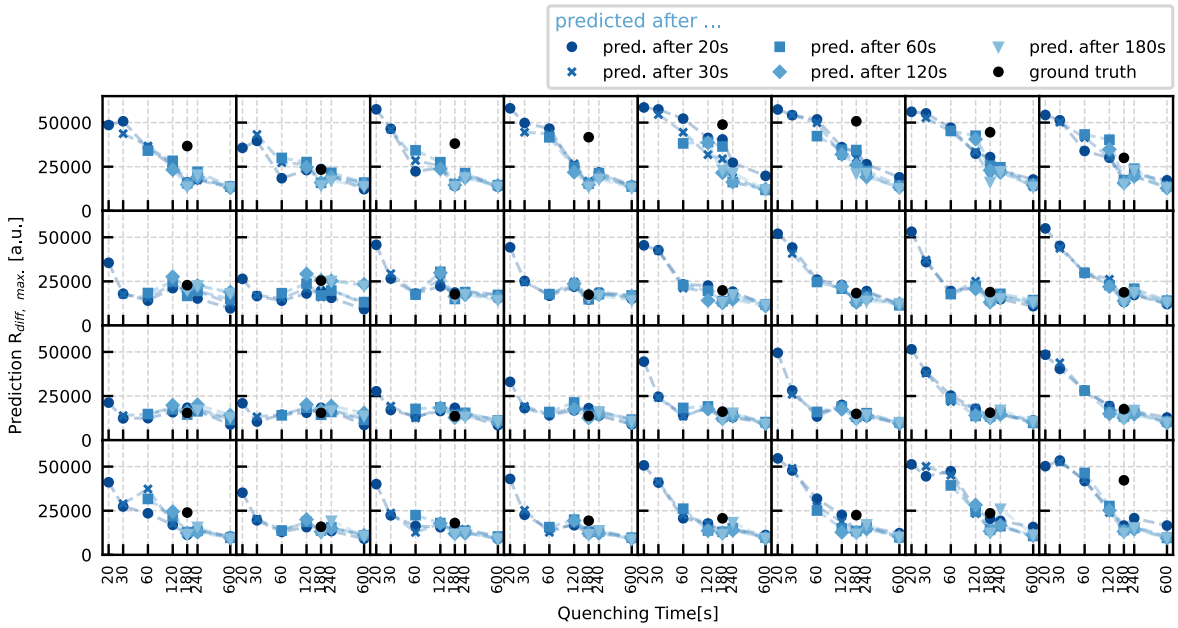

Figure A.20: Forecasting diffuse reflection (R_{diff}) as an indicator for thin film morphology for different substrate locations. The figure presents spatially resolved forecasts of diffuse reflection (R_{diff}) intensity for each of the 32 solar cell locations on the large-area substrate, with each subplot corresponding to a specific substrate location. The local *in situ* imaging data is used as input to the random forest models to forecast R_{diff} values under different quenching scenarios. As the blade coating applicator moves from left to right, spatial variations in wet film thickness appear, with thicker films forming at the substrate edges, especially on the right side (see Figure 5.12 for the spatial distribution of thin film thickness). These thickness variations affect the forecasted R_{diff}, as quenching occurs faster in areas with thinner films (e.g., middle left) compared to areas with thicker films (e.g., top right and bottom right). This spatially resolved forecasting capability highlights the advantage of imaging techniques, which provide spatial information that cannot be captured by single-spot measurements.

A.8 Enhanced Understanding of Thin-Film Formation through Machine Learning

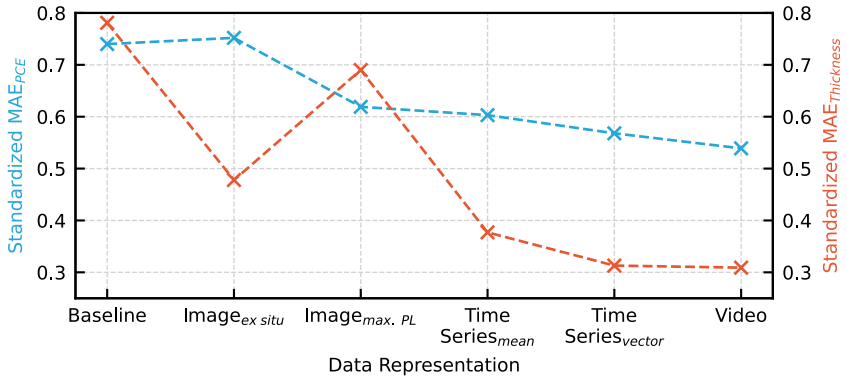

Figure A.21: Standardized mean absolute error (MAE) for power conversion efficiency (PCE) and thin film thickness predictions using different data representations as model input. Standardized MAE is calculated by dividing the common MAE by the standard deviation of the respective ground truth label so that results are comparable between labels with different value ranges. Models trained on the *video* representation achieve the lowest standardized MAE for both PCE and thickness, benefiting from preserved temporal and spatial information. Thickness predictions consistently outperform PCE predictions for most representations, likely due to additional processing steps that negatively affect PCE that are not captured in the input data. The *image*$_{ex\ situ}$ representation shows improved accuracy for thickness prediction, while *image*$_{max.\ PL}$ provides better results for PCE prediction. Adapted with permission from [347].

List of Figures

1.1 Global energy trends and projected PV capacity growth . . . 1
1.2 Trends in PV system costs and efficiencies . . . 3
1.3 Learning rates and projected price reductions for PV modules . . . 4
2.1 Schematic representation of the perovskite crystal structure . . . 8
2.2 Working principle of a perovskite solar cell illustrating charge carrier generation and extraction . . . 10
2.3 Electrical and photovoltaic characteristics of a solar cell . . . 13
2.4 Relationship between artificial intelligence, machine learning, and deep learning . . . 15
2.5 Overview of supervised and unsupervised learning approaches in machine learning . . . 16
2.6 Illustration of the machine learning models used in this work . . . 18
2.7 Machine learning workflow of training, validation, and testing . . . 20
2.8 Dimensionality reduction for high-dimensional video data of the perovskite thin-film formation . . . 25
2.9 Machine learning in materials science and perovskite photovoltaics . . . 27
3.1 Blade coating and vacuum quenching process . . . 33
3.2 Entangled phases of perovskite thin-film formation . . . 35
3.3 Vapor phase deposition techniques used in this work . . . 36
3.4 Fabrication process of an inverted p-i-n perovskite solar cell . . . 38
3.5 Band diagram and PL spectrum of a perovskite thin film . . . 41
4.1 Schematic of the multi-channel imaging system . . . 48
4.2 Exemplary images of blade-coated DCP thin films after vacuum quenching . . . 50
4.3 PL and EL imaging of individual tandem module subcells using multi-channel imaging . . . 53
4.4 Exemplary images of combined EL signals from both subcells and individual subcell EL images . . . 54
4.5 Schematics of the *in situ* monitoring setup integrated into two experimental quenching setups . . . 56
4.6 Exemplary *in situ* time series of multi-channel images capturing the DCP thin-film formation . . . 57
4.7 Transient *in situ* evolution of multi-channel signals during the perovskite thin-film formation . . . 58
4.8 Discrimination of process parameters based on the characteristic *in situ* signal transients . . . 61
5.1 Schematic of the integration of ML into the conventional fabrication process of perovskite solar cells . 65
5.2 Experimental dataset containing 1129 blade-coated solar cells . . . 66
5.3 Distribution of the target variables for the full dataset, training set, and test set . . . 67
5.4 Highlighting the rationale for *in situ* monitoring by comparing *in situ* and *ex situ* features for PCE prediction . . . 69
5.5 Schematic representation of correlating extracted *in situ* data patterns with solar cell PCE . . . 71
5.6 Clustering of human-selected features reveals correlations with solar cell performance . . . 73
5.7 Determining the optimal number of clusters using the elbow plot . . . 75
5.8 Clustering of photoluminescence transients without human feature selection . . . 76
5.9 Statistical tests show the significance of the difference between the target variable distributions of the clusters . . . 77
5.10 In-depth investigation of the clusters confirms distinct spatial distribution of the clusters . . . 79
5.11 Comparison of clustering and subclustering approaches for photoluminescence transients . . . 80
5.12 Spatial distribution of average PCE and thin film thickness across the substrate . . . 81
5.13 Schematic representation of predicting PCE using k-nearest neighbors prior to device completion . . . 82
5.14 Parity plots of k-nearest neighbors predictions for PV performance metrics and thin film thickness . . . 85
5.15 Prediction performance of kNN using different *in situ* channels as model input . . . 87
5.16 Parity plots of kNN predictions using different *in situ* channels as input . . . 88
5.17 Comparison of prediction performance for different supervised machine learning models . . . 90

6.1 Schematic representation of the integration of AI-driven monitoring into the perovskite thin-film formation process . . . 95
6.2 Sequential workflow for the generation of the experimental *in situ* dataset . . . 96
6.3 Description of the second generated dataset consisting of *in situ* monitoring data and material and device target variables . . . 97
6.4 Distribution of solar cell performance metrics used as device target variables for the full dataset, training set, and test set . . . 97
6.5 Dataset distribution and fivefold cross-validation setup for predicting PCE and classifying precursor properties. . . . 98
6.6 Schematic representation of material composition monitoring using an *in situ* characterization setup and deep learning . . . 100
6.7 Transients of the monitoring data for different molar ratio classes . . . 101
6.8 Transients of the monitoring data for different molarity classes . . . 102
6.9 Confusion matrices for predicting molar ratio and precursor molarity using deep neural networks . . . 103
6.10 Comparison of deep learning and classical machine learning models for predicting molar ratio and precursor molarity . . . 104
6.11 Impact of training dataset size on model performance for molar ratio and molarity classification . . . 105
6.12 Schematic representation of device performance prediction using the *in situ* characterization setup and deep learning . . . 106
6.13 Transients of the monitoring data for different quenching times, color-coded by PCE . . . 107
6.14 Comparison of predicted and ground truth PCE values for the test set . . . 108
6.15 Parity plots showing predicted versus ground truth PCE for different vacuum quenching times . . . 109
6.16 Comparison of predictive performance for PCE prediction using different machine learning ML models and the effect of training dataset size on model accuracy . . . 111
6.17 Schematic representation of *in situ* AI recommendations for process control in perovskite solar cell fabrication . . . 113
6.18 Workflow of the AI-driven *in situ* recommendation system for process control . . . 113
6.19 Forecasting different vacuum quenching scenarios using random forest regressors . . . 114
6.20 All random forest models are trained to optimize forecasting accuracy . . . 115
6.21 Parity plots illustrate the agreement between predicted and ground truth PCE for various combinations of total actual quenching time and time of the prediction . . . 116
6.22 MAE when predicting PCE as a function of *in situ* forecast and prediction time for different total quenching times . . . 117
6.23 *In situ* forecasting and performance prediction for two solar cell samples with different perovskite thin film thickness . . . 118
6.24 Schematic representation of diffuse reflection monitoring for thin film surface roughness assessment . 119
6.25 *In situ* AI recommendation system for PCE and morphology on large-area perovskite substrates . . . 121
7.1 Schematic representation of applying XAI to render model predictions humanly understandable . . . 127
7.2 MAE for PCE and thin film thickness predictions using different data representations as model input . 128
7.3 Feature attribution for prediction of PCE and thin film thickness . . . 130
7.4 Phases of perovskite thin-film formation and corresponding PL and pressure transients . . . 131
7.5 Counterfactuals for PCE and thin film thickness predictions . . . 132
7.6 Iterative feedback loop connecting experimental research with XAI for data-driven optimization of the experimental process . . . 133
A.1 PL and EL imaging of all-perovskite tandem solar mini-modules . . . 149
A.2 Photograph of IPDRI integrated into experimental setups . . . 150
A.3 *In situ* time-series of multi-channel images capturing the MAPI thin-film formation during laminar airflow quenching . . . 151
A.4 Additional examples of clustering two human-selected features . . . 152
A.5 Additional examples of clustering three human-selected features . . . 153
A.6 Clustering of diffuse reflection transients without human feature selection . . . 154
A.7 Clustering of PL peak wavelength transients without human feature selection . . . 155

A.8 Heat maps showing the spatial distribution of solar cells assigned to all clusters and subclusters 156
A.9 Analysis of location-dependent PCE on large-area substrates 157
A.10 Solar cell performance over time for the two different experimental datasets 158
A.11 Effect of the number of ensemble members on the classification accuracy for molar ratio and molarity 159
A.12 Top-2 score performance of models for molar ratio and molarity classification as a function of training dataset size 159
A.13 Hyperparameter optimization for RF and HGB models for PCE regression 160
A.14 Performance of RF, HGB, and NN models for PCE regression as a function of training dataset size . . 161
A.15 Performance comparison of NN, RF, and HGB models for molarity, molar ratio, and PCE prediction as a function of training dataset size 161
A.16 Gaussian process approximation of continuous functions for PCE and R_{diff} intensity forecasts 162
A.17 *Ex situ* images of perovskite thin films quenched for different time intervals showing variations in reflection intensity 163
A.18 Quenching time-dependent PCE of perovskite solar cells 164
A.19 Forecasting and predicting PCE for different substrate locations 165
A.20 Forecasting R_{diff} as an indicator for thin film morphology for different substrate locations 166
A.21 Standardized MAE for PCE and thin film thickness predictions using different data representations as model input 167

List of Tables

5.1 Comparison of correlation metrics of *in situ* and *ex situ* features . . . 70
5.2 Reduction of prediction error using the k-nearest neighbors regressor . . . 83
5.3 Predictive performance of the kNN model measured in different error metrics . . . 86
6.1 Predictive performance of the neural network for predicting PCE for different vacuum quenching times . 110
A.1 Contributor Role Taxonomy (CRediT) . . . 144
A.2 Author CRediT – Correlative In Situ Multichannel Imaging for Large-Area Monitoring of Morphology Formation in Solution-Processed Perovskite Layers . . . 145
A.3 Author CRediT – Process Insights into Perovskite Thin-Film Photovoltaics from Machine Learning with In Situ Luminescence Data . . . 146
A.4 Author CRediT – Deep learning for augmented process monitoring of scalable perovskite thin-film fabrication . . . 147
A.5 Author CRediT – Discovering Process Dynamics for Scalable Perovskite Solar Cell Manufacturing with Explainable AI . . . 148
A.6 Rate of improvement per 100 additional training samples for RF, HGB, and NN models over various data intervals and metrics . . . 160

Bibliography

[1] Katherine Calvin et al. *IPCC, 2023: Climate Change 2023: Synthesis Report, Summary for Policymakers. Contribution of Working Groups I, II and III to the Sixth Assessment Report of the Intergovernmental Panel on Climate Change [Core Writing Team, H. Lee and J. Romero (eds.)]. IPCC, Geneva, Switzerland*. Ed. by Paola Arias et al. 2023, 1–34. DOI: 10.59327/ipcc/ar6-9789291691647.001.

[2] James Hansen et al. "Earth's Energy Imbalance: Confirmation and Implications". In: *Science* 308.5727 (2005), 1431–1435. DOI: 10.1126/science.1110252.

[3] Malte Meinshausen et al. "Realization of Paris Agreement pledges may limit warming just below 2°C". In: *Nature* 604.7905 (2022), 304–309. DOI: 10.1038/s41586-022-04553-z.

[4] William J Ripple et al. "World Scientists' Warning of a Climate Emergency". In: *BioScience* (2019). DOI: 10.1093/biosci/biz088.

[5] Nancy M. Haegel et al. "Terawatt-scale photovoltaics: Transform global energy". In: *Science* 364.6443 (2019), pp. 836–838. DOI: 10.1126/science.aaw1845.

[6] Laura Cozzi et al. *World Energy Outlook*. International Energy Agency (IEA). 2018. URL: https://iea.blob.core.windows.net/assets/77ecf96c-5f4b-4d0d-9d93-d81b938217cb/World_Energy_Outlook_2018.pdf (visited on 12/12/2024).

[7] Simon Philipps et al. *Photovoltaics Report*. Fraunhofer Institute for Solar Energy Systems (ISE). 2024. URL: https://www.ise.fraunhofer.de/en/publications/studies/photovoltaics-report.html (visited on 12/12/2024).

[8] Christoph Kost et al. *Stromgestehungskosten erneuerbare Energien*. Fraunhofer Institute for Solar Energy Systems (ISE). 2024. URL: https://www.ise.fraunhofer.de/de/veroeffentlichungen/studien/studie-stromgestehungskosten-erneuerbare-energien.html (visited on 12/12/2024).

[9] Femke J. M. M. Nijsse et al. "The momentum of the solar energy transition". In: *Nature Communications* 14.1 (2023). DOI: 10.1038/s41467-023-41971-7.

[10] Nancy M. Haegel et al. "Photovoltaics at multi-terawatt scale: Waiting is not an option". In: *Science* 380.6640 (2023), 39–42. DOI: 10.1126/science.adf6957.

[11] Jan Christoph Goldschmidt et al. "Technological learning for resource efficient terawatt scale photovoltaics". In: *Energy & Environmental Science* 14.10 (2021), 5147–5160. DOI: 10.1039/d1ee02497c.

[12] The Economist. *The energy transition will be much cheaper than you think*. The Economist. 2024. URL: https://www.economist.com/interactive/briefing/2024/11/14/the-energy-transition-will-be-much-cheaper-than-you-think (visited on 10/30/2024).

[13] Chris Case et al. "Industrial Insights into Perovskite Photovoltaics". In: *ACS Energy Letters* 4.11 (2019), 2760–2762. DOI: 10.1021/acsenergylett.9b02105.

[14] Martin A. Green et al. "Solar Cell Efficiency Tables (Version 65)". In: *Progress in Photovoltaics: Research and Applications* 33.1 (2024), 3–15. DOI: 10.1002/pip.3867.

[15] A De Vos. "Detailed balance limit of the efficiency of tandem solar cells". In: *Journal of Physics D: Applied Physics* 13.5 (1980), 839–846. DOI: 10.1088/0022-3727/13/5/018.

[16] Thomas G. Allen et al. "A Practical Efficiency Target for Perovskite/Silicon Tandem Solar Cells". In: *ACS Energy Letters* 10.1 (2024), 238–245. DOI: 10.1021/acsenergylett.4c02152.

[17] National Renewable Energy Laboratory (NREL). *Best Research-Cell Efficiency Chart*. URL: https://www.nrel.gov/pv/cell-efficiency.html (visited on 12/12/2024).

[18] Junjie Zhou et al. "Highly efficient and stable perovskite solar cells via a multifunctional hole transporting material". In: *Joule* 8.6 (2024), 1691–1706. DOI: 10.1016/j.joule.2024.02.019.

[19] Hao Chen et al. "Improved charge extraction in inverted perovskite solar cells with dual-site-binding ligands". In: *Science* 384.6692 (2024), 189–193. DOI: 10.1126/science.adm9474.

[20] Jiang Liu et al. "Perovskite/silicon tandem solar cells with bilayer interface passivation ". In: *Nature* 635.8039 (2024), 596–603. DOI: 10.1038/s41586-024-07997-7.

[21] Esma Ugur et al. "Enhanced cation interaction in perovskites for efficient tandem solar cells with silicon". In: *Science* 385.6708 (2024), 533–538. DOI: 10.1126/science.adp1621.

[22] Tobias Abzieher et al. "Vapor phase deposition of perovskite photovoltaics: short track to commercialization?" In: *Energy & Environmental Science* 17.5 (2024), 1645–1663. DOI: 10.1039/d3ee03273f.

[23] Longbin Qiu et al. "Scalable Fabrication of Metal Halide Perovskite Solar Cells and Modules". In: *ACS Energy Letters* 4.9 (2019), 2147–2167. DOI: 10.1021/acsenergylett.9b01396.

[24] Xiaoming Zhao et al. "Operationally stable perovskite solar modules enabled by vapor-phase fluoride treatment". In: *Science* 385.6707 (2024), 433–438. DOI: 10.1126/science.adn9453.

[25] Yunxiu Shen et al. "Strain regulation retards natural operation decay of perovskite solar cells". In: *Nature* 635.8040 (2024), 882–889. DOI: 10.1038/s41586-024-08161-x.

[26] Nam-Gyu Park et al. "Scalable fabrication and coating methods for perovskite solar cells and solar modules". In: *Nature Reviews Materials* 5.5 (2020), 333–350. DOI: 10.1038/s41578-019-0176-2.

[27] Pengchen Zhu et al. "Toward the Commercialization of Perovskite Solar Modules". In: *Advanced Materials* 36.15 (2024), p. 2307357. DOI: 10.1002/adma.202307357.

[28] Ian A. Howard et al. "Coated and Printed Perovskites for Photovoltaic Applications". In: *Advanced Materials* 31.26 (2019), p. 1806702. DOI: 10.1002/adma.201806702.

[29] Karen Forberich et al. "A Stage-Gate Framework for Upscaling of Single-Junction Perovskite Photovoltaics". In: *Advanced Energy Materials* (2024). DOI: 10.1002/aenm.202404036.

[30] Oxford PV. *Oxford PV debuts residential solar module with record-setting 26.9% efficiency*. Oxford PV. 2024. URL: https://www.oxfordpv.com/news/oxford-pv-debuts-residential-solar-module-record-setting-269-efficiency (visited on 10/30/2024).

[31] Oxford PV. *20% more powerful tandem solar panels enter commercial use for the first time in the US*. Oxford PV. 2024. URL: https://www.oxfordpv.com/news/20-more-powerful-tandem-solar-panels-enter-commercial-use-first-time-us (visited on 10/30/2024).

[32] Markus Fischer et al. *International Technology Roadmap for Photovoltaics (ITRPV, 14th Edition)*. Verband Deutscher Maschinen- und Anlagenbau e. V. (VDMA). 2023. URL: https://www.vdma.org/international-technology-roadmap-photovoltaic (visited on 12/12/2024).

[33] Molang Cai et al. "Cost-Performance Analysis of Perovskite Solar Modules". In: *Advanced Science* 4.1 (2016). DOI: 10.1002/advs.201600269.

[34] Nathan L. Chang et al. "A manufacturing cost estimation method with uncertainty analysis and its application to perovskite on glass photovoltaic modules". In: *Progress in Photovoltaics: Research and Applications* 25.5 (2017), pp. 390–405. DOI: 10.1002/pip.2871.

[35] Zhaoning Song et al. "A technoeconomic analysis of perovskite solar module manufacturing with low-cost materials and techniques". In: *Energy & Environmental Science* 10.6 (2017), 1297–1305. DOI: 10.1039/c7ee00757d.

[36] Jacob J. Cordell et al. “Technoeconomic analysis of perovskite/silicon tandem solar modules”. In: *Joule* (2024). DOI: 10.1016/j.joule.2024.10.013.

[37] Pavel Čulík et al. “Design and Cost Analysis of 100 MW Perovskite Solar Panel Manufacturing Process in Different Locations”. In: *ACS Energy Letters* 7.9 (2022), 3039–3044. DOI: 10.1021/acsenergylett.2c01728.

[38] Christoph J. Brabec. *Acceleration of Emerging Photovoltaics*. Conference Talk. Materials for Sustainable Development Conference Spring Meeting. 2024.

[39] Ian Mathews et al. “Economically Sustainable Growth of Perovskite Photovoltaics Manufacturing”. In: *Joule* 4.4 (2020), pp. 822–839. DOI: 10.1016/j.joule.2020.01.006.

[40] Jan Oliver Löfken. *Perovskites move into production*. pv-magazine-usa.com. 2024. URL: https://pv-magazine-usa.com/2024/05/24/perovskites-move-into-production/ (visited on 10/30/2024).

[41] Marian Willuhnn. *Commercial perovskite solar modules at SNEC 2024 trade show*. pv-magazine.com. 2024. URL: https://www.pv-magazine.com/2024/06/13/commercial-perovskite-solar-modules-at-snec-2024-trade-show/ (visited on 10/30/2024).

[42] V. M. Goldschmidt. “Die Gesetze der Krystallochemie”. In: *Die Naturwissenschaften* 14.21 (1926), 477–485. DOI: 10.1007/bf01507527.

[43] Jin-Wook Lee et al. “Rethinking the A cation in halide perovskites”. In: *Science* 375.6583 (2022). DOI: 10.1126/science.abj1186.

[44] T. Jesper Jacobsson et al. “Goldschmidt’s Rules and Strontium Replacement in Lead Halogen Perovskite Solar Cells: Theory and Preliminary Experiments on $CH_3NH_3SrI_3$”. In: *The Journal of Physical Chemistry C* 119.46 (2015), 25673–25683. DOI: 10.1021/acs.jpcc.5b06436.

[45] Zhen Li et al. “Stabilizing Perovskite Structures by Tuning Tolerance Factor: Formation of Formamidinium and Cesium Lead Iodide Solid-State Alloys”. In: *Chemistry of Materials* 28.1 (2015), 284–292. DOI: 10.1021/acs.chemmater.5b04107.

[46] Qiaojiao Gao et al. “Halide Perovskite Crystallization Processes and Methods in Nanocrystals, Single Crystals, and Thin Films”. In: *Advanced Materials* 34.52 (2022). DOI: 10.1002/adma.202200720.

[47] Saba Gharibzadeh et al. “2D/3D Heterostructure for Semitransparent Perovskite Solar Cells with Engineered Bandgap Enables Efficiencies Exceeding 25% in Four-Terminal Tandems with Silicon and CIGS”. In: *Advanced Functional Materials* 30.19 (2020). DOI: 10.1002/adfm.201909919.

[48] Zewen Xiao et al. “Progress in Theoretical Study of Metal Halide Perovskite Solar Cell Materials”. In: *Advanced Energy Materials* 7.22 (2017). DOI: 10.1002/aenm.201701136.

[49] Michael Saliba et al. “Cesium-containing triple cation perovskite solar cells: improved stability, reproducibility and high efficiency”. In: *Energy & Environmental Science* 9.6 (2016), 1989–1997. DOI: 10.1039/c5ee03874j.

[50] Akihiro Kojima et al. “Novel Photoelectrochemical Cell with Mesoscopic Electrodes Sensitized by Lead-Halide Compounds (2)”. In: *ECS Meeting Abstracts* MA2006-02.7 (2006), 397–397. DOI: 10.1149/ma2006-02/7/397.

[51] Akihiro Kojima et al. “Organometal Halide Perovskites as Visible-Light Sensitizers for Photovoltaic Cells”. In: *Journal of the American Chemical Society* 131.17 (2009), 6050–6051. DOI: 10.1021/ja809598r.

[52] Shuxia Tao et al. “Absolute energy level positions in tin- and lead-based halide perovskites”. In: *Nature Communications* 10.1 (2019). DOI: 10.1038/s41467-019-10468-7.

[53] Jun Hong Noh et al. “Chemical Management for Colorful, Efficient, and Stable Inorganic–Organic Hybrid Nanostructured Solar Cells”. In: *Nano Letters* 13.4 (Mar. 2013), 1764–1769. ISSN: 1530-6992. DOI: 10.1021/nl400349b. URL: http://dx.doi.org/10.1021/nl400349b.

[54] Nam-Gyu Park. “Perovskite solar cells: an emerging photovoltaic technology”. In: *Materials Today* 18.2 (2015), 65–72. DOI: 10.1016/j.mattod.2014.07.007.

[55] Stefaan De Wolf et al. “Organometallic Halide Perovskites: Sharp Optical Absorption Edge and Its Relation to Photovoltaic Performance”. In: *The Journal of Physical Chemistry Letters* 5.6 (2014), 1035–1039. DOI: 10.1021/jz500279b.

[56] Krzysztof Galkowski et al. “Determination of the exciton binding energy and effective masses for methylammonium and formamidinium lead tri-halide perovskite semiconductors”. In: *Energy & Environmental Science* 9.3 (2016), 962–970. DOI: 10.1039/c5ee03435c.

[57] Valerio D’Innocenzo et al. “Excitons versus free charges in organo-lead tri-halide perovskites”. In: *Nature Communications* 5.1 (2014). DOI: 10.1038/ncomms4586.

[58] Jun Kang et al. “High Defect Tolerance in Lead Halide Perovskite $CsPbBr_3$”. In: *The Journal of Physical Chemistry Letters* 8.2 (2017), 489–493. DOI: 10.1021/acs.jpclett.6b02800.

[59] K. Xerxes Steirer et al. “Defect Tolerance in Methylammonium Lead Triiodide Perovskite”. In: *ACS Energy Letters* 1.2 (2016), 360–366. DOI: 10.1021/acsenergylett.6b00196.

[60] Christian Wehrenfennig et al. “High Charge Carrier Mobilities and Lifetimes in Organolead Trihalide Perovskites”. In: *Advanced Materials* 26.10 (2013), 1584–1589. DOI: 10.1002/adma.201305172.

[61] Y. Chen et al. “Extended carrier lifetimes and diffusion in hybrid perovskites revealed by Hall effect and photoconductivity measurements”. In: *Nature Communications* 7.1 (2016). DOI: 10.1038/ncomms12253.

[62] Chelsea Q. Xia et al. “Limits to Electrical Mobility in Lead-Halide Perovskite Semiconductors”. In: *The Journal of Physical Chemistry Letters* 12.14 (2021), 3607–3617. DOI: 10.1021/acs.jpclett.1c00619.

[63] Sarah E. Sofia et al. “Roadmap for cost-effective, commercially-viable perovskite silicon tandems for the current and future PV market”. In: *Sustainable Energy & Fuels* 4.2 (2020), 852–862. DOI: 10.1039/c9se00948e.

[64] Peter Würfel et al. *Physics of Solar Cells: From Principles to New Concepts*. 3rd ed. 2016. ISBN: 9783527413126.

[65] Iván Mora-Seró. “How Do Perovskite Solar Cells Work?” In: *Joule* 2.4 (2018), 585–587. DOI: 10.1016/j.joule.2018.03.020.

[66] Juan Bisquert. *The Physics of Solar Cells: Perovskites, Organics, and Photovoltaic Fundamentals*. 2017. ISBN: 9781138305243. DOI: 10.1201/b22380.

[67] Uli Würfel et al. “Charge Carrier Separation in Solar Cells”. In: *IEEE Journal of Photovoltaics* 5.1 (2015), 461–469. DOI: 10.1109/jphotov.2014.2363550.

[68] Pietro Caprioglio et al. “On the Relation between the Open-Circuit Voltage and Quasi-Fermi Level Splitting in Efficient Perovskite Solar Cells”. In: *Advanced Energy Materials* 9.33 (2019). DOI: 10.1002/aenm.201901631.

[69] Tim Hellmann et al. “The Electronic Structure of MAPI-Based Perovskite Solar Cells: Detailed Band Diagram Determination by Photoemission Spectroscopy Comparing Classical and Inverted Device Stacks”. In: *Advanced Energy Materials* 10.42 (2020). DOI: 10.1002/aenm.202002129.

[70] Arthur L. Samuel. “Some Studies in Machine Learning Using the Game of Checkers”. In: *IBM Journal of Research and Development* 3.3 (1959), 210–229. DOI: 10.1147/rd.33.0210.

[71] Kevin P. Murphy. *Probabilistic Machine Learning: An introduction*. MIT Press, 2022. URL: http://probml.github.io/book1.

[72] Christopher M. Bishop. *Pattern Recognition and Machine Learning (Information Science and Statistics)*. Springer-Verlag, 2006. ISBN: 0387310738.

[73] Stefan Sandfeld. *Materials Data Science: Introduction to Data Mining, Machine Learning, and Data-Driven Predictions for Materials Science and Engineering*. Springer International Publishing, 2024. ISBN: 9783031465659. DOI: 10.1007/978-3-031-46565-9.

[74] David Silver et al. "Mastering the game of Go with deep neural networks and tree search". In: *Nature* 529.7587 (2016), 484–489. DOI: 10.1038/nature16961.

[75] James B. MacQueen. "Some Methods for Classification and Analysis of MultiVariate Observations". In: *Proc. of the fifth Berkeley Symposium on Mathematical Statistics and Probability*. Vol. 5. 1. 1967, pp. 281–297.

[76] scikit learn. *Machine Learning in Python*. URL: https://scikit-learn.org/stable/#. (visited on 10/03/2024).

[77] Robert L. Thorndike. "Who belongs in the family?" In: *Psychometrika* 18.4 (1953), 267–276. DOI: 10.1007/bf02289263.

[78] Corinna Cortes et al. "Support-vector networks". In: *Machine Learning* 20.3 (1995), 273–297. DOI: 10.1007/bf00994018.

[79] Y. LeCun et al. "Gradient-based learning applied to document recognition". In: *Proceedings of the IEEE* 86.11 (1998), 2278–2324. DOI: 10.1109/5.726791.

[80] Naomi S. Altman. "An Introduction to Kernel and Nearest-Neighbor Nonparametric Regression". In: *The American Statistician* 46.3 (1992), 175–185. DOI: 10.1080/00031305.1992.10475879.

[81] Leo Breiman. "Random Forests". In: *Machine Learning* 45.1 (2001), 5–32. ISSN: 0885-6125. DOI: 10.1023/a:1010933404324.

[82] Leo Breiman et al. *Classification And Regression Trees*. Routledge, 1984. ISBN: 9781315139470. DOI: 10.1201/9781315139470.

[83] Yoav Freund et al. "A Decision-Theoretic Generalization of On-Line Learning and an Application to Boosting". In: *Journal of Computer and System Sciences* 55.1 (1997), 119–139. DOI: 10.1006/jcss.1997.1504.

[84] Jerome H. Friedman. "Greedy function approximation: A gradient boosting machine." In: *The Annals of Statistics* 29.5 (2001). DOI: 10.1214/aos/1013203451.

[85] Jerome H. Friedman. "Stochastic gradient boosting". In: *Computational Statistics & Data Analysis* 38.4 (2002), 367–378. DOI: 10.1016/s0167-9473(01)00065-2.

[86] Tianqi Chen et al. "XGBoost: A Scalable Tree Boosting System". In: *Proceedings of the 22nd ACM SIGKDD International Conference on Knowledge Discovery and Data Mining*. KDD '16. 2016, 785–794. DOI: 10.1145/2939672.2939785. URL: http://dx.doi.org/10.1145/2939672.2939785.

[87] Liudmila Prokhorenkova et al. "CatBoost: unbiased boosting with categorical features". In: (2017). DOI: 10.48550/ARXIV.1706.09516.

[88] Guolin Ke et al. "LightGBM: A Highly Efficient Gradient Boosting Decision Tree". In: *Advances in Neural Information Processing Systems*. Vol. 30. 2017. URL: https://proceedings.neurips.cc/paper_files/paper/2017/file/6449f44a102fde848669bdd9eb6b76fa-Paper.pdf.

[89] Frank Rosenblatt. "The perceptron: A probabilistic model for information storage and organization in the brain." In: *Psychological Review* 65.6 (1958), 386–408. DOI: 10.1037/h0042519.

[90] Juergen Schmidhuber. "Annotated History of Modern AI and Deep Learning". In: (2022). DOI: 10.48550/ARXIV.2212.11279.

[91] Yann LeCun et al. "Deep learning". In: *Nature* 521.7553 (2015), 436–444. DOI: 10.1038/nature14539.

[92] Kurt Hornik et al. "Multilayer feedforward networks are universal approximators". In: *Neural Networks* 2.5 (1989), 359–366. DOI: 10.1016/0893-6080(89)90020-8.

[93] Alex Krizhevsky et al. “ImageNet classification with deep convolutional neural networks”. In: *Communications of the ACM* 60.6 (2017), 84–90. DOI: 10.1145/3065386.

[94] Kaiming He et al. “Deep Residual Learning for Image Recognition”. In: (2015). DOI: 10.48550/ARXIV.1512.03385.

[95] Y. LeCun et al. “Backpropagation Applied to Handwritten Zip Code Recognition”. In: *Neural Computation* 1.4 (1989), 541–551. DOI: 10.1162/neco.1989.1.4.541.

[96] David E. Rumelhart et al. “Learning representations by back-propagating errors”. In: *Nature* 323.6088 (1986), 533–536. DOI: 10.1038/323533a0.

[97] Adam Paszke et al. “PyTorch: An Imperative Style, High-Performance Deep Learning Library”. In: (2019). DOI: 10.48550/ARXIV.1912.01703.

[98] Trevor Hastie et al. *The Elements of Statistical Learning*. Springer New York, 2009. ISBN: 9780387848587. DOI: 10.1007/978-0-387-84858-7.

[99] Diederik P. Kingma et al. “Adam: A Method for Stochastic Optimization”. In: (2014). DOI: 10.48550/ARXIV.1412.6980.

[100] Nitish Shirish Keskar et al. “On Large-Batch Training for Deep Learning: Generalization Gap and Sharp Minima”. In: (2016). DOI: 10.48550/ARXIV.1609.04836.

[101] Nitish Srivastava et al. “Dropout: A Simple Way to Prevent Neural Networks from Overfitting”. In: *Journal of Machine Learning Research* 15.56 (2014), pp. 1929–1958. URL: http://jmlr.org/papers/v15/srivastava14a.html.

[102] Klaus-Robert Müller. “Regularization Techniques to Improve Generalization”. In: *Neural Networks: Tricks of the Trade*. Springer Berlin Heidelberg, 2012, 49–51. ISBN: 9783642352898. DOI: 10.1007/978-3-642-35289-8_4.

[103] Lutz Prechelt. “Early Stopping - But When?” In: *Neural Networks: Tricks of the Trade*. Springer Berlin Heidelberg, 1998, 55–69. ISBN: 9783540494300. DOI: 10.1007/3-540-49430-8_3.

[104] Sepp Hochreiter et al. “Long Short-Term Memory”. In: *Neural Computation* 9.8 (1997), 1735–1780. DOI: 10.1162/neco.1997.9.8.1735.

[105] Y. Bengio et al. “Learning long-term dependencies with gradient descent is difficult”. In: *IEEE Transactions on Neural Networks* 5.2 (1994), 157–166. DOI: 10.1109/72.279181.

[106] David Balduzzi et al. “The Shattered Gradients Problem: If resnets are the answer, then what is the question?” In: (2017). DOI: 10.48550/ARXIV.1702.08591.

[107] Hanchen Wang et al. “Scientific discovery in the age of artificial intelligence”. In: *Nature* 620.7972 (2023), 47–60. DOI: 10.1038/s41586-023-06221-2.

[108] Wojciech Samek et al. *Explainable AI: Interpreting, Explaining and Visualizing Deep Learning*. Springer International Publishing, 2019. ISBN: 9783030289546. DOI: 10.1007/978-3-030-28954-6. URL: http://dx.doi.org/10.1007/978-3-030-28954-6.

[109] Finale Doshi-Velez et al. “Towards A Rigorous Science of Interpretable Machine Learning”. In: (2017). DOI: 10.48550/ARXIV.1702.08608.

[110] Grégoire Montavon et al. “Methods for interpreting and understanding deep neural networks”. In: *Digital Signal Processing* 73 (2018), 1–15. DOI: 10.1016/j.dsp.2017.10.011.

[111] Zachary C. Lipton. “The Mythos of Model Interpretability”. In: (2016). DOI: 10.48550/ARXIV.1606.03490.

[112] Scott Lundberg et al. “A Unified Approach to Interpreting Model Predictions”. In: (2017). DOI: 10.48550/ARXIV.1705.07874.

[113] Karen Simonyan et al. “Deep Inside Convolutional Networks: Visualising Image Classification Models and Saliency Maps”. In: (2013). DOI: 10.48550/ARXIV.1312.6034.

[114] Jinghao Hu et al. “Interpretable machine learning predictions for efficient perovskite solar cell development”. In: *Solar Energy Materials and Solar Cells* 271 (2024), p. 112826. DOI: 10.1016/j.solmat.2024.112826.

[115] Yibo Sun et al. “Interpretable Machine Learning to Discover Perovskites with High Spontaneous Polarization”. In: *The Journal of Physical Chemistry C* 127.49 (2023), 23897–23905. DOI: 10.1021/acs.jpcc.3c05742.

[116] Yiming Liu et al. “How Machine Learning Predicts and Explains the Performance of Perovskite Solar Cells”. In: *Solar RRL* 6.6 (2022). DOI: 10.1002/solr.202101100.

[117] Jiazheng Wang et al. “Advancing vapor-deposited perovskite solar cells via machine learning”. In: *Journal of Materials Chemistry A* 11.25 (2023), 13201–13208. DOI: 10.1039/d3ta00027c.

[118] Kjersti Aas et al. “Explaining individual predictions when features are dependent: More accurate approximations to Shapley values”. In: *Artificial Intelligence* 298 (2021), p. 103502. DOI: 10.1016/j.artint.2021.103502.

[119] Mukund Sundararajan et al. “Axiomatic Attribution for Deep Networks”. In: (2017). DOI: 10.48550/ARXIV.1703.01365.

[120] Gabriel Erion et al. “Improving performance of deep learning models with axiomatic attribution priors and expected gradients”. In: (2019). DOI: 10.48550/ARXIV.1906.10670.

[121] Sandra Wachter et al. “Counterfactual Explanations without Opening the Black Box: Automated Decisions and the GDPR”. In: (2017). DOI: 10.48550/ARXIV.1711.00399.

[122] Susanne Dandl et al. “Multi-Objective Counterfactual Explanations”. In: *Parallel Problem Solving from Nature – PPSN XVI*. Springer International Publishing, 2020, 448–469. ISBN: 9783030581121. DOI: 10.1007/978-3-030-58112-1_31.

[123] Ilia Stepin et al. “An empirical study on how humans appreciate automated counterfactual explanations which embrace imprecise information”. In: *Information Sciences* 618 (2022), 379–399. DOI: 10.1016/j.ins.2022.10.098.

[124] Been Kim et al. “Interpretability Beyond Feature Attribution: Quantitative Testing with Concept Activation Vectors (TCAV)”. In: (2017). DOI: 10.48550/ARXIV.1711.11279.

[125] C. O. S. Sorzano et al. “A survey of dimensionality reduction techniques”. In: (2014). DOI: 10.48550/ARXIV.1403.2877.

[126] Weikuan Jia et al. “Feature dimensionality reduction: a review”. In: *Complex & Intelligent Systems* 8.3 (2022), 2663–2693. DOI: 10.1007/s40747-021-00637-x.

[127] Urszula Stańczyk. “Feature Evaluation by Filter, Wrapper, and Embedded Approaches”. In: *Feature Selection for Data and Pattern Recognition*. Springer Berlin Heidelberg, 2014, 29–44. ISBN: 9783662456200. DOI: 10.1007/978-3-662-45620-0_3.

[128] Ian T. Jolliffe et al. “Principal component analysis: a review and recent developments”. In: *Philosophical Transactions of the Royal Society A: Mathematical, Physical and Engineering Sciences* 374.2065 (2016), p. 20150202. DOI: 10.1098/rsta.2015.0202.

[129] G. E. Hinton et al. “Reducing the Dimensionality of Data with Neural Networks”. In: *Science* 313.5786 (2006), 504–507. DOI: 10.1126/science.1127647.

[130] Zhaoxiang Liu et al. “Feature Aggregation Network for Video Face Recognition”. In: (2019). DOI: 10.48550/ARXIV.1905.01796.

[131] Python. URL: https://www.python.org/. (visited on 10/03/2024).

[132] jupyter. *Free software, open standards, and web services for interactive computing across all programming languages*. URL: https://jupyter.org/ (visited on 10/03/2024).

[133] tifffile. *Read and write TIFF files*. URL: https://pypi.org/project/tifffile/. (visited on 10/03/2024).

[134] OpenCV. *Computer Vision Library*. URL: https://opencv.org/. (visited on 10/03/2024).

[135] Pillow. *Python Imaging Library*. URL: https://pypi.org/project/Pillow/. (visited on 10/03/2024).

[136] The HDF5 Library & File Format. *High-performance data management and storage suite*. URL: https://www.hdfgroup.org/solutions/hdf5/. (visited on 10/03/2024).

[137] pandas. *Python Data Analysis Library*. URL: https://pandas.pydata.org/. (visited on 10/03/2024).

[138] NumPy. *The fundamental package for scientific computing with Python*. URL: https://numpy.org/. (visited on 10/03/2024).

[139] Matplotlib. *Visualization with Python*. URL: https://matplotlib.org/. (visited on 10/03/2024).

[140] SciPy. *Fundamental algorithms for scientific computing in Python*. URL: https://scipy.org/ (visited on 12/12/2024).

[141] statsmodels. *statistical models, hypothesis tests, and data exploration*. URL: https://www.statsmodels.org/stable/index.html (visited on 12/12/2024).

[142] Krishna Rajan. "Materials informatics". In: *Materials Today* 8.10 (2005), 38–45. DOI: 10.1016/s1369-7021(05)71123-8.

[143] M. I. Jordan et al. "Machine learning: Trends, perspectives, and prospects". In: *Science* 349.6245 (2015), 255–260. DOI: 10.1126/science.aaa8415.

[144] Edward O. Pyzer-Knapp et al. "Accelerating materials discovery using artificial intelligence, high performance computing and robotics". In: *npj Computational Materials* 8.1 (2022). DOI: 10.1038/s41524-022-00765-z.

[145] Amil Merchant et al. "Scaling deep learning for materials discovery". In: *Nature* 624.7990 (2023), 80–85. DOI: 10.1038/s41586-023-06735-9.

[146] Keith T. Butler et al. "Machine learning for molecular and materials science". In: *Nature* 559.7715 (2018), 547–555. DOI: 10.1038/s41586-018-0337-2.

[147] Paul Raccuglia et al. "Machine-learning-assisted materials discovery using failed experiments". In: *Nature* 533.7601 (2016), 73–76. DOI: 10.1038/nature17439.

[148] Rampi Ramprasad et al. "Machine learning in materials informatics: recent applications and prospects". In: *npj Computational Materials* 3.1 (2017). DOI: 10.1038/s41524-017-0056-5.

[149] Ziyuan Rao et al. "Machine learning–enabled high-entropy alloy discovery". In: *Science* 378.6615 (2022), 78–85. DOI: 10.1126/science.abo4940.

[150] Pascal Friederich et al. "Machine-learned potentials for next-generation matter simulations". In: *Nature Materials* 20.6 (2021), 750–761. DOI: 10.1038/s41563-020-0777-6.

[151] Jonathan Schmidt et al. "Recent advances and applications of machine learning in solid-state materials science". In: *npj Computational Materials* 5.1 (2019). DOI: 10.1038/s41524-019-0221-0.

[152] Logan Ward et al. "A general-purpose machine learning framework for predicting properties of inorganic materials". In: *npj Computational Materials* 2.1 (2016). DOI: 10.1038/npjcompumats.2016.28.

[153] Beyza Yılmaz et al. "Critical review of machine learning applications in perovskite solar research". In: *Nano Energy* 80 (2021), p. 105546. DOI: 10.1016/j.nanoen.2020.105546.

[154] Yiming Liu et al. "Machine Learning for Perovskite Solar Cells and Component Materials: Key Technologies and Prospects". In: *Advanced Functional Materials* 33.17 (2023). DOI: 10.1002/adfm.202214271.

[155] Chen Chen et al. “The role of machine learning in perovskite solar cell research”. In: *Journal of Alloys and Compounds* 960 (2023), p. 170824. DOI: 10.1016/j.jallcom.2023.170824.

[156] Rishi E. Kumar et al. “Opportunities for machine learning to accelerate halide-perovskite commercialization and scale-up”. In: *Matter* 5.5 (2022), 1353–1366. DOI: 10.1016/j.matt.2022.04.016.

[157] Lei Zhang et al. “Machine learning for halide perovskite materials”. In: *Nano Energy* 78 (2020), p. 105380. DOI: 10.1016/j.nanoen.2020.105380.

[158] Qiuling Tao et al. “Machine learning for perovskite materials design and discovery”. In: *npj Computational Materials* 7.1 (2021). DOI: 10.1038/s41524-021-00495-8.

[159] Tiantian Liu et al. “Machine-Learning Accelerating the Development of Perovskite Photovoltaics”. In: *Solar RRL* 7.23 (2023). DOI: 10.1002/solr.202300650.

[160] Bonghyun Jo et al. “Comprehensive review of advances in machine-learning-driven optimization and characterization of perovskite materials for photovoltaic devices”. In: *Journal of Energy Chemistry* 101 (2025), 298–323. DOI: 10.1016/j.jechem.2024.09.043.

[161] Ling Mao et al. “A comprehensive review of machine learning applications in perovskite solar cells: Materials discovery, device performance, process optimization and systems integration”. In: *Materials Today Energy* 47 (2025), p. 101742. DOI: 10.1016/j.mtener.2024.101742.

[162] Subham Subba et al. “Machine Learning Approaches in Advancing Perovskite Solar Cells Research”. In: *Advanced Theory and Simulations* (2024). DOI: 10.1002/adts.202400652.

[163] Meghna Srivastava et al. “Machine Learning Roadmap for Perovskite Photovoltaics”. In: *The Journal of Physical Chemistry Letters* 12.32 (2021), 7866–7877. DOI: 10.1021/acs.jpclett.1c01961.

[164] Abigail R. Hering et al. “Emerging opportunities for hybrid perovskite solar cells using machine learning”. In: *APL Energy* 1.2 (2023). DOI: 10.1063/5.0146828.

[165] Chang Woo Myung et al. “Challenges, Opportunities, and Prospects in Metal Halide Perovskites from Theoretical and Machine Learning Perspectives”. In: *Advanced Energy Materials* 12.45 (2022). DOI: 10.1002/aenm.202202279.

[166] Juan-Pablo Correa-Baena et al. “Accelerating Materials Development via Automation, Machine Learning, and High-Performance Computing”. In: *Joule* 2.8 (2018), 1410–1420. DOI: 10.1016/j.joule.2018.05.009.

[167] John M. Howard et al. “Machine Learning for Perovskites’ Reap-Rest-Recovery Cycle”. In: *Joule* 3.2 (2019), 325–337. DOI: 10.1016/j.joule.2018.11.010.

[168] Ankit Agrawal et al. “Perspective: Materials informatics and big data: Realization of the “fourth paradigm” of science in materials science”. In: *APL Materials* 4.5 (2016). DOI: 10.1063/1.4946894.

[169] Liang Gao et al. “Machine Learning-Assisted Design of Advanced Polymeric Materials”. In: *Accounts of Materials Research* 5.5 (2024), 571–584. DOI: 10.1021/accountsmr.3c00288.

[170] Cheng-Zhou Zhang et al. “Applications and potentials of machine learning in optoelectronic materials research: An overview and perspectives”. In: *Chinese Physics B* 32.12 (2023), p. 126103. DOI: 10.1088/1674-1056/ad01a4.

[171] Daniel P Tabor et al. “Accelerating the discovery of materials for clean energy in the era of smart automation”. In: *Nature Reviews Materials* 5 (2018), pp. 5–20. DOI: 10.1038/s41578-018-0005-z.

[172] Florian Häse et al. “Designing and understanding light-harvesting devices with machine learning”. In: *Nature Communications* 11.1 (2020). DOI: 10.1038/s41467-020-17995-8.

[173] Zhenpeng Yao et al. “Machine learning for a sustainable energy future”. In: *Nature Reviews Materials* 8.3 (2022), 202–215. DOI: 10.1038/s41578-022-00490-5.

[174] Shuaihua Lu et al. “Accelerated discovery of stable lead-free hybrid organic-inorganic perovskites via machine learning”. In: *Nature Communications* 9.1 (2018). DOI: 10.1038/s41467-018-05761-w.

[175] Jino Im et al. “Identifying Pb-free perovskites for solar cells by machine learning”. In: *npj Computational Materials* 5.1 (2019). DOI: 10.1038/s41524-019-0177-0.

[176] Xia Cai et al. “Discovery of Lead-Free Perovskites for High-Performance Solar Cells via Machine Learning: Ultrabroadband Absorption, Low Radiative Combination, and Enhanced Thermal Conductivities”. In: *Advanced Science* 9.4 (2021). DOI: 10.1002/advs.202103648.

[177] Arun Mannodi-Kanakkithodi et al. “Data-driven design of novel halide perovskite alloys”. In: *Energy & Environmental Science* 15.5 (2022), 1930–1949. DOI: 10.1039/d1ee02971a.

[178] Jinxin Li et al. “Predictions and Strategies Learned from Machine Learning to Develop High-Performing Perovskite Solar Cells”. In: *Advanced Energy Materials* 9.46 (2019). DOI: 10.1002/aenm.201901891.

[179] Heesoo Park et al. “Data-driven enhancement of cubic phase stability in mixed-cation perovskites”. In: *Machine Learning: Science and Technology* 2.2 (2021), p. 025030. DOI: 10.1088/2632-2153/abdaf9.

[180] Xia Liang et al. “Structural Dynamics Descriptors for Metal Halide Perovskites”. In: *The Journal of Physical Chemistry C* 127.38 (2023), 19141–19151. DOI: 10.1021/acs.jpcc.3c03377.

[181] Chenyang Zhu et al. “Exploration of highly stable and highly efficient new lead-free halide perovskite solar cells by machine learning”. In: *Cell Reports Physical Science* 5.12 (2024), p. 102321. DOI: 10.1016/j.xcrp.2024.102321.

[182] Yang Pu et al. “Machine Learning Co-pilot for Screening of Organic Molecular Additives for Perovskite Solar Cells”. In: (2024). DOI: 10.48550/ARXIV.2412.14109.

[183] Xin Zhang et al. “Machine Learning for Screening Small Molecules as Passivation Materials for Enhanced Perovskite Solar Cells”. In: *Advanced Functional Materials* 34.30 (2024). DOI: 10.1002/adfm.202314529.

[184] Marcos del Cueto et al. “Data-Driven Analysis of Hole-Transporting Materials for Perovskite Solar Cells Performance”. In: *The Journal of Physical Chemistry C* 126.31 (2022), 13053–13061. DOI: 10.1021/acs.jpcc.2c04725.

[185] Wu Liu et al. “Screening interface passivation materials intelligently through machine learning for highly efficient perovskite solar cells”. In: *Journal of Materials Chemistry A* 10.34 (2022), 17782–17789. DOI: 10.1039/d2ta04788h.

[186] Jianchang Wu et al. “Inverse design workflow discovers hole-transport materials tailored for perovskite solar cells”. In: *Science* 386.6727 (2024), 1256–1264. DOI: 10.1126/science.ads0901.

[187] G. Pilania et al. “Machine learning bandgaps of double perovskites”. In: *Scientific Reports* 6.1 (2016). DOI: 10.1038/srep19375.

[188] Wissam A. Saidi et al. “Machine-learning structural and electronic properties of metal halide perovskites using a hierarchical convolutional neural network”. In: *npj Computational Materials* 6.1 (2020). DOI: 10.1038/s41524-020-0307-8.

[189] Vladislav Gladkikh et al. “Machine Learning for Predicting the Band Gaps of ABX_3 Perovskites from Elemental Properties”. In: *The Journal of Physical Chemistry C* 124.16 (2020), 8905–8918. DOI: 10.1021/acs.jpcc.9b11768.

[190] Pravan Omprakash et al. “Graph representational learning for bandgap prediction in varied perovskite crystals”. In: *Computational Materials Science* 196 (2021), p. 110530. DOI: 10.1016/j.commatsci.2021.110530.

[191] Ruoyu Li et al. “Predicting Perovskite Performance with Multiple Machine-Learning Algorithms”. In: *Crystals* 11.7 (2021), p. 818. DOI: 10.3390/cryst11070818.

[192] Yingjie Hu et al. “Machine-Learning Modeling for Ultra-Stable High-Efficiency Perovskite Solar Cells”. In: *Advanced Energy Materials* 12.41 (2022). DOI: 10.1002/aenm.202201463.

[193] Md. Shafiqul Islam et al. “Machine Learning Approach to Delineate the Impact of Material Properties on Solar Cell Device Physics”. In: *ACS Omega* 7.26 (2022), 22263–22278. DOI: 10.1021/acsomega.2c01076.

[194] Xing-Yu Ma et al. “Accelerated Discovery of Two-Dimensional Optoelectronic Octahedral Oxyhalides via High-Throughput Ab Initio Calculations and Machine Learning”. In: *The Journal of Physical Chemistry Letters* 10.21 (2019), 6734–6740. DOI: 10.1021/acs.jpclett.9b02420.

[195] Shijing Sun et al. “Accelerated Development of Perovskite-Inspired Materials via High-Throughput Synthesis and Machine-Learning Diagnosis”. In: *Joule* 3.6 (2019), 1437–1451. DOI: 10.1016/j.joule.2019.05.014.

[196] Ruiyang Lyu et al. “Predictive Design Model for Low-Dimensional Organic–Inorganic Halide Perovskites Assisted by Machine Learning”. In: *Journal of the American Chemical Society* 143.32 (2021), 12766–12776. DOI: 10.1021/jacs.1c05441.

[197] Florian Massuyeau et al. “Perovskite or Not Perovskite? A Deep-Learning Approach to Automatically Identify New Hybrid Perovskites from X-ray Diffraction Patterns”. In: *Advanced Materials* 34.41 (2022). DOI: 10.1002/adma.202203879.

[198] Qichen Xu et al. “Rationalizing Perovskite Data for Machine Learning and Materials Design”. In: *The Journal of Physical Chemistry Letters* 9.24 (2018), 6948–6954. DOI: 10.1021/acs.jpclett.8b03232.

[199] Shilin Zhang et al. “Predicting the Formability of Hybrid Organic–Inorganic Perovskites via an Interpretable Machine Learning Strategy”. In: *The Journal of Physical Chemistry Letters* 12.31 (2021), 7423–7430. DOI: 10.1021/acs.jpclett.1c01939.

[200] Zhenzhu Li et al. “Thermodynamic Stability Landscape of Halide Double Perovskites via High-Throughput Computing and Machine Learning”. In: *Advanced Functional Materials* 29.9 (2019). DOI: 10.1002/adfm.201807280.

[201] Anjana Talapatra et al. “A Machine Learning Approach for the Prediction of Formability and Thermodynamic Stability of Single and Double Perovskite Oxides”. In: *Chemistry of Materials* 33.3 (2021), 845–858. DOI: 10.1021/acs.chemmater.0c03402.

[202] Jonathan Schmidt et al. “Predicting the Thermodynamic Stability of Solids Combining Density Functional Theory and Machine Learning”. In: *Chemistry of Materials* 29.12 (2017), 5090–5103. DOI: 10.1021/acs.chemmater.7b00156.

[203] Çağla Odabaşı et al. “Performance analysis of perovskite solar cells in 2013–2018 using machine-learning tools”. In: *Nano Energy* 56 (2019), 770–791. DOI: 10.1016/j.nanoen.2018.11.069.

[204] Chenglong She et al. “Machine learning-guided search for high-efficiency perovskite solar cells with doped electron transport layers”. In: *Journal of Materials Chemistry A* 9.44 (2021), 25168–25177. DOI: 10.1039/d1ta08194b.

[205] Yao Lu et al. “Predicting the device performance of the perovskite solar cells from the experimental parameters through machine learning of existing experimental results”. In: *Journal of Energy Chemistry* 77 (2023), 200–208. DOI: 10.1016/j.jechem.2022.10.024.

[206] Eita Nakanishi et al. “Multivariate Analysis of Mixed Ternary and Quaternary A-Site Organic Cations in Tin Iodide Perovskite Solar Cells”. In: *ACS Materials Letters* 4.6 (2022), 1124–1131. DOI: 10.1021/acsmaterialslett.2c00229.

[207] Antai Yang et al. “Enhancing Power Conversion Efficiency of Perovskite Solar Cells Through Machine Learning Guided Experimental Strategies”. In: *Advanced Functional Materials* 35.4 (2024). DOI: 10.1002/adfm.202410419.

[208] Xiaoyan Du et al. “Elucidating the Full Potential of OPV Materials Utilizing a High-Throughput Robot-Based Platform and Machine Learning”. In: *Joule* 5.2 (2021), 495–506. DOI: 10.1016/j.joule.2020.12.013.

[209] Tobias Osterrieder et al. “Autonomous optimization of an organic solar cell in a 4-dimensional parameter space”. In: *Energy & Environmental Science* 16.9 (2023), 3984–3993. DOI: 10.1039/d3ee02027d.

[210] Stefan Langner et al. “Beyond Ternary OPV: High-Throughput Experimentation and Self-Driving Laboratories Optimize Multicomponent Systems”. In: *Advanced Materials* 32.14 (2020). DOI: 10.1002/adma.201907801.

[211] Jiyun Zhang et al. “Optimizing Perovskite Thin-Film Parameter Spaces with Machine Learning-Guided Robotic Platform for High-Performance Perovskite Solar Cells”. In: *Advanced Energy Materials* 13.48 (2023). DOI: 10.1002/aenm.202302594.

[212] Jian Xu et al. “Anion optimization for bifunctional surface passivation in perovskite solar cells”. In: *Nature Materials* 22.12 (2023), 1507–1514. DOI: 10.1038/s41563-023-01705-y.

[213] Zhe Liu et al. “Machine learning with knowledge constraints for process optimization of open-air perovskite solar cell manufacturing”. In: *Joule* 6.4 (2022), 834–849. DOI: 10.1016/j.joule.2022.03.003.

[214] Cody R. Allen et al. “Machine learning enhanced characterization and optimization of photonic cured $MAPbI_3$ for efficient perovskite solar cells”. In: *Journal of Materials Informatics* (2024). DOI: 10.20517/jmi.2024.72.

[215] Shijing Sun et al. “A data fusion approach to optimize compositional stability of halide perovskites”. In: *Matter* 4.4 (2021), 1305–1322. DOI: 10.1016/j.matt.2021.01.008.

[216] Kate Higgins et al. “Chemical Robotics Enabled Exploration of Stability in Multicomponent Lead Halide Perovskites via Machine Learning”. In: *ACS Energy Letters* 5.11 (2020), 3426–3436. DOI: 10.1021/acsenergylett.0c01749.

[217] Ryan J. Stoddard et al. “Forecasting the Decay of Hybrid Perovskite Performance Using Optical Transmittance or Reflected Dark-Field Imaging”. In: *ACS Energy Letters* 5.3 (2020), 946–954. DOI: 10.1021/acsenergylett.0c00164.

[218] Dohyung Kim et al. “Exploring Transport Behavior in Hybrid Perovskites Solar Cells via Machine Learning Analysis of Environmental-Dependent Impedance Spectroscopy”. In: *Advanced Science* 8.15 (2021). DOI: 10.1002/advs.202002510.

[219] Kate Higgins et al. “High-Throughput Study of Antisolvents on the Stability of Multicomponent Metal Halide Perovskites through Robotics-Based Synthesis and Machine Learning Approaches”. In: *Journal of the American Chemical Society* 143.47 (2021), 19945–19955. DOI: 10.1021/jacs.1c10045.

[220] Hao Zou et al. “Predicting thermodynamic stability of inorganic compounds using ensemble machine learning based on electron configuration”. In: *Nature Communications* 16.1 (2025). DOI: 10.1038/s41467-024-55525-y.

[221] Paolo Graniero et al. “The challenge of studying perovskite solar cells’ stability with machine learning”. In: *Frontiers in Energy Research* 11 (2023). DOI: 10.3389/fenrg.2023.1118654.

[222] Yongze Yu et al. “Machine Learning for Understanding Compatibility of Organic–Inorganic Hybrid Perovskites with Post-Treatment Amines”. In: *ACS Energy Letters* 4.2 (2019), 397–404. DOI: 10.1021/acsenergylett.8b02451.

[223] Çağla Odabaşı et al. “Machine learning analysis on stability of perovskite solar cells”. In: *Solar Energy Materials and Solar Cells* 205 (2020), p. 110284. DOI: 10.1016/j.solmat.2019.110284.

[224] Noor Titan Putri Hartono et al. “How machine learning can help select capping layers to suppress perovskite degradation”. In: *Nature Communications* 11.1 (2020). DOI: 10.1038/s41467-020-17945-4.

[225] Yicheng Zhao et al. “Discovery of temperature-induced stability reversal in perovskites using high-throughput robotic learning”. In: *Nature Communications* 12.1 (2021). DOI: 10.1038/s41467-021-22472-x.

[226] Felipe Oviedo et al. “DeepDeg: Forecasting and explaining degradation in novel photovoltaics”. In: (2023). DOI: 10.26434/chemrxiv-2023-j2pvp.

[227] Jiacheng Chen et al. “Predicting and analyzing stability in perovskite solar cells: Insights from machine learning models and SHAP analysis”. In: *Materials Today Energy* 48 (2025), p. 101769. DOI: 10.1016/j.mtener.2024.101769.

[228] Wiley A. Dunlap-Shohl et al. “Physiochemical machine learning models predict operational lifetimes of $CH_3NH_3PbI_3$ perovskite solar cells”. In: *Journal of Materials Chemistry A* 12.16 (2024), 9730–9746. DOI: 10.1039/d3ta06668a.

[229] Sofiia Kosar et al. “Imaging Locally Inhomogeneous Properties of Metal Halide Perovskites”. In: *Advanced Materials* (2024). DOI: 10.1002/adma.202406886.

[230] Alexander E. Siemenn et al. “Using scalable computer vision to automate high-throughput semiconductor characterization”. In: *Nature Communications* 15.1 (2024). DOI: 10.1038/s41467-024-48768-2.

[231] Jeffrey Kirman et al. “Machine-Learning-Accelerated Perovskite Crystallization”. In: *Matter* 2.4 (2020), 938–947. DOI: 10.1016/j.matt.2020.02.012.

[232] Nina Taherimakhsousi et al. “A machine vision tool for facilitating the optimization of large-area perovskite photovoltaics”. In: *npj Computational Materials* 7.1 (2021). DOI: 10.1038/s41524-021-00657-8.

[233] M. Harth et al. “Optoelectronic perovskite film characterization via machine vision”. In: *Solar Energy* 262 (2023), p. 111840. DOI: 10.1016/j.solener.2023.111840.

[234] Yongtao Liu et al. “Exploring the Relationship of Microstructure and Conductivity in Metal Halide Perovskites via Active Learning-Driven Automated Scanning Probe Microscopy”. In: *The Journal of Physical Chemistry Letters* 14.13 (2023), 3352–3359. DOI: 10.1021/acs.jpclett.3c00223.

[235] John M. Howard et al. “Quantitative Predictions of Moisture-Driven Photoemission Dynamics in Metal Halide Perovskites via Machine Learning”. In: *The Journal of Physical Chemistry Letters* 13.9 (2022), 2254–2263. DOI: 10.1021/acs.jpclett.2c00131.

[236] Meghna Srivastava et al. “Machine Learning Enables Prediction of Halide Perovskites’ Optical Behavior with >90% Accuracy”. In: *ACS Energy Letters* 8.4 (2023), 1716–1722. DOI: 10.1021/acsenergylett.2c02555.

[237] Calvin Fai et al. “Machine learning for enhanced semiconductor characterization from time-resolved photoluminescence”. In: *Joule* 6.11 (2022), 2585–2610. DOI: 10.1016/j.joule.2022.09.002.

[238] Ruiqi Zhang et al. “Predicting Organic-Inorganic Halide Perovskite Photovoltaic Performance from Optical Properties of Constituent Films through Machine Learning”. In: (2024). DOI: 10.48550/ARXIV.2412.09638.

[239] Erkan Aydin et al. “Pathways toward commercial perovskite/silicon tandem photovoltaics”. In: *Science* 383.6679 (2024). DOI: 10.1126/science.adh3849.

[240] Elham Foadian et al. “From Sunlight to Solutions: Closing the Loop on Halide Perovskites”. In: *ACS Materials Au* (2024). DOI: 10.1021/acsmaterialsau.4c00096.

[241] Mahshid Ahmadi et al. “Machine learning for high-throughput experimental exploration of metal halide perovskites”. In: *Joule* 5.11 (2021), 2797–2822. DOI: 10.1016/j.joule.2021.10.001.

[242] Benjamin Burger et al. “A mobile robotic chemist”. In: *Nature* 583.7815 (2020), 237–241. DOI: 10.1038/s41586-020-2442-2.

[243] Ying Shang et al. “Materials genome engineering accelerates the research and development of organic and perovskite photovoltaics”. In: *Materials Genome Engineering Advances* 2.1 (2024). DOI: 10.1002/mgea.28.

[244] Joshua Schrier et al. “In Pursuit of the Exceptional: Research Directions for Machine Learning in Chemical and Materials Science”. In: *Journal of the American Chemical Society* 145.40 (2023), 21699–21716. DOI: 10.1021/jacs.3c04783.

[245] Kedar Hippalgaonkar et al. “Knowledge-integrated machine learning for materials: lessons from gameplaying and robotics”. In: *Nature Reviews Materials* 8.4 (2023), 241–260. DOI: 10.1038/s41578-022-00513-1.

[246] Zhi Li et al. “Robot-Accelerated Perovskite Investigation and Discovery”. In: *Chemistry of Materials* 32.13 (2020), 5650–5663. DOI: 10.1021/acs.chemmater.0c01153.

[247] Elisabeth Reinhardt et al. “Rapid Characterization and Parameter Space Exploration of Perovskites Using an Automated Routine”. In: *ACS Combinatorial Science* 22.1 (2019), 6–17. DOI: 10.1021/acscombsci.9b00068.

[248] Mojan Omidvar et al. “Accelerated discovery of perovskite solid solutions through automated materials synthesis and characterization”. In: *Nature Communications* 15.1 (2024). DOI: 10.1038/s41467-024-50884-y.

[249] Jonghee Yang et al. “High-Throughput Automated Exploration of Phase Growth Behaviors in Quasi-2D Formamidinium Metal Halide Perovskites”. In: *Advanced Energy Materials* 13.43 (2023). DOI: 10.1002/aenm.202302337.

[250] Jonghee Yang et al. “Accelerating Materials Discovery by High-Throughput GIWAXS Characterization of Quasi-2D Formamidinium Metal Halide Perovskites”. In: *Advanced Functional Materials* 34.49 (2024). DOI: 10.1002/adfm.202409293.

[251] Yicheng Zhao et al. “A bilayer conducting polymer structure for planar perovskite solar cells with over 1, 400 hours operational stability at elevated temperatures”. In: *Nature Energy* 7.2 (2021), 144–152. DOI: 10.1038/s41560-021-00953-z.

[252] Tonghui Wang et al. “Sustainable materials acceleration platform reveals stable and efficient wide-bandgap metal halide perovskite alloys”. In: *Matter* 6.9 (2023), 2963–2986. DOI: 10.1016/j.matt.2023.06.040.

[253] Jiyun Zhang et al. “Autonomous Optimization of Air-Processed Perovskite Solar Cell in a Multidimensional Parameter Space”. In: *Advanced Energy Materials* (2025). DOI: 10.1002/aenm.202404957.

[254] Ening Gu et al. “Robot-Based High-Throughput Screening of Antisolvents for Lead Halide Perovskites”. In: *Joule* 4.8 (2020), 1806–1822. DOI: 10.1016/j.joule.2020.06.013.

[255] B. P. MacLeod et al. “Self-driving laboratory for accelerated discovery of thin-film materials”. In: *Science Advances* 6.20 (2020). DOI: 10.1126/sciadv.aaz8867.

[256] Milad Abolhasani et al. “The rise of self-driving labs in chemical and materials sciences”. In: *Nature Synthesis* 2.6 (2023), 483–492. DOI: 10.1038/s44160-022-00231-0.

[257] Sina Sadeghi et al. “Engineering a Sustainable Future: Harnessing Automation, Robotics, and Artificial Intelligence with Self-Driving Laboratories”. In: *ACS Sustainable Chemistry & Engineering* 12.34 (2024), 12695–12707. DOI: 10.1021/acssuschemeng.4c02177.

[258] Phillip M. Maffettone et al. “What is missing in autonomous discovery: open challenges for the community”. In: *Digital Discovery* 2.6 (2023), 1644–1659. DOI: 10.1039/d3dd00143a.

[259] Eric Stach et al. “Autonomous experimentation systems for materials development: A community perspective”. In: *Matter* 4.9 (2021), 2702–2726. DOI: 10.1016/j.matt.2021.06.036.

[260] Jiyun Zhang et al. “Toward Self-Driven Autonomous Material and Device Acceleration Platforms (AMADAP) for Emerging Photovoltaics Technologies”. In: *Accounts of Chemical Research* 57.9 (2024), 1434–1445. DOI: 10.1021/acs.accounts.4c00095.

[261] Jiyun Zhang et al. “Self-driving AMADAP laboratory: Accelerating the discovery and optimization of emerging perovskite photovoltaics”. In: *MRS Bulletin* 49.12 (2024), 1284–1294. DOI: 10.1557/s43577-024-00816-4.

[262] Ying-Yi Hong et al. “Methods of photovoltaic fault detection and classification: A review”. In: *Energy Reports* 8 (2022), 5898–5929. DOI: 10.1016/j.egyr.2022.04.043.

[263] B. Li et al. “Application of Artificial Neural Networks to photovoltaic fault detection and diagnosis: A review”. In: *Renewable and Sustainable Energy Reviews* 138 (2021), p. 110512. DOI: 10.1016/j.rser.2020.110512.

[264] Adel Mellit et al. “Assessment of machine learning and ensemble methods for fault diagnosis of photovoltaic systems”. In: *Renewable Energy* 184 (2022), 1074–1090. DOI: 10.1016/j.renene.2021.11.125.

[265] Gabriel Narvaez et al. “Machine learning for site-adaptation and solar radiation forecasting”. In: *Renewable Energy* 167 (2021), 333–342. DOI: 10.1016/j.renene.2020.11.089.

[266] ASM Shihavuddin et al. “Image based surface damage detection of renewable energy installations using a unified deep learning approach”. In: *Energy Reports* 7 (2021), 4566–4576. DOI: 10.1016/j.egyr.2021.07.045.

[267] Lukas Bommes et al. “Computer vision tool for detection, mapping, and fault classification of photovoltaics modules in aerial IR videos”. In: *Progress in Photovoltaics: Research and Applications* 29.12 (2021), 1236–1251. DOI: 10.1002/pip.3448.

[268] M. Aghaei et al. “Autonomous Intelligent Monitoring of Photovoltaic Systems: An In-Depth Multidisciplinary Review”. In: *Progress in Photovoltaics: Research and Applications* (2024). DOI: 10.1002/pip.3859.

[269] Mario Krenn et al. “On scientific understanding with artificial intelligence”. In: *Nature Reviews Physics* 4.12 (2022), 761–769. DOI: 10.1038/s42254-022-00518-3.

[270] Hitarth Choubisa et al. “Interpretable discovery of semiconductors with machine learning”. In: *npj Computational Materials* 9.1 (2023). DOI: 10.1038/s41524-023-01066-9.

[271] Vahe Tshitoyan et al. “Unsupervised word embeddings capture latent knowledge from materials science literature”. In: *Nature* 571.7763 (2019), 95–98. DOI: 10.1038/s41586-019-1335-8.

[272] James A. Evans et al. “Metaknowledge”. In: *Science* 331.6018 (2011), 721–725. DOI: 10.1126/science.1201765.

[273] Aaron Clauset et al. “Data-driven predictions in the science of science”. In: *Science* 355.6324 (2017), 477–480. DOI: 10.1126/science.aal4217.

[274] Mara Schilling-Wilhelmi et al. “From text to insight: large language models for chemical data extraction”. In: *Chemical Society Reviews* (2025). DOI: 10.1039/d4cs00913d.

[275] Andrew D. White. “The future of chemistry is language”. In: *Nature Reviews Chemistry* 7.7 (2023), 457–458. DOI: 10.1038/s41570-023-00502-0.

[276] Adrian Mirza et al. “Are large language models superhuman chemists?” In: (2024). DOI: 10.48550/ARXIV.2404.01475.

[277] Kevin Maik Jablonka et al. “Leveraging large language models for predictive chemistry”. In: *Nature Machine Intelligence* 6.2 (2024), 161–169. DOI: 10.1038/s42256-023-00788-1.

[278] Andres M. Bran et al. “Augmenting large language models with chemistry tools”. In: *Nature Machine Intelligence* 6.5 (2024), 525–535. DOI: 10.1038/s42256-024-00832-8.

[279] Mayk Caldas Ramos et al. “A Review of Large Language Models and Autonomous Agents in Chemistry”. In: (2024). DOI: 10.48550/ARXIV.2407.01603.

[280] Kevin Maik Jablonka et al. “14 examples of how LLMs can transform materials science and chemistry: a reflection on a large language model hackathon”. In: *Digital Discovery* 2.5 (2023), 1233–1250. DOI: 10.1039/d3dd00113j.

[281] Lei Zhang et al. “Fast Exploring Literature by Language Machine Learning for Perovskite Solar Cell Materials Design”. In: *Advanced Intelligent Systems* 6.6 (2024). DOI: 10.1002/aisy.202300678.

[282] T. Jesper Jacobsson et al. “An open-access database and analysis tool for perovskite solar cells based on the FAIR data principles”. In: *Nature Energy* 7.1 (2021), 107–115. DOI: 10.1038/s41560-021-00941-3.

[283] Osbel Almora et al. “Device Performance of Emerging Photovoltaic Materials (Version 4)”. In: *Advanced Energy Materials* 14.4 (2023). DOI: 10.1002/aenm.202303173.

[284] Ekaterina I. Marchenko et al. “Database of Two-Dimensional Hybrid Perovskite Materials: Open-Access Collection of Crystal Structures, Band Gaps, and Atomic Partial Charges Predicted by Machine Learning”. In: *Chemistry of Materials* 32.17 (2020), 7383–7388. DOI: 10.1021/acs.chemmater.0c02290.

[285] Michael Götte et al. *Thin-film solar cell ontology*. matportal.org. 2024. URL: https://matportal.org/ontologies/TFSCO (visited on 01/03/2025).

[286] Anubhav Jain et al. “Commentary: The Materials Project: A materials genome approach to accelerating materials innovation”. In: *APL Materials* 1.1 (2013). DOI: 10.1063/1.4812323.

[287] Markus Scheidgen et al. “NOMAD: A distributed web-based platform for managing materials science research data”. In: *Journal of Open Source Software* 8.90 (2023), p. 5388. DOI: 10.21105/joss.05388.

[288] Michael Götte. *NOMAD base sections for solar cell and electro catalysis research*. Software. 2025. URL: https://github.com/nomad-hzb/nomad-baseclasses (visited on 01/03/2025).

[289] Claudio Zeni et al. “A generative model for inorganic materials design”. In: *Nature* (2025). DOI: 10.1038/s41586-025-08628-5.

[290] Yabo Dan et al. “Generative adversarial networks (GAN) based efficient sampling of chemical composition space for inverse design of inorganic materials”. In: *npj Computational Materials* 6.1 (2020). DOI: 10.1038/s41524-020-00352-0.

[291] Viggo Moro et al. “Multimodal Learning for Materials”. In: (2023). DOI: 10.48550/ARXIV.2312.00111.

[292] Yana Vaynzof. “The Future of Perovskite Photovoltaics—Thermal Evaporation or Solution Processing?” In: *Advanced Energy Materials* 10.48 (2020). DOI: 10.1002/aenm.202003073.

[293] Jorge Ávila et al. “Vapor-Deposited Perovskites: The Route to High-Performance Solar Cell Production?” In: *Joule* 1.3 (2017), 431–442. DOI: 10.1016/j.joule.2017.07.014.

[294] Hang Li et al. “Applications of vacuum vapor deposition for perovskite solar cells: A progress review”. In: *iEnergy* 1.4 (2022), 434–452. DOI: 10.23919/ien.2022.0053.

[295] Joo-Hong Lee et al. “Opportunities and Challenges for Perovskite Solar Cells Based on Vacuum Thermal Evaporation”. In: *Advanced Materials Technologies* 8.20 (2022). DOI: 10.1002/admt.202200928.

[296] Fu Yang et al. “Upscaling Solution-Processed Perovskite Photovoltaics”. In: *Advanced Energy Materials* 11.42 (2021). DOI: 10.1002/aenm.202101973.

[297] Chunjie Huang et al. “Meniscus-modulated blade coating enables high-quality α-phase formamidinium lead triiodide crystals and efficient perovskite minimodules”. In: *Joule* (2024). DOI: 10.1016/j.joule.2024.06.008.

[298] Anand Selvin Subbiah et al. “Efficient blade-coated perovskite/silicon tandems via interface engineering”. In: *Joule* (2024). DOI: 10.1016/j.joule.2024.09.014.

[299] Jinzhao Li et al. “Ink Design Enabling Slot-Die Coated Perovskite Solar Cells with >22% Power Conversion Efficiency, Micro-Modules, and 1 Year of Outdoor Performance Evaluation”. In: *Advanced Energy Materials* 13.33 (2023), p. 2203898. DOI: 10.1002/aenm.202203898.

[300] Jadel Tsiba Matondo et al. “Slot-Die Coating for Scalable Fabrication of Perovskite Solar Cells and Modules”. In: *Advanced Materials Technologies* 9.10 (2024), p. 2302082. DOI: 10.1002/admt.202302082.

[301] Simon Ternes et al. “Modeling and Fundamental Dynamics of Vacuum, Gas, and Antisolvent Quenching for Scalable Perovskite Processes”. In: *Advanced Science* 11.14 (2024), p. 2308901. DOI: 10.1002/advs.202308901.

[302] Florian Mathies et al. “Advances in Inkjet-Printed Metal Halide Perovskite Photovoltaic and Optoelectronic Devices”. In: *Energy Technology* 8.4 (2019). DOI: 10.1002/ente.201900991.

[303] Florian Mathies et al. “Gas flow-assisted vacuum drying: identification of a novel process for attaining high-quality perovskite films”. In: *Materials Advances* 2.16 (2021), 5365–5370. DOI: 10.1039/d1ma00494h.

[304] Fabian Schackmar et al. “In Situ Process Monitoring and Multichannel Imaging for Vacuum-Assisted Growth Control of Inkjet-Printed and Blade-Coated Perovskite Thin-Films”. In: *Advanced Materials Technologies* 8.5 (2023), p. 2201331. DOI: 10.1002/admt.202201331.

[305] Nam Joong Jeon et al. “Solvent engineering for high-performance inorganic–organic hybrid perovskite solar cells”. In: *Nature Materials* 13.9 (2014), 897–903. DOI: 10.1038/nmat4014.

[306] Manda Xiao et al. “A Fast Deposition-Crystallization Procedure for Highly Efficient Lead Iodide Perovskite Thin-Film Solar Cells”. In: *Angewandte Chemie* 126.37 (2014), 10056–10061. DOI: 10.1002/ange.201405334.

[307] Michael Saliba et al. “How to Make over 20% Efficient Perovskite Solar Cells in Regular (n–i–p) and Inverted (p–i–n) Architectures”. In: *Chemistry of Materials* 30.13 (2018), 4193–4201. DOI: 10.1021/acs.chemmater.8b00136.

[308] Anand S. Subbiah et al. “Enhancing the Performance of Blade-Coated Perovskite/Silicon Tandems via Molecular Doping and Interfacial Energy Alignment”. In: *ACS Energy Letters* 9.2 (2024), 727–731. DOI: 10.1021/acsenergylett.4c00070.

[309] Kristina Geistert et al. “Controlling Thin Film Morphology Formation during Gas Quenching of Slot-Die Coated Perovskite Solar Modules”. In: *ACS Applied Materials & Interfaces* (2023). DOI: 10.1021/acsami.3c11923.

[310] Aslihan Babayigit et al. “Gas Quenching for Perovskite Thin Film Deposition”. In: *Joule* 2.7 (2018), 1205–1209. DOI: 10.1016/j.joule.2018.06.009.

[311] Florian Mathies et al. “Multipass inkjet printed planar methylammonium lead iodide perovskite solar cells”. In: *Journal of Materials Chemistry A* 4.48 (2016), 19207–19213. DOI: 10.1039/c6ta07972e.

[312] Bahram Abdollahi Nejand et al. “Vacuum-Assisted Growth of Low-Bandgap Thin Films $FA_{0.8}MA_{0.2}Sn_{0.5}Pb_{0.5}I_3$) for All-Perovskite Tandem Solar Cells”. In: *Advanced Energy Materials* 10.5 (2019). DOI: 10.1002/aenm.201902583.

[313] Fabian Schackmar et al. “Perovskite Solar Cells with All-Inkjet-Printed Absorber and Charge Transport Layers”. In: *Advanced Materials Technologies* 6.2 (2020). DOI: 10.1002/admt.202000271.

[314] Bahram Abdollahi Nejand et al. “Scalable two-terminal all-perovskite tandem solar modules with a 19.1% efficiency”. In: *Nature Energy* 7.7 (2022), 620–630. DOI: 10.1038/s41560-022-01059-w.

[315] Victor K. LaMer et al. “Theory, Production and Mechanism of Formation of Monodispersed Hydrosols”. In: *Journal of the American Chemical Society* 72.11 (1950), 4847–4854. DOI: 10.1021/ja01167a001.

[316] Minsu Jung et al. “Perovskite precursor solution chemistry: from fundamentals to photovoltaic applications”. In: *Chemical Society Reviews* 48.7 (2019), 2011–2038. DOI: 10.1039/c8cs00656c.

[317] Jon Tomas Gudmundsson et al. “Foundations of physical vapor deposition with plasma assistance”. In: *Plasma Sources Science and Technology* 31.8 (2022). DOI: 10.1088/1361-6595/ac7f53.

[318] Minjun Feng et al. “The Photophysics of Perovskite Emitters: from Ensemble to Single Particle”. In: *Advanced Materials* (2024). DOI: 10.1002/adma.202413836.

[319] Thomas Kirchartz et al. “Photoluminescence-Based Characterization of Halide Perovskites for Photovoltaics”. In: *Advanced Energy Materials* 10.26 (2020). DOI: 10.1002/aenm.201904134.

[320] Arman Mahboubi Soufiani et al. “Electro- and photoluminescence imaging as fast screening technique of the layer uniformity and device degradation in planar perovskite solar cells”. In: *Journal of Applied Physics* 120.3 (2016). DOI: 10.1063/1.4956436.

[321] Susanne Siebentritt et al. “Photoluminescence assessment of materials for solar cell absorbers”. In: *Faraday Discussions* 239 (2022), 112–129. DOI: 10.1039/d2fd00057a.

[322] Christian M. Wolff et al. “Nonradiative Recombination in Perovskite Solar Cells: The Role of Interfaces”. In: *Advanced Materials* 31.52 (2019). DOI: 10.1002/adma.201902762.

[323] Deying Luo et al. “Minimizing non-radiative recombination losses in perovskite solar cells”. In: *Nature Reviews Materials* 5.1 (2019), 44–60. DOI: 10.1038/s41578-019-0151-y.

[324] Valerio Campanari et al. “Reevaluation of Photoluminescence Intensity as an Indicator of Efficiency in Perovskite Solar Cells”. In: *Solar RRL* 6.8 (2022). DOI: 10.1002/solr.202200049.

[325] Martin Stolterfoht et al. “Voltage-Dependent Photoluminescence and How It Correlates with the Fill Factor and Open-Circuit Voltage in Perovskite Solar Cells”. In: *ACS Energy Letters* 4.12 (2019), 2887–2892. DOI: 10.1021/acsenergylett.9b02262.

[326] Benjamin Hacene et al. “Intensity Dependent Photoluminescence Imaging for In-Line Quality Control of Perovskite Thin Film Processing”. In: *Advanced Materials Technologies* 9.11 (2023), p. 2301279. DOI: 10.1002/admt.202301279.

[327] Paul Fassl et al. “Revealing the internal luminescence quantum efficiency of perovskite films via accurate quantification of photon recycling”. In: *Matter* 4.4 (2021), 1391–1412. DOI: 10.1016/j.matt.2021.01.019.

[328] Jiaming Li et al. “Temperature-dependent photoluminescence of inorganic perovskite nanocrystal films”. In: *RSC Advances* 6.82 (2016), 78311–78316. DOI: 10.1039/c6ra17008k.

[329] Sarah Wieghold et al. “Understanding the effect of light and temperature on the optical properties and stability of mixed-ion halide perovskites”. In: *Journal of Materials Chemistry C* 8.28 (2020), 9714–9723. DOI: 10.1039/d0tc02103b.

[330] Martin C. Schubert et al. “Spatially Resolved Performance Analysis for Perovskite Solar Cells”. In: *Advanced Energy Materials* 10.26 (2020). DOI: 10.1002/aenm.201904001.

[331] Elizabeth M. Tennyson et al. “Heterogeneity at multiple length scales in halide perovskite semiconductors”. In: *Nature Reviews Materials* 4.9 (2019), 573–587. DOI: 10.1038/s41578-019-0125-0.

[332] Liangliang Min et al. “Carrier dynamic identification enables wavelength and intensity sensitivity in perovskite photodetectors”. In: *Light: Science & Applications* 13.1 (2024). DOI: 10.1038/s41377-024-01636-6.

[333] Arman Mahboubi Soufiani et al. “Luminescence Imaging Characterization of Perovskite Solar Cells: A Note on the Analysis and Reporting the Results”. In: *Advanced Energy Materials* 8.12 (2018). DOI: 10.1002/aenm.201702256.

[334] Ziv Hameiri et al. “Photoluminescence and electroluminescence imaging of perovskite solar cells”. In: *Progress in Photovoltaics: Research and Applications* 23.12 (2015), 1697–1705. DOI: 10.1002/pip.2716.

[335] Arman Mahboubi Soufiani et al. “Lessons Learnt from Spatially Resolved Electro- and Photoluminescence Imaging: Interfacial Delamination in $CH_3NH_3PbI_3$ Planar Perovskite Solar Cells upon Illumination”. In: *Advanced Energy Materials* 7.9 (2016). DOI: 10.1002/aenm.201602111.

[336] Thorsten Trupke et al. “Photoluminescence Imaging for Photovoltaic Applications”. In: *Energy Procedia* 15 (2012), 135–146. DOI: 10.1016/j.egypro.2012.02.016.

[337] Martin Stolterfoht et al. “Visualization and suppression of interfacial recombination for high-efficiency large-area pin perovskite solar cells”. In: *Nature Energy* 3.10 (2018), 847–854. DOI: 10.1038/s41560-018-0219-8.

[338] S. Mastroianni et al. “Analysing the effect of crystal size and structure in highly efficient $CH_3NH_3PbI_3$ perovskite solar cells by spatially resolved photo- and electroluminescence imaging”. In: *Nanoscale* 7.46 (2015), 19653–19662. DOI: 10.1039/c5nr05308k.

[339] Daniel Walter et al. “On the Use of Luminescence Intensity Images for Quantified Characterization of Perovskite Solar Cells: Spatial Distribution of Series Resistance”. In: *Advanced Energy Materials* 8.2 (2017). DOI: 10.1002/aenm.201701522.

[340] Boyi Chen et al. “Imaging Spatial Variations of Optical Bandgaps in Perovskite Solar Cells”. In: *Advanced Energy Materials* 9.7 (2018). DOI: 10.1002/aenm.201802790.

[341] Simon Ternes et al. “Correlative In Situ Multichannel Imaging for Large-Area Monitoring of Morphology Formation in Solution-Processed Perovskite Layers”. In: *Solar RRL* 6.3 (2021). DOI: 10.1002/solr.202100353.

[342] Felix Laufer. *Large-area luminescence imaging of perovskite photovoltaics for in situ characterization*. Master’s Thesis. Karlsruhe Institute of Technology. 2019.

[343] David B. Ritzer et al. “Upscaling of perovskite solar modules: The synergy of fully evaporated layer fabrication and all-laser-scribed interconnections”. In: *Progress in Photovoltaics: Research and Applications* 30.4 (2022), pp. 360–373. DOI: 10.1002/pip.3489.

[344] Marco A. Ruiz-Preciado et al. “Monolithic Two-Terminal Perovskite/CIS Tandem Solar Cells with Efficiency Approaching 25%”. In: *ACS Energy Letters* 7.7 (2022), pp. 2273–2281. DOI: 10.1021/acsenergylett.2c00707.

[345] Julie Roger et al. “Laminated Monolithic Perovskite/Silicon Tandem Photovoltaics”. In: *Advanced Energy Materials* 12.27 (2022), p. 2200961. DOI: 10.1002/aenm.202200961.

[346] Felix Laufer et al. “Process Insights into Perovskite Thin-Film Photovoltaics from Machine Learning with In-Situ Luminescence Data”. In: *Solar RRL* 7.7 (2023), p. 2201114. DOI: 10.1002/solr.202201114.

[347] Lukas Klein et al. “Discovering Process Dynamics for Scalable Perovskite Solar Cell Manufacturing with Explainable AI”. In: *Advanced Materials* 36.7 (2023), p. 2307160. DOI: 10.1002/adma.202307160.

[348] Hang Hu et al. “Triple-junction perovskite–perovskite–silicon solar cells with power conversion efficiency of 24.4%”. In: *Energy & Environmental Science* 17.8 (2024), pp. 2800–2814. DOI: 10.1039/D3EE03687A.

[349] Raphael Pesch et al. “Hybrid Two-Step Inkjet-Printed Perovskite Solar Cells”. In: *Solar RRL* 8.13 (2024), p. 2400165. DOI: 10.1002/solr.202400165.

[350] Roja Singh et al. “Danger in the Dark: Stability of Perovskite Solar Cells with Varied Stoichiometries and Morphologies Stressed at Various Conditions”. In: *ACS Applied Materials & Interfaces* 16.21 (2024), pp. 27450–27462. DOI: 10.1021/acsami.4c04350.

[351] Daniel O. Baumann et al. “Repeatable Perovskite Solar Cells through Fully Automated Spin-Coating and Quenching”. In: *ACS Applied Materials & Interfaces* 16.40 (2024), 54007–54016. DOI: 10.1021/acsami.4c13024.

[352] Felix Laufer et al. “Deep learning for augmented process monitoring of scalable perovskite thin-film fabrication”. In: *Energy & Environmental Science* 18.4 (2025). DOI: 10.1039/d4ee03445g.

[353] Vincent Shaw. *Longi claims 34.6% efficiency for perovskite-silicon tandem solar cell*. pv-magazine.com. 2024. URL: https://www.pv-magazine.com/2024/06/14/longi-claims-34-6-efficiency-for-perovskite-silicon-tandem-solar-cell/ (visited on 12/12/2024).

[354] R. Ebner et al. “Optical Characterization of Different Thin Film Module Technologies”. In: *International Journal of Photoenergy* 2015.1 (2015), p. 159458. DOI: 10.1155/2015/159458.

[355] Lucija Rakocevic et al. “Loss Analysis in Perovskite Photovoltaic Modules”. In: *Solar RRL* 3.12 (2019), p. 1900338. DOI: 10.1002/solr.201900338.

[356] Shudi Qiu et al. “In Situ Probing the Crystallization Kinetics in Gas-Quenching-Assisted Coating of Perovskite Films”. In: *Advanced Energy Materials* 14.10 (2024), p. 2303210. DOI: 10.1002/aenm.202303210.

[357] Nada Mrkyvkova et al. “Combined in Situ Photoluminescence and X-ray Scattering Reveals Defect Formation in Lead-Halide Perovskite Films”. In: *The Journal of Physical Chemistry Letters* 12.41 (2021), 10156–10162. DOI: 10.1021/acs.jpclett.1c02869.

[358] Justin M. Hoffman et al. “In Situ Grazing-Incidence Wide-Angle Scattering Reveals Mechanisms for Phase Distribution and Disorientation in 2D Halide Perovskite Films”. In: *Advanced Materials* 32.33 (2020). DOI: 10.1002/adma.202002812.

[359] Minchao Qin et al. “A Systematic Review of Metal Halide Perovskite Crystallization and Film Formation Mechanism Unveiled by In Situ GIWAXS”. In: *Advanced Materials* 33.51 (2021). DOI: 10.1002/adma.202105290.

[360] Minchao Qin et al. “Manipulating the Mixed-Perovskite Crystallization Pathway Unveiled by In Situ GIWAXS”. In: *Advanced Materials* 31.25 (2019). DOI: 10.1002/adma.201901284.

[361] Sehyun Lee et al. “In situ study of the film formation mechanism of organic–inorganic hybrid perovskite solar cells: controlling the solvate phase using an additive system”. In: *Journal of Materials Chemistry A* 8.16 (2020), 7695–7703. DOI: 10.1039/d0ta00048e.

[362] Ming-Chun Tang et al. “Efficient Hybrid Mixed-Ion Perovskite Photovoltaics: In Situ Diagnostics of the Roles of Cesium and Potassium Alkali Cation Addition”. In: *Solar RRL* 4.9 (2020). DOI: 10.1002/solr.202000272.

[363] Maged Abdelsamie et al. “Impact of Processing on Structural and Compositional Evolution in Mixed Metal Halide Perovskites during Film Formation”. In: *Advanced Functional Materials* 30.38 (2020). DOI: 10.1002/adfm.202001752.

[364] Klara Suchan et al. “Multi-Stage Phase-Segregation of Mixed Halide Perovskites under Illumination: A Quantitative Comparison of Experimental Observations and Thermodynamic Models”. In: *Advanced Functional Materials* 33.3 (2022). DOI: 10.1002/adfm.202206047.

[365] Vivek Thampy et al. “Solution-Phase Halide Exchange and Targeted Annealing Kinetics in Lead Chloride Derived Hybrid Perovskites”. In: *Inorganic Chemistry* 59.18 (2020), 13364–13370. DOI: 10.1021/acs.inorgchem.0c01732.

[366] Chao Zhang et al. “Crystallography-derived optoelectronic and photovoltaic properties of $CsPbBr_3$ perovskite single crystals as revealed by in situ transmission electron microscopy”. In: *Applied Materials Today* 20 (2020), p. 100788. DOI: 10.1016/j.apmt.2020.100788.

[367] You-Hyun Seo et al. “In situ TEM observation of the heat–induced degradation of single– and triple–cation planar perovskite solar cells”. In: *Nano Energy* 77 (2020), p. 105164. DOI: 10.1016/j.nanoen.2020.105164.

[368] Johanna Zikulnig et al. “Photoluminescence Imaging for the In-Line Quality Control of Thin-Film Solar Cells”. In: *Solar* 2.1 (2022), 1–11. DOI: 10.3390/solar2010001.

[369] Mohammad-Reza Ahmadian-Yazdi et al. “Effect of Marangoni Convection on the Perovskite Thin Liquid Film Deposition”. In: *Langmuir* 37.8 (2021), 2596–2606. DOI: 10.1021/acs.langmuir.0c03120.

[370] Laura E. Mundt et al. “Quantitative Local Loss Analysis of Blade-Coated Perovskite Solar Cells”. In: *IEEE Journal of Photovoltaics* 9.2 (2019), 452–459. DOI: 10.1109/jphotov.2018.2888835.

[371] Mengling Liao et al. “In Situ Raman Spectroscopic Studies of Thermal Stability of All-Inorganic Cesium Lead Halide ($CsPbX_3$, X = Cl, Br, I) Perovskite Nanocrystals”. In: *The Journal of Physical Chemistry Letters* 10.6 (2019), 1217–1225. DOI: 10.1021/acs.jpclett.9b00344.

[372] Shogo Toda et al. “Mapping of Grain Orientation In Situ of 2D Perovskite Thin Films with Low-Frequency Polarized Raman Microspectroscopy”. In: *The Journal of Physical Chemistry C* 125.51 (2021), 27996–28003. DOI: 10.1021/acs.jpcc.1c08533.

[373] Simon Ternes et al. “Drying Dynamics of Solution-Processed Perovskite Thin-Film Photovoltaics: In Situ Characterization, Modeling, and Process Control”. In: *Advanced Energy Materials* 9.39 (2019), p. 1901581. DOI: 10.1002/aenm.201901581.

[374] Jacobus J. van Franeker et al. “Monitoring Thermal Annealing of Perovskite Solar Cells with In Situ Photoluminescence”. In: *Advanced Energy Materials* 7.7 (2016). DOI: 10.1002/aenm.201601822.

[375] Carolin Rehermann et al. “Origin of Ionic Inhomogeneity in $MAPb(I_xBr_{1-x})_3$ Perovskite Thin Films Revealed by In-Situ Spectroscopy during Spin Coating and Annealing”. In: *ACS Applied Materials & Interfaces* 12.27 (2020), 30343–30352. DOI: 10.1021/acsami.0c05894.

[376] Konstantin Schötz et al. “Double peak emission in lead halide perovskites by self-absorption”. In: *Journal of Materials Chemistry C* 8.7 (2020), 2289–2300. DOI: 10.1039/c9tc06251c.

[377] Konstantin Schötz et al. “Using In Situ Optical Spectroscopy to Elucidate Film Formation of Metal Halide Perovskites”. In: *The Journal of Physical Chemistry A* 125.11 (2021), 2209–2225. DOI: 10.1021/acs.jpca.0c10765.

[378] Finn Babbe et al. “Optical Absorption-Based In Situ Characterization of Halide Perovskites”. In: *Advanced Energy Materials* 10.26 (2020). DOI: 10.1002/aenm.201903587.

[379] Yang Sun et al. “Lewis Base-Mediated Perovskite Crystallization as Revealed by In Situ, Real-Time Optical Absorption Spectroscopy”. In: *The Journal of Physical Chemistry Letters* 12.22 (2021), 5357–5362. DOI: 10.1021/acs.jpclett.1c01246.

[380] Patrick Wai-Keung Fong et al. “Printing High-Efficiency Perovskite Solar Cells in High-Humidity Ambient Environment—An In Situ Guided Investigation”. In: *Advanced Science* 8.6 (2021). DOI: 10.1002/advs.202003359.

[381] Aboma Merdasa et al. “Eye in the process: Formation of “triple cation” perovskite thin films rationalized by in-situ optical monitoring”. In: *PREPRINT available at Research Square* (2020). DOI: 10.21203/rs.3.rs-102041/v1.

[382] Klara Suchan et al. “Optical in situ monitoring during the synthesis of halide perovskite solar cells reveals formation kinetics and evolution of optoelectronic properties”. In: *Journal of Materials Chemistry A* 8.20 (2020), 10439–10449. DOI: 10.1039/d0ta01237h.

[383] Mihirsinh Chauhan et al. “Investigating two-step $MAPbI_3$ thin film formation during spin coating by simultaneous in situ absorption and photoluminescence spectroscopy”. In: *Journal of Materials Chemistry A* 8.10 (2020), 5086–5094. DOI: 10.1039/c9ta12409h.

[384] Mai Do et al. “Low-dimensional perovskite nanoplatelet synthesis using in situ photophysical monitoring to establish controlled growth”. In: *Nanoscale* 11.37 (2019), 17262–17269. DOI: 10.1039/c9nr04010b.

[385] Jun Li et al. “Luminescent Intermediates and Humidity-Dependent Room-Temperature Conversion of the $MAPbI_3$ Perovskite Precursor”. In: *ACS Omega* 3.10 (2018), 14494–14502. DOI: 10.1021/acsomega.8b01799.

[386] Klara Suchan et al. “Complex evolution of photoluminescence during phase segregation of $MAPb(I_{1-x}Br_x)_3$ mixed halide perovskite”. In: *Journal of Luminescence* 221 (2020), p. 117073. DOI: 10.1016/j.jlumin.2020.117073.

[387] Michael Buchhorn et al. “Setup to Study the in Situ Evolution of Both Photoluminescence and Absorption during the Processing of Organic or Hybrid Semiconductors”. In: *The Journal of Physical Chemistry A* 122.46 (2018), 9115–9122. DOI: 10.1021/acs.jpca.8b07495.

[388] Jianbo Li et al. “Phase Transition Control for High-Performance Blade-Coated Perovskite Solar Cells”. In: *Joule* 2.7 (2018), 1313–1330. DOI: 10.1016/j.joule.2018.04.011.

[389] Hanlin Hu et al. “Room-Temperature Meniscus Coating of >20Solar Cells: A Film Formation Mechanism Investigation”. In: *Advanced Functional Materials* 29.25 (2019). DOI: 10.1002/adfm.201900092.

[390] P Edelman et al. “Photoluminescence and minority carrier diffusion length imaging in silicon and GaAs”. In: *Semiconductor Science and Technology* 7.1A (1992), A22–A26. DOI: 10.1088/0268-1242/7/1a/004.

[391] Steve Johnston et al. “Imaging, microscopic analysis, and modeling of a CdTe module degraded by heat and light”. In: *Solar Energy Materials and Solar Cells* 178 (2018), 46–51. DOI: 10.1016/j.solmat.2017.12.021.

[392] A. Gerber et al. “Advanced large area characterization of thin-film solar modules by electroluminescence and thermography imaging techniques”. In: *Solar Energy Materials and Solar Cells* 135 (2015), 35–42. DOI: 10.1016/j.solmat.2014.09.020.

[393] Ryan J. Stoddard et al. “Correlation between Photoluminescence and Carrier Transport and a Simple In Situ Passivation Method for High-Bandgap Hybrid Perovskites”. In: *The Journal of Physical Chemistry Letters* 8.14 (2017), 3289–3298. DOI: 10.1021/acs.jpclett.7b01185.

[394] Laura E. Mundt et al. “Nondestructive Probing of Perovskite Silicon Tandem Solar Cells Using Multi-wavelength Photoluminescence Mapping”. In: *IEEE Journal of Photovoltaics* 7.4 (2017), 1081–1086. DOI: 10.1109/jphotov.2017.2688022.

[395] Rodrigo Szostak et al. “In Situ and Operando Characterizations of Metal Halide Perovskite and Solar Cells: Insights from Lab-Sized Devices to Upscaling Processes”. In: *Chemical Reviews* 123.6 (2023), 3160–3236. DOI: 10.1021/acs.chemrev.2c00382.

[396] Yicheng Zhao et al. “Perovskite seeding growth of formamidinium-lead-iodide-based perovskites for efficient and stable solar cells”. In: *Nature Communications* 9.1 (2018). DOI: 10.1038/s41467-018-04029-7.

[397] Dane W. deQuilettes et al. “Photo-induced halide redistribution in organic–inorganic perovskite films”. In: *Nature Communications* 7.1 (2016). DOI: 10.1038/ncomms11683.

[398] Sheng Chen et al. “Spatial Distribution of Lead Iodide and Local Passivation on Organo-Lead Halide Perovskite”. In: *ACS Applied Materials & Interfaces* 9.7 (2017), 6072–6078. DOI: 10.1021/acsami.6b15504.

[399] Xiaofan Deng et al. “Dynamic study of the light soaking effect on perovskite solar cells by in-situ photoluminescence microscopy”. In: *Nano Energy* 46 (2018), 356–364. DOI: 10.1016/j.nanoen.2018.02.024.

[400] Cheng Li et al. “Real-Time Observation of Iodide Ion Migration in Methylammonium Lead Halide Perovskites”. In: *Small* 13.42 (2017). DOI: 10.1002/smll.201701711.

[401] Yanjun Fang et al. “Quantification of re-absorption and re-emission processes to determine photon recycling efficiency in perovskite single crystals”. In: *Nature Communications* 8.1 (2017). DOI: 10.1038/ncomms14417.

[402] Adrien Bercegol et al. “Quantitative optical assessment of photonic and electronic properties in halide perovskite”. In: *Nature Communications* 10.1 (2019). DOI: 10.1038/s41467-019-09527-w.

[403] Jay B. Patel et al. “Light Absorption and Recycling in Hybrid Metal Halide Perovskite Photovoltaic Devices”. In: *Advanced Energy Materials* 10.10 (2020). DOI: 10.1002/aenm.201903653.

[404] Konstantin Schötz et al. “Double peak emission in lead halide perovskites by self-absorption”. In: *Journal of Materials Chemistry C* 8.7 (2020), 2289–2300. DOI: 10.1039/c9tc06251c.

[405] Loreta A. Muscarella et al. “Crystal Orientation and Grain Size: Do They Determine Optoelectronic Properties of MAPbI3 Perovskite?” In: *The Journal of Physical Chemistry Letters* 10.20 (2019), 6010–6018. DOI: 10.1021/acs.jpclett.9b02757.

[406] Gilbert El-Hajje et al. “Quantification of spatial inhomogeneity in perovskite solar cells by hyperspectral luminescence imaging”. In: *Energy & Environmental Science* 9.7 (2016), 2286–2294. DOI: 10.1039/c6ee00462h.

[407] Hang Hu et al. “Void-free buried interface for scalable processing of p-i-n-based $FAPbI_3$ perovskite solar modules”. In: *Joule* 7.7 (2023), 1574–1592. DOI: 10.1016/j.joule.2023.05.017.

[408] Simon Ternes. *In Situ Characterization and Modelling of Drying Dynamics for Scalable Printing of Hybrid Perovskite Photovoltaics*. PhD Thesis. Karlsruhe Institute of Technology. 2023. DOI: 10.5445/KSP/1000152603.

[409] Anke Helbig et al. “Quantitative electroluminescence analysis of resistive losses in Cu(In, Ga)Se2 thin-film modules”. In: *Solar Energy Materials and Solar Cells* 94.6 (2010), 979–984. DOI: 10.1016/j.solmat.2010.01.028.

[410] Jackson W. Schall et al. “Accelerated Stress Testing of Perovskite Photovoltaic Modules: Differentiating Degradation Modes with Electroluminescence Imaging”. In: *Solar RRL* 7.14 (2023). DOI: 10.1002/solr.202300229.

[411] Jincheol Kim et al. “Overcoming the Challenges of Large-Area High-Efficiency Perovskite Solar Cells”. In: *ACS Energy Letters* 2.9 (2017), 1978–1984. DOI: 10.1021/acsenergylett.7b00573.

[412] Gyumin Jang et al. “Cold Antisolvent Bathing Derived Highly Efficient Large-Area Perovskite Solar Cells”. In: *Advanced Energy Materials* 9.36 (2019). DOI: 10.1002/aenm.201901719.

[413] Helge Eggers et al. “Inkjet-Printed Micrometer-Thick Perovskite Solar Cells with Large Columnar Grains”. In: *Advanced Energy Materials* 10.6 (2019). DOI: 10.1002/aenm.201903184.

[414] B. Schmidt-Hansberg et al. “In situ monitoring the drying kinetics of knife coated polymer-fullerene films for organic solar cells”. In: *Journal of Applied Physics* 106.12 (2009). DOI: 10.1063/1.3270402.

[415] Lukas Wagner et al. “Distinguishing crystallization stages and their influence on quantum efficiency during perovskite solar cell formation in real-time”. In: *Scientific Reports* 7.1 (2017). DOI: 10.1038/s41598-017-13855-6.

[416] Wanyi Nie et al. “High-efficiency solution-processed perovskite solar cells with millimeter-scale grains”. In: *Science* 347.6221 (2015), 522–525. DOI: 10.1126/science.aaa0472.

[417] Valerio D’Innocenzo et al. “Tuning the Light Emission Properties by Band Gap Engineering in Hybrid Lead Halide Perovskite”. In: *Journal of the American Chemical Society* 136.51 (2014), 17730–17733. DOI: 10.1021/ja511198f.

[418] Simon Ternes et al. “In situ reflectance- photoluminescence imaging on solution-processed perovskite thin-films”. In: *2021 IEEE 48th Photovoltaic Specialists Conference (PVSC)*. 2021. DOI: 10.1109/PVSC43889.2021.9518569.

[419] Tze-Bin Song et al. “Dynamics of Antisolvent Processed Hybrid Metal Halide Perovskites Studied by In Situ Photoluminescence and Its Influence on Optoelectronic Properties”. In: *ACS Applied Energy Materials* 3.3 (2020), 2386–2393. DOI: 10.1021/acsaem.9b02052.

[420] Vladimir Held et al. “Evolution of Structure and Optoelectronic Properties During Halide Perovskite Vapor Deposition”. In: *The Journal of Physical Chemistry Letters* 13.51 (2022), 11905–11912. DOI: 10.1021/acs.jpclett.2c03422.

[421] Vladimir Held et al. “Evolution of Defects, Morphology, and Strain during $FAMAPbI_3$ Perovskite Vacuum Deposition: Insights from In Situ Photoluminescence and X-ray Scattering”. In: *ACS Applied Materials & Interfaces* 16.27 (2024), 35723–35731. DOI: 10.1021/acsami.4c04095.

[422] Felix Laufer et al. *In Situ Photoluminescence Imaging Dataset of Blade-Coated Perovskite Photovoltaics*. Dataset. Version v1.0. 2023. DOI: 10.5281/zenodo.7503391.

[423] Felix Laufer et al. *Machine Learning for In Situ Photoluminescence Data of Perovskite Photovoltaics*. Software. 2023. URL: https://github.com/AI-InSu-Pero/ML-PerovskitePV-InSituLuminescene (visited on 01/03/2025).

[424] Martin A. Green et al. “Solar cell efficiency tables (Version 64)”. In: *Progress in Photovoltaics: Research and Applications* 32.7 (2024), pp. 425–441. DOI: 10.1002/pip.3831.

[425] Lukas Bommes et al. “Anomaly detection in IR images of PV modules using supervised contrastive learning”. In: *Progress in Photovoltaics: Research and Applications* 30.6 (2022), 597–614. DOI: 10.1002/pip.3518.

[426] Keisuke Takahashi et al. “Searching for Hidden Perovskite Materials for Photovoltaic Systems by Combining Data Science and First Principle Calculations”. In: *ACS Photonics* 5.3 (2018), 771–775. DOI: 10.1021/acsphotonics.7b01479.

[427] Sheryl L. Sanchez et al. “Physics-driven discovery and bandgap engineering of hybrid perovskites”. In: *Digital Discovery* 3.8 (2024), 1577–1590. DOI: 10.1039/d4dd00080c.

[428] Felix Laufer et al. *In Situ Photoluminescence Dataset for Exploring Material and Processing Variabilities in Blade-Coated Perovskite Photovoltaics*. Dataset. Version v1.0. 2025. DOI: 10.5281/zenodo.14609789.

[429] Felix Laufer et al. *Deep learning for augmented process monitoring of scalable perovskite thin-film fabrication*. Software. 2025. URL: https://github.com/PerovskitePV/DL-Fabrication-Monitoring (visited on 01/03/2025).

[430] Leilei Gu et al. “Vacuum Quenching for Large-Area Perovskite Film Deposition”. In: *ACS Applied Materials & Interfaces* 14.2 (2022), 2949–2957. DOI: 10.1021/acsami.1c22128.

[431] Linxiang Zeng et al. “Controlling the crystallization dynamics of photovoltaic perovskite layers on larger-area coatings”. In: *Energy & Environmental Science* 13.12 (2020), 4666–4690. DOI: 10.1039/d0ee02575e.

[432] Xiong Li et al. “A vacuum flash–assisted solution process for high-efficiency large-area perovskite solar cells”. In: *Science* 353.6294 (2016), 58–62. DOI: 10.1126/science.aaf8060.

[433] Byung-wook Park et al. “Understanding how excess lead iodide precursor improves halide perovskite solar cell performance”. In: *Nature Communications* 9.1 (2018). DOI: 10.1038/s41467-018-05583-w.

[434] Bart Roose et al. “Critical Assessment of the Use of Excess Lead Iodide in Lead Halide Perovskite Solar Cells”. In: *The Journal of Physical Chemistry Letters* 11.16 (2020), 6505–6512. DOI: 10.1021/acs.jpclett.0c01820.

[435] T. Jesper Jacobsson et al. “Unreacted PbI_2 as a Double-Edged Sword for Enhancing the Performance of Perovskite Solar Cells”. In: *Journal of the American Chemical Society* 138.32 (2016), 10331–10343. DOI: 10.1021/jacs.6b06320.

[436] Fangzhou Liu et al. “Is Excess PbI_2 Beneficial for Perovskite Solar Cell Performance?” In: *Advanced Energy Materials* 6.7 (2016). DOI: 10.1002/aenm.201502206.

[437] Dongqin Bi et al. “Efficient luminescent solar cells based on tailored mixed-cation perovskites”. In: *Science Advances* 2.1 (2016). DOI: 10.1126/sciadv.1501170.

[438] Wenya Song et al. “Critical Role of Perovskite Film Stoichiometry in Determining Solar Cell Operational Stability: a Study on the Effects of Volatile A-Cation Additives”. In: *ACS Applied Materials & Interfaces* 14.24 (2022), 27922–27931. DOI: 10.1021/acsami.2c05241.

[439] Ganbaatar Tumen-Ulzii et al. “Detrimental Effect of Unreacted PbI_2 on the Long-Term Stability of Perovskite Solar Cells”. In: *Advanced Materials* 32.16 (2020). DOI: 10.1002/adma.201905035.

[440] Fabian Schackmar. *Tintenstrahldruck für die Metall-Halogenid-Perowskit-Photovoltaik*. PhD Thesis. Karlsruhe Institute of Technology. 2023. DOI: 10.5445/IR/1000159198.

[441] Mengjin Yang et al. “Perovskite ink with wide processing window for scalable high-efficiency solar cells”. In: *Nature Energy* 2.5 (2017). DOI: 10.1038/nenergy.2017.38.

[442] Dong-Nyuk Jeong et al. “Perovskite Cluster-Containing Solution for Scalable D-Bar Coating toward High-Throughput Perovskite Solar Cells”. In: *ACS Energy Letters* 4.5 (2019), 1189–1195. DOI: 10.1021/acsenergylett.9b00042.

[443] Paul Fassl et al. “Fractional deviations in precursor stoichiometry dictate the properties, performance and stability of perovskite photovoltaic devices”. In: *Energy & Environmental Science* 11.12 (2018), 3380–3391. DOI: 10.1039/c8ee01136b.

[444] Jared Kaplan et al. “Scaling Laws for Neural Language Models”. In: (2020). DOI: 10.48550/ARXIV.2001.08361.

[445] Yasaman Bahri et al. “Explaining Neural Scaling Laws”. In: (2021). DOI: 10.48550/ARXIV.2102.06701.

[446] Joel Hestness et al. “Deep Learning Scaling is Predictable, Empirically”. In: (2017). DOI: 10.48550/ARXIV.1712.00409.

[447] Xia Cai et al. “Data-driven design of high-performance $MASn_xPb_{1-x}I_3$ perovskite materials by machine learning and experimental realization”. In: *Light: Science & Applications* 11.1 (2022). DOI: 10.1038/s41377-022-00924-3.

[448] Jin-Feng Wang et al. “Surface engineering of perovskite films for efficient solar cells”. In: *Scientific Reports* 7.1 (2017). DOI: 10.1038/s41598-017-14920-w.

[449] Lukas Klein et al. “Understanding Scalable Perovskite Solar Cell Manufacturing with Explainable AI”. In: *NeurIPS Workshop XAI in Action: Past, Present, and Future Applications*. 2023. URL: https://openreview.net/forum?id=xrEpp63kz7 (visited on 12/12/2024).

[450] Sebastian Ziegler. *Model weights for the publication "Discovering Process Dynamics for Scalable Perovskite Solar Cell Manufacturing with Explainable AI"*. Model Weights. Version v1.0. 2023. DOI: 10.5281/zenodo.10058818.

[451] Marco Tulio Ribeiro et al. “"Why Should I Trust You?": Explaining the Predictions of Any Classifier”. In: (2016). DOI: 10.48550/ARXIV.1602.04938.

[452] Christian Meske et al. “Explainable Artificial Intelligence: Objectives, Stakeholders, and Future Research Opportunities”. In: *Information Systems Management* 39.1 (2020), 53–63. DOI: 10.1080/10580530.2020.1849465.

[453] Juliana Jansen Ferreira et al. “The human-AI relationship in decision-making: AI explanation to support people on justifying their decisions”. In: (2021). DOI: 10.48550/ARXIV.2102.05460.

[454] Ribana Roscher et al. “Explainable Machine Learning for Scientific Insights and Discoveries”. In: *IEEE Access* 8 (2020), 42200–42216. DOI: 10.1109/access.2020.2976199.

[455] Chao Yang et al. “Accelerating the Discovery of Hybrid Perovskites with Targeted Band Gaps via Interpretable Machine Learning”. In: *ACS Applied Materials & Interfaces* 15.34 (2023), 40419–40427. DOI: 10.1021/acsami.3c06392.

[456] Christoph Feichtenhofer et al. “SlowFast Networks for Video Recognition”. In: (2018). DOI: 10.48550/ARXIV.1812.03982.

[457] Or Sharir et al. “The Cost of Training NLP Models: A Concise Overview”. In: (2020). DOI: 10.48550/ARXIV.2004.08900.

[458] Roy Schwartz et al. “Green AI”. In: (2019). DOI: 10.48550/ARXIV.1907.10597.

[459] Payal Dhar. “The carbon impact of artificial intelligence”. In: *Nature Machine Intelligence* 2.8 (2020), 423–425. DOI: 10.1038/s42256-020-0219-9.

[460] Kate Crawford. “Generative AI’s environmental costs are soaring - and mostly secret”. In: *Nature* 626.8000 (2024), 693–693. DOI: 10.1038/d41586-024-00478-x.

[461] David Patterson et al. “Carbon Emissions and Large Neural Network Training”. In: (2021). DOI: 10.48550/ARXIV.2104.10350.

[462] Dan Milmo. *Google’s emissions climb nearly 50% in five years due to AI energy demand*. The Guardian. 2024. URL: https://www.theguardian.com/technology/article/2024/jul/02/google-ai-emissions (visited on 10/30/2024).

[463] Karen Hao. *AI Is Taking Water From the Desert*. The Atlantic. 2024. URL: https://www.theatlantic.com/technology/archive/2024/03/ai-water-climate-microsoft/677602/ (visited on 10/30/2024).

[464] Matt O’Brian et al. *A.I. tools fueled a 34% spike in Microsoft’s water consumption, and one city with its data centers is concerned about the effect on residential supply*. Fortune. 2024. URL: https://fortune.com/2023/09/09/ai-chatgpt-usage-fuels-spike-in-microsoft-water-consumption/ (visited on 10/30/2024).

[465] Cindy Gordon. *AI Is Accelerating the Loss of Our Scarcest Natural Resource: Water*. Forbes. 2024. URL: https://www.forbes.com/sites/cindygordon/2024/02/25/ai-is-accelerating-the-loss-of-our-scarcest-natural-resource-water/ (visited on 10/30/2024).

[466] Charlotte Debus et al. “Reporting electricity consumption is essential for sustainable AI”. In: *Nature Machine Intelligence* 5.11 (2023), 1176–1178. DOI: 10.1038/s42256-023-00750-1.

[467] Ryan Browne. *Why Big Tech is turning to nuclear to power its energy-intensive AI ambitions*. CNBC. 2024. URL: https://www.cnbc.com/2024/10/15/big-tech-turns-to-nuclear-energy-to-fuel-power-intensive-ai-ambitions.html (visited on 10/30/2024).

[468] Maximilian Schleich et al. “GeCo: Quality Counterfactual Explanations in Real Time”. In: (2021). DOI: 10.48550/ARXIV.2101.01292.

[469] Amy Brand et al. “Beyond authorship: attribution, contribution, collaboration, and credit”. In: *Learned Publishing* 28.2 (2015), pp. 151–155. DOI: 10.1087/20150211.

List of Publications, Conference Contributions, Awards, and Published Datasets

Journal Articles

Peer-Reviewed Publications (First Author)

- Simon Ternes*, **Felix Laufer***, Philip Scharfer, Wilhelm Schabel, Bryce S. Richards, Ian A. Howard, and Ulrich W. Paetzold. "Correlative In Situ Multichannel Imaging for Large-Area Monitoring of Morphology Formation in Solution-Processed Perovskite Layers". In: *Solar RRL* 6.3 (2021), p. 2100353. DOI: 10.1002/solr.202100353.

- **Felix Laufer**, Sebastian Ziegler, Fabian Schackmar, Edwin A. Moreno Viteri, Markus Götz, Charlotte Debus, Fabian Isensee, and Ulrich W. Paetzold. "Process Insights into Perovskite Thin-Film Photovoltaics from Machine Learning with In Situ Luminescence Data". In: *Solar RRL* 7.7 (2023), p. 2201114. DOI: 10.1002/solr.202201114.

- **Felix Laufer**, Markus Götz, and Ulrich W. Paetzold. "Deep learning for augmented process monitoring of scalable perovskite thin-film fabrication". In: *Energy & Environmental Science* (2025). DOI: 10.1039/D4EE03445G

Peer-Reviewed Publications (Co-Author)

- David B. Ritzer, Tobias Abzieher, Agit Basibüyük, Thomas Feeney, **Felix Laufer**, Simon Ternes, Bryce S. Richards, Stefan Bergfeld, and Ulrich W. Paetzold. "Upscaling of perovskite solar modules: The synergy of fully evaporated layer fabrication and all-laser-scribed interconnections". In: *Progress in Photovoltaics: Research and Applications* 30.4 (2022), pp. 360–373. DOI: 10.1002/pip.3489.

- Marco A. Ruiz-Preciado, Fabrizio Gota, Paul Fassl, Ihteaz M. Hossain, Roja Singh, **Felix Laufer**, Fabian Schackmar, Thomas Feeney, Ahmed Farag, Isabel Allegro, Hang Hu, Saba Gharibzadeh, Bahram Abdollahi Nejand, Veronique S. Gevaerts, Marcel Simor, Pieter J. Bolt, and Ulrich W. Paetzold. "Monolithic Two-Terminal Perovskite/CIS Tandem Solar Cells with Efficiency Approaching 25%". In: *ACS Energy Letters* 7.7 (2022), pp. 2273–2281. DOI: 10.1021/acsenergylett.2c00707.

- Julie Roger, Luisa K. Schorn, Minasadat Heydarian, Ahmed Farag, Thomas Feeney, Daniel Baumann, Hang Hu, **Felix Laufer**, Weiyuan Duan, Kaining Ding, Andreas Lambertz, Paul Fassl, Matthias Worgull, and Ulrich W. Paetzold. "Laminated Monolithic Perovskite/Silicon Tandem Photovoltaics". In: *Advanced Energy Materials* 12.27 (2022), p. 2200961. DOI: 10.1002/aenm.202200961.

- Bahram Abdollahi Nejand, David B. Ritzer, Hang Hu, Fabian Schackmar, Somayeh Moghadamzadeh, Thomas Feeney, Roja Singh, **Felix Laufer**, Raphael Schmager, Raheleh Azmi, Milian Kaiser, Tobias Abzieher, Saba

Gharibzadeh, Erik Ahlswede, Uli Lemmer, Bryce S. Richards, and Ulrich W. Paetzold. "Scalable two-terminal all-perovskite tandem solar modules with a 19.1% efficiency". In: *Nature Energy* 7.7 (July 2022), 620–630. DOI: 10.1038/s41560-022-01059-w.

- Fabian Schackmar, **Felix Laufer**, Roja Singh, Ahmed Farag, Helge Eggers, Saba Gharibzadeh, Bahram Abdollahi Nejand, Uli Lemmer, Gerardo Hernandez-Sosa, and Ulrich W. Paetzold. "In Situ Process Monitoring and Multichannel Imaging for Vacuum-Assisted Growth Control of Inkjet-Printed and Blade-Coated Perovskite Thin-Films". In: *Advanced Materials Technologies* 8.5 (2023), p. 2201331. DOI: 10.1002/admt.202201331.
- Ahmed Farag, Thomas Feeney, Ihteaz M. Hossain, Fabian Schackmar, Paul Fassl, Kathrin Küster, Rainer Bäuerle, Marco A. Ruiz-Preciado, Mario Hentschel, David B. Ritzer, Alexander Diercks, Yang Li, Bahram Abdollahi Nejand, **Felix Laufer**, Roja Singh, Ulrich Starke, and Ulrich W. Paetzold. "Evaporated Self-Assembled Monolayer Hole Transport Layers: Lossless Interfaces in p-i-n Perovskite Solar Cells". In: *Advanced Energy Materials* 13.8 (2023), p. 2203982. DOI: 10.1002/aenm.202203982.
- Benjamin Hacene, **Felix Laufer**, Simon Ternes, Ahmed Farag, Ronja Pappenberger, Paul Fassl, Somayeh Moghadamzadeh, Bahram Abdollahi Nejand, Thomas Feeney, Ian Howard, and Ulrich W. Paetzold. "Intensity Dependent Photoluminescence Imaging for In-Line Quality Control of Perovskite Thin Film Processing". In: *Advanced Materials Technologies* 9.11 (2023), p. 2301279. DOI: 10.1002/admt.202301279.
- Lukas Klein, Sebastian Ziegler, **Felix Laufer**, Charlotte Debus, Markus Götz, Klaus Maier-Hein, Ulrich W. Paetzold, Fabian Isensee, and Paul F. Jäger. "Discovering Process Dynamics for Scalable Perovskite Solar Cell Manufacturing with Explainable AI". In: *Advanced Materials* 36.7 (2023), p. 2307160. DOI: 10.1002/adma.202307160.
- Simon Ternes, **Felix Laufer**, and Ulrich W. Paetzold. "Modeling and Fundamental Dynamics of Vacuum, Gas, and Antisolvent Quenching for Scalable Perovskite Processes". In: *Advanced Science* 11.14 (2024), p. 2308901. DOI: 10.1002/advs.202308901.
- Hang Hu, Sophie X. An, Yang Li, Seyedamir Orooji, Roja Singh, Fabian Schackmar, **Felix Laufer**, Qihao Jin, Thomas Feeney, Alexander Diercks, Fabrizio Gota, Somayeh Moghadamzadeh, Ting Pan, Michael Rienäcker, Robby Peibst, Bahram Abdollahi Nejand, and Ulrich W. Paetzold. "Triple-junction perovskite–perovskite–silicon solar cells with power conversion efficiency of 24.4%". In: *Energy & Environmental Science* 17.8 (2024), pp. 2800-2814. DOI: 10.1039/D3EE03687A.
- Roja Singh, Hang Hu, Thomas Feeney, Alexander Diercks, **Felix Laufer**, Yang Li, The Duong, Fabian Schackmar, Bahram A. Nejand, and Ulrich W. Paetzold. "Danger in the Dark: Stability of Perovskite Solar Cells with Varied Stoichiometries and Morphologies Stressed at Various Conditions". In: *ACS Applied Materials & Interfaces* 16.21 (2024), pp. 27450-27462. DOI: 10.1021/acsami.4c04350.
- Daniel O. Baumann, **Felix Laufer**, Julie Roger, Roja Singh, Mohammad Gholipoor, and Ulrich W. Paetzold. "Repeatable Perovskite Solar Cells through Fully Automated Spin-Coating and Quenching". In: *ACS Applied Materials & Interfaces* 16.40 (2024), pp. 54007–54016. DOI: 10.1021/acsami.4c13024.

Conference Contributions

Conference Proceedings

- Simon Ternes, **Felix Laufer**, Philip Scharfer, Wilhelm Schabel, Bryce S. Richards, Ian A. Howard, and Ulrich Paetzold. "In situ reflectance-photoluminescence imaging on solution-processed perovskite thin-films". In: *2021 IEEE 48th Photovoltaic Specialists Conference (PVSC)*. 2021. DOI: 10.1109/PVSC43889.2021.9518569.
- Lukas Klein, Sebastian Ziegler, **Felix Laufer**, Charlotte Debus, Markus Götz, Klaus Maier-Hein, Ulrich Paetzold, Fabian Isensee, and Paul Jäger. "Understanding Scalable Perovskite Solar Cell Manufacturing with Explainable AI". In: *NeurIPS Workshop XAI in Action: Past, Present, and Future Applications*. 2023. URL: https://openreview.net/forum?id=xrEpp63 kz7.

Oral and Poster Contributions (First Author Only)

- **Poster – AI Hub Karlsruhe 2022**
  Felix Laufer, Sebastian Ziegler, Fabian Schackmar, Edwin A. Moreno Viteri, Markus Götz, Charlotte Debus, Fabian Isensee, and Ulrich W. Paetzold. "Machine Learning for Perovskite Thin-Film Photovoltaics". *AI Hub Karlsruhe 2022*. Karlsruhe, Germany. November 5-7, 2022.
- **Poster (online) – PVSEC-33 Asia 2022**
  Felix Laufer, Sebastian Ziegler, Fabian Schackmar, Edwin A. Moreno Viteri, Markus Götz, Charlotte Debus, Fabian Isensee, and Ulrich W. Paetzold. "Process insights into scalable perovskite thin-film fabrication using unsupervised machine learning of in situ luminescence data". *International Photovoltaic Science and Engineering Conference Asia 2022*. Nagoya, Japan. November 13-17 2022.
- **Talk – MRS Fall 2022**
  Felix Laufer, Sebastian Ziegler, Fabian Schackmar, Edwin A. Moreno Viteri, Markus Götz, Charlotte Debus, Fabian Isensee, and Ulrich W. Paetzold. "Process Understanding of Scalable Perovskite Thin-Film Formation through Unsupervised Machine Learning of in situ Luminescence Data". *Materials Research Society Fall Meeting 2022*. Boston, United States of America. November 27 - December 2, 2022.
- **Talk – E-MRS Fall 2023**
  Felix Laufer, Sebastian Ziegler, Fabian Schackmar, Edwin A. Moreno Viteri, Markus Götz, Charlotte Debus, Fabian Isensee, and Ulrich W. Paetzold. "Exploring Perovskite Thin Film Formation by Machine Learning on In Situ Photoluminescence Data". *European Materials Research Society Fall Meeting 2023*. Warsaw, Poland. September 18-21, 2023.
- **Talk – MATSUS Spring 2024**
  Felix Laufer, Lukas Klein, Sebastian Ziegler, Charlotte Debus, Markus Götz, Klaus Maier-Hein, Ulrich W. Paetzold, Fabian Isensee, and Paul F. Jäger. "Analyzing Perovskite Thin-Film Formation with Machine Learning and Explainable AI". *Materials for Sustainable Development Conference Spring Meeting 2024*. Barcelona, Spain. March 4-8, 2024.
- **Poster – tandemPV Workshop 2024**
  Felix Laufer, Sebastian Ziegler, Lukas Klein, Fabian Schackmar, Charlotte Debus, Klaus Maier-Hein, Paul F. Jäger, Markus Götz, Fabian Isensee, and Ulrich W. Paetzold. "Machine-learning-based in situ metrology for monitoring and predicting scalable perovskite thin-film formation". *tandemPV Workshop 2024*. Amsterdam, the Netherlands. June 25-27, 2024.

- **Talk – PSCO 2024 (presented by Paul Fassl)**
  Felix Laufer, Sebastian Ziegler, Lukas Klein, Fabian Schackmar, Charlotte Debus, Klaus Maier-Hein, Paul F. Jäger, Markus Götz, Fabian Isensee, Paul Fassl, and Ulrich W. Paetzold. "Augmenting In Situ Monitoring Of Perovskite Thin-Film Formation Using Deep Learning". *International Conference on Perovskite Solar Cells and Optoelectronics 2024*. Perugia, Italy. September 16-18, 2024.

Invited Contributions

- **Talk (online) – Helmholtz AI FFT Seminar 2022**
  Felix Laufer, Sebastian Ziegler, Jens Hauch, Markus Götz, Charlotte Debus, Fabian Isensee, and Ulrich W. Paetzold. "Machine Learning of in situ Luminescence Data for Process Insights into Perovskite Thin-Film Photovoltaics". Helmholtz AI project: AI-InSu-Pero. *Helmholtz AI Food for Thoughts (FFT) Seminar 2022*. Karlsruhe, Germany. September 1, 2022.
- **Talk – Helmholtz AI Consulting Roadshow @ KIT**
  Felix Laufer, Sebastian Ziegler, Fabian Schackmar, Edwin A. Moreno Viteri, Markus Götz, Charlotte Debus, Fabian Isensee, and Ulrich W. Paetzold. "Helmholtz AI Consulting Showcase: Perovskite Solar Cell Production Supervision System (PerSeuS)". *Helmholtz AI Consulting Roadshow @ KIT*. Karlsruhe, Germany. November 18, 2023.

Awards

- **Best Poster Award – KSOP Summer School 2022**
  Felix Laufer, Sebastian Ziegler, Fabian Schackmar, Edwin A. Moreno Viteri, Markus Götz, Charlotte Debus, Fabian Isensee, and Ulrich W. Paetzold. "Machine learning in situ photoluminescence data of the fabrication process of perovskite photovoltaics". *Karlsruhe School of Optics and Photonics Summer School 2022*. Research Area V - Solar Energy. Karlsruhe, Germany. September 29-30, 2022.
- **Young Researcher Award – E-MRS Fall 2023**
  Felix Laufer, Sebastian Ziegler, Fabian Schackmar, Edwin A. Moreno Viteri, Markus Götz, Charlotte Debus, Fabian Isensee, and Ulrich W. Paetzold. "Exploring Perovskite Thin Film Formation by Machine Learning on In Situ Photoluminescence Data". *European Materials Research Society Fall Meeting 2023*. Perovskites: from materials science to devices. Warsaw, Poland. September 18-21, 2023.

Published Datasets

- **Felix Laufer**, Sebastian Ziegler, Fabian Schackmar, Edwin A. Moreno Viteri, Markus Götz, Charlotte Debus, Fabian Isensee, and Ulrich W. Paetzold. "In Situ Photoluminescence Imaging Dataset of Blade-Coated Perovskite Photovoltaics". *Dataset*. Version v1.0. 2023. DOI: 10.5281/zenodo.7503391.
- **Felix Laufer**, Markus Götz, and Ulrich W. Paetzold. "In Situ Photoluminescence Dataset for Exploring Material and Processing Variabilities in Blade-Coated Perovskite Photovoltaics". *Dataset*. Version v1.0. 2025. DOI: 10.5281/zenodo.14609789.

Supervised Student Projects

- Vagner Takiya Bonadio. “Automated post-processing of white light interferometer measurement raw data”. Europhotonics internship. 2020.
- Roja Sudhakumar. “Solar cell device fabrication for experimental dataset generation”. Student assistant. 2021.
- Edwin Andres Moreno Viteri. “Experimental determination of labels for generated dataset”. Student assistant. 2021.
- Edwin Andres Moreno Viteri. “Acquisition and automated processing of perovskite layer thickness data for machine learning algorithms”. Research project. 2022.
- Edwin Andres Moreno Viteri. “Convolutional neural network for prediction of solar cell thickness”. KSOP internship. 2022.
- Sunny Abraham. “Comparison of prediction performance using different machine learning regressors”. Student assistant. 2023.
- Kerem Kağan Güçlü. “Labeling of photoluminescence images for semantic segmentation”. Student assistant. 2024.
- SeyedehFatemeh MousaviMatin. “Labeling of photoluminescence images for semantic segmentation”. Student assistant. 2024.

Acknowledgments

This PhD thesis and all the work associated with it would not have been possible without the guidance and support of my supervisor, colleagues, collaborators, friends, and family.

First and foremost, I want to thank my doctoral supervisor Prof. Dr. Ulrich W. Paetzold for giving me the opportunity to pursue my PhD in his research group. I am grateful for his confidence in allowing me to be the first student to explore research topics at the intersection of perovskite photovoltaics and machine learning, hopefully to be followed by many more in this direction. His guidance, creativity, and enthusiasm were invaluable, providing motivation and fresh perspectives, especially in moments when things were not going as planned. Our discussions always left me with renewed motivation and determination.
I would also like to take the opportunity to thank TT-Prof. Dr. Sebastian Krumscheid for taking on the role of second reviewer.
In addition, I would like to offer my special thanks to Dr. Ian A. Howard for encouraging me to join Prof. Paetzold's research group and for helping us to implement *in situ* multi-channel imaging. I also want to thank Prof. Dr. Uli Lemmer for his continuous support during my long time at the Light Technology Institute at KIT.
I want to express my special gratitude to all current and former members of the Perovskite Taskforce at KIT. The continuous collaboration, the exchange of knowledge and expertise as well as the technical support have been fundamental for this work. Without the contributions of my colleagues, the results of this thesis would not have been possible. In particular, I want to thank Dr. Fabian Schackmar and Dr. Simon Ternes for the close collaboration, which not only led to valuable and insightful results but also made working together an pleasant experience.
I am also deeply grateful to all my colleagues from partner research institutes and universities. In particular, I would like to thank Dr. Charlotte Debus and Dr. Markus Götz from Helmholtz AI for initiating the interdisciplinary collaboration working on machine learning for perovskite photovoltaics and for their invaluable support in helping us take the first steps in this direction. I sincerely appreciate the fruitful collaboration between the Perovskite Taskforce and Helmholtz AI, which was further strengthened by the contributions of Dr. Fabian Isensee and Sebastian Ziegler, as well as Dr. Paul F. Jäger and Lukas Klein from Helmholtz Imaging, whose expertise significantly enriched this project. Additionally, I would like to express my gratitude to Dr. Michael Götte from Helmholtz-Zentrum Berlin for his continuous support in countless Zoom calls, guiding us through the implementation of electronic lab notebooks essential for managing the research data of our entire group.
I would like to thank all the students I have supervised over the past five years for their dedication and hard work, which have contributed to the success of this work.
In addition, I would also like to extend my heartfelt thanks to all my colleagues at LTI, who have made coming to work an absolute pleasure. A special thanks to my office mates Benjamin Hacene, Julian Petermann, Dr. Saba Gharibzadeh, Dr. Sara Moghadamzadeh, Dr. Simon Ternes, and Xuzheng Liu for the enjoyable moments we shared. I am grateful for the many entertaining lunch breaks and countless *Currywurst* meals I shared with Dr. Ahmed Farag, Alexander Diercks, Dr. Bahram Abdollahi Nejand, Daniel Baumann, Dr. Fabian Schackmar, Dr. Hang Hu, Joshua Damm, Julian Petry, Julie Roger, Dr. Paul Faßl, Roja Singh, and Ronja Pappenberger. Additionally, I sincerely want to thank all current and former members of the Perovskite Taskforce, as well as Dr. Andres Rösch, Dr. Dominik Theobald, Dr. Henning Mescher, Jan Feßler, Dr. Junchi Chen, and Dr. Robert Huber, for the memorable after-work events and get-togethers that made my time at LTI special.
I would like to sincerely thank Nicole Klöfer, Dr. Jurana Hetterich, Astrid Henne, Reza Akbarzadeh Naseri, Christian Kayser, Julian Schickle, Felix Geislhöringer, and Mario Sütsch for their administrative and technical

support over the past few years, which enabled a smooth working environment. I would also like to thank the Karlsruhe School of Optics and Photonics (KSOP) for the opportunity to participate in their graduate program and for organizing numerous scientific and social events.
Special thanks to Benjamin Hacene, Daniel Baumann, Dr. Fabian Schackmar, Dr. Helge Eggers, Joshua Damm, Julian Petermann, Julian Petry, Kristina Geistert, and Raphael Pesch for proofreading parts of this thesis.

Zuletzt möchte ich mich bei all den Menschen bedanken, die mich während meiner Promotion im privaten Umfeld unterstützt und motiviert haben. Meiner Familie, insbesondere meinen Eltern, gilt mein tiefer Dank für ihre unerschütterliche Unterstützung in allen Lebenslagen. Meinen Freunden danke ich für die wertvollen Ablenkungen abseits der Arbeit und die stetige Motivation, die Promotion erfolgreich abzuschließen. Ein ganz besonderer Dank gilt meiner Verlobten Stefanie, deren unermüdliche Unterstützung und unzählige Ermutigungen mir stets Kraft gegeben haben. Ohne sie wäre dieser Weg um vieles schwerer gewesen. Vielen Dank!